Integrated Photonic Circuits on SOI and SiNOI Platforms for High-Sensitivity Sensing and Reconfigurable Multi-Passband Filtering

Simeng Zhu

Submitted in fulfilment of the requirements for the degree of

Doctor of Philosophy (Ph.D.)

James Watt School of Engineering

College of Science and Engineering

University of Glasgow

November 2025

Abstract

Integrated photonics offers compact and energy-efficient platforms for label-free biochemical sensing and agile spectrum control. This thesis establishes a unified design framework on silicon on insulator (SOI) and silicon nitride on insulator (SiNOI) that links two capabilities: enhancing light-matter interaction for refractometric sensing while constraining excess loss, and realising reconfigurable multi-passband photonic filters with predictable, programmable spectra. The work combines electromagnetic and coupled-mode modelling, reconstruction equivalent chirp design, heater-matrix control, foundry-compatible fabrication, and system-level characterisation using optical frequency comb sources and thermo-optic tuning. It demonstrates that sensitivity enhancement and spectral programmability can be obtained through spatially distributed design and algorithmically coordinated actuation, rather than by accepting large insertion-loss penalties.

For sensing, three-slot hybrid plasmonic waveguides are engineered to localise the evanescent field at the analyte interface while routing most optical power through low-loss analyte sections. This architecture supports stable C-band operation and provides a route to array-scalable sensors intended for monitoring biomolecular binding and concentration changes in microfluidic lab-on-chip diagnostics.

For filtering, phase-shifted sampled Bragg grating devices are synthesised using the reconstruction equivalent chirp (REC) technique to spatially decouple reflection points, enabling independent control of multiple passbands. Integrated micro-heater matrices provide reconfiguration and algorithm-assisted phase synthesis, combining self-adaptive differential evolution with local optimisation, coordinates multi-parameter tuning to obtain low-ripple spectra. Three architectures validate the framework: a dual-passband filter based on coupled phase-shifted cavities, a programmable four-phase shift sampled Bragg grating (4PS-SBG) on SiNOI enabling selectable multi-passband and stopband responses, and a cascaded superstructure grating with a microring resonator enabling optical-domain frequency multiplication and hopping.

Overall, the thesis provides design rules for co-optimising waveguide confinement, photon distribution, and heater matrix control in integrated photonics, underpinning scalable programmable photonic circuits and future heterogeneous integration with on-chip light sources.

Publications

Journal papers

1. **S. Zhu**, B. Yuan, Y. Fan, M. Al-Rubaiee, X. Sun, Z. Li, A. S. Hezarfen, A. E. Kelly, J. H. Marsh, and L. Hou, "A reconfigurable multi-channel on-chip photonic filter for programmable optical frequency division," *Nanophotonics* **14**, 2619-2631 (2025).

2. **S. Zhu**, B. Yuan, W. Cheng, Y. Fan, Y. Sun, M. Al-Rubaiee, J. Akbar, J. Marsh, and L. Hou, "Dual-band Photonic Filters with Wide Tunable Range Using Chirped Sampled Gratings," *IEEE Photonics Technology Letters* **37**, 169-172 (2025).

3. **S. Zhu**, B. Yuan, M. Al-Rubaiee, Y. Sun, Y. Fan, A. S. Hezarfen, S. J. Sweeney, J. H. Marsh, and L. Hou, "Widely tunable photonic filter based on equivalent chirped Four-Phase-Shifted sampled Bragg gratings," *ACS Photonics* **12**, 899-907 (2025).

4. M. Al-Rubaiee, **S. Zhu**, X. Sun, J. Wang, A. Hezarfen, Z. Wang, J. Marsh, S. Sweeney and L. Hou, "Dual-wavelength distributed feedback laser based on waveguide Bragg grating microcavities," *Optics Letters* **50**, 7219-7222 (2025).

5. Ahmet Hezarfen, Z. Li, Mohanad Al-Rubaiee, **S. Zhu**, Z. Wang, J. Marsh, and L. Hou, "Energy-efficient all-optical control of optomechanical photonic crystal nanobeam cavities," *Optics Letters* **50**, 6598-6601 (2025).

6. M. Al-Rubaiee, Y. Fan, B. Yuan, Y. Sun, **S. Zhu**, A. Seckin, Z. Wang, X. Sun, J. Marsh, S. J. Sweeney, and L. Hou, "Monolithic Multi-Wavelength Mode-Locked DFB Laser Using Chirped Conventional and Four-Phase-Shifted Sampled Bragg Gratings," *IEEE Journal of Quantum Electronics* (2025). (Early Online Publication)

7. S. Wu, **S. Zhu**, K. T. Lai, L. Hou, V. Pusino, and D. R. S. Cumming, "A Linear-to-Linear Cross-Polarization Conversion q-BIC Metasurface for Transmission Mode Mid-Infrared Spectral Filtering," *Laser & Photonics Review* (2025). (Early Online Publication)

8. M. Al-Rubaiee, B. Qiu, **S. Zhu**, X. Sun, A. S. Hezarfen, Z. Wang, J. Marsh, S. J. Sweeney, and L. Hou, "Broadband 100 GHz Frequency Comb From an Asymmetric MQW Passively Mode-Locked Laser," *IEEE Photonics Technology Letters* **37**, 1365-1368 (2025).

9. M. Al-Rubaiee, X. Sun, B. Yuan, Y. Fan, **S. Zhu**, Y. Sun, J. H. Marsh, S. J. Sweeney, and L. Hou, "Simultaneous Multi-Wavelength Mode-Locked DFB Laser based on waveguide Bragg grating microcavities," *Optics Express* **33**, 22222-22234 (2025).

10. A. S. Hezarfen, **S. Zhu**, M. Al-Rubaiee, J. H. Marsh, and L. Hou, "All-Optical Reconfigurable Photonic Crystal-Microring Hybrid Cavities with High-Efficiency Tuning via the Mechanical Kerr Effect," *Optics Express* **33**, 20722-20735 (2025).

11. Y. Fan, M. Al-Rubaiee, **S. Zhu**, B. Yuan, X. Sun, Y. Sun, A. E. Kelly, J. H. Marsh, and L. Hou, "Mode-Locked DBR and DFB Lasers with Multiple Phase-Shifted Gratings for THz Generation," *Journal of Lightwave Technology* **43**, 7752-7760 (2025).

12. Y. Sun, B. Yuan, X. Sun, **S. Zhu**, Y. Fan, M. Al-Rubaiee, J. H. Marsh, S. J. Sweeney, and L. Hou, "Narrow linewidth distributed feedback lasers utilizing distributed phase shift," *Optics Letters* **50**, 471-474 (2024).

13. Y. Sun, **S. Zhu**, B. Yuan, Y. Fan, M. Al-Rubaiee, X. Sun, J. H. Marsh, S. J. Sweeney, and L. Hou, "Continuous phase modulation technology based on grating period interval for high grating coupling efficiency and precise wavelength control," *Optics Letters* **50**, 750-753 (2024).

14. M. Al-Rubaiee, B. Yuan, Y. Fan, **S. Zhu**, J. Marsh, and L. Hou, "Ultrastable 10 GHz Mode-Locked laser on Semi-Insulating substrate through RF injection locking," *IEEE Photonics Technology Letters* **36**, 1189-1192 (2024).

15. Y. Fan, B. Yuan, M. Al-Rubaiee, Y. Sun, **S. Zhu**, J. H. Marsh, and L. Hou, "Dual-wavelength distributed feedback laser array based on four-phase-shifted sampled Bragg grating for terahertz generation," *Optics Letters* **49**, 3472-3475 (2024).

16. Y. Fan, B. Yuan, M. Al-Rubaiee, Y. Sun, **S. Zhu**, J. Akbar, J. Marsh, and L. Hou, "Millimeter-Wave generation based on four Phase-Shifted sampled Moiré grating Dual-Wavelength DFB laser," *IEEE Photonics Technology Letters* **36**, 282-285 (2024).

17. L. Hou, B. Yuan, Y. Fan, X. Sun, Y. Sun, **S. Zhu**, S. J. Sweeney, and J. H. Marsh, "Monolithic dual wavelength DFB lasers based on sidewall gratings for THZ/MMW signal generation," *IEEE Journal of Selected Topics in Quantum Electronics* **31**, 1-13 (2024).

18. B. Yuan, Y. Fan, **S. Zhu**, W. Cheng, Y. Zhang, X. Chen, S. Ye, S. Liang, Y. Huang, R. Zhang, J. Akbar, J. H. Marsh, and L. Hou, "Millimeter-wave generation based on a monolithic dual-wavelength DFB laser with four phase-shifted sampled gratings and equivalent chirp technology," *Optics Letters* **48**, 5093-5096 (2023).

Conference papers

1. **S. Zhu**, M. Al-Rubaiee, Y. Fan, X. Sun, Y. Sun, J. H. Marsh and L. Hou, "A Programmable and Reconfigurable On-Chip Photonic Filter for Next-Generation Multi-Channel DWDM," in *ECOC 2025; 51st European Conference on Optical Communication* (2025).

2. **S. Zhu**, T. Wu, Y. Fan, X. Sun, B. Liu, J. H. Marsh and L. Hou, "Integrated Multi-Band Photonic Filter Based on MRR-SSG for Tunable Frequency Hopping," in *ECOC 2025; 51st European Conference on Optical Communication* (2025).

3. **S. Zhu**, M. Al-Rubaiee, B. Yuan, Y. Fan, Y. Sun, J. H. Marsh, and L. Hou, "Broadband tunable microwave photonic filter utilizing equivalent chirped sampled Bragg gratings for optical frequency division," in *Optical Fiber Communication Conference (OFC) 2025*, Technical Digest Series (2025).

4. **S. Zhu**, M. J. A. Al-Rubaiee, B. Yuan, Y. Fan, Y. Sun, J. H. Marsh, and L. Hou, "Dual-band microwave photonic filter utilizing equivalent chirped four-phase-shifted sampled Bragg grating for 52.1GHz-439.5GHz range," in *SPIE Photonics West 2025* (2025).

5. **S. Zhu**, B. Yuan, Y. Fan, Y. Sun, J. H. Marsh and L. Hou, "Tunable Dual-band Microwave Photonic Filters Covering 37.2 GHz to 186.1 GHz Utilizing Chirped Sampled Gratings," in *ECOC 2024; 50th European Conference on Optical Communication* (2024).

6. **S. Zhu**, W. Cheng, B. Yuan, Y. Fan, Y. Sun, A. S. Hezarfen, J. H. Marsh and L. Hou, "High Sensitivity Biochemical Sensors Based on a Mach-Zehnder Interferometer with a

Slot Bus Waveguide and Double Slot Hybrid Plasmonic Waveguide," in *ECOC 2024; 50th European Conference on Optical Communication* (2024).

7. A. S. Hezarfen, **S. Zhu**, M. Al-Rubaiee, Z. Wang, J. H. Marsh, L. Hou, "Highly Efficient All-Optical Control of Optomechanical Photonic Crystal Nanobeam Cavities via the Mechanical Kerr Effect," in *ECOC 2025; 51st European Conference on Optical Communication* (2025).

8. M. Al-Rubaiee, X. Sun, Y. Fan, **S. Zhu**, Y. Sun, A. Seckin, J. H. Marsh, S. J. Sweeney, L. Hou, "Monolithic Multi-Wavelength Mode-Locked DFB Laser Based on Waveguide Bragg Grating Microcavities," in *ECOC 2025; 51st European Conference on Optical Communication* (2025).

9. M. Al-Rubaiee, B. Yuan, Y. Fan, **S. Zhu**, Y. Sun, X. Sun, J. H. Marsh, S. J. Sweeney, L. Hou, "Four-Wavelength Mode-Locked DFB Laser Using Chirped Sampled Bragg Grating," in *Conference on Lasers and Electro-Optics/Europe (CLEO/Europe 2025) and European Quantum Electronics Conference (EQEC 2025)* (2025)

10. A. S. Hezarfen, **S. Zhu**, B. Yuan, S. J. Sweeney, L. Hou, "Harnessing the Mechanical Kerr Effect for Optical Control in Photonic Crystal Nanobeam Cavities," in *2025 Conference on Lasers and Electro-Optics (CLEO 2025)* (2025)

11. M. Al-Rubaiee, Y. Fan, B. Yuan, **S. Zhu**, Y. Sun, A. S. Hezarfen, J. H. Marsh, S. J. Sweeney, L. Hou, "Four-Wavelength Mode-Locked DFB Laser with Four Phase-Shifted Chirped Sampled Bragg Grating," in *2025 Conference on Lasers and Electro-Optics (CLEO 2025)* (2025)

12. Z. Wang, Y. Fan, X. Sun, B. Yuan, Y. Sun, M. Al-Rubaiee, A. S. Hezarfen, **S. Zhu**, J. H. Marsh, A. E. Kelly, L. Hou, "Linewidth-Reduced Optical Injection-Locked Laser Utilizing Four-Phase-Shifted Sampled Bragg Gratings," in *2025 Conference on Lasers and Electro-Optics (CLEO 2025)* (2025)

13. A. S. Hezarfen, **S. Zhu**, B. Yuan, J. H. Marsh, L. Hou, "Photonic Crystal-Microring Hybrid Cavities for Enhanced Optomechanical Tuning," in *2025 Conference on Lasers and Electro-Optics (CLEO 2025)* (2025)

14. B. Yuan, Y. Fan, **S. Zhu**, Y. Zhang, J. H. Marsh, L. Hou, "Dual-wavelength DFB Laser Based on Four Phase-shifts Sections and Equivalent Chirp Technology for Millimeter-wave Generation," in *Conference on Lasers and Electro-Optics/Europe (CLEO/Europe 2023) and European Quantum Electronics Conference (EQEC 2023)* (2023)

Table of contents

List of figures

Acronyms

4PS-SBG	Four-Phase-Shift Sampled Bragg Grating
AI	Artificial-Intelligence
AWG	Arrayed Waveguide Grating
BIC	Bound-State-in-the-Continuum
BOX	Buried Oxide
CMOS	Complementary Metal-Oxide-Semiconductor
CPO	Co-Packed Optic
C-SBG	Conventional Sampled Bragg Grating
CWDM	Coarse Wavelength Division Multiplexing
DEMUX	Demultiplexing
DFB	Distributed Feedback
DWDM	Dense Wavelength Division Multiplexing
EBL	Electron-Beam Lithography
EDFA	Erbium-Doped Fibre Amplifier
EO	Electro-Optic
EPS	Equivalent Phase Shift
ER	Extinction Ratio
FDE	Finite-Difference Eigenmode
FDTD	Finite-Difference Time-Domain
FoM	Figure of Merit
FSR	Free Spectral Range
GC	Grating Coupler
GHz	Gigahertz
GPIB	General-purpose Interface Bus
HF	Hydrofluoric Acid
HPW	Hybrid Plasmonic Waveguides
HSQ	Hydrogen Silsesquioxane
ICP	Inductively Coupled Plasma
IPA	Isopropyl Alcohol
ISO	Isolator
JWNC	James Watt Nanofabrication Centre
LED	light-Emitting Diode
MDM	Metal-Dielectric-Metal
MH	Micro Heater
MMW	Millimetre-Wave
MPF	Microwave Photonic Filter
MRR	Microring Resonator
MWP	Microwave Photonics
MZI	Mach-Zehnder Interferometer
OE	Opto-Electronic
OFC	Optical Frequency Comb
OFD	Optical Frequency Division
OSA	Optical Spectrum Analyser
PC	Polarization Controller
PD	Photodetector
PECVD	Plasma-Enhanced Chemical Vapour Deposition

PF	Photonic Filter
PIC	Photonic Integrated Circuit
PMMA	Polymethyl Methacrylate
PS	Phase Shift
PS-BG	Phase-Shifted Bragg Grating
PSW	Plasmonic Slot Waveguide
QAM	Quadrature Amplitude Modulation
RBW	Resolution Bandwidth
REC	Reconstruction Equivalent Chirp
RF	Radio-Frequency
RO	Reverse-Osmosis
RoF	Radio-over-Fibre
SA	Saturable-Absorber
SaDE	Self-adaptive Differential Evolution
SBS	Stimulated Brillouin Scattering
SBW-DSHPW	Slot Bus Waveguide and Double Slot Hybrid Plasmonic Waveguide
SiNOI	Silicon Nitride On Insulator
SLD	Superluminescent Diode
SMF	Single-Mode Fibre
SMLL	Semiconductor Mode Locked Laser
SMSR	Side Mode Suppression Ratio
SNR	Signal-to-Noise Ratio
SOI	Silicon On Insulator
SPP	Surface Plasmon Polariton
SQP	Sequential Quadratic Programming
SSG	Superstructure Grating
SWG	Subwavelength-Grating
SWGS	Subwavelength-Grating Slot
TE	Transverse-Electric
TFLN	Thin Film Lithium Niobate
THz	Terahertz
TM	Transverse-Magnetic
TMM	Transfer-Matrix Method
TO	Thermo-Optic
UBG	Uniform Bragg Grating
WDM	Wavelength-Division Multiplexing

Acknowledgements

This thesis gathers the lessons of three years and closes a four-and-a-half-year journey in Scotland. To look back is to be grateful—for the people and the small mercies that stayed with me, for the moments that steadied my hands and widened my heart.

I owe my first thanks to Professor Lianping Hou. At the beginning, research felt like a thicket. He met confusion with patience, offered courage as well as guidance, and set my feet on the path. His scholarship and rigour trained my mind, taught me to think for myself, and formed in me a careful, pragmatic habit that I will carry for life. He opened the door to a first-class lab and to chances to learn on international stages; this thesis stands on that ground.

I thank Professor John H. Marsh for his commanding perspective and gracious example, which always lifted my ambitions and broadened my view. I am also indebted to Professor Stephen J. Sweeney and Professor Anthony E. Kelly for their timely help, wise advice, and even material support when it mattered most.

My appreciation goes to Dr Bocheng Yuan, Dr Yizhe Fan, Dr Xiao Sun, Dr Yiming Sun, Mohanad Al-Rubaiee, and Tao Wu, whose steady help kept the project on time and on track, and whose conversations often lit up new ideas. I am grateful to Dr Shengwei Ye, Dr Xiao Jin, and Shuhao Wu for bringing warmth and laughter into long, hurried days. To the colleagues and staff at JWNC: thank you for your quiet, generous work in process development and tool support.

To my parents and my family: thank you for trusting my choices, for indulging my stubborn streak, and for making it possible for me to live and study in Glasgow without worry. I was not often by your side, and that weighs on me. I owe my parents more than I can ever repay. And to my grandfather, who will not hear this good news, I send my love all the same.

Ten years ago, a lazier and more timid self would never have pictured this distance. Perhaps I have not changed so much, but I am grateful to that earlier self for one brave step at a time, and for the patience to keep going. A new road opens now. May I be more diligent, braver. The road is long; the walking will bring me there. In the quiet hum of the cleanroom, devices took shape—and so did a steadier, more reverent me.

Author declaration

I hereby declare that the submitted PhD thesis, titled ***Integrated Photonic Circuits on SOI/SiNOI Platforms for High-Sensitivity Sensing and Advanced Multi-Passband Filtering***, is the result of my independent and original research conducted at the James Watt School of Engineering, University of Glasgow. All sources of information and materials used in the thesis have been clearly cited and acknowledged within the text. Where the work of others has been included, it has been properly referenced following academic conventions.

I solemnly declare that this thesis does not contain any instances of academic misconduct, such as plagiarism, fabrication, or falsification of data. This work has not been submitted, either in whole or in part, for any other degree or qualification. I assume full responsibility for the legitimacy and authenticity of the findings presented in this thesis.

Simeng Zhu 21/11/2025

1 Introduction

This thesis investigates reconfigurable on-chip photonic filters for microwave photonics and waveguide-based biochemical sensors because both require engineered spectral selectivity and phase control in compact, scalable photonic integrated circuits (PICs). A common silicon-on-insulator (SOI) and silicon nitride on insulator (SiNOI) platform, along with shared building blocks such as Bragg gratings, microring resonators (MRR), and interferometric structures, enables a unified design, fabrication, and characterisation methodology for addressing high-frequency RF and THz signal processing and label-free refractive-index transduction.

1.1 Overview of microwave photonics

Microwave photonics (MWP) is an interdisciplinary field that fuses optics, microwave engineering and electronics to generate, transport, control and process microwave and millimetre-wave signals using photonic means. Its central premise is to map a microwave signal onto an optical carrier, to perform broadband and low-loss operations in the optical domain, then to recover the microwave information by photodetection. Compared with purely electronic systems, MWP offers ultrawide bandwidth, low transmission loss, strong immunity to electromagnetic interference and largely frequency-independent operation, thereby overcoming long-standing constraints on speed and spectral efficiency in electronics.

In terms of frequency, microwaves typically span 300 MHz to 300 GHz, corresponding to wavelengths from 1 m to 1 mm [1,2]. With the rapid development of wireless communications, radar and satellite systems, spectral congestion in the microwave bands has intensified, and operating frequencies are steadily extending into the millimetre-wave (MMW) and terahertz (THz) regimes. At such high frequencies, conventional electrical media such as coaxial cables and metallic waveguides incur severe attenuation and dispersion, while electronic devices face limitations in high-frequency response, dynamic range and linearity. Photonic technologies provide an alternative route. Owing to their low-loss transmission, extreme bandwidth, and immunity to electromagnetic interference, optical fibre and integrated waveguides allow microwave signals to propagate and be processed efficiently as optical signals, enabling a complementary fusion of electronics and photonics [3,4].

The emergence of MWP is closely tied to advances in radar and communication systems. Early work can be traced to radar developments during the Second World War, when the value of optical delay lines for low-loss signal timing became apparent [5]. In the late 1980s and early 1990s, the maturity of erbium-doped fibre amplifiers (EDFAs) and wavelength-division multiplexing (WDM) established the foundations for high-capacity optical communications, in turn catalysing systematic research in MWP [6]. The field has since expanded to encompass radio-over-fibre (RoF), optically generated microwaves and MMW, microwave photonic filters (MPFs), optically controlled phase shifting and delay, and photonic phased-array radar.

As illustrated schematically in Figure 1.1, a typical MWP link comprises three core modules, namely the optical source, the electro-optic (EO) modulator and the photodetector (PD) [7]. A radio-frequency (RF) signal is impressed onto an optical carrier by direct or external modulation, after which the optical waveform propagates through fibre or on-chip waveguides, where operations such as filtering, frequency conversion, distribution and amplification may be performed, before photodetection converts the modulated light back to a microwave signal. The mapping of frequency, phase and amplitude between the optical and microwave domains determines the EO and opto-electronic (OE) transfer characteristics, which allow precise control of microwave phase and spectral content through optical processing. This approach achieves high-frequency performance that is challenging for conventional microwave systems and substantially enhances system flexibility and scalability.

MWP supports a broad application space spanning communications, radar, sensing, electronic warfare, metrology and navigation. In wireless communications, RoF transports high-frequency radio signals between central offices and distributed base stations through optical fibre, extending coverage, improving spectral utilisation and reducing attenuation [8–10]. The technology has been deployed commercially in fifth-generation systems. In defence and radar, photonic phased arrays built from fibre delay lines and optically controlled phase shifters enable wide instantaneous bandwidth, reduced beam squint and excellent phase stability, and they have seen extensive use in airborne and shipborne radar platforms [11,12]. Photonic inertial and acoustic sensors, such as fibre-optic gyroscopes and hydrophones, are key instruments in navigation and underwater monitoring [13,14].

Photonic sensing architectures further allow highly sensitive measurements of temperature, strain, vibration and refractive index, which are exploited in structural health monitoring of

bridges and dams, in aerospace systems and in medical instrumentation [15–17]. With the rapid progress of PICs, MWP is migrating from discrete optical benches to chip-scale implementations [18,19]. Integration reduces footprint and power consumption, enhances stability and repeatability, and provides a versatile platform for reconfigurable high-frequency signal processing. Integrated MWP is now a central research focus and a credible route to compact, low-cost and high-performance MWP systems [7,20].

In summary, MWP represents a deep fusion of electronics and photonics. It inherits the large bandwidth and low loss of photonics while compensating for the high-frequency limitations of microwave electronics. Its continuing development in high-speed communications, wideband radar, advanced sensing and emerging computing paradigms signals a progressive transition of modern information systems towards tightly integrated EO platforms.

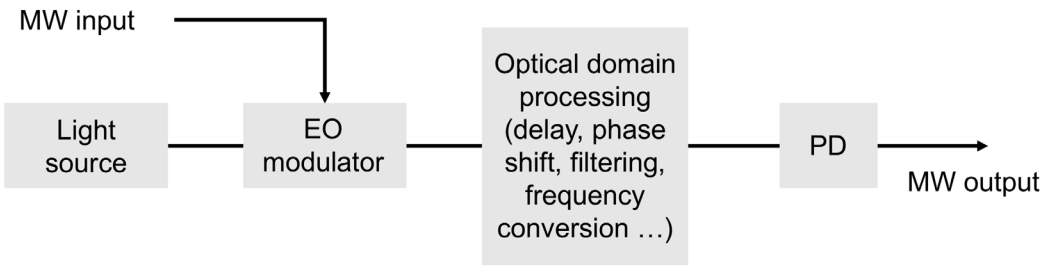

Fig. 1.1 Basic architecture of a microwave photonic link.

Although MWP and biochemical sensing are often discussed separately, they converge at the device level when implemented on a chip. In both cases, information is encoded into measurable spectral features, such as passbands, notches or resonance shifts, through controlled interference, resonance or Bragg reflection. Integrated photonics, therefore, provides a common route to scalability, stability and low power by co-integrating low-loss waveguides, spectral-selective elements and thermo-optic (TO) tuning. The following section outlines waveguide-based biochemical sensors and motivates why the same SOI and SiNOI integration toolkit is adopted in this thesis.

1.2 Overview of biochemical sensors

Biochemical sensors convert biological or chemical quantities of interest into measurable physical signals and have become indispensable in biomedicine, environmental surveillance, food safety and industrial process control [21,22]. From a detection standpoint, they can be categorised as label-based and label-free. Label-based methods rely on fluorescent or related amplification mechanisms to report binding events. Label-free approaches interrogate the

intrinsic light-matter interaction, including absorption, Raman scattering and refractive-index perturbations, and they enable real-time measurements with small sample volumes and in situ operation. Among these, refractive-index sensing is particularly attractive because high-performance device structures can be realised readily [23].

Compared with fibre-based or other free-space-coupled solutions, planar waveguide sensors implemented on chip, hereafter referred to as waveguide-based on-chip biochemical sensors, can be tightly integrated with optoelectronic components and microfluidics. They offer compact form factor, strong immunity to electromagnetic interference, multiplexing capability and portability, which together support low-cost and rapid lab-on-chip systems [24–26]. Common waveguide platforms include SiO_2, Si_3N_4, Si_2N_2O, SOI and polymers, all of which permit heterogeneous device integration on a single substrate. Representative device archetypes, sketched in Figure 1.2, include the Mach-Zehnder interferometer (MZI) [27,28], MRR and microdisk resonator [29, 30], Bragg and long-period gratings [31,32], two- and multimode interferometers [33,34] and directional couplers [35]. These structures provide different compromises among sensitivity, dynamic range and integrability for distinct application scenarios.

The essence of label-free refractive-index sensing is to transduce the environmental refractive-index variation into a measurable change in optical phase, amplitude or resonance. In interferometric and resonant devices, the MZI converts a differential phase shift (PS) between its arms into intensity modulation or spectral drift. MRRs exploit strong field localisation and narrow linewidths to deliver high sensitivity within a small footprint. Grating structures employ Bragg conditions or modal coupling to generate readout spectral features. Rings are often favourable for dense arrays and minute sample volumes, although their linear dynamic range can be limited. Gratings occupy a larger footprint yet offer a wider range and can be well matched to system-level readout.

Performance is commonly quantified by the sensitivity S (equation (1.1)). The quality factor Q (equation (1.2)), and a typical aggregate metric is the figure of merit FoM (equation (1.3)) [23]. Practical design requires a balance between strengthening light-matter overlap, which increases S, and suppressing loss to achieve high Q and narrow linewidth. This trade-off motivates innovation in device structures alongside materials and process optimisation.

$$S = \Delta f / \Delta n \tag{1.1}$$

$$Q = f_0 / FWHM \tag{1.2}$$

$$FoM = S / FWHM \tag{1.3}$$

where Δf is the shift of the resonance centre frequency caused by a refractive index perturbation Δn in the analyte or cladding. Spectral selectivity is characterised by f_0, the unperturbed resonance frequency, and the FWHM (full width at half maximum) of the resonance line. The Q is dimensionless and represents the combined effects of intrinsic and coupling losses.

The design space is broad. Subwavelength and micro-nanostructured waveguides such as slot waveguides, plasmonic or photonic-crystal configurations, and slow-light or field-enhanced cavities can markedly increase near-field overlap and surface sensitivity. At the system level, hybrid architectures such as MZI-slot, MZI-plasmonic or ring-photonic-crystal combinations can reconcile sensitivity, linear range, selectivity and multiplexing. Recent work on coupled rings with photonic crystals, including one-dimensional photonic-crystal rings, offers new device paradigms for stronger coupling and improved multiplexing potential.

Materials and platform selection are equally important. SOI provides high index contrast that supports tight confinement and miniaturisation, although nonlinear effects and absorption may introduce additional loss. Si_3N_4 exhibits excellent transparency in the near-infrared and visible, low propagation loss and mature fabrication, which make it a strong low-loss passive platform. Polymers allow low-cost deposition and refractive-index engineering, though chemical stability and environmental robustness need careful engineering. Differences across platforms in surface functionalisation, biocompatibility, thermal stability and packaging compatibility directly affect system-level performance and application readiness.

In terms of applications, waveguide-based on-chip biochemical sensors have been deployed for label-free detection of nucleic acids, proteins, ions and small molecules, and for in situ monitoring of volatile hazardous gases and heavy-metal ions [36–41]. For extremely low concentrations and minute refractive-index variations, as encountered with certain small-molecule gases, further enhancement of light-matter interaction and suppression of system noise remain critical challenges, key to advancing sensitivity and lowering the detection limit.

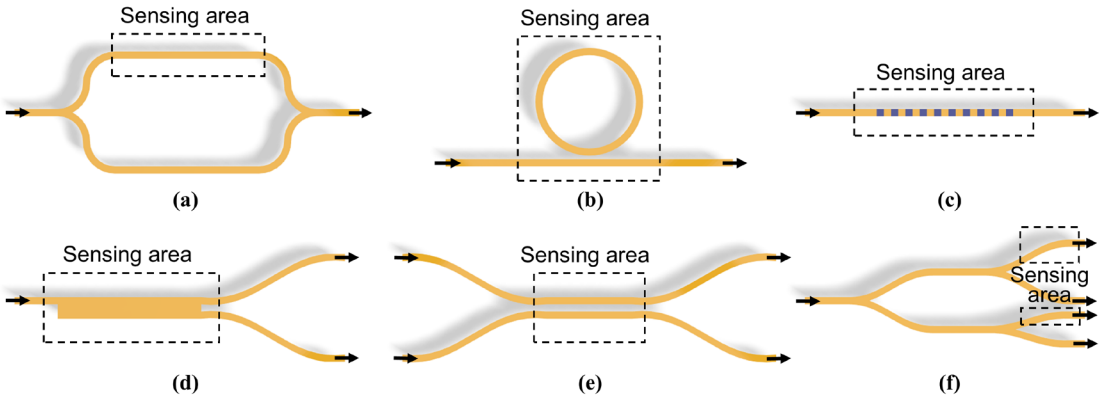

Fig. 1.2 Representative planar waveguide biochemical sensor structures. (a) MZI, (b) MRR, (c) grating, (d) two-mode interferometer, (e) directional coupler and (f) Young's double-slit interferometer.

In summary, waveguide-based on-chip biochemical sensors combine strong integrability, scalability and real-time measurement capability, and they underpin the broader trend towards miniaturised and multiplexed biochemical analysis. There remains substantial scope for systematic research on jointly achieving high sensitivity and high Q, on monolithic integration of device, microfluidics and readout, on selective and interference-resistant surface functionalisation, and on engineering suppression of thermal and mechanical drift. Subsequent chapters of this thesis focus on the design and realisation of refractive-index waveguide sensors that leverage micro- and nanostructures and on-chip integration to enhance sensitivity, dynamic range and array multiplexing while maintaining manufacturability and low cost.

1.3 Advantages of photonic integrated circuit

Sections 1.1 and 1.2 introduce the application drivers in MWP and label-free biochemical sensing. Both are ultimately enabled by PICs, which offer broadband, low-loss transport, compact resonant and interferometric building blocks, and scalable integration of tuning, routing and readout. This section, therefore, summarises the platform-level advantages that directly underpin the two technology threads developed in this thesis.

Within modern information systems, PICs are emerging as a key platform driving the next phase of optoelectronic evolution after fibre-optic communications. Relative to electrical wiring, chip-scale photonic platforms deliver compelling advantages in bandwidth capacity, transmission loss, immunity to electromagnetic interference, energy efficiency and degree of integration [42]. By co-integrating light sources, modulators, filters, WDMs and PDs on a single chip, PICs enable monolithic generation, modulation, routing and detection of optical signals. This substantially lowers system complexity and power consumption and

provides the physical basis for next-generation communications and information processing [43,44].

As illustrated in Figure 1.3(a), Si_3N_4 waveguides exhibit very low propagation loss at high frequencies [45]. Typical losses for SiNOI or SOI waveguides can be as low as 0.1-0.5 dB/cm, whereas RG401 to RG405 coaxial cables incur about 0.1-1 dB/m in the 5 to 20 GHz range, with loss increasing approximately with the square root of frequency [46]. Consequently, as the signal frequency enters the MMW and THz bands, electrical transmission suffers severe attenuation, while optical-waveguide loss remains comparatively stable [3]. Figure 1.3(b) compares total loss for optical-fibre and PIC links, including EO and OE conversion penalties, with RG-405 cable loss versus distance at three exemplar radio frequencies. The fibre and PIC links include 5 dB and 10 dB loss, respectively, for the two conversions. At lower frequencies and short distances, coaxial cables can be preferable, whereas at higher frequencies, the advantages of photonic transmission become pronounced. Strong sub-micrometre confinement further raises optical power density and enhances nonlinear effects, which are beneficial for high-speed optical signal processing and on-chip frequency synthesis.

Beyond loss, PICs provide strengths in cost, noise performance, phase stability, footprint and resilience to electromagnetic interference [47]. Additional advantages include more than 10 THz of usable bandwidth. Figure 1.3(c) highlights the compactness of on-chip waveguides, whose core areas are on the order of 10^{-13} to 10^{-12} m^2, far smaller than single-mode fibre at about 10^{-11} to 10^{-10} and coaxial cables at about 10^{-6} to 10^{-4} [48]. PICs are lighter than cabling, contain no metals and are therefore suited to electrically isolated environments. They are compatible with diverse operating conditions, including immersion in fluids or liquid nitrogen (N_2), and exhibit strong resistance to corrosion. Photonic links also deliver capabilities that are difficult for electronic links, notably continuously variable true time delay for RF signals and carrier-multiplexed distribution. The small size of single-mode on-chip waveguides assists temperature management across links and supports precise phase tracking, which is valuable in phased arrays [49]. The enormous optical bandwidth enables multiplexing of many RF channels on distinct optical carriers within a single waveguide, facilitating distribution in antenna arrays [50].

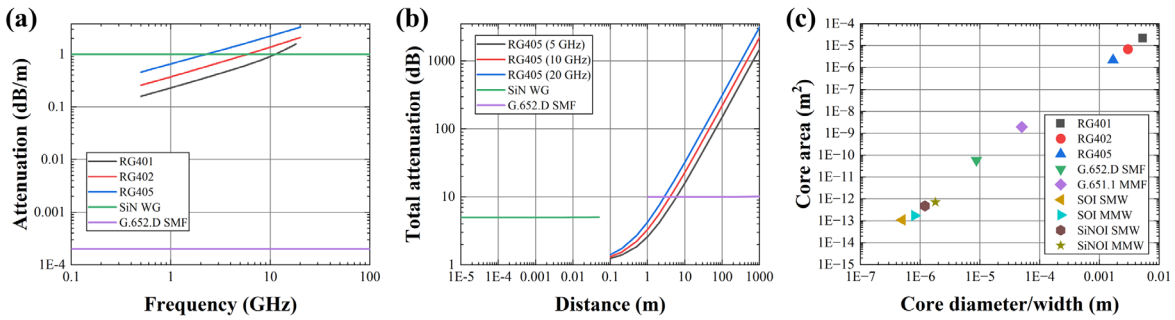

Fig. 1.3 (a) Transmission loss versus frequency for coaxial cable, optical fibre and on-chip waveguides. (b) Transmission loss versus distance at three radio frequencies for coaxial cable, fibre and on-chip waveguides. (c) Representative core geometries and areas for electrical wiring and photonic-link waveguides.

In communications, a flagship PIC application is the data-centre interconnect and optical transceiver [51–54]. Driven by cloud computing and artificial-intelligence (AI) accelerators, inter-server data rates continue to rise, and traditional copper interconnects no longer meet bandwidth and power-efficiency requirements. As sketched in Figure 1.4, PIC-based transceivers on silicon photonics integrate modulators, multiplexers and PDs to realise 400, 800 and even 1600 Gbit/s optical links, which have become the principal interfaces in mainstream data centres [55–57]. For long-haul transmission, coherent systems use on-chip in-phase and quadrature modulation and polarisation-division multiplexing, support high-order formats such as 16-quadrature amplitude modulation (QAM) and 64-QAM, and integrate local-oscillator lasers with coherent receivers to achieve long-reach operation with low error rates [58]. Operation in the C and L bands (C-band: approximately 1530 to 1565 nm; L-band: approximately 1565 to 1625 nm) over distances beyond 1000 km underpins transoceanic backbones and metropolitan networks [59].

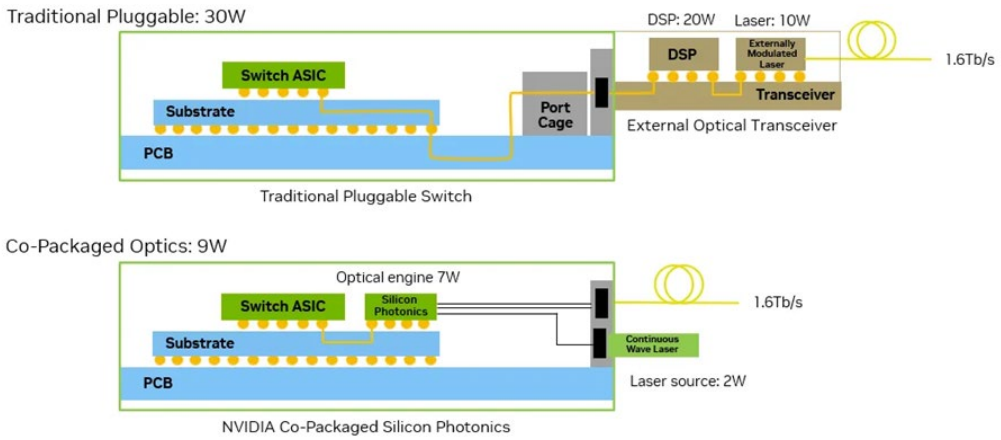

Fig. 1.4 Pluggable optical transceiver and a conceptual visualisation of NVIDIA co-packaged optics (CPO) with a compute die [60].

In RF and MWP, PICs are displacing fibre-based delay lines and electronic filters. Reconfigurable photonic filters (PFs) [61], phase shifters [62] and delay networks [63] on SOI or SiNOI, we can process frequencies from GHz to THz with dynamic tuning. For example, tunable Bragg gratings actuated by integrated heaters or carrier injection enable dual- or multi-channel optical frequency division (OFD), which translates into frequency partitioning and optical-domain filtering of microwave signals. These chips apply to RoF and radio-over-chip links, fifth- and sixth-generation communication fronthaul and backhaul, and phased-array radar, where multi-channel distribution and delay control improve phase coherence and spatial resolution. In optical phased arrays, shown conceptually in Figure 1.5, PIC-based delay networks provide nanosecond-scale true time delay that supports faster and more stable beamforming and reduces electromagnetic crosstalk and phase drift [64,65]. In some state-of-the-art optical phased arrays for LiDAR, the radiating elements are implemented as bound-state-in-the-continuum (BIC) waveguide grating antennas. By exploiting quasi-BIC resonances that suppress parasitic radiation channels and side scattering, BIC antennas can enhance upward emission efficiency and reduce vertical beam divergence, which improves beam quality and angular resolution in beam-steering systems.

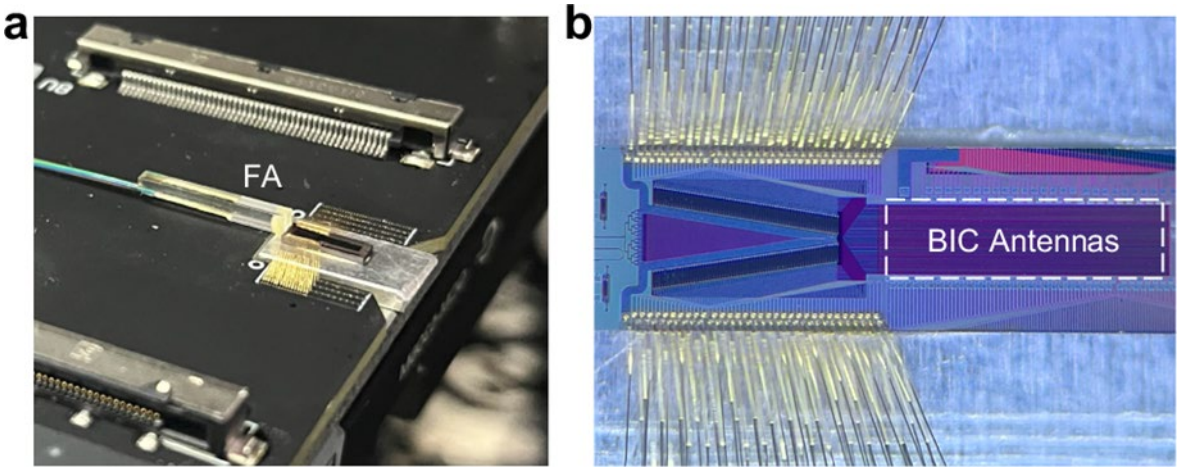

Fig. 1.5 A packaged LiDAR chip and a fabricated optical phased array chip [65].

PICs are also gaining traction in optical computing and AI acceleration [66]. Reconfigurable interferometric meshes implemented on a chip can execute matrix multiplications in the optical domain and thereby realise optical neural networks [67–69]. Relative to graphics and tensor-processing units, photonic processors, exemplified in Figure 1.6, can perform parallel matrix operations at lower energy consumption and are promising for inference and optical-signal-processing workloads. Key building blocks are on-chip phase shifters, modulators and vector-sum networks, all available in mature silicon photonics processes.

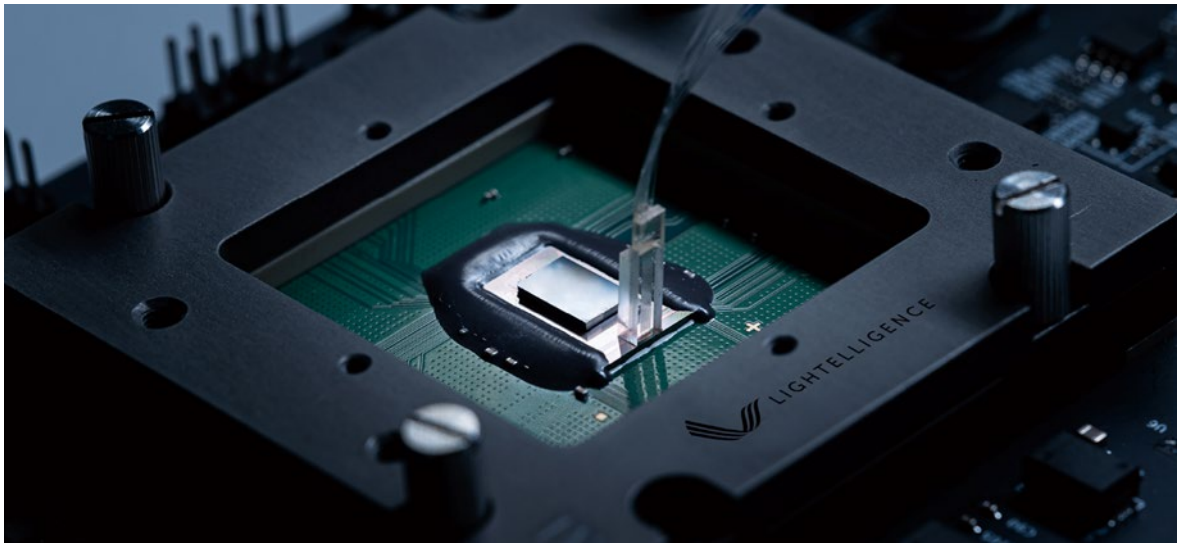

Fig. 1.6 Optical processing unit by *Lightelligence Inc.* within a hybrid optoelectronic accelerator card [70].

Beyond communications and computing, PICs have significant roles in precision metrology and optical-frequency synthesis. Integrated MRR optical frequency combs (OFCs) support on-chip OFD and high-precision clock synchronisation [71–73]. Integrated spectrometers based on interferometers and gratings, as in Figure 1.7, achieve nanometre-scale spectral resolution and have been deployed in THz detection, quantum communications and high-speed spectroscopy [74–77].

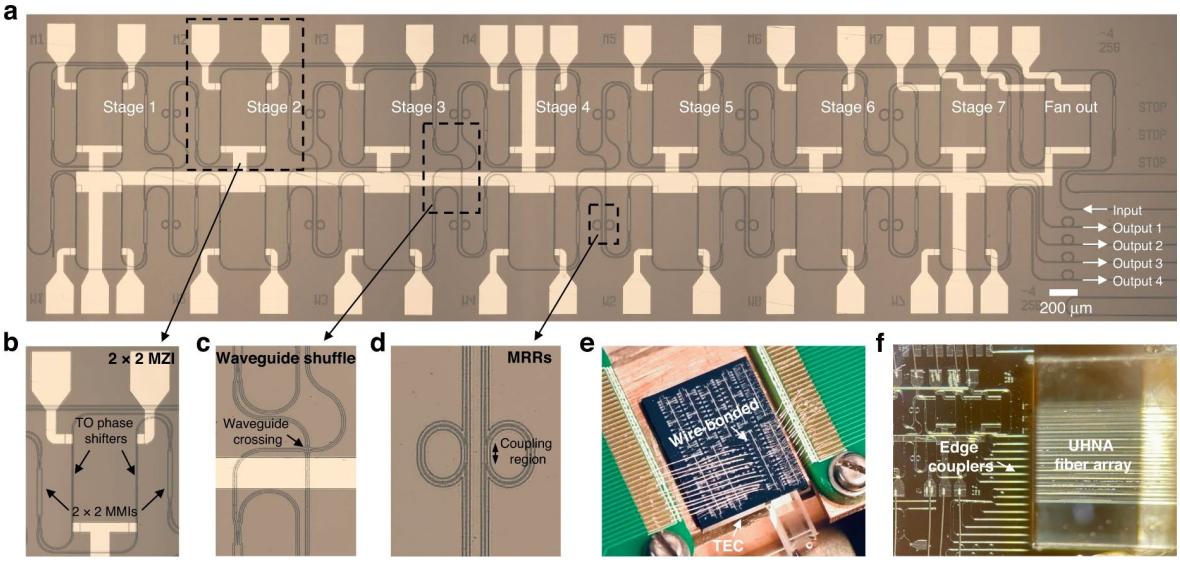

Fig. 1.7 Microscope image of an integrated on-chip spectrometer designed and fabricated at the University of Cambridge [77].

In biochemical sensing, PIC technology exploits high-Q resonators and tight optical confinement to detect minute refractive-index variations with high sensitivity. MRR, Bragg

gratings and MZIs on SOI or SiNOI enable label-free sensing without fluorescent markers for medical diagnostics, environmental monitoring and food safety. Their miniaturisation and compatibility with batch fabrication make them easier to integrate and deploy than many fibre-based sensors [30,78,79].

In summary, PICs deliver a holistic improvement in loss, footprint, bandwidth, energy efficiency and integrability, enabling a transition from fibre-based interconnects to fully on-chip optical interconnects. They retain the wide bandwidth and low loss of optical communications and, at micro- and nanoscale, provide dense, low-power and reconfigurable signal processing. From ultrahigh-speed communications and optoelectronic computing to intelligent radar and biochemical detection, PICs provide a robust physical foundation and a credible path to industrial adoption, and they are central to the drive towards higher integration and energy efficiency in photonic systems.

1.4 Thesis outline

This thesis develops a unified SOI and SiNOI integrated-photonics framework for reconfigurable frequency-selective signal processing and label-free refractive-index sensing. For filtering, it introduces reconstruction-enabled phase-shifted sampled Bragg gratings with integrated MHs to realise multi-passband responses, wide-range tunability and low insertion loss within a compact footprint, enabling OFD and high-frequency signal synthesis. For sensing, it proposes tri-slot hybrid plasmonic waveguide MRR and MZI devices that enhance surface interaction while maintaining manufacturability and repeatability through lithography-tolerant layouts and microfluidic referencing.

Chapter 1 presents the research background and application drivers. It identifies the bandwidth and loss limitations set by the electronic bottleneck and motivates optical-domain filtering as a means of overcoming them. It clarifies the research objectives, technical route, evaluation metrics and chapter organisation of the thesis.

Chapter 2 reviews the state of the art of two closely linked classes of integrated photonic devices that underpin this thesis: integrated PFs for frequency-selective signal processing and waveguide-based biochemical sensors for label-free refractive index transduction. Although their target applications differ, both rely on engineered spectral selectivity realised by common on-chip building blocks including MRRs, interferometric networks, Bragg gratings, and dispersion-tailored waveguides. The chapter, therefore, adopts a unified

quantitative benchmarking perspective, explicitly comparing representative devices in terms of footprint and functional density, tuning or stabilisation power, and scalability as the number of controllable channels increases, thereby establishing a consistent basis for positioning the advantages of the proposed devices in the subsequent chapters.

Chapter 3 establishes a unified theoretical foundation and analysis toolkit. It first develops eigenmode analysis for waveguides and fields, covering ridge and slot structures on SOI and SiNOI, and discusses how bending loss and coupling efficiency influence system-level metrics. It then derives coupled-mode and transfer-matrix models for Bragg gratings, SBG and multi-PS gratings, together with Fourier-domain characterisation and group-delay analysis. The notions of REC technique and equivalent phase shift (EPS) are introduced to show how refractive-index profile reconstruction can yield controllable reflection-point distributions and higher coupling coefficients without changing the physical parameters, thereby relaxing manufacturing tolerance, lowering insertion loss and enhancing side mode suppression ratio (SMSR). The chapter forms a complete chain from materials and geometry to spectral shape and group delay, providing a repeatable workflow for parameter selection, tuning strategy and performance assessment.

Chapter 4 presents a dedicated account of the experimental facilities and methods that underpin the thesis, consolidating the device fabrication, integration, and characterisation workflows to support reproducibility and cross-chapter traceability. It summarises the core process modules used to realise SOI and SiNOI photonic integrated circuits, including high-energy electron beam lithography (EBL), high-density plasma etching, plasma-enhanced chemical vapour deposition, and electron beam evaporation, with emphasis on the operating principles and practical control points that govern linewidth fidelity, etch anisotropy, sidewall quality, cladding formation, metallisation, and MH integration. The chapter also documents the optical and electrical measurement chains used throughout the thesis, including fibre coupling and polarisation management, optical spectrum and comb-based interrogation, TO tuning, and automated data acquisition, thereby establishing a consistent experimental baseline for the sensing and filtering demonstrations that follow.

Chapter 5 targets on-chip biochemical detection and proposes two classes of sensors based on a tri-slot HPW, namely an MRR and an MZI. Through the synergy of plasmonic near-field enhancement and low-loss waveguide transport, the designs strengthen surface interaction while suppressing propagation loss, yielding compact and sensitive read-out units suited to array integration. In the C band, stable transmission spectra and clear red shifts are

observed, with refractive-index sensitivity around 900 nm/RIU alongside low insertion loss and good repeatability, demonstrating compatibility of hybrid plasmonics with the silicon photonics platform and its suitability for multi-point parallel sensing and chip-level integration.

Chapter 6 introduces a dual-passband MPF based on REC-enabled sampling and PS design, with MHs integrated at the PS locations to realise independent thermal tuning of the two passband centres. In conjunction with a passive semiconductor mode locked laser (SMLL) that generates an OFC, the passband spacing is continuously tunable from 52.1 to 439.5 GHz. The filter exhibits a favourable Q factor and 3 dB bandwidth with balanced SMSR and insertion loss. An improved 4PS-SBG architecture raises the coupling coefficient and shortens the cavity, mitigating crosstalk due to 0^{th} reflection and enabling stronger spectral selectivity within a small footprint. The chapter closes the loop from design through fabrication to experiment and shows suitability for frequency synthesis and multi-channel selection.

Chapter 7 advances towards programmable multi-passband operation using a reconfigurable filter that combines a 4PS-SBG with a heater matrix. REC provides spatial decoupling of passbands within the cavity, achieving strong optical isolation and independent tuning. The device supports single-, dual- and quad-passband modes as well as band-stop operation. Passband spacing is flexibly configured from 50 to 450 GHz, with rapid switching between band-pass and band-stop spectral shapes. In the quad-passband mode, all peaks translate together with fixed spacing, while single-point actuation moves only the targeted passband. The minimum insertion loss is about 0.5 dB, and the SMSR generally exceeds 15 dB. Combined with an OFC, the device demonstrates multi-channel selection and suppression at 50, 100 and 150 GHz uniform spacing, evidencing engineering practicality and flexibility for DWDM and on-chip spectral shaping.

Chapter 8 proposes a system architecture that cascades a superstructure grating (SSG) with an MRR and introduces a memetic optimisation framework that combines Self-adaptive Differential Evolution (SaDE) algorithm with Sequential Quadratic Programming (SQP) to design the SSG phase distribution under multiple objectives, balancing passband flatness, centre power and out-of-band suppression. Multiple sampling periods are implemented on the same platform, corresponding to channel spacings of 670, 869 and 1050 GHz, with channel counts configurable as 5, 7, 9, 11 and 13. Stand-alone SSGs exhibit minimum insertion loss of about 0.1 to 1.2 dB, passband-power variance down to the 10^{-6} level and

crosstalk suppression beyond 20 dB. When cascaded with an MRR of FSR about 335 GHz, dual-stage filtering compresses the MRR's single-peak 3 dB bandwidth from about 52 to about 15 GHz and produces a cleaner spectrum. Thermal tuning realises interval doubling from 335 to 670 GHz with stable maintenance. Time-domain chirped-current experiments reveal continuous transitions and extinction-regeneration across multiple channels, confirming dynamic reconfiguration and robustness. The chapter exemplifies the co-design of algorithms and devices and provides a linear and integrable solution for on-chip frequency multiplication and frequency hopping.

Chapter 9 summarises the overall contributions and outlines engineering directions, including heterogeneous epitaxy or bonding to co-integrate comb sources and lower coupling loss, buried gratings to reduce scattering and raise coupling coefficient, selective doping for high-speed silicon-based EO modulation and the construction of test platforms that cover higher frequency ranges, thereby shortening the path from prototype to industrial deployment.

2 State of the art

This chapter reviews the state of the art of two closely related classes of integrated photonic devices that underpin the thesis: integrated PFs for microwave photonics and optical frequency-domain signal processing, and waveguide-based biochemical sensors for label-free refractive-index transduction. Although the target applications differ, both device classes rely on engineered spectral selectivity realised by common on-chip building blocks, including MRR, interferometric networks, Bragg gratings, and dispersion-tailored waveguides. As a result, their practical competitiveness is governed by the same system-level constraints, namely footprint, tuning or stabilisation power, and scalability.

To enable a consistent positioning of the research contributions in later chapters, the discussion in this chapter adopts a quantitative benchmarking viewpoint. Footprint is considered together with functional density, power consumption is interpreted primarily as electrical power required for trimming, tuning, or drift compensation, and scalability is assessed through the number of independently controllable degrees of freedom and the associated penalties in loss, thermal crosstalk, and calibration overhead. The chapter first surveys integrated PFs with an emphasis on narrow passbands, multi-passband operation, and reconfigurability. It then examines on-chip biochemical sensors, focusing on strategies that enhance light-matter interaction and amplify the conversion from effective-index perturbations into measurable spectral or intensity changes.

2.1 State of the art in integrated photonic filters

In conventional electronic filters, splitters, delays and weighting are implemented with electrical components, as sketched in Figure 2.1(a). With the continual growth of communication capacity, modern microwave links must process ever higher carrier frequencies and, in some cases, signals that span multiple bands. Owing to the electronic bottleneck, traditional electrical filters struggle to satisfy these requirements [80].

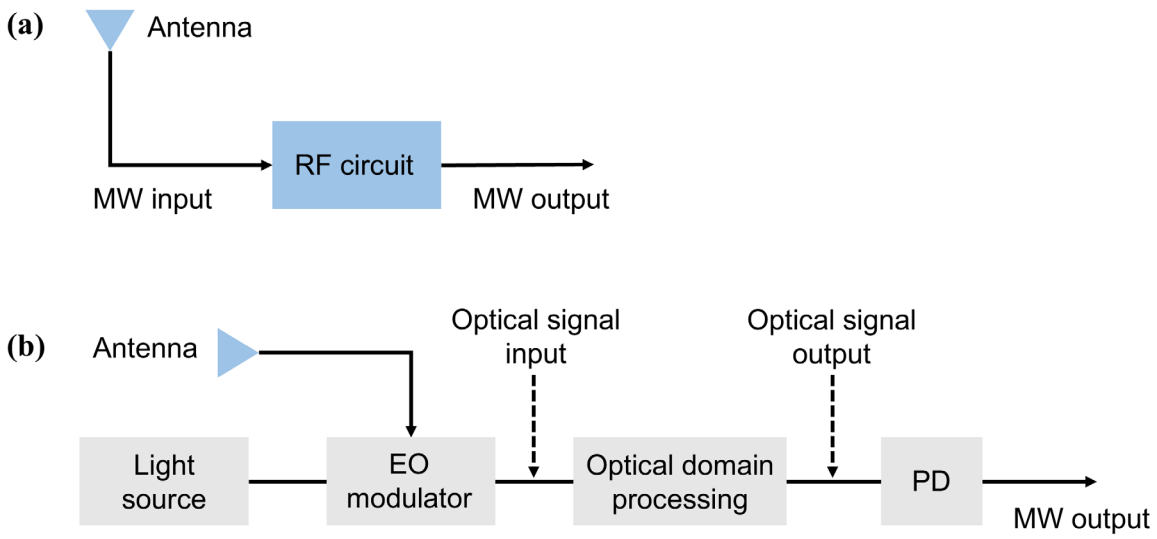

Fig. 2.1 Structural diagrams of two microwave filters: (a) microwave filter and (b) MPF.

MPFs offer an effective route. The same functions of tapped sampling, delay and weighting can be realised optically. For example, taps may be generated by lasers or OFC [81,82]; delays may be provided by fibre, on-chip waveguides or optical resonators [83–85]; different tap weights may be set by optical amplifiers or optical attenuators [86,87]; and coherent summation can be performed by optical couplers or WDMs [88,89]. An MPF results when a microwave signal is mapped to the optical domain, filtered optically and then recovered by photodetection [90]. The canonical MPF architecture, shown in Figure 2.1(b), contains four principal modules, namely the optical source, the modulator, the optical-domain signal-processing element and the PD. When the filtering is executed by an optical filter in the optical domain, the overall microwave response is governed primarily by the PF, which therefore sets the performance ceiling.

Current research on integrated PFs concentrates on four themes: narrow passband, multiple passbands, reconfigurability and high integration.

Although electronic filters face well-known limits in modulation bandwidth and large range tuning, the comparatively low operating frequencies of electronic devices make it easier to realise narrow passbands for fine spectral selection. By contrast, achieving narrow passbands in PFs remains a central challenge.

Regarding on-chip narrowband filtering, two mainstream approaches have emerged. The first exploits high-Q resonators; the second relies on Brillouin or acousto-optic enhancement, with active progress on SOI and thin film lithium niobate (TFLN) platforms. On TFLN,

phase-shifted Bragg gratings (PS-BG) achieve ultra-narrow transmission windows through careful sidewall trimming while providing Pockels tuning. Device dimensions are smaller than 1 μm by 1 μm. Measured passbands between about 1.1 and 1.8 GHz have been reported, with peak wavelength tuning sensitivity of 25.1 pm/V and extinction ratio (ER) of 25 dB, demonstrating a materials advantage for low-power reconfigurable narrowband filtering [91]. On silicon, high-Q MRRs or racetrack resonators combined with a tunable interferometric coupler allow continuous control of bandwidth between weak coupling and critical coupling. By employing a multimode racetrack to suppress sidewall scattering, a free spectral range (FSR) around 35 GHz and a 3 dB bandwidth tunable from 240 MHz to 1.375 GHz have been achieved, which acts as a programmable narrowband slider for dense wavelength division multiplexer (DWDM) channels and fine allocation of MWP signals [92].

For narrowband RF filtering via optical to electrical mapping, cascaded silicon MRRs with tunable coupling regions have realised sub-GHz bandpass responses. The centre frequency is tunable from about 5.2 to 35.8 GHz, the 3 dB bandwidth can be reconfigured between 0.7 and 2.0 GHz, and the suppression exceeds 40 dB, which suits narrowband preselection in MMW receivers [93]. A silicon platform employing bent coupled waveguides with dual end heaters has demonstrated a ring array with very wide tunability for notch filtering. The 3 dB bandwidth can be tuned from 0.178 to 22.7 GHz while the maximum suppression exceeds 75 dB, enabling a single platform to cover both narrowband discrimination and broadband monitoring [94]. On TFLN, a thermally tuned two-stage cascaded MRR produces a box-shaped flat top narrowband response with 3 dB bandwidth around 4.8 GHz and out-of-band suppression near 35 dB. The thermal power required to shift one FSR is about 89.4 mW, which supports monolithic co-integration with high-performance LN modulators for on-chip switching and monitoring of narrow DWDM sub bands [95]. Using SOI distributed feedback (DFB) resonators and waveguide gratings, bandpass RF filters have been reported with more than 40 dB out-of-band rejection and steep edges, while enabling centre frequency tuning beyond 70 GHz and bandwidth reconfiguration from 5 to 10 GHz. The layout and process are fully CMOS compatible, and parameter convergence suggests that the bandwidth can be compressed further towards the order of 1 GHz, preserving design headroom for on-chip narrowband operation [96]. At the extreme of narrowband performance, silicon Brillouin acousto-optic transfer has demonstrated MHz resolution. A pure silicon optoacoustic system achieved a notch with a 3 dB bandwidth of about 2.7 MHz and suppression of 57 dB, with continuous tuning over roughly 6 GHz [97]. A heterogeneous on-chip solution combining chalcogenide glass for stimulated Brillouin scattering (SBS) gain with active silicon for

modulation and detection in a footprint of about 5 by 5 mm^2 achieved RF spectral resolution of about 37 MHz, laying a foundation for unifying high resolution with wide tunability [98].

Despite these advances, several bottlenecks remain. First, it is difficult to combine a wide tuning range with a narrow passband in a single structure. Physical limits such as FSR and Brillouin frequency shift constrain the simultaneous achievement of a wide range, fine granularity, low power and low insertion loss. Second, while SBS-based approaches offer outstanding resolution, on-chip propagation loss, pump power and packaging complexity are still high for large-scale parallel channels. Third, schemes based on tunable coupling and multi resonators often involve trade-offs among stopband suppression, flat top profile and ripple when targeting sub-GHz or even MHz bandwidth. Engineering repeatable joint optimisation of narrowband, flat top shape, high suppression and low insertion loss remains a core requirement for communication front ends.

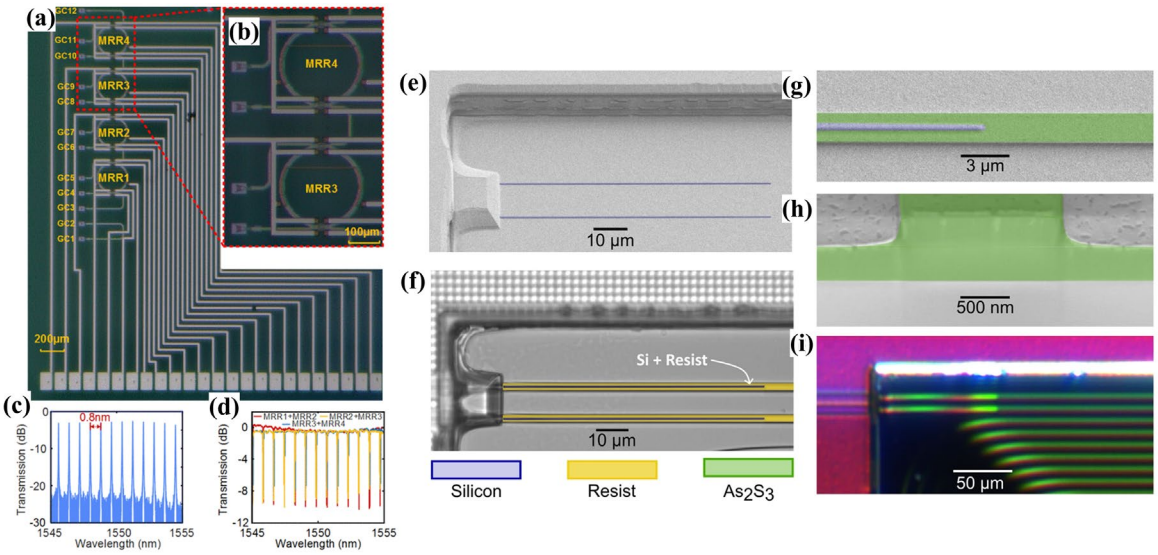

Fig. 2.2 (a-b) Microscope images of cascaded silicon MRRs after fabrication and (c-d) measured transmission spectra at different ports [93]. (e-f) Silicon waveguide taper regions, (g) silicon and antimonide waveguides and (h) the cross section of the antimonide waveguide in SEM, together with a true colour photo of (i) the silicon antimonide taper region [98].

Compared with single-channel filters, multi-channel PFs markedly improve system capacity and functional flexibility. A single-channel filter extracts one frequency point or a narrow band, whereas a multi-channel structure selects and controls several independent channels within the same device, enabling parallel processing and multiplexed transmission that raise spectral efficiency and processing throughput. With the growth of multi-service convergence and broadband demand, multi-passband filters provide several tunable channels within a limited on-chip area, which strengthens flexibility in frequency allocation and signal control. Consequently, multi-channel operation has become an important development trend that

increases integration level and processing parallelism and underpins chip reconfigurable wideband MPF systems.

For multi-passband on-chip filters, recent emphasis has been on parallel channel selection and flat-top passband shaping for coarse wavelength division multiplexer (CWDM) and DWDM. In 2018, a four-channel flat top CWDM filter based on bent directional couplers combined with cascaded MZIs offered a compact, low-loss loss and fabrication-tolerant route. The key innovation is that the bent coupler strongly suppresses wavelength sensitivity of the coupling ratio and thereby reduces passband ripple and crosstalk in the cascaded MZI chain. Implemented on SOI, the measured 3 dB bandwidth is about 19 nm, the adjacent and non-adjacent channel isolation exceeds 18 and 19 dB, respectively, and the crosstalk is below 20 dB. The structure admits subsequent fine trimming by TO PSs and is well matched to O-band CWDM transceivers and multi-carrier orthogonal frequency-division multiplexing front ends [99].

In 2020, a four-channel CWDM filter on SOI combined a multimode waveguide grating with a mode demultiplexer (DEMUX) to form a cascaded flat top filtering block. Longitudinal anodization together with mode routing suppresses sidelobes and reflections, and the measured 1 dB bandwidth is about 15 nm. Through an SU8 cladding with a negative TO coefficient, the thermal sensitivity was reduced from about 85 pm/ºC to 46 pm/ºC, which markedly improves passive stability without thermoelectric cooling. The device is principally a fixed multi-passband DEMUX without wide range tunability and is well suited to low power on-chip CWDM backplane interconnects or multi-carrier upconversion chains [100].

For high channel density DWDM, a silicon arrayed waveguide grating (AWG) reported in 2023 with 1.6 nm spacing employed Euler bends to widen array waveguides and curved taper transitions to suppress random phase error and modal mismatch. A compact footprint of about 600 by 800 μm was achieved with low loss and crosstalk better than 30 dB. The FSR is about 29 nm. The device again serves as a fixed multi-passband filter suitable for dense DEMUX in high-capacity DWDM OFD transceivers [101].

To obtain tunable passband positions and spacing in a multi-passband device, a dual-channel phase-shifted Bragg filter on TFLN provides a paradigm of EO tuning. Two narrow passbands are formed by multiple uniform gratings and PS sections within the same device and can be tuned in a linked manner through the strong EO effect of TFLN. Measured

linewidths around 10 to 20 pm and independent movement of passband centres at designed GHz level spacing were demonstrated, which offers fine spectral control for dynamic channel shifting, bypassing or notch-transmission functions in WDM and OFD systems [102].

From the perspective of multi-passband MPFs, a programmable dual injection ring combined with modulation spectrum shaping on Si_3N_4 has produced multiple RF responses. A single on-chip circuit synthesised six configurable notches and bandpass types over 5 to 20 GHz through optical multi-passband spectral shaping and response synthesis with MRRs. In the optical domain, this network is equivalent to a multi-passband filter [103].

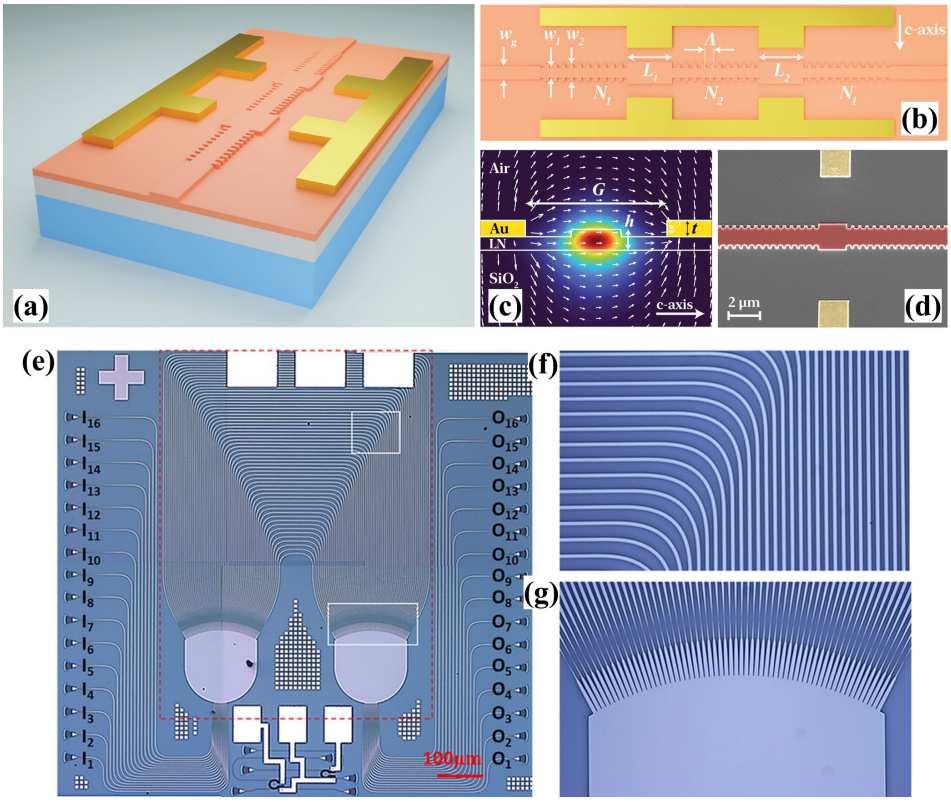

Fig. 2.3 (a-b) Schematic of a dual-channel Bragg filter on TFLN, (c) optical TE mode from waveguide simulation and (d) SEM image of the PS section [102]. (e) Fabricated 16 by 16 AWG matrix, microscope images of (f) Euler bent arrayed waveguides and (g) curved tapered waveguides [101].

Significant challenges still stand in the way of practical multi-passband devices. The first is independent tuning. Many devices with four or more channels are fixed DEMUX or exhibit only collective shifts, which makes it difficult to tune each passband independently without mutual disturbance. The second is inter-channel uniformity. As the number of channels increases, differences in passband shape, insertion loss and crosstalk become more pronounced due to fabrication variability and thermal drift. The third is compatibility between narrowband and multi-channel operation. Extending narrowband reconfigurable

techniques such as TFLN PS-BG to many channels is hindered by integrating coupling, reflection sidelobes and driver crosstalk.

Because PFs provide strong tunability and repeatability, MPFs formed through optoelectronic mapping inherit these advantages. Reconfigurable PFs may be grouped into two classes. The first class adjusts filter parameters such as bandwidth and stopband rejection. The second class changes the filter type between high pass, low pass, bandpass, bandstop and all pass.

For on-chip reconfigurable filters based on resonators and gratings, reconfigurable gratings and DFB Bragg grating devices offer high selectivity and strong control over spectral shape. A fully electrically reconfigurable waveguide Bragg grating on SOI used segmented PN junctions to programme the refractive index modulation profile, allowing switching among several functions, including phase-shifted, uniform and chirped gratings on the same chip. Independent tuning of notch depth and centre wavelength was demonstrated. The reflected notch had a 3 dB bandwidth of about 49 pm; the notch depth was adjustable from about 0.8 to about 8.9 dB; and the centre wavelength could be red shifted by about 35 pm under a positive bias of 20 V or blue shifted by about 380 pm under a negative bias of 1 V, with the possibility to alter ER without moving the centre wavelength [104].

Further, a DFB resonator on SOI has yielded a flat-top bandpass core with wide range tuning. The passband position is shifted by a long heater while the passband bandwidth is controlled independently by micro heaters (MHs) in the PS sections. Experiments demonstrated continuous tuning of the 3 dB bandwidth around 5 GHz with out-of-band suppression exceeding 40 dB, which facilitates reconfigurable MWP bandpass operation through OE mapping [96].

At the level of programmable spectral shaping, the combination of algorithmic design, structural programmability and high-speed EO mechanisms expands the reconfiguration space. On TFLN, an MRR and MZI coupling modulation architecture decouples the electrical control over coupling strength, which determines ER, from the control over resonance wavelength. Tuning at a fixed operating wavelength achieved ER from nearly 0 to greater than 25 dB and a wavelength sensitivity of around 12.5 pm/V. The measured Q factor is about 1.67×10^4, and the footprint is about 1.2 by 0.65 mm, combining high speed, low loss and strong controllability [105]. For structural programmability, a finite impulse response beamline and multi-tap MZI with integrated genetic algorithm tuning achieved a

fitting error below 4.5% and passband ripple as low as about 0.24 dB, enabling rapid synthesis of Gaussian, super Gaussian, triangular and trapezoidal target profiles on the same chip, which suits system-level target-driven spectral tracking [106].

In addition, a nano-opto-electromechanical pixelated grating introduces per-pixel control of the coupling coefficient through symmetry breaking. The chip area is only about 0.007 mm^2. Theoretical on-off contrast exceeds 100 dB, and experiments report 40 to 50 dB. The bandwidth is tunable and the in-band selection switching time is below 10 ns, which points to large-scale OFD spectral switching and on-chip optical cross-connect with ns-class reconfiguration [107]. A complementary pole-zero synthesis approach maps closed-form elliptic or Chebyshev specifications onto silicon ring MZI kernels. Multiple thermal phase shifters and power splitters allow reconfiguration of in-band ripple, cut off steepness, and FSR, about 0.51 nm, and sideband suppression greater than 20 dB has been reported [108].

For reconfigurable applications in MWP and DWDM parallel links, MRR arrays and coupled waveguides provide three-dimensional independent control over spectral shape, centre frequency and bandwidth. On SOI, a four-MRRs coupled-resonator optical waveguide with MZI tunable couplers achieves reconfigurable filter order from one to four and centre frequency tuning from about 4 to 36 GHz. The 3 dB bandwidth is tunable from about 0.24 to 1.76 GHz, with maximum suppression around 42.8 dB and a maximum roll off near 8.85 dB/GHz [109]. Complementarily, a dual MRRs-assisted MZI infinite impulse response filter on SOI functions as an optical pre-emphasis element. Experiments extended the equivalent 3 dB EO bandwidth of a transmitter from 18 to 40 GHz and quantified improvements in eye diagram Q factor and ER for on-off keying at 10 to 50 Gbit/s. The passband centre can be moved across one FSR, and the stopband suppression is tunable up to about 25 dB [110]. A multifunctional self-coupled MRR assisted MZI filter realised five operating modes on a single chip by employing three tunable couplers and three phase shifters, namely switch, asymmetric MZI, ring-assisted MZI, dual injection MRR and self-coupled MRR assisted MZI. The FSR was halved from about 0.3966 to about 0.1983 nm, and both passband-to-notch switching and bandwidth tuning were demonstrated [111].

Even with these extensive demonstrations, multiple thermal phase shifters and decoupling heaters still raise area and power, and system-level suppression of thermal drift and crosstalk remains insufficient. Thermal tuning is limited to ms dynamics and cannot deliver high-speed reconfiguration. Although nano-opto-electro-mechanical provides ns-scale actuation,

it requires large-scale pixel drivers and resilient control algorithms to handle fabrication variability and drift [107].

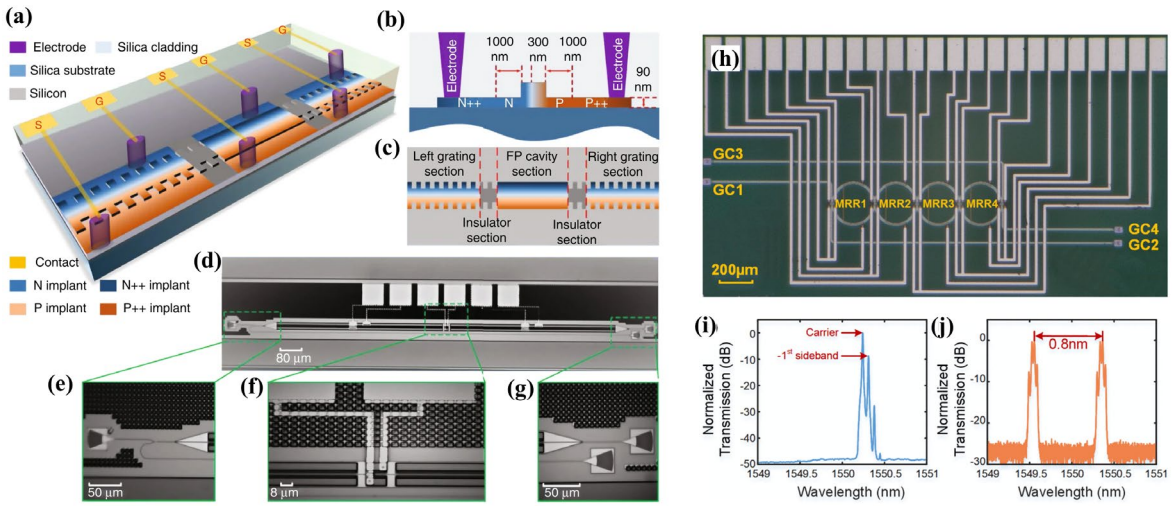

Fig. 2.4 (a-c) Schematic of a fully electrically reconfigurable waveguide Bragg grating and (d-g) SEM images after fabrication [104]. (h) Microscope image of a coupled-resonator optical waveguide based photonic bandpass filter after fabrication. Measured single sideband (i) optical spectrum and (j) transmission spectrum [109].

For multi-channel filters, discrete photonic implementations suffer from large volume, weight, power and limited stability. Integration addresses these issues and supports volume manufacture, so miniaturisation and integration of multi-passband PFs is a clear trend. Two main classes are pursued for integrated PFs. The first employs networks of multiple resonators in series or in parallel. The second exploits a single resonator that produces multiple periodic channels in the frequency domain.

The survey above highlights that on-chip multi-passband progress relies heavily on stacking and cooperative cascading of sub-devices. This raises functional density but inevitably increases insertion loss and complexity. For example, interleaved MZIs combined with AWGs raise both device-level and system-level loss [112]; multiple phase-shifted cavities on TFLN increase the number of drive and thermal management channels [102]; and programmable resonator networks require more couplers and phase control units to achieve independent tuning. Co-integrated filtering and light sources across heterogeneous platforms need cross-platform calibration and packaging solutions [113]. Structural constraints often bind FSR and the tunable range. Interleaved AWGs must match FSR and channel spacing. In multi-phase shifted gratings, the passband spacing is generally set by cavity length and is not easily altered independently. Stepwise selection with gratings and MRRs is not naturally friendly to continuous and independent multi-passband configurations. In contrast, the single

cavity route has clear advantages in device count and area. For instance, sub-μm bend MRRs with sub-μm radii achieve FSR around 93 nm, insertion loss at the drop port around 1.8 dB and bandwidth about 0.8 nm. This approach offers outstanding functional density per unit area, yet it is intrinsically single passband. Realising multi-passbands with independent tuning then requires parallel cavities or forfeits independence, so achieving both multi-passbands and high integration within one framework remains difficult [114].

2.2 State of the art in on-chip biochemical sensors

The above progress in integrated PFs highlights a recurring engineering trade-off: increasing functionality, whether by narrowing the passband, adding passbands, or enabling reconfiguration, often requires additional resonant sections and control elements, which in turn increases footprint, tuning power, and the complexity of scaling to many channels. These trade-offs are not unique to filtering. Waveguide-based biochemical sensors employ many of the same resonant and grating concepts, but use them to transduce refractive-index perturbations into spectral shifts or intensity variations. Consequently, sensor performance and deployability are likewise determined by the coupled constraints of device footprint, stabilisation power, and scalable multiplexed readout. This section therefore reviews on-chip biochemical sensors using the same benchmarking lens, establishing a consistent basis for quantitative comparison across the thesis.

Most waveguide-based refractive-index biochemical sensors operate by means of the evanescent field interacting with the analyte at the waveguide boundary [26]. The modal field that extends into the cladding or analyte and decays exponentially along the surface normal constitutes the evanescent tail. When the analyte concentration varies, its refractive index changes accordingly. Coupling between the evanescent field and the analyte perturbs the effective index n_{eff} of the guided mode. Distinct sensor architectures then transduce the n_{eff} change Δn_{eff} into a measurable variation of the optical output. By detecting this output and invoking the one-to-one physical relation between the refractive-index change and the optical response, quantitative sensing is achieved.

To date, a wide array of high-sensitivity waveguide sensors has been reported. Two complementary strategies dominate. The first increases light-matter interaction to raise the intrinsic waveguide sensitivity. The second employs dispersion engineering or cascaded structures so that a given Δn_{eff} is converted into a much larger wavelength or intensity change at the device output, thereby enhancing device-level sensitivity.

The slot waveguide, introduced by Almeida in 2004, established that a low-index slot can tightly confine and guide light, a property that rapidly attracted attention in biochemical sensing [115]. When the slot region is filled with analyte, the large field discontinuity across the slot produces strong overlap and high waveguide sensitivity, motivating extensive investigation of slot-based sensors.

For phase-shifted sidewall Bragg-slot waveguides, theory and simulation indicate a linear spectral response and a detection limit at the order of 10^{-6} with an ultra-short cavity of approximately 11.7 μm, suited to dense array integration [116]. On SOI, phase-shifted Bragg-slot devices operating in aqueous environments have demonstrated Q approximately 1.5×10^{4}, sensitivity near 340 nm/RIU and an intrinsic detection limit around 3×10^{-4} RIU, while remaining fully CMOS compatible [117]. For slot MRRs, a SiC-on-insulator platform has yielded intrinsic Q near 1.74×10^{4} with bulk sensitivity of 264 to 300 nm/RIU, expanding both material and application windows [118]. Sidewall-grating slot MRRs have reported 620 nm/RIU and a detection limit around 1.4×10^{-4} RIU, and an electromagnetically induced transparency-like lineshape mitigates FSR constraints and enlarges dynamic range [78]. Beyond resonators, grating-assisted couplers based on bar-slot waveguides have exhibited an absolute sensitivity close to 1970 nm/RIU, enabling low-cost spectrometric readout [119]. To reconcile high sensitivity with high Q and low loss, hybrid slot-bar MRRs and slot ring-assisted MZI architectures have been proposed and validated, improving overall FoM or delivering a quasi-FSR several times larger than that of a comparable MRR while retaining elevated sensitivity [120,121].

Multi- and dual-slot waveguides enhance the transverse-electric (TE) field inside multiple low-index gaps so that a greater fraction of optical energy resides in the analyte, boosting both bulk and surface sensitivity. Systematic optimisation shows that wider slots degrade surface sensitivity and that increasing slot count offers diminishing returns for bulk sensitivity, whereas ridge width and residual silicon thickness are more critical. Under optimised parameters, multi-slot MRRs can achieve bulk sensitivity up to 912 nm/RIU, with controllable bending and substrate-radiation losses for small radii [122]. Experimentally, a dual-slot MRR on SOI with an inner sidewall azimuthal grating achieved 563 nm/RIU bulk sensitivity, a detection limit of 3.7×10^{-6} RIU, an effective measurement span of 72.62 nm and Q around 1.6×10^{4}, demonstrating the combined advantages of high sensitivity and wide dynamic range [123]. On SiNOI, multimode-multislot interferometric arrays that exploit coupling and self-imaging have delivered calculated sensitivity greater than 1700 nm/RIU

across the visible and near-infrared, highlighting the synergy between multislot arrays and low-loss materials [124].

Hollow-core and suspended slot waveguides redistribute energy that would otherwise leak into the buried oxide (BOX) or substrate back into the analyte by removing the substrate or introducing an air cavity. In the mid-infrared, suspended chalcogenide-glass and SiO_2 or Si slot waveguides formed by selective removal of the underlying SiO_2 and gas filling in the slot have achieved a power-confinement factor near 85.77% at 3.291 μm, an optimal length around 1.45 cm and a methane limit of detection close to 1.70 ppm, with μm-scale diffusion enabling μs response and favourable fabrication tolerance alongside low-loss propagation [125]. Nanofluidic slot waveguides integrate optics and fluidics by confining the probing light directly within a liquid core of at most 100 nm. Compared with bar waveguides that rely on an evanescent tail, this approach improves sensitivity by roughly a factor of 50 and supports label-free multi-component recognition and quantification in the 2.5 to 4 μm band [126]. On SOI, fully suspended slot waveguides employing transverse subwavelength gratings as an effective low-index cladding exhibit measured loss near 7.9 dB/cm at 2.25 μm; simulations indicate that it overcomes BOX absorption limits on bandwidth and sensitivity and favour high-FoM interferometric or resonant readouts [127].

Hybrid plasmonic waveguides (HPW) leverage nm-scale low-index gaps at metal-dielectric interfaces so that the tight confinement of surface plasmon polaritons (SPPs) combines with the field discontinuity of slot waveguides. The result is strong localisation within analyte-filled gaps and significantly amplified phase or resonance shifts for a given homogeneous or surface perturbation, offering a potent route to sensitivity and integration. A representative dual-slot hybrid plasmonic configuration on SOI has achieved an optical confinement factor in the IPA approaching 88%. As the sensing arm of an MZI with 40 μm interaction length, it yielded 1061 nm/RIU while retaining sub-wavelength scale and acceptable propagation loss, demonstrating strong readout for concentration changes [128]. A complementary hollow-type hybrid plasmonic waveguide, realised by placing a metal film above a releasable nano-air gap on a silicon ridge so that the analyte directly fills the gap, maintained propagation loss below 0.25 dB/μm. Embedded in an MZI, the device delivered 160 to 245 nm/RIU for 20 to 40 μm effective length, with an estimated detection limit at the order of 10^{-6} RIU [129]. For resonant readout, a dual-slot hybrid plasmonic MRR achieved an experimental sensitivity of 687.5 nm/RIU by coupling a silicon bus waveguide to a metal-clad MRR with lateral apertures. This is about five times that of a similarly sized all-silicon MRR. Strategies for phase matching can further raise the loaded Q and reduce the

detection limit, suggesting co-integration of sensing and EO modulation [130]. Beyond liquid-index sensing, slot HPW combined with straight or slotted resonators have been used for label-free DNA hybridisation. With three-slot designs or bottom metal electrodes, simulations and full 3D modelling indicate sensitivity around 1890 nm/RIU and robustness beyond 1.7×10^3 nm/RIU within ±5% fabrication tolerance, evidencing practicality for integrated manufacture [131].

Subwavelength-grating (SWG) waveguides alternate high- and low-index segments with a pitch far below the wavelength along the propagation direction so that the guided mode experiences an engineered n_{eff} and field distribution without diffraction [132]. This draws a stronger field into the analyte and markedly enhances both bulk and surface response, with duty cycle, pitch and cross-section as key degrees of freedom. When the low-index analyte is directly introduced into the grating gaps, SWG sensors operating in TE mode achieve high waveguide sensitivity. Three-dimensional (3D) finite-difference time-domain (FDTD) analyses report surface sensitivity about 1.5×10^{-3} RIU/nm, with sensitivity rising as duty cycle decreases, balanced against leakage and minimum feature size [133]. On resonator platforms, SWG MRRs increase the optical path within the gaps and thereby strengthen the index response. Experiments have shown Q near 7×10^3, bulk sensitivity about 490 nm/RIU and system detection limits of order 2×10^{-6} RIU [134]. Importantly, the effective sensing region of an SWG MRR covers the propagation channel between the pillars or slots, so surface sensitivity remains high and approximately constant at around 1 nm/nm as the thickness of the surface layer increases, overcoming the degradation seen in devices that rely solely on an evanescent tail [135]. In interferometric schemes, the dispersion of SWGs enables bimodal single-channel sensing. Theory and FDTD simulations indicate bulk sensitivity approaching 1300 nm/RIU, while substantially shortening device length [136]. Coupling SWGs to slots to form subwavelength-grating slot (SWGS) structures further increases modal overlap with the analyte. Measured modal sensitivity near 79% agrees with theory around 83%, and suspension through BOX removal or thinning affords further improvement [137]. More recently, multi-box SWGs combined with cascaded MRRs on SOI have reached a record refractive-index sensitivity of 810 nm/RIU with a detection limit of 2.04×10^{-5} RIU, underlining the continuing promise of SWGs for high-performance biochemical sensing [30].

To heighten light-matter coupling, a widely adopted approach deposits a high-index or functional layer on the sensor surface so that the modal field is lifted towards the analyte and the effective interaction length is increased. On polymer inverted-ridge or planar waveguides,

sputtered Ta_2O_5 markedly improves both bulk and surface-adsorption sensitivity. Reported limits of detection reach 3×10^{-7} RIU for refractive-index sensing and about 100 fg/mm^2 for surface mass loading, while the Ta_2O_5 layer also acts as a moisture barrier and stabilises the baseline [138]. Studies using atomic-layer-deposited Al_2O_3 and TiO_2 bilayers show that the coating can improve response but may introduce non-monotonic PSs due to polar-molecule adsorption, underscoring the need to co-optimise surface chemistry with sensitivity [139]. At the resonator level, high-index sol-gel coatings can compress the modal volume of SiO_2 microcavities by more than 30% while maintaining Q near 10^6, raising the Q-to-V ratio and drawing more of the field into the coating to amplify surface bio-interactions [140]. Functional overlayers for specificity are also attractive. Periodic iron nanodisks on silicon MRRs enable corrosion monitoring via refractive-index change, with theoretical sensitivity around 517 nm/RIU and an enlarged FSR, and the same concept can inform biochemical recognition layers [141]. Metal-assisted interfaces can suppress downward leakage and push the field into the overlayer. Simulations indicate a gas-region confinement factor of 85% and ring sensitivities above 1000 nm/RIU, demonstrating the synergy of overlayers with metal assistance [142]. Composite functional films and selective polymer membranes have likewise been used to realise selective biochemical detection. For example, an Er^{3+}:$YAlO_3$/SiO_2/TiO_2 (EYST) composite combined with a permeable polymer membrane achieved high selectivity and low detection limits for phenols, illustrating the transferability of the overlayer plus enrichment or catalysis concept [143].

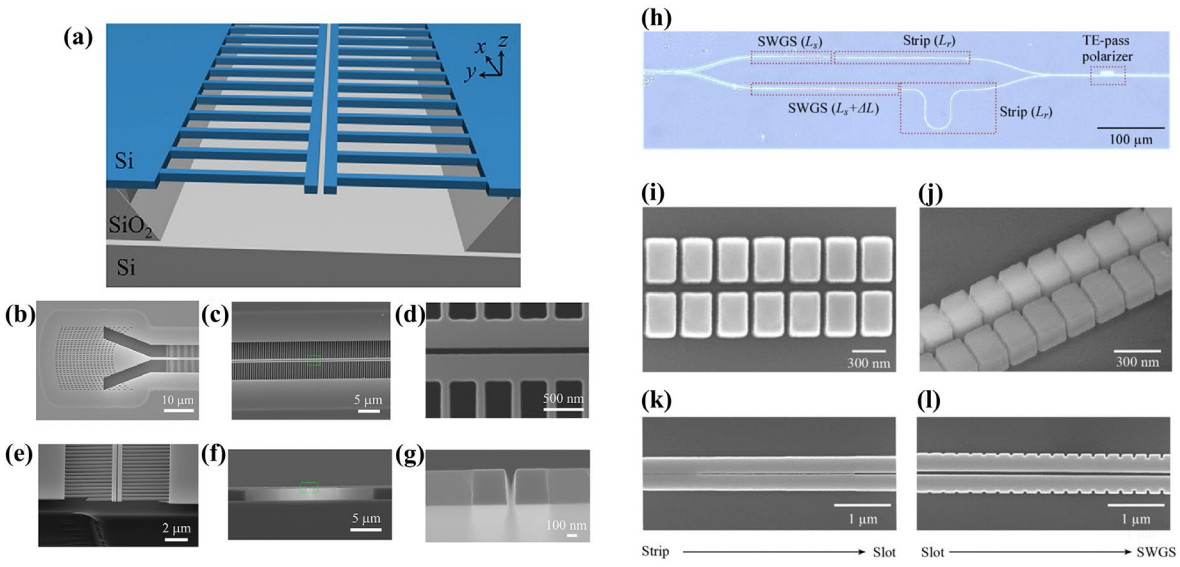

Fig. 2.5 (a) Schematic of a fully suspended slot waveguide for on-chip biochemical sensing and (b-g) SEM images of fabricated devices [127]. On SOI, a microscope image of (h) an MZI integrating an SWGS sensor and (i-l) local SEM images [137].

Engineering the waveguide dispersion so that a small Δn_{eff} produces a much larger change in the output signal is an effective means to raise sensor sensitivity. In wavelength-tracking schemes, increasing the spectral shift $\Delta\lambda$ for the same Δn_{eff} through dispersion engineering directly improves sensitivity.

One important route is by designing the dispersion of the coupling region and the ring so that the self-coupling coefficient and the round-trip attenuation are both strongly dispersive but have opposite slopes over the operating band, the resonance envelope exhibits pronounced undulation. Tracking the envelope peak rather than a single resonance alleviates the FSR constraint. Narrow-rail slot-ring couplers have raised sensitivity to approximately 1300 nm/RIU [144]. With SWGS rings, envelope tracking has achieved 1420 nm/RIU experimentally with good thermal stability of about 10 pm/ºC, significantly extending the dynamic range [145]. Raceway-type SWG MRRs have likewise delivered 860.8 nm/RIU, a detection limit of 1.9×10^{-5} RIU and Q around 6200 using envelope tracking [146].

A second route is phase-matching-dispersion turning-point amplification. In long-period gratings or bimodal or hetero-modal couplers, when the group-index difference between two modes approaches 0, the sensitivity scales as the inverse of this difference and diverges. Asymmetric sidewall long-period gratings in silicon waveguides have reached 5078 nm/RIU experimentally [32]. Writing a long-period grating in a metal-backed ridge waveguide and operating near the dispersion turning point exploits the stronger external field of higher-order modes to deliver refractive-index sensitivity of order 100 μm/RIU, namely 10^5 nm/RIU, in a more compact structure [147]. Adding a high-index surface layer to induce modal transition and combining dual resonance with a turning point similarly exceeds 100 μm/RIU with good tolerance to fabrication [148]. In dual-mode silicon waveguides incorporating an asymmetric top diffraction grating, theoretical and numerical analyses reveal dispersion-enhanced sensitivities exceeding 3000 nm/RIU [149].

Interferometric readout can also exploit spectral splitting caused by arm-to-arm dispersion difference so that a minute Δn_{eff} is converted into a large bidirectional separation of spectral peaks. Responses up to 10^4 nm/RIU have been reported, while mitigating phase ambiguity and extending dynamic range [150]. Taken together, dispersion control through coupling and phase matching leverages structural dispersion to convert Δn_{eff} into $\Delta\lambda$, providing key pathways to circumvent FSR limits while combining high sensitivity with a wide range and low detection limit.

Cascaded structures offer an additional means of magnifying the conversion from Δn_{eff} to a measurable output. The introduction of cascades enables the exploitation of the Vernier effect or Fano resonance to improve sensitivity.

The Vernier effect uses a slight mismatch in FSR between two or more resonant elements so that the same Δn_{eff} induces a much larger shift of the envelope peak, markedly elevating wavelength-tracking sensitivity and measurable span. Common designs employ dual- or multi-MRR cascades. On a polymer platform, embedding an MRR into the two arms of an MZI to form an MRR-MZI-MRR structure delivered bulk sensitivity of 17558 nm/RIU with a detection limit near 1.1×10^{-6} RIU, evidencing high Vernier gain [151]. On silicon, three-MRR cascades have balanced high sensitivity and very wide measurement range, reporting 5866 nm/RIU with a span roughly 24.7 times that of conventional dual-MRR devices [152]. To extend to the mid-infrared and leverage fingerprint selectivity, SOI dual-MRR Vernier cascades have achieved approximately 3000 nm/RIU for organic liquids with thermal-tuning compensation [153]. To suppress temperature drift stemming from the large TO coefficient of silicon, MRR and MZI cascades can be parameterised so that the MZI drift compensates that of the MRR. Temperature sensitivity then falls below 4 pm/K while bulk sensitivity of 3552 nm/RIU is retained, enabling passive temperature-stabilised Vernier sensing without polymer claddings [154]. Recently, combining SWG or SWGS waveguides with envelope tracking provides Vernier-like large-range readout with higher sensitivity. An SWGS MRR achieved 1420 nm/RIU while breaking the FSR limit [145], and a dual-MRR Vernier cascade on SWG raceway rings reached 7061 nm/RIU with a detection limit of 1.74×10^{-5} RIU [155]. SWG-based envelope trackers with high Q and detection limits at the 10^{-5} level further confirm that subwavelength field release combined with envelope or Vernier tracking is a key direction in cascaded sensing [146].

Fano-resonant cascades harness coherent interference between a discrete resonant state and a continuum waveguide mode to produce an asymmetric lineshape with high local slope within a narrow band. This converts a small Δn_{eff} into a readily measurable change of transmission, reflection or wavelength and has become a prominent route to higher sensitivity [156]. On side-coupled MRR platforms, introducing a local phase delay in the bus waveguide controls the phase difference between discrete and continuum states, enabling programmable transformation between a Lorentzian peak or dip and an arbitrary Fano profile within a single ring. This markedly increases lineshape slope and resolution and provides a device-level basis for high-sensitivity sensing [157]. For practical sensing, cascaded resonator or cavity-waveguide systems combining wide and narrow linewidths

with controlled detuning achieve steeper intensity-wavelength slopes. Parallel, series and nested dual-MRR configurations have been systematically compared and optimised, reaching slopes around 7.6×10^2 /nm. Using TiO_2 or Si_3N_4 waveguides with a negligible TO coefficient suppresses temperature drift and loss noise, suiting on-chip gas or volatile detection [158]. In silicon slot waveguides, Fano resonators implemented with multiple cavities in parallel and a phase shifter have been experimentally verified, combining strong field–matter overlap with a clear asymmetric lineshape. In aqueous claddings, the refractive-index sensitivity of 92 nm/RIU has been measured [159]. By coupling Fano resonances to porous or microporous waveguides and to plasmonic elements, photonic and plasmonic cascades can simultaneously raise coupling strength and quality factor. Measurements have reported refractive-index sensitivity of 56.24 μm/RIU with FoM near 2999 /RIU and quantitative detection of carcinoembryonic antigen protein, underscoring potential for high-performance label-free biochemical sensing [160].

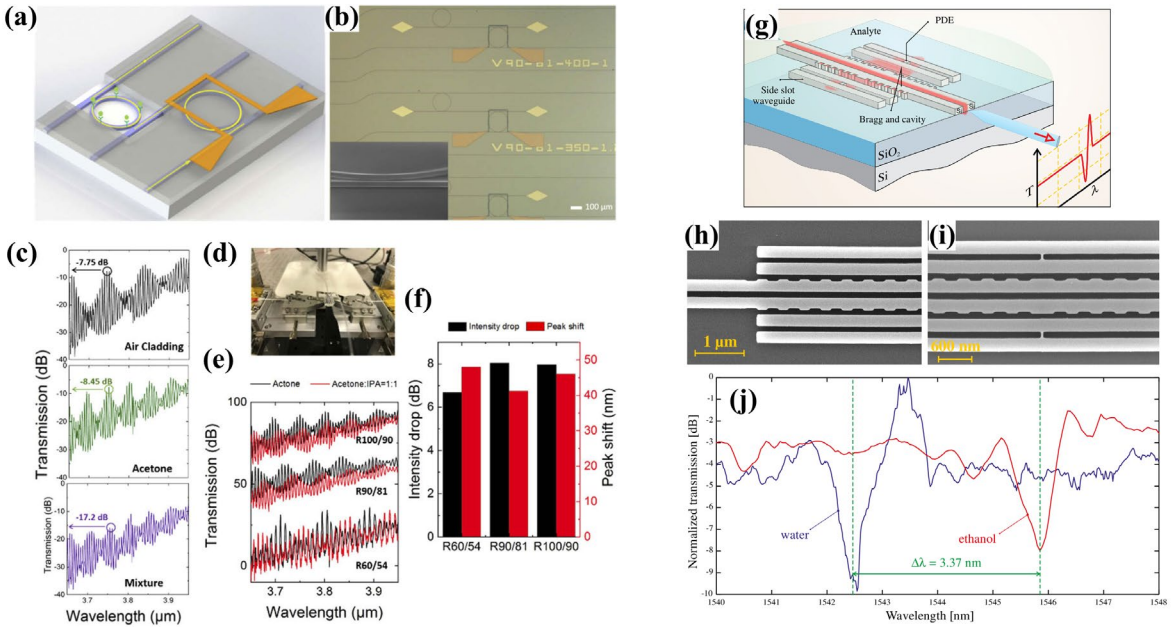

Fig. 2.6 (a-b) Schematic and microscope images of cascaded MRRs exploiting the Vernier effect for biochemical sensing. (c) Measured spectra under distinct claddings, (d) experimental platform, (e) Vernier envelopes for different devices and solutions and (f) the corresponding intensity attenuation and peak shift [153]. (g) Schematic of a photonic-crystal cavity and a slot-waveguide device producing Fano resonances and (h-i) SEM images after fabrication. (j) Transmitted spectra for water and ethanol, shown in blue and red, respectively [159].

2.3 Chapter summary

This chapter reviewed the state of the art of integrated PFs and on-chip biochemical sensors from a unified system-level perspective. For integrated PFs, narrowband responses have been pursued using high-Q resonators and Brillouin or acousto-optic enhancement, while

multi-passband and programmable operation have been enabled through cascaded interferometric networks, resonator arrays, and reconfigurable gratings. These approaches demonstrate strong spectral selectivity and tunability, yet they also reveal persistent constraints when scaling towards many independently controllable channels: additional sub-devices and tuning sections typically increase footprint, insertion loss, and thermal crosstalk, and they raise the electrical power required for trimming and drift management.

For on-chip biochemical sensors, high sensitivity has been achieved by increasing light–matter overlap using slot, suspended, SWG, and HPW, and by amplifying the transduction of n_{eff} perturbations through dispersion engineering and cascaded concepts such as turning-point enhancement, Vernier envelopes, and Fano resonances. While many sensing elements are intrinsically passive, practical large-scale deployment introduces power and scalability considerations through temperature stabilisation, resonance locking, and multiplexed readout and calibration.

Across both device classes, the literature indicates a common bottleneck: achieving high functional density in a compact footprint without incurring prohibitive tuning or stabilisation power and without sacrificing scalability due to control-channel proliferation and crosstalk. This benchmarking viewpoint motivates the subsequent chapters, where the proposed device frameworks aim to increase functionality per unit area while preserving a feasible power and control budget for scalable integration.

3 Theory

3.1 Bragg grating analysis

3.1.1 Bragg condition

A Bragg grating is realised by imposing a refractive-index perturbation that is periodic along the propagation direction of a waveguide. In a sidewall grating, this is achieved by etching periodic corrugations on the waveguide sidewalls, which produces a periodic modulation of the n_{eff} through a periodic variation of the waveguide boundary. The periodic structure gives rise to Bragg scattering, diffraction and reflection of guided light.

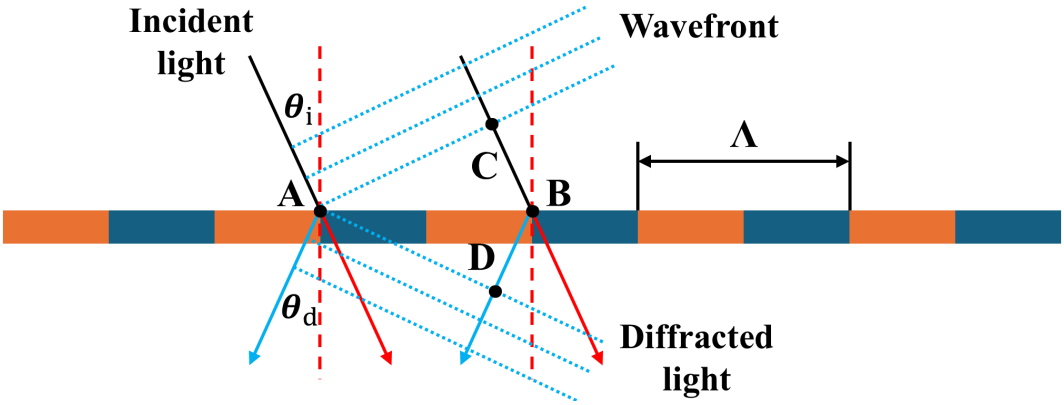

Fig. 3.1 Schematic of grating diffraction.

As sketched in Figure 3.1, a plane wave is incident at angle θ_i and diffracts at angle θ_d from points A and B on the grating. For the case in which the incident and diffracted rays lie on the same side of the surface normal, the optical-path difference along an equal-phase surface is $d_{BC}+d_{BD}$. For the two diffracted rays to interfere constructively in accordance with Huygens' principle, the phase difference must be an integer multiple of 2π, namely, the path difference must equal an integer multiple of the wavelength:

$$d_{BC}+d_{BD}=m\lambda \tag{3.1}$$

where $d_{BC}=\sin(\theta_i)n_{eff}\Lambda$, $d_{BD}=\sin(\theta_d)n_{eff}\Lambda$, Λ is the grating period, n_{eff} is the effective refractive index, m is the grating order, and λ is the wavelength of light in free space. Including the case in which the incident and diffracted rays lie on opposite sides of the normal yields the grating equation:

$$|\sin(\theta_i) \pm \sin(\theta_d)|\, n_{eff}\Lambda = m\lambda \tag{3.2}$$

For on-chip Bragg gratings in this thesis, the incidence is normal, so θ_i equals 90º. Although the indices of the waveguide core and cladding differ, the incidence condition reduces to the classical Bragg relation:

$$m\lambda = 2n_{eff}\Lambda \tag{3.3}$$

The presence of a periodic grating enables coupling between counter-propagating guided modes and between guided and radiation modes. Assuming the waveguide supports only the fundamental quasi-TE mode, the forward-propagating guided mode with propagation constant $\beta_{c,m}$ interacts with Fourier components of the grating perturbation to excite radiation modes with propagation constant $\beta_R = RE(\beta_{c,m}) - 2\pi p/\Lambda \ \ (p = \pm 1, \pm 2, \cdots)$. For a 1st order grating, since $RE(\beta_{c,m}) \approx \pi/\Lambda$, the phase-matching condition to radiation modes is not satisfied, and thus no radiation is generated. For higher-order gratings, however, the condition can be satisfied. For a 2nd-order grating, $RE(\beta_{c,m}) \approx 2\pi/\Lambda = \beta_B$, β_R is approximately 0 for $p = \pm 1$ so that the guided mode couples to a radiation mode propagating at 90º, giving rise to 1st order radiation loss, as illustrated in Figure 3.2. Higher-order gratings, therefore, relax fabrication-resolution constraints but allow more wavelengths to satisfy the phase condition, which degrades single-mode selectivity in fine filtering.

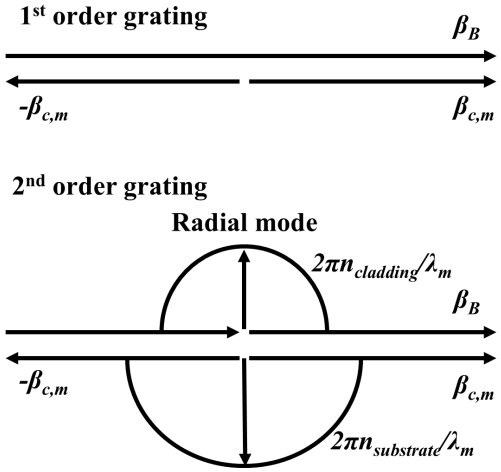

Fig. 3.2 Graphical representation of the guided mode, radiation mode and grating wavevectors in a waveguide.

3.1.2 Coupled mode theory

Any refractive-index perturbation that causes the natural modes of a waveguide to no longer satisfy the unperturbed wave equation can induce coupling. In many practical devices, such as Bragg gratings considered here, the perturbation is small so that over a short section, the field remains guided and modal, yet the cumulative effect of the perturbation produces measurable changes in the field evolution. Coupled-mode theory provides a standard framework for analysing such small-amplitude index perturbations [161–163].

Under refractive index disturbance, the optical field in the waveguide can still be described by the superposition of a limited number of eigenmodes. In the absence of perturbation, the scalar wave equation of a waveguide at a fixed optical wavelength can be written as:

$$\nabla_T^2 E + \frac{\partial^2 E}{\partial z^2} + k_0^2 n(x,y)^2 E = 0 \tag{3.4}$$

where E is the optical field distribution, $n(x,y)$ is the refractive index distribution of the optical waveguide cross-section, and k_0 is the propagation constant of the electromagnetic field in a vacuum. When a small index perturbation Δn is introduced, the perturbed field becomes:

$$\nabla_T^2 E + \frac{\partial^2 E}{\partial z^2} + k_0^2 (n^2 + 2n\Delta n) E = 0 \tag{3.5}$$

Bragg gratings induce coupling between two transverse modes that propagate in opposite directions but share the same frequency. Under the refractive index perturbation, the total optical field is expressed as:

$$E = RE_T e^{j\frac{\pi}{\Lambda/m}z} + SE_T e^{-j\frac{\pi}{\Lambda/m}z} \tag{3.6}$$

R and S are the positive and reverse optical field complex amplitude envelopes, E_T is the transverse cross-sectional field distribution, and Λ is the period of the grating. To avoid ambiguity between angular notation and complex-number notation, the imaginary unit is denoted by j throughout this thesis, where $j^2 = -1$. Accordingly, complex quantities are written in the form $n = n' + jn''$ (and $\beta = \beta' + j\beta''$ where relevant). Substituting equation (3.6) into the wave equation (3.4), applying the slowly varying envelope approximation to

neglect 2nd order derivatives and enforcing the wave equation $\nabla_T^2 E_T + k_0^2 n^2 E_T = \beta^2 E_T$ within the waveguide gives the new perturbed evolution equation:

$$\begin{aligned} & j\frac{2\pi}{\Lambda/m} S' e^{-j\frac{\pi}{\Lambda/m}z} E_T - j\frac{2\pi}{\Lambda/m} R' e^{j\frac{\pi}{\Lambda/m}z} E_T \\ =& \left\{ k_0^2 2n\Delta n + \left[\beta^2 - \left(\frac{\pi}{\Lambda/m} \right)^2 \right] \right\} R\,\mathrm{e}^{j\frac{\pi}{\Lambda/m}z} E_T \\ +& \left\{ k_0^2 2n\Delta n + \left[\beta^2 - \left(\frac{\pi}{\Lambda/m} \right)^2 \right] \right\} S\,\mathrm{e}^{j\frac{\pi}{\Lambda/m}z} E_T \end{aligned} \tag{3.7}$$

Let β denote the propagation constant. For further simplification, assume that the transverse distribution of the index perturbation is uniform across the waveguide cross-section. Introduce a normalised overlap function $\Gamma(x,y)$, and since both R and S are defined as envelopes, E_T can be considered normalised by power:

$$\int E_T^* \cdot E_T \, dxdy = 1 \tag{3.8}$$

Define the overlap integrals and coupling parameters as follows:

$$\int E_T^* \cdot n\Gamma E_T \, dxdy = n_{eff}\Gamma_0 \tag{3.9}$$

From equation (3.9), it can be seen that Γ_0 represents the overlap between the fluctuations in refractive index and the field distribution. If the cross-sectional distribution of the refractive index fluctuations covers the entire optical field evenly, then $\Gamma_0 = 1$. With these definitions, the vector equation reduces to a one-dimensional system for the forward and backward envelopes:

$$\begin{aligned} R' e^{j\frac{\pi}{\Lambda/m}z} - S' e^{-j\frac{\pi}{\Lambda/m}z} &= j\sigma_m R\,\mathrm{e}^{j\frac{\pi}{\Lambda/m}z} + j\sigma S\,\mathrm{e}^{-j\frac{\pi}{\Lambda/m}z} \\ &+ j\sum_{m'=1}^{\infty} \left({\kappa_m}' e^{-j\frac{2m'\pi}{\Lambda}z} + c.c \right) R\,\mathrm{e}^{j\frac{\pi}{\Lambda/m}z} \\ &+ j\sum_{m'=1}^{\infty} \left({\kappa_m}' e^{-j\frac{2m'\pi}{\Lambda}z} + c.c \right) S\,\mathrm{e}^{-j\frac{\pi}{\Lambda/m}z} \end{aligned} \tag{3.10}$$

$$\begin{cases} \kappa_m = \dfrac{\Lambda/m}{2\pi} n_{eff} k_0^2 \Gamma_0 n_{AC,m} \\ \sigma_m = \dfrac{\Lambda/m}{2\pi}\left[\beta^2 - \left(\dfrac{\pi}{\Lambda/m}\right)^2\right] \end{cases} \tag{3.11}$$

Under a rotating wave approximation, only equal spatial-harmonic terms on both sides of the equation (3.10) are retained. Since *R* and *S* are slowly varying envelopes, their derivatives *R'* and *S'* are also slowly varying. The system then decouples into the standard pair of 1st order coupled-mode equations:

$$\begin{pmatrix} R \\ S \end{pmatrix}' = j\begin{bmatrix} \sigma_m & \kappa_m^* \\ -\kappa_m & -\sigma_m \end{bmatrix}\begin{pmatrix} R \\ S \end{pmatrix} \tag{3.12}$$

When the grating couples forward and backward waves, the Bragg condition must hold under the rotating wave approximation $\beta = n_{eff} k_0 \approx m\pi/\Lambda$. The modal coupling coefficient κ_m and the detuning σ_m simplify to:

$$\begin{cases} \kappa_m = \dfrac{\pi}{2 n_{eff} \Lambda/m} \Gamma_0 n_{AC,m} \\ \sigma_m = n_{eff} k_0 - \dfrac{\pi}{\Lambda/m} \end{cases} \tag{3.13}$$

In the fabricated devices considered in this thesis, we employ 1st-order sidewall rectangular gratings, so $m = 1$. Here, Δn_{AC} denotes the n_{eff} difference between the unetched and etched segments of the grating. The average effective index of the grating waveguide is n_{eff}. For a 1st-order grating, the κ attains its maximum at a duty cycle of 0.5. Physically, the κ represents the per-unit-length index contrast of the periodic structure.

3.1.3 Transfer matrix method

For a uniform Bragg grating (UBG), the index modulation can be written in the form:

$$n_{AC}(z) = \Delta n \cdot w(z) \tag{3.14}$$

Here, Δn is the modulation amplitude, and $w(z)$ is a window function of unit peak between $-L/2$ and $L/2$, outside which $w(z)$ equals 0. The UBG corresponds to a rectangular function:

$$w(z)=\begin{cases}1, & -L/2\leqslant z<L/2\\ 0, & else\end{cases} \tag{3.15}$$

In this subsection, we focus on 1st-order gratings with m = 1. For a sidewall UBG with a constant κ over a length L, the equation (3.12) admits a closed-form solution. The solution can be expressed as a 2×2 complex transfer matrix T that relates the complex field amplitudes at the two ends of the grating. Diagonalising the system matrix and exponentiating the diagonal form gives the compact expression:

$$\begin{pmatrix}R\\ S\end{pmatrix}_{|z=L}=\exp\left[j\begin{pmatrix}\sigma & \kappa^*\\ -\kappa & -\sigma\end{pmatrix}L\right]\cdot\begin{pmatrix}R\\ S\end{pmatrix}_{|z=0} \tag{3.16}$$

with the auxiliary definitions:

$$T=\exp\left[j\begin{pmatrix}\sigma & \kappa^*\\ -\kappa & -\sigma\end{pmatrix}L\right]=\begin{pmatrix}t_{11} & t_{12}\\ t_{21} & t_{22}\end{pmatrix} \tag{3.17}$$

$$\begin{cases}t_{11}=\cosh(j\gamma L)+\dfrac{\sigma}{\gamma}\sinh(j\gamma L)=\cos(\gamma L)+i\dfrac{\sigma}{\gamma}\sin(\gamma L)\\ t_{12}=\dfrac{\kappa^*}{\gamma}\sinh(j\gamma L)=j\dfrac{\kappa^*}{\gamma}\sin(\gamma L)\\ t_{21}=-\dfrac{\kappa}{\gamma}\sinh(j\gamma L)=-j\dfrac{\kappa}{\gamma}(\gamma L)\\ t_{22}=\cosh(j\gamma L)-\dfrac{\sigma}{\gamma}\sinh(j\gamma L)=\cos(\gamma L)-j\dfrac{\sigma}{\gamma}\sin(\gamma L)\end{cases} \tag{3.18}$$

$$\gamma^2=\sigma^2-|\kappa|^2 \tag{3.19}$$

Each term admits an equivalent representation in terms of hyperbolic or trigonometric functions. Knowing the transfer matrix T and the boundary conditions, one can compute all relevant physical quantities of a uniform Bragg grating. As a three-parameter structure defined by period, length and modulation amplitude, the uniform grating offers limited degrees of freedom and therefore restricted spectral shaping. To obtain improved performance or new functionalities, one must design more general index profiles. A cascaded transfer-matrix framework (Figure 3.3) enables numerical synthesis and analysis of arbitrary grating structures.

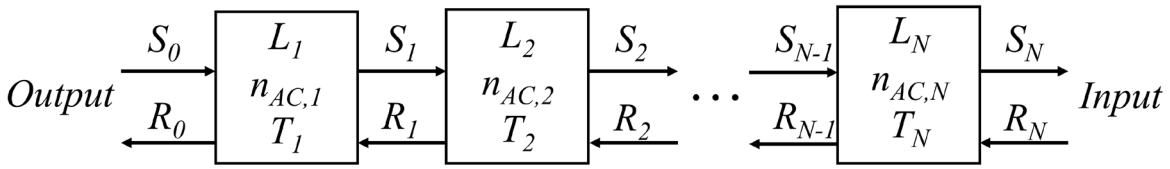

Fig. 3.3 Schematic of the transfer-matrix method (TMM).

The grating cavity is first discretised into N segments, each of which is considered to be a UBG unit and has three independent parameters, length L, coupling coefficient κ and alternating current refractive index n_{AC}. Then, the transmission matrix of all discrete gratings is solved separately. Finally, the transmission matrix of the entire Bragg grating is:

$$T = T_N \times T_{N-1} \times \cdots \times T_2 \times T_1 \tag{3.20}$$

This TMM is actually a discrete form of differential equations by mathematical definition, and in terms of physical structure, when observing Bragg gratings of sufficiently short lengths, it can be approximated as a uniform grating.

3.1.4 Sampled Bragg grating

For a typical Bragg reflector, the refractive-index modulation along the cavity can be written as:

$$n(z) = n_0 + \Delta n(z_0) \tag{3.21}$$

where n_0 is the basic n_{eff} and $\Delta n(z)$ is the modulation of n_{eff}. It can be shown from Figure 3.4(a) that, for a seed grating, the modulation is commonly represented as a cosine function. The Fourier-series expansion of a UBG contains only the 0^{th} term, which is consistent with the familiar fact that a UBG produces a single stopband around the Bragg frequency. This observation embodies the mapping between the physical structure and the spectral response through the Fourier transform.

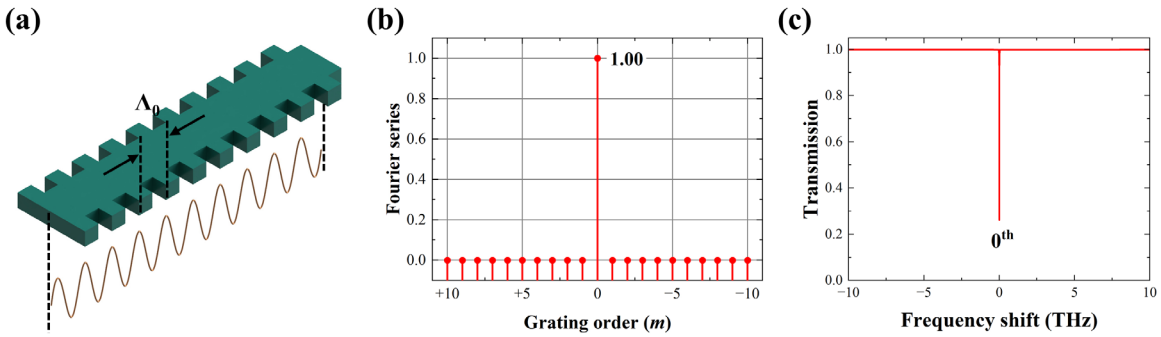

Fig. 3.4 UBG: (a) schematic, (b) Fourier-series distribution and (c) transmission spectrum.

In a periodically sampled structure, one defines a spatial sampling function $s(z)$ and incorporates it into the modulation. Using Euler expansion and introducing $s(z)$, the varying component of the modulation can be written as:

$$\Delta n(z) = s(z) \cdot \frac{1}{2} \cdot (\Delta n_0 e^{j\frac{2\pi z}{\Lambda_0}} + c.c) \tag{3.22}$$

Here, Δn_0 is the seed-grating modulation amplitude, z is the longitudinal coordinate of the grating cavity, and Λ_0 is the period of the seed grating. The $s(z)$ admits a Fourier-series expansion:

$$s(z) = \sum_m F_m e^{-j\frac{2m\pi z}{P_s}} \tag{3.23}$$

where m indexes the Fourier components, F_m are the corresponding channel intensity coefficients, and P_s is the sampling period. For a conventional sampled Bragg grating (C-SBG), each unit cell comprises a grating section and a non-grating section, each of length equal to half of P_s. The corresponding $s(z)$ within a complete sampling period is:

$$s(z)_{C-SBG} = \begin{cases} 1, & 0 < z \leqslant P_s/2 \\ 0, & P_s/2 < z \leqslant P_s \end{cases} \tag{3.24}$$

Fourier analysis decomposes the periodic $s(z)$ into multiple channels, each corresponding to a ghost grating. After applying the Fourier expansion and substituting into the modulation, one obtains:

$$\Delta n(z) = \frac{1}{2} \cdot \Delta n_0 \sum_m F_m e^{-j\frac{2m\pi z}{P_s}} e^{-j\frac{2m\pi z}{\Lambda_0}} + c.c \tag{3.25}$$

Equation (3.25) shows that a sampled grating is a superposition of sub-gratings of different orders (m) with different effective seed periods Λ_m given by:

$$\Lambda_m = \frac{P_s \Lambda_0}{P_s + m\Lambda_0} \tag{3.26}$$

The central wavelength of each ghost grating is still governed by the Bragg condition. For the m^{th} order channel:

$$\lambda_m = 2n_{eff}\Lambda_m \tag{3.27}$$

The 0^{th}-order channel is determined by the seed period Λ_0:

$$\lambda_0 = 2n_{eff}\Lambda_0 \tag{3.28}$$

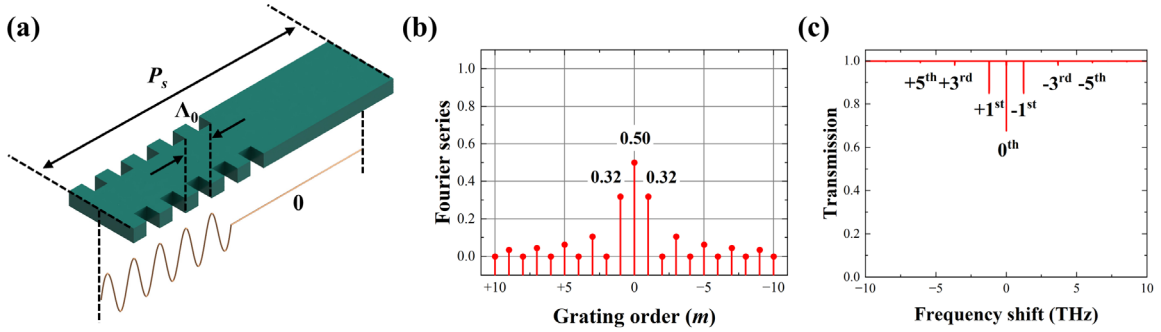

Fig. 3.5 C-SBG: (a) schematic, (b) Fourier-series distribution and (c) transmission spectrum.

In the C-SBG (Figure 3.5) considered here, the $+1^{st}$ channel $m = +1$ is used as the working channel of the following PFs. The Fourier coefficients show that the κ of the $+1^{st}$ sub-grating is approximately $1/\pi$ of that of the UBG. The reduced κ leads to narrower stopbands and weaker ER, which in filter applications implies a narrower tuning range and lower SMSR. A common remedy is to increase the cavity length to compensate for the low κ. In sidewall grating waveguides on chip, however, longer cavities incur stronger sidewall scattering and greater propagation loss, and they run counter to miniaturisation and high integration.

To address these issues, we employ a 4PS-SBG, as shown in Figure 3.6. In the 4PS-SBG, each P_s is partitioned into four equal segments, and adjacent segments carry relative phase shifts of π/2. The corresponding $s(z)$ is:

$$s(z)_{4PS-SBG}=\begin{cases}1,\ 0<z\leqslant P_s/4\\ e^{j\pi/2},\ P_s/4<z\leqslant P_s/2\\ e^{j\pi},\ P_s/2<z\leqslant 3P_s/4\\ e^{j3\pi/2},\ 3P_s/4<z\leqslant P_s\end{cases} \tag{3.29}$$

Fourier analysis (Figure 3.6(b)) shows that the 4PS-SBG increases the κ of the +1st channel to about 0.9 times that of the UBG while suppressing the 0th channel. Consequently, using the +1st channel as the working channel, a 4PS-SBG can achieve the same ER performance with a shorter cavity and deliver a broader stopband than a C-SBG. Notably, the 4PS sampling structure not only boosts the +1st sub-grating channel by about 3 times compared to C-SBG, but also effectively suppresses the 0th order channel.

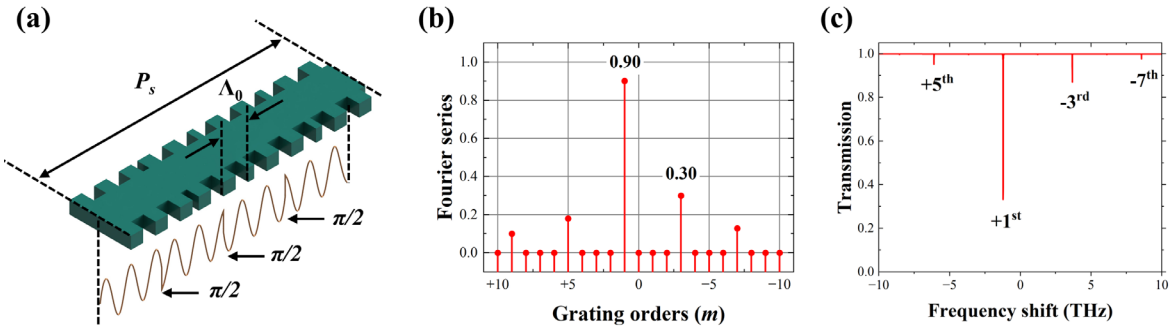

Fig. 3.6 4PS-SBG: (a) schematic, (b) Fourier-series distribution and (c) transmission spectrum.

3.1.5 Equivalent chirped grating

A chirped grating has a seed period $\Lambda(z)$ that varies along the longitudinal coordinate z [164], typically linearly as:

$$\Lambda(z)=\Lambda_0+C\cdot z \tag{3.30}$$

Here, Λ_0 is the period at z = 0, and C is the linear chirp rate. Chirp is equivalent to a phase modulation of the refractive-index perturbation, so the modulation function can be written as:

$$\Delta n(z) = \frac{1}{2}\Delta n_0 e^{j\varphi(z)} \cdot e^{j\frac{2\pi z}{\Lambda_0}} + c.c. \tag{3.31}$$

Assuming constant modulation amplitude Δn_0, the additional phase $\varphi(z)$ arises from the varying period. By definition of period, the local period is inversely related to the derivative of the phase, so:

$$\frac{d\varphi(z)}{dz} = 2\pi\left[\frac{1}{\Lambda(z)} - \frac{1}{\Lambda_0}\right] \tag{3.32}$$

Let L be the chirped grating length. When $C \cdot L \ll \Lambda_0$, substitution equation (3.30) into (3.32) yields:

$$\varphi(z) = -\frac{\pi C z^2}{\Lambda_0^2} \tag{3.33}$$

Hence, the refractive index modulation function of a linear chirped grating becomes:

$$\Delta n(z) = \frac{1}{2}\Delta n_0 e^{-j\frac{\pi C z^2}{\Lambda_0^2}} \cdot e^{j\frac{2\pi z}{\Lambda_0}} + c.c. \tag{3.34}$$

The concept of equivalent chirp originates in the study of SBG. An SBG can be viewed as the product of a UBG and a $s(z)$, namely a slowly varying envelope applied to a fine seed grating. If the P_s varies along the cavity, the $s(z)$ becomes chirped and an equivalent chirp is induced.

For a uniform SBG, the sampling function is given above (equation (3.23)). When the P_s is chirped, the new $s(z)$ is:

$$s'(z) = \sum_m F'_m e^{j\varphi_m(z)} \cdot e^{j\frac{2\pi m z}{P_s}} \tag{3.35}$$

The corresponding index modulation is:

$$\Delta n(z) = s'(z) \cdot \frac{1}{2} \cdot \Delta n_0 e^{j\frac{2\pi z}{\Lambda_0}} + c.c. \tag{3.36}$$

Combining these expressions yields:

$$\Delta n(z) = \frac{1}{2}\sum_m F_m' e^{j\varphi_m(z)} \cdot e^{j\frac{2\pi m z}{P_s}} \cdot \Delta n_0 e^{j\frac{2\pi z}{\Lambda_0}} + c.c. \tag{3.37}$$

The modulation of the m^{th} order channel becomes:

$$\Delta n_m(z) = \frac{1}{2}\Delta n_0 F_m' e^{j\varphi_m(z)} \cdot e^{j\frac{2\pi m z}{P_s}} \cdot e^{j\frac{2\pi z}{\Lambda_0}} + c.c. \tag{3.38}$$

Substituting into the equation (3.26) gives:

$$\Delta n_m(z) = \frac{1}{2}\Delta n_0 F_m' e^{j\varphi_m(z)} \cdot e^{j\frac{2\pi z}{\Lambda_m}} + c.c. \tag{3.39}$$

Compared with the equation (3.31), the only difference lies in the grating period. Therefore, a response like the modulation of seed grating chirps is obtained in the m^{th} order channel, i.e., equivalent chirps are introduced.

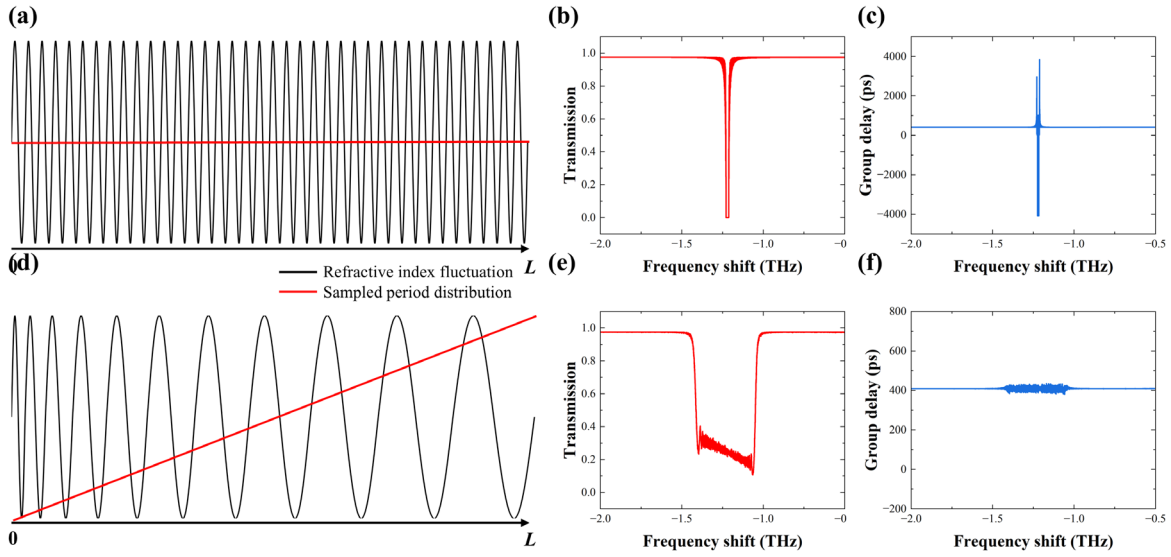

Fig. 3.7 Uniform SBG and its (a) period distribution, (b) +1st subgrating transmission and (c) time delay; and equivalent chirped SBG and its (d) period distribution, (e) +1st subgrating transmission and (f) time delay.

As shown in Figure 3.7, a chirp widens the transmission spectrum. Different wavelengths are reflected at various positions, yielding different group delays in reflection and equalised delay in transmission. Chirped gratings are therefore widely used for dispersion compensation in optical fibre [165].

3.1.6 Equivalent phase shift

In conventional on-chip gratings, the Λ_0 is on the order of hundreds of nm. Realising a well-controlled PS necessitates high-resolution EBL, and the imposed phase step is typically $\Lambda_0/2$. Nanometre-scale fabrication errors can shift the centre wavelength by tens of GHz, which significantly increases process difficulty and cost. The concept of EPS markedly relaxes fabrication tolerance by at least two orders of magnitude.

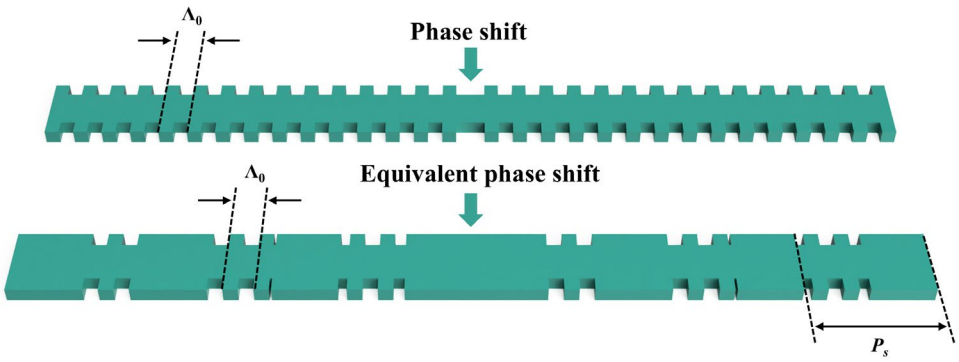

Fig. 3.8 Schematic of true PS in UBG and EPS in C-SBG.

The principle again relies on SBGs. By introducing a phase step in the sampling period rather than in the seed grating, one can reproduce the spectral response of a true PS in the grating core, as sketched in Figure 3.8 and Figure 3.9.

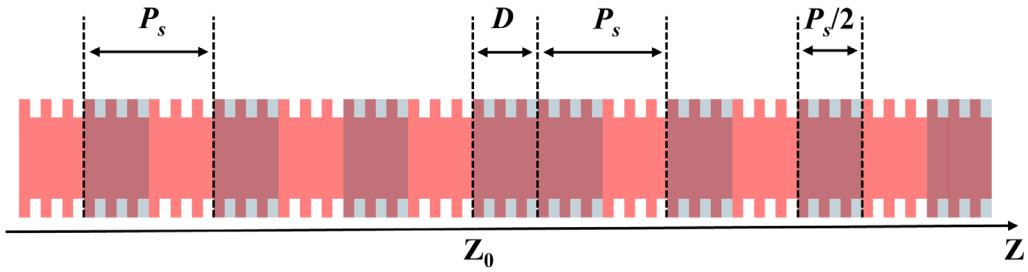

Fig. 3.9 SBG incorporating an EPS.

In Figure 3.9, consider a uniform SBG in which the sampling unit centred at position z_0 is lengthened by D. The sampling functions on the two sides then become:

$$s(z)=\begin{cases} s_L(z) & z<z_0 \\ s_R(z) & z\geqslant z_0 \end{cases} \tag{3.40}$$

Fourier-series analysis gives:

$$
\begin{aligned}
s_L(z) &= \sum_m \frac{1}{m\pi}\sin\left(\frac{m\pi}{2}\right)\cdot e^{j^{2\pi mz}/_{P_s}+j^{\pi m}/_2} \\
s_R(z) &= \sum_m \frac{1}{m\pi}\sin\left(\frac{m\pi}{2}\right)\cdot e^{j^{2\pi mz}/_{P_s}+j^{\pi m}/_2-j^{2\pi mD}/_{P_s}}
\end{aligned}
\tag{3.41}
$$

Substituting into the equation (3.22) yields:

$$
\Delta n = \begin{cases} \sum_m F_m e^{j^{2\pi z}/_{\Lambda_0}+j^{2\pi mz}/_{P_s}} + c.c. & z < z_0 \\ \sum_m F_m e^{j^{2\pi z}/_{\Lambda_0}+j^{2\pi mz}/_{P_s}-j^{2\pi mD}/_{P_s}} + c.c.\ z \geqslant z_0 \end{cases}
\tag{3.42}
$$

with the Fourier factor defined by:

$$
F_m = \frac{1}{2\pi m}\Delta n_0 \sin\left(\frac{\pi m}{2}\right)e^{j^{\pi m}/_2}
\tag{3.43}
$$

Hence the m^{th} channel acquires an EPS of amplitude θ_m given by:

$$
\theta_m = -\frac{2\pi mD}{P_s}
\tag{3.44}
$$

Because this PS difference is different from the real PS of traditional gratings, we call it EPS. By adjusting D, one can realise an arbitrary PS in any chosen channel. In particular, when $D = P_s/2$, the C-SBG introduces an equivalent $m\pi$ PS in all sub-channels. The transmission spectra in Figure 3.10 illustrate how the EPS breaks the degeneracy of the uniform grating and produces transmission peaks at the ghost Bragg wavelengths of $\pm1^{\text{st}}$ channels, analogous to a true π shift [166].

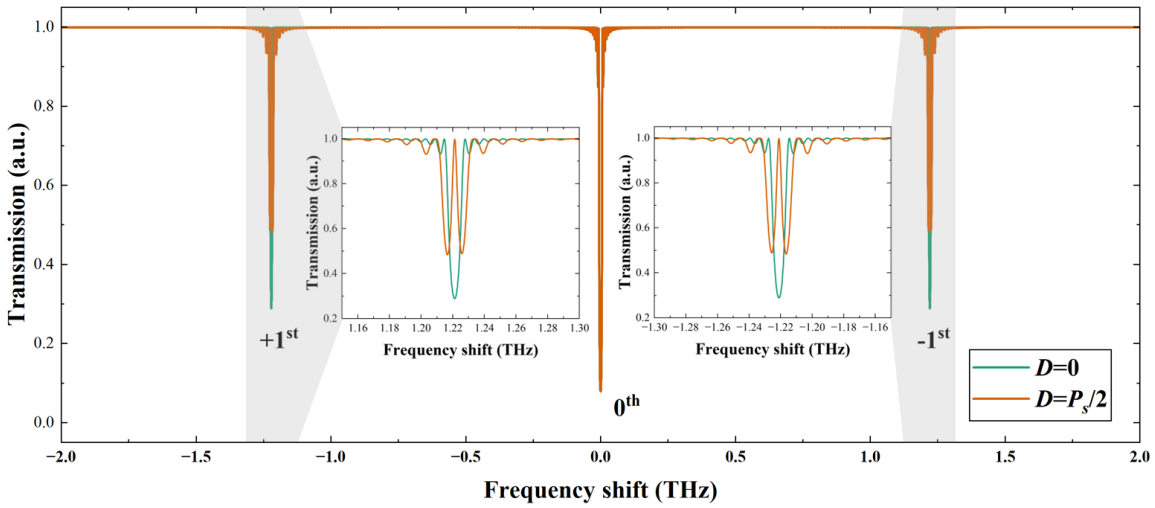

Fig. 3.10 Transmission spectra of a sampled grating for $D = 0$ and $D = P_s/2$.

3.1.7 Superstructure grating

The Bragg condition constrains the inherent bandwidth of a grating, whereas many applications require broadband operation. Sampled gratings create multiple channels by convolving the seed grating with the Fourier transform of the sampling function, translating spatial sampling into a comb-like spectral response. However, relying solely on amplitude sampling tends to produce Gaussian- or Lorentzian-like lines with fixed channel spacing, sharp peaks and in-band ripple that do not satisfy the flat-top and low-crosstalk requirements of optical communications. Deep amplitude modulation demands a low duty cycle and reduces grating utilisation. Phase engineering is a more efficient means of broadening the spectrum and shaping the passbands. Compared with overprint gratings, phase modulation is easier to implement [167]. However, the phase mask plates required for phase sampling are extremely complex and difficult to manufacture [168].

Beyond superimposed gratings and pure amplitude sampling, an additional route to multi-channel Bragg responses uses the Talbot self-imaging effect. When a chirped grating is sampled so that the sampling period and the chirp rate satisfy specific relations, a multi-channel reflection spectrum emerges.

A widely adopted technique is phase sampling with quasi-square phase modulation, first proposed in semiconductor lasers [169]. In contrast to amplitude sampling, which adjusts the local modulation intensity, phase sampling introduces discrete phase steps such as π, π/2 and 3π/2 within or between sampling sections, thereby altering the interference conditions of the reflected field at different positions. In intuitive terms, amplitude sampling opens or

closes local reflection windows, whereas phase sampling applies a distinct phase code to each window so that the fields superpose to form a more complex interference spectrum.

In particular, when the square phase jump is periodically introduced in the entire P_s, the so-called SSG is formed. The basic idea is that based on the original sampling grating, by accurately designing a series of phase modulation modes, the reflected light field generated by each sampling segment can not only coherently enhance some frequency points when the frequency domain is superimposed, but also suppress the fluctuation of the passband through destructive interference, so as to form a flat and customizable multi-channel filter response. Based on this method, another square phase sampling has evolved, known in the literature as SSG, as a multi-phase shift technique [170]. This phase modulation is applied to the entire SBG and occurs discretely between samples. Its refractive index modulation function can be expressed as:

$$s(z)=\sum_{k} f(z-kP)\exp\left[j\frac{k(k-1)}{2}\varphi\right] \tag{3.45}$$

where $f(z)$ is the refractive index modulation of a single sample, the k^{th} sampling period is P, φ is the basic phase step in square-law phase modulation, and φ_k determines the phase of the k^{th} sample end $\varphi_k = k(k-1)\varphi/2$ and the growth rate of the phase difference in adjacent segments.

Fourier analysis provides a clear interpretation. Let the UBG reflection be a main envelope centred at the Bragg wavelength, and let the transform of the sampling function determine the channel positions. With amplitude sampling alone, a periodic rectangular $s(z)$ yields equally spaced sinc-like lines under the main envelope, but the line strengths are non-uniform, and channel ripple is significant. Introducing a designed sequence φ_k causes the frequency-domain superposition of sub-grating reflections to reweight and flatten each channel [171]. Binary, quadrature and higher-order discrete sequences can be used to tailor passband width, ER and inter-channel crosstalk. In DWDM systems, such control is crucial because crosstalk and filter non-uniformity directly affect error rate and spectral efficiency.

Viewed in the time domain, each sampling section behaves as a partial reflector. Discrete phase codes function as path-length corrections for the reflected fields. At the design wavelengths, the phase sequence ensures constructive interference to form flat passbands, while destructive interference suppresses out-of-band components. Compared with pure

amplitude sampling, phase-coded SSGs offer greater freedom, robustness and manufacturability, since phase steps can be realised by refractive-index modulation amplitude control or by thermally induced PSs with high accuracy.

3.2 Waveguide and optical mode

Unless stated otherwise, all numerical simulations reported in this section are performed at a free-space wavelength of 1550 nm. This wavelength lies in the telecom C-band, where laboratory components and characterisation instrumentation are mature and readily available. More importantly, the sensors and Bragg-grating-based PFs developed in subsequent chapters are designed to operate around 1550 nm; adopting a consistent reference wavelength enables a like-for-like comparison of n_{eff}, dispersion and loss across different waveguide and grating designs.

3.2.1 Hybrid plasmonic waveguide

SOI nanowire waveguides with very high index contrast provide sub-μm optical confinement [172]. Nevertheless, purely dielectric nanophotonic waveguides remain bounded by the diffraction limit, which restricts further downscaling of the waveguide cross-section towards 100 nm. By contrast, SPP waveguides enable optical confinement at 100 nm and below, offering a viable route to genuinely nanoscale guidance. In addition, plasmonic waveguides can convey electrical and optical signals within the same circuit, forming a natural bridge between photonics and electronics. In recent years, HPWs have attracted broad attention for their relatively long propagation distance and for reducing the loss of metal-strip waveguides.

Propagation loss quantifies the attenuation of guided optical power per unit length. For a guided mode with a complex propagation constant $\beta = \beta' + j\beta''$, the modal power decays as $P(z) = P(0)\exp(-2\beta'' z)$. The corresponding loss in decibels is $\alpha_{dB} = 8.686 \times 2\beta''$ (dB/cm). When the loss is extracted from an eigenmode solver via the complex effective index $n_{eff} = n' + jn''$, one has $\beta'' = k_0 n''$ with $k_0 = 2\pi/\lambda_0$. Unless otherwise stated, the simulated propagation loss reported here accounts for material absorption and any radiation leakage captured by the modal solution, and does not include fabrication-induced scattering loss.

We introduce a low-loss HPW that incorporates three low refractive index nano-slots and is designed for TE polarisation. By employing two nm-scale hybrid plasmonic slots, field enhancement arising from the discontinuity of the normal electric field and from the SPP effect produces very high-power density in the slots. The strengthened field in the slots reduces the effective area. The high-power density within the slots is also advantageous for optical sensing. We refer to this structure as the slot bus waveguide and double slot hybrid plasmonic waveguide (SBW-DSHPW).

The cross-section comprises an SOI slot waveguide with metal sidewalls. A thin analyte layer is placed between the silicon and the metal claddings so that three slots form, one on each side of the silicon core and one at the centre. The structure is straightforward to fabricate and is compatible with CMOS processes.

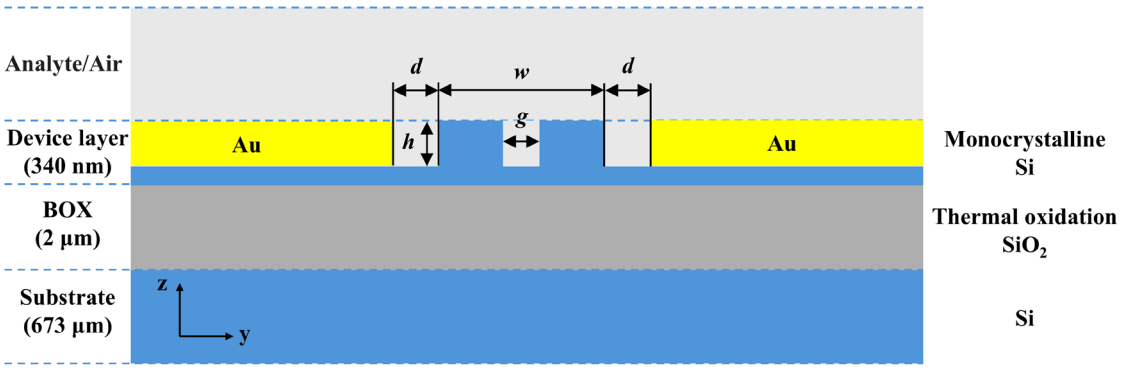

Fig. 3.11 Cross-section of the SBW-DSHPW.

When the analyte layer between silicon and the metal is relatively thick, for instance 0.5 µm, and the silicon slot waveguide is wide, for example 400 nm, the fundamental mode is well confined within the silicon slot, and the metal has minimal influence on the modal distribution. In this regime, the structure behaves similarly to a conventional SOI slot waveguide. When the dielectric spacer becomes thin, for example, below 50 nm, the metal layers significantly affect the guided mode.

As an illustrative geometry in Figure 3.11, we choose silicon-ridge width w equal to 300 nm, metal thickness h = 210 nm, slot width g equal to 50 nm, silicon rib height h equal to 210 nm and silicon-analyte-metal gap width d equal to 150 nm. At wavelength 1550 nm, the refractive indices are $n_{metal} = 0.5747 + j9.6643$ for gold (Au) [173,174], n_{SiO2} equal to 1.445 and n_{Si} equal to 3.455.

At the silicon-analyte-metal interfaces, the normal component of the electric field exhibits a strong discontinuity, as in purely dielectric vertical slot waveguides. At the analyte-metal interface, an SPP wave is excited whose field decays exponentially away from the interface and peaks at the boundary. Even when the slot area is minute, the two slots in the proposed HPW yield a very high power-confinement factor in the low-index region [128]. Consequently, the effective area can be made exceedingly small, which is beneficial for nonlinear optics, modulation and sensing.

As shown in Figure 3.12, we first examine the influence of the *w*. With decreasing *w*, the fraction of optical power in the analyte slot increases, while the fraction confined within silicon decreases. When *w* falls below about 200 nm, the confinement factor *Γ* in the analyte-filled slot can reach approximately 64%. This intense localisation is attractive for compact and sensitive sensing. The stronger hybrid SPP field, however, also increases absorption in the metal, and the propagation loss rises rapidly as *w* decreases. Hence, SBW-DSHPW designs must balance confinement against loss. Notably, even for *w* around 200 nm, the hybrid guided mode remains supported, demonstrating nanoscale optical confinement and an extremely small effective area.

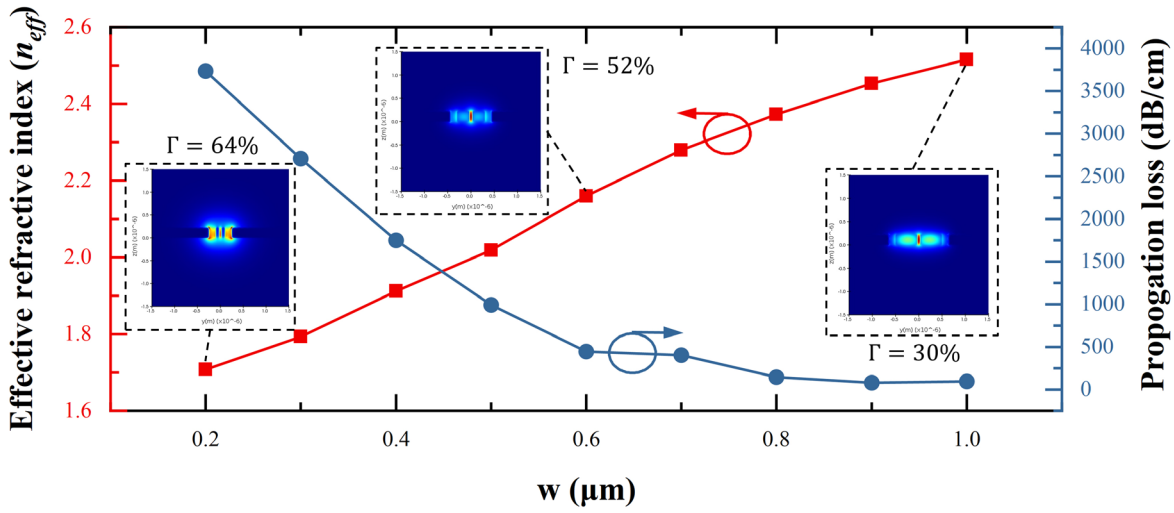

Fig. 3.12 Effective index, propagation loss and mode profiles of the SBW-DSHPW for varied silicon ridge width *w*.

Narrower silicon-analyte-metal gaps (*d*) reduce the effective area and increase power density, although *Γ* may change only modestly (Figure 3.13). For exceedingly small gaps, the SPP field squeezes a portion of the energy into the silicon core near the diffraction limit. As *d* increases, the plasmonic mode broadens, and the power density decreases, whereas the silicon slot mode remains largely unchanged and governed by the silicon geometry,

indicating weak dependence on the metal. Reducing *d* further can shrink the effective area, which is advantageous for enhanced nonlinear interaction or compact modulation.

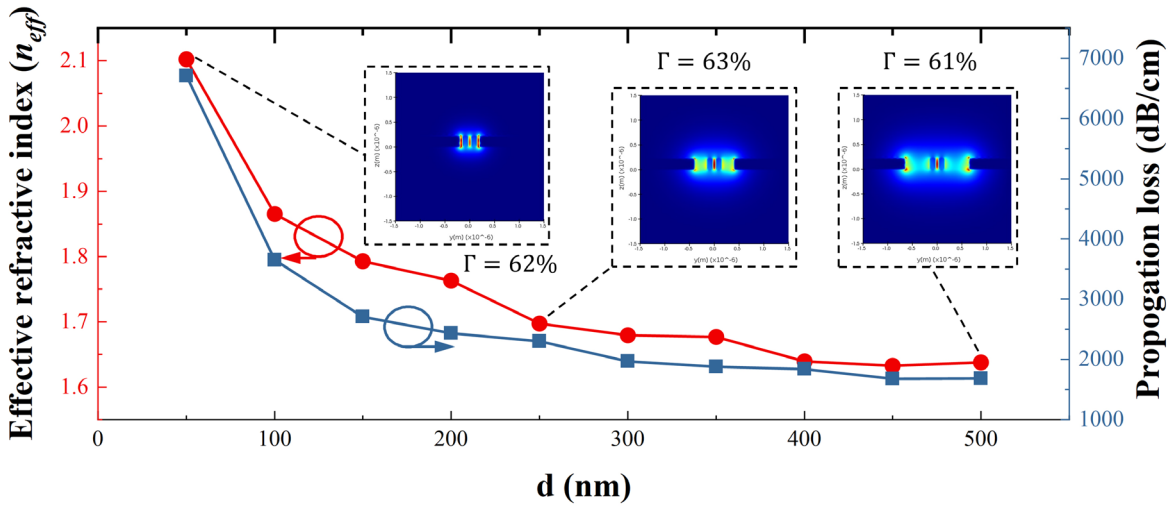

Fig. 3.13 Effective index, propagation loss and mode profiles of the SBW-DSHPW for varied silicon-metal gap *d*.

Next, we assess the effect of the silicon-slot width *g* while keeping the silicon-metal gap and the silicon-ridge width fixed in Figure 3.14. The propagation loss initially increases and then tends to level off as *g* grows. Once the slot becomes sufficiently wide, the interfaces approximate an metal-dielectric-metal (MDM) configuration, and the loss tends to that of a plasmonic slot waveguide (PSW). The confinement factor decreases gradually with g because a wider silicon slot weakens optical confinement and allows some power to leak into the BOX. Similar to the variation of *d*, the hybrid silicon-metal plasmonic mode remains comparatively stable, while the mode in the silicon slot broadens and its power density falls. The weak coupling between these modes allows independent tuning to balance sensitivity and loss.

Overall, maintaining a high *Γ*, the gap *d* plays a leading role in determining propagation length. Thinner *d* shortens the propagation length. A general trade-off exists between plasmonic waveguide dimensions and propagation distance. For the single-mode SOI nanowire with *w* equal to 300 nm, a propagation length exceeding 10^4 μm is readily achieved. Here, we emphasise the potential of the proposed HPW for relatively long propagation of 10^2 μm together with nanoscale optical confinement near 100 nm, substantially surpassing many reported HPWs. To avoid excessive metal absorption, we favour relatively thick *d*. Narrow *w* raises the aspect ratio and complicates etching in slot structures. For manufacturability, we adopt g = 50 nm, h = 210 nm, w = 300 nm and symmetric silicon-metal gaps of 150 nm as a balanced design.

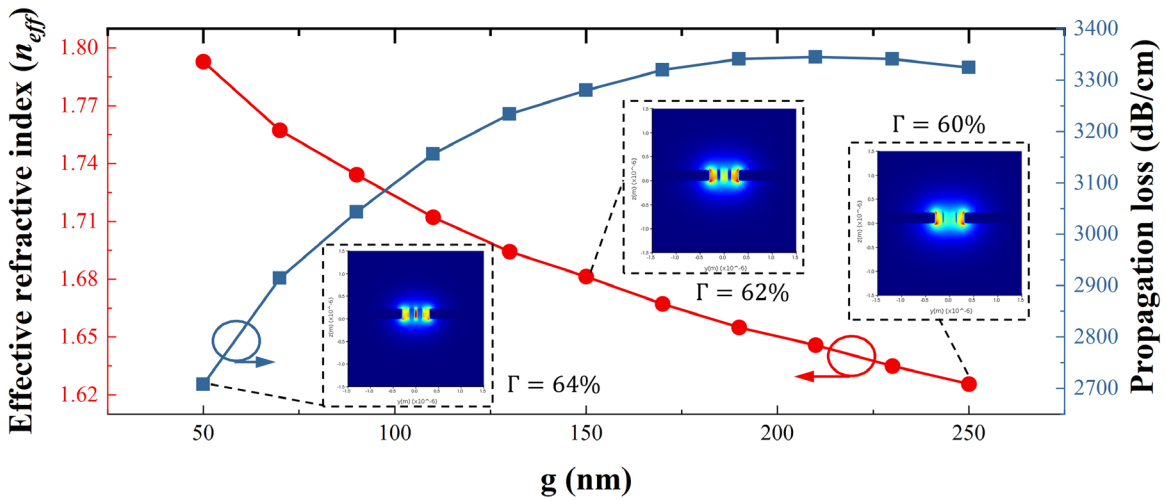

Fig. 3.14 Effective index, propagation loss and mode profiles of the SBW-DSHPW for varied silicon-slot width *g*.

3.2.2 Silicon on insulator ridge waveguide

Using Si or Si_3N_4 as the core material, planar devices such as couplers, switches, filters, modulators and attenuators can be fabricated on SOI or SiNOI wafers by lithography, etching and ion implantation [175,176]. The silicon waveguide is the basic building block for these devices and strongly influences performance. Here, we outline the SOI ridge waveguides used in this thesis.

A typical SOI waveguide geometry is shown schematically in Figure 3.15. The core is the top crystalline-silicon layer on a commercial SOI wafer with a thickness typically 220 nm. At 1550 nm, the refractive index of silicon is about 3.476. The BOX undercladding thickness is 2 μm with a refractive index of about 1.444 at 1550 nm. The upper cladding is usually deposited with SiO_2 using plasma-enhanced chemical vapour deposition (PECVD).

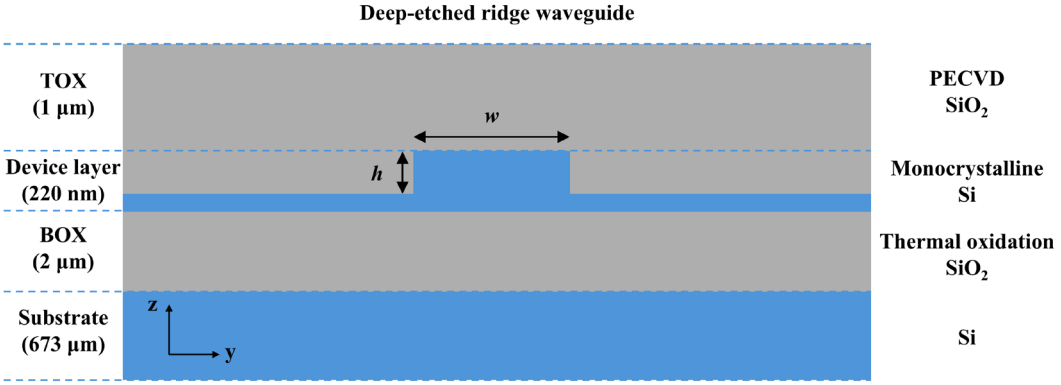

Fig. 3.15 Schematic of a deeply etched ridge waveguide on a commercial 220 nm SOI platform.

The single-mode SOI waveguides used here are deeply etched ridge waveguides. A finite-difference eigenmode (FDE) solver is employed to compute the TE fundamental mode and the n_{eff} at 1550 nm. Deeply etched ridge waveguides confine light strongly and exhibit a relatively large group index. Partial etching at the waveguide sides allows subsequent implementation of carrier-injection devices.

For commercial SOI wafers, single-mode ridge waveguides transmit in a w window between about 305 and 677 nm [177,178]. Within this range, low-loss single-mode operation can be achieved. To understand the transmission mechanism, we simulate deeply etched single-mode ridge waveguides with the FDE solver in Figure 3.16. The single-mode region for quasi-TE operation at 1550 nm corresponds to h = 220 nm and w below about 560 nm. In this regime, the waveguide supports one quasi-TE and one quasi- transverse-magnetic (TM) mode. As the w increases further, a second quasi-TE mode appears and above about 760 nm, a second quasi-TM mode appears.

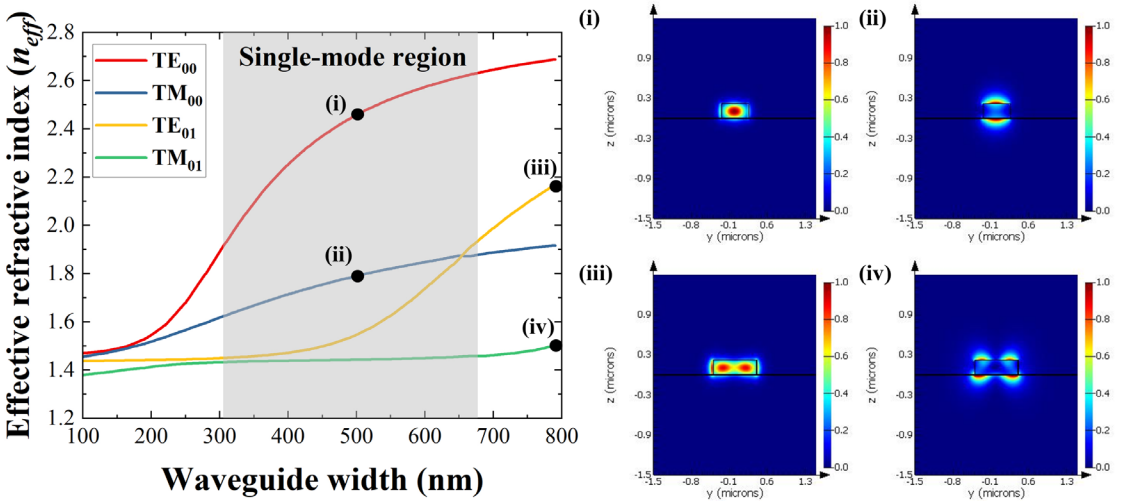

Fig. 3.16 Supported modes and field profiles of deeply etched SOI ridge waveguides versus width *w*.

Waveguide propagation loss is a key performance parameter. On-chip losses mainly originate from scattering within the waveguide caused by crystal defects and fabrication-induced sidewall roughness, as well as from bending loss. With advances in fabrication, scattering loss continues to fall. Bending loss stems from radiation of a portion of the mode outside the core in curved sections and from modal mismatch between straight and bent segments. As the bend radius increases, the bent-waveguide mode approaches that of the straight waveguide and mismatch loss decreases.

Using a FDTD solver, we compute the loss simulation of 180º arc bends for a typical deeply etched SOI ridge waveguide with w = 500 nm and h = 210 nm at 1550 nm, excluding scattering loss. It can be seen from Figure 3.17, when the bend radius (R) exceeds 10 µm, the 180º bend loss is below 0.02 dB/cm, so insertion loss can be neglected. Specially designed bends, such as Euler bends, allow adiabatic transition between straight and bent eigenmodes, enabling ultra-low-loss bends and very high-Q filters [179].

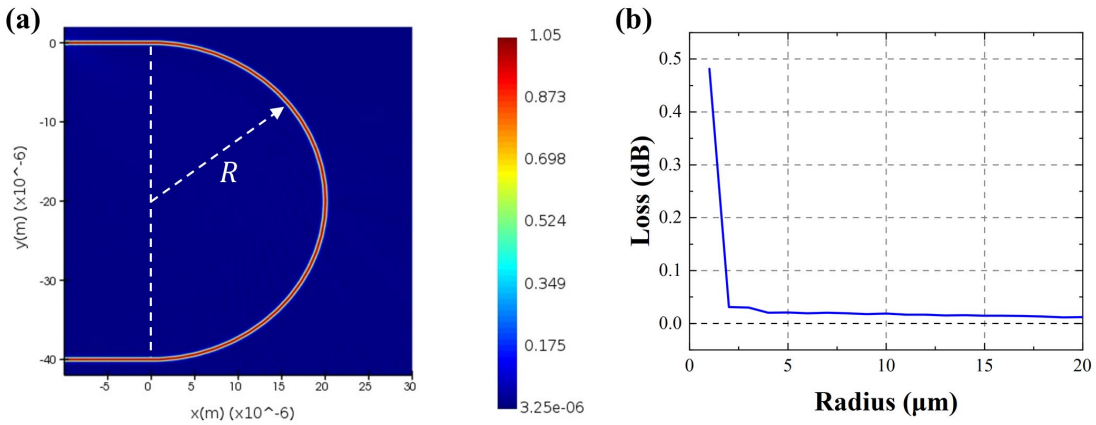

Fig. 3.17 (a) Electric-field profile of a 180º bend with radius 20 µm at 1550 nm for a 500 nm ridge width and (b) propagation loss versus bend radius.

3.2.3 Silicon nitride on insulator ridge waveguide

Relative to the SOI platform, SiNOI offers distinct advantages. Owing to its lower refractive index and broader transparency window, SiNOI exhibits lower transmission loss from the near-infrared to the mid-infrared and a higher nonlinear threshold, which suits broadband communications and nonlinear photonics. Weaker photon-lattice scattering in SiNOI also favours high-power and highly stable integrated circuits. We use an FDE solver to analyse SiNOI waveguides of different widths (w) to guide device design.

A representative geometry on the adopted SiNOI platform is shown schematically in Figure 3.18. The wafer employs an insulator-on-silicon stack with a 5 µm BOX undercladding. The core is a 340 nm Si_3N_4 film deposited by PECVD. The refractive index of PECVD Si_3N_4 at 1550 nm is approximately 1.996.

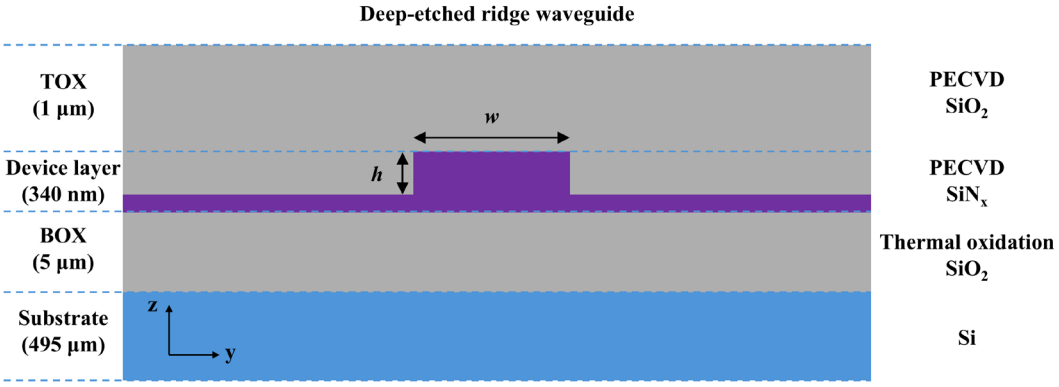

Fig. 3.18 Schematic of a deeply etched ridge waveguide on a 340 nm device-layer SiNOI platform.

Single-mode ridge waveguides of w = 800 nm and etch depth (h) 300 nm are widely used in SiN photonics. In Figure 3.19, simulations for an 800 nm wide single-mode waveguide show tight confinement of the fundamental mode. However, the field lies close to the sidewalls, so sidewall roughness during etching can induce scattering and additional loss.

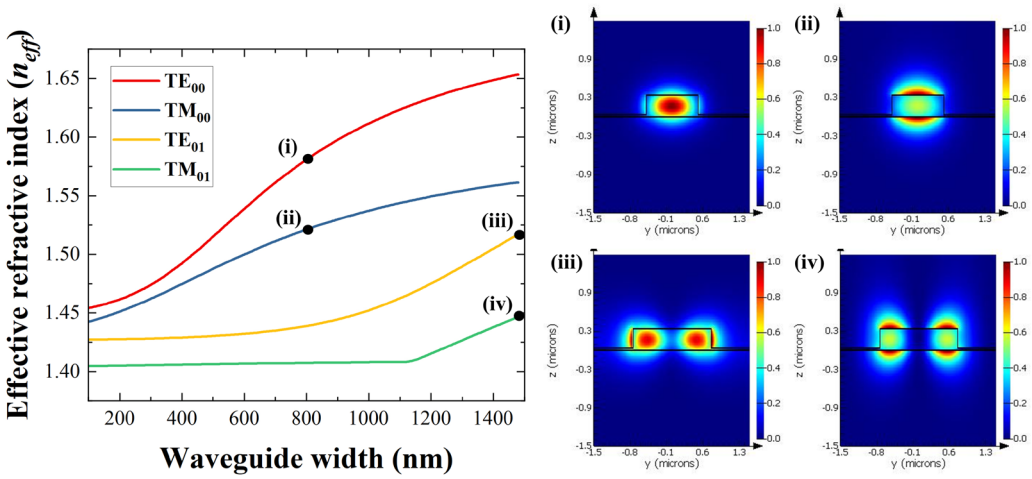

Fig. 3.19 Supported modes and field profiles of deeply etched SiNOI ridge waveguides versus width *w*.

Increasing the w is an effective means to reduce loss. As shown in Figure 3.20, we therefore compare a w = 1.2 µm multimode waveguide with an 800 nm single-mode waveguide. In the wider waveguide, the optical field concentrates in the central region and remains far from the sidewalls, with negligible overlap with the rough sidewalls. Wide waveguides can therefore mitigate sidewall scattering, which is valuable for grating waveguides to reduce propagation loss and to raise the passband Q factor [179,180]. A potential trade-off is the emergence of higher-order modes in wide waveguides.

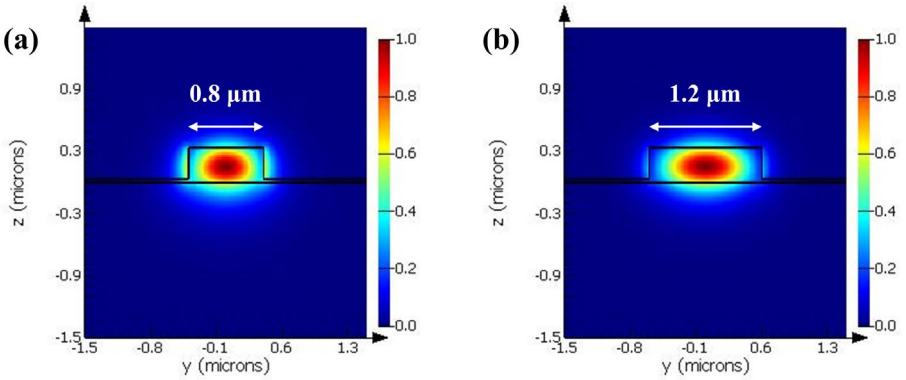

Fig. 3.20 TE mode optical field distribution at SiNOI ridge waveguide widths of (a) 0.8 µm and (b) 1.2 µm.

3.3 Chapter summary

This chapter has presented the theoretical foundations relevant to the thesis, encompassing Bragg-grating filtering mechanisms and associated modelling, and the structural design and simulation of SBW-DSHPW, SOI and SiNOI waveguides.

The analysis began with Bragg gratings; we derived the reflection characteristics of sidewall Bragg structures from the Bragg condition using coupled-mode theory, and we employed the TMM to model uniform and non-uniform gratings with high fidelity. Building on this, we discussed C-SBG and 4PS-SBG, explained their frequency-domain features and coupling enhancement, and introduced equivalent chirp and EPS to relax fabrication tolerances while enabling reconfigurable integrated PFs.

For on-chip waveguides, we described deeply etched ridge structures on SOI and SiNOI platforms and modelled their single-mode or multimode behaviour and bending loss using FDE and FDTD, thereby providing the groundwork for subsequent filter design. A low-loss SBW-DSHPW was proposed that combines subwavelength confinement with relatively long propagation and demonstrates potential for on-chip integration and biochemical sensing.

4 Fabrication and characterisation workflows

This chapter consolidates the experimental infrastructure underpinning the thesis, covering fabrication, integration, and characterisation in a form that supports reproducibility and cross-chapter traceability. The emphasis is placed on the practical implementation of silicon photonic and silicon nitride PICs on SOI and SiNOI, where device performance is determined not only by design intent but also by process fidelity, integration yield, and measurement repeatability.

4.1 Key fabrication facilities

4.1.1 Lithography module

The *Raith* EBPG 5200 is a high-energy EBL system that patterns nanoscale features by scanning a focused electron beam over an electron-sensitive resist, followed by post-exposure development. Pattern definition is achieved through beam blanking and electrostatic deflection within a main writing field, while stage motion enables stitching across larger areas. High accelerating voltages up to 100 kV are commonly used to reduce forward scattering and mitigate proximity effects relative to lower-energy EBL, supporting dense and high-resolution patterning.

In typical EBPG 5200 configurations, selectable accelerating voltages of 20, 50, and 100 kV are available, with beam currents spanning the pA to hundreds of nA range depending on aperture and spot-size requirements. Main-field sizes up to approximately 1 mm by 1 mm and high-resolution digital deflection are reported, enabling both high-throughput exposure of larger photonic structures and high-resolution exposure of critical nanoscale features.

Alignment is realised using reference markers and beam-based metrology, enabling overlay and stitching accuracies in the order of 10 nm in well-controlled processes. In the present thesis workflow, the EBPG 5200 is used to define high-fidelity MRR, MZI, grating and heater-pattern layouts where linewidth control, placement accuracy, and repeatability directly impact coupling strength, phase control, and the tolerance budget of PF responses.

4.1.2 Pattern etching

The *SPTS* Omega LPX 200 Rapier RP is an inductively coupled plasma (ICP) etch platform widely used for anisotropic silicon etching and deep reactive ion etching. In ICP operation,

a radio-frequency source, commonly at 13.56 MHz, drives a high-density plasma at low pressure, providing a high flux of reactive radicals. A separate RF bias applied to the substrate electrode controls ion energy and directionality, enabling vertical profiles through ion-assisted passivation removal at the feature bottom while retaining sidewall protection.

For deep silicon pattern transfer, the system is frequently operated using fast-switching Bosch cycling, alternating between an SF_6-based etch step and a C_4F_8-based passivation step. This temporal modulation decouples etch rate from sidewall protection, supporting high aspect ratio trenches and through-silicon features with strong selectivity to common masks such as photoresist and silicon dioxide.

Facility descriptions indicate compatibility with wafer-scale processing up to 200 mm, as well as smaller dies mounted on carriers, which is advantageous for research fabrication where multiple device variants are iterated across a wafer.

Within this thesis, the Rapier RP is used as the primary pattern-transfer module to realise low-roughness waveguide sidewalls and high-fidelity grating corrugations, where control of anisotropy, microloading, and mask selectivity is critical to achieving reproducible loss and spectral responses.

4.1.3 Deposition

The *Oxford Instruments* PlasmaPro 100 PECVD system deposits thin films by plasma-enhanced chemical vapour deposition, in which precursor gases are dissociated in a low-pressure plasma to generate reactive species that condense and react at the substrate surface. Compared with purely thermal chemical vapour deposition, PECVD enables deposition at reduced substrate temperatures while maintaining practical growth rates and film conformality, which is important for photonic platforms requiring controlled cladding thickness, refractive index, and stress.

The PlasmaPro 100 PECVD architecture is commonly described as using a showerhead electrode design and controlled electrode temperatures to improve uniformity and reduce particle generation. Dual-frequency power delivery is supported, with 13.56 MHz and a lower-frequency component around 100 kHz applied to the upper electrode, enabling tuning of ion energy, film densification, and intrinsic stress.

The platform is positioned for deposition of dielectric and silicon-based films relevant to integrated photonics, including SiO_2 and SiN_x, as well as amorphous silicon and silicon carbide, depending on gas chemistry. Published descriptions emphasise control of refractive index, stress, and wet etch rate, which are directly linked to optical confinement, thermo-optic behaviour, and long-term stability.

In this thesis workflow, PECVD is used to realise optical claddings and passivation layers, and to support heater integration through electrically insulating and mechanically stable overcladdings. Process control is treated as part of the optical tolerance budget because film thickness and stress influence propagation loss, birefringence, and thermal tuning efficiency.

4.1.4 Metallisation

The *Plassys* MEB550S evaporator is an electron beam physical vapour deposition tool in which a high-energy electron beam is focused onto a source material in a crucible, locally heating and evaporating the target under high vacuum. The evaporated species travel in a line-of-sight flux and condense on the substrate, enabling deposition of metals and selected dielectrics with controllable rates and thickness.

Facility documentation for MEB 550-class systems highlights automated control, load-lock operation to reduce cycle time, and capability for substrates up to approximately 6 inches, with substrate rotation and adjustable source angle to improve thickness uniformity. In situ thickness monitoring is commonly implemented using a quartz crystal microbalance, supporting closed-loop control of deposited thickness for thin-film heaters and contact pads.

Plassys electron beam evaporation configurations in the fabrication centre report electron guns around 10 kV, high-vacuum base pressures in the 10^{-8} mbar class for the main chamber, and multi-pocket sources enabling sequential deposition without breaking vacuum. Many systems include an ion gun for in situ pre-clean or surface activation to improve adhesion and reduce interfacial contamination.

In this thesis, the MEB550S is used to deposit MH and contact metallisation stacks where sheet resistance, adhesion, and thermal stability determine tuning efficiency, long-term drift, and electrical reliability. The evaporator is therefore treated as a critical enabler of repeatable thermo-optic actuation and heater-matrix programmability.

4.2 Fabrication process

4.2.1 Fabrication process for sensors

First, the fabrication process for the SOI-based on-chip biosensor described in Chapter 5 is presented. The MRR and MZI devices share the same process flow and starting wafer. Commercial 220 nm SOI wafers were procured from *University Wafer Inc.*, a standard platform in silicon photonics. From top to bottom, the stack comprises a 220 nm crystalline-silicon device layer, an approximately 2 μm BOX layer and a high-resistivity silicon substrate. Fabrication relied on the high-precision micro and nanofabrication capabilities at the James Watt Nanofabrication Centre (JWNC) to integrate silicon-photonic structures with plasmonic metal features.

Before processing, the 6-inch wafers were diced along crystal orientation into 11 mm by 12 mm dies for experimental use. Surface preparation is critical to high-fidelity pattern transfer and device stability. The die was cleaned by sequential immersion in acetone and isopropyl alcohol (IPA), assisted by ultrasonication to accelerate particle removal through cavitation, followed by N_2 drying. This removed organic residues, particulates, metallic ions and dicing debris, ensuring excellent resist adhesion and etch uniformity for the subsequent steps.

Hydrogen silsesquioxane (HSQ) was spin-coated as the electron-beam resist at 4000 RPM for 60 seconds, yielding an approximately 400 nm film. A soft bake at 90 ºC removed residual solvent and improved adhesion. EBL with proximity-effect correction, beam-step-size control and dose optimisation was performed on a *Raith* EBPG 5200 direct-write system to define the nanoscale patterns with high-dimensional fidelity. HSQ, a negative resist, crosslinks under electron exposure so that exposed regions remain during development. Development employed 25% tetramethylammonium hydroxide at room temperature for 30 seconds, then an IPA rinse for 60 seconds to terminate the reaction and a further IPA rinse for 30 seconds. If inspection revealed incomplete development, the tetramethylammonium hydroxide step was extended by 5 to 10 seconds and the rinses repeated to ensure complete pattern formation.

Pattern transfer into the silicon device layer was carried out by ICP etching using an *SPTS* Rapier tool, employing C_4F_8/SF_6 flow rates of 90/30 sccm, a chamber pressure of 20 mTorr, and a platen power of 28 W to tailor ion energy and sidewall profile. An in situ interferometric monitor tracked the etch depth in real time. An optimised etch of approximately 51 seconds completed the 220 nm silicon pattern transfer, yielding near-

vertical sidewalls with a measured angle of around 89º. According to the process experience, the stop point is point B in Figure 4.1.

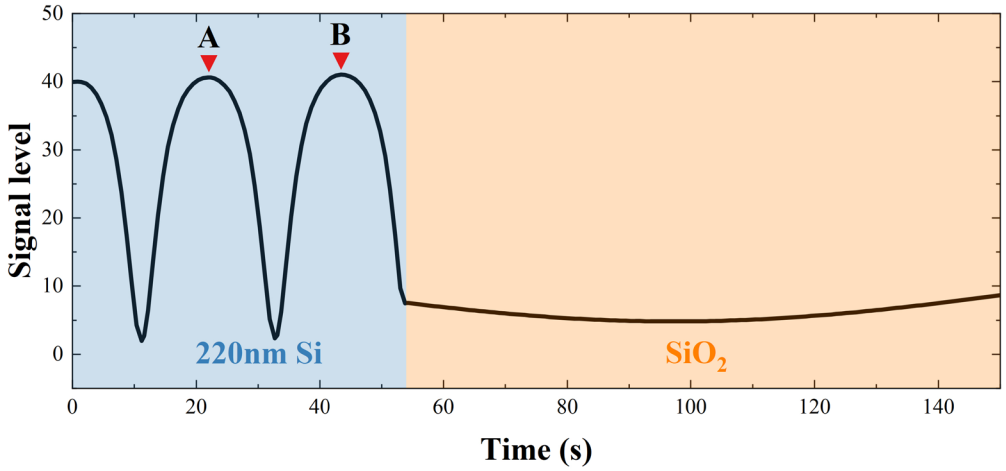

Fig. 4.1 Interface of the interferometric endpoint monitor used during deep etching of SOI ridge waveguides.

Because of the finite selectivity between HSQ and crystalline silicon, the HSQ mask is partially consumed during etching at roughly 1/3 of the silicon etch rate. To prevent contamination and interfacial issues in subsequent processes, residual crosslinked HSQ was removed by wet etching in a 6:1 diluted hydrofluoric acid (HF) solution for 60 seconds, followed by a 60-second rinse in RO water to remove HF residues.

Surface GCs were then patterned using a positive polymethyl methacrylate (PMMA) process suited to shallow, small-area features. A 12 %, 200K-molecular-weight *Allresist* PMMA was spin-coated at 4000 RPM for 60 seconds to form an approximately 780 nm film, soft baked at 155 ºC for 5 minutes and exposed by EBL. Development used a 2.5:1 solution of methyl isobutyl ketone in IPA for 30 seconds, followed by a 30-second IPA rinse. A brief oxygen-plasma descum in an Asher at 200 W for 2 minutes removed residual resist in the grating trenches with negligible impact on profile, and the gratings were shallow-etched on the SPTS Rapier, where the etching stop point is shown at point A in Figure 4.1. Unwanted PMMA was stripped in acetone to restore a clean surface.

For the plasmonic metal sidewalls, a bilayer PMMA stack with different molecular weights was employed to form an undercut suitable for robust lift-off, with a total thickness of about 850 nm. After EBL and development as above, electron-beam evaporation deposited 3 nm titanium (Ti) as an adhesion layer, followed by 210 nm Ag to form the plasmonic metal.

Lift-off was completed in an acetone bath held in 55 ºC water to accelerate dissolution, producing sharply defined metal patterns.

To improve fibre coupling and overall optical performance, an approximately 700 nm PMMA overcladding was spin-coated across the wafer to assist refractive-index matching at the grating-fibre interface and reduce reflection and scattering loss. Finally, EBL opened windows in the PMMA above the sensing regions to create surface microfluidic channels, enabling precise delivery of liquid analytes and facilitating integration with microfluidic systems.

Representative SEM images after fabrication are shown in Figure 4.2, including MRR and MZI biosensors that employ the SBW-DSHPW waveguide, magnified views of the hybrid waveguide and the surface GCs on the SOI platform.

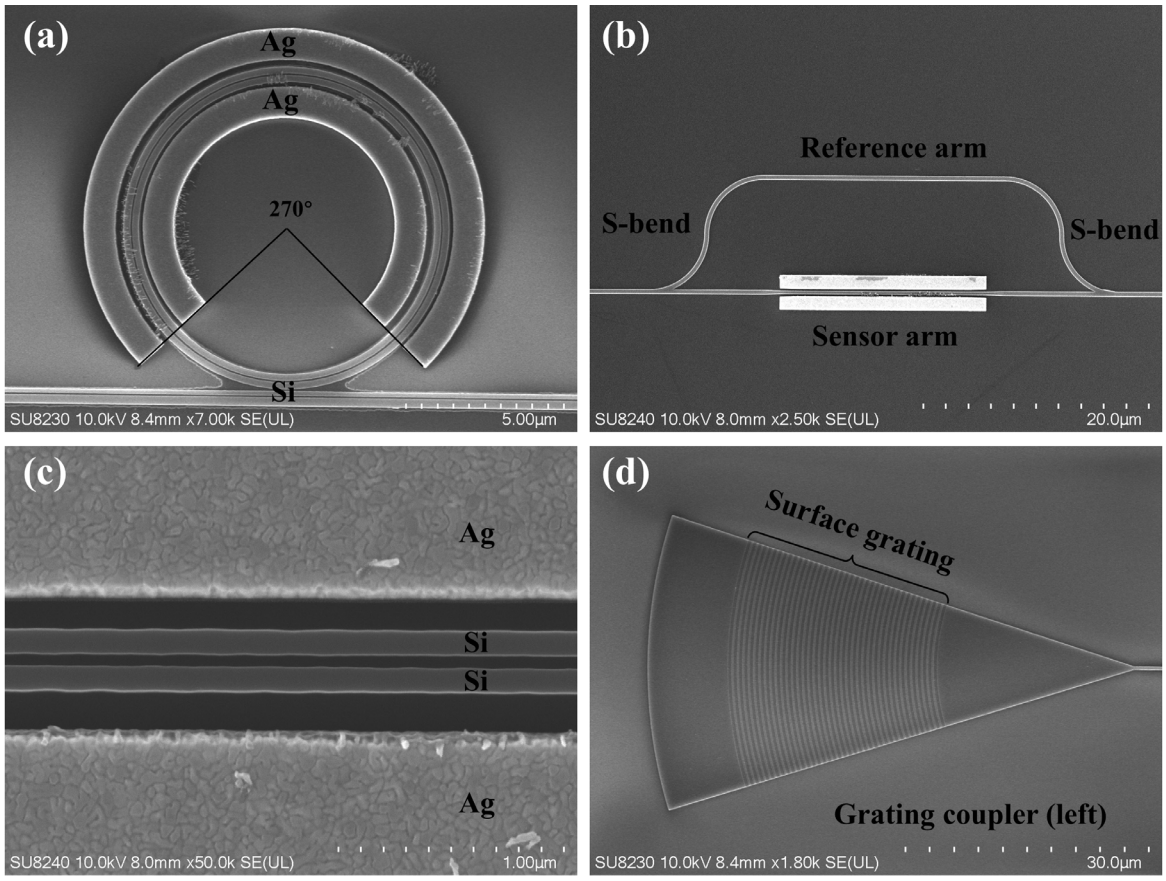

Fig. 4.2 SEM images of (a) MRR and (b) MZI biosensors incorporating the (c) SBW-DSHPW waveguide and (d) GCs on SOI.

4.2.2 Fabrication process for filters

For on-chip filters, the primary material platforms are SOI and SiNOI. We shall first outline the fabrication process for the SOI-based dual-band PF described in Chapter 6. The fabrication flow largely follows that of the biochemical sensors in the preceding chapter, including silicon-waveguide definition (Figures 4.3(a) to (b)), GC formation, HSQ and PMMA pattern transfer, dry etching and cleaning. The principal difference is that, after completing the GCs, the present device does not require electron-beam evaporation of metals to form plasmonic structures. Instead, a passivation process is performed directly to cover the device surface (Figure 4.3(c)).

Passivation proceeds as follows. The chip is first placed in a PECVD system (PlasmaPro 100). With the chamber held at 300 ºC, gases are introduced in the ratio argon (Ar) to silane (SiH_4) to nitrous oxide (N_2O) equal to 161 to 8.5 to 710 sccm, depositing an approximately 600 nm SiO_2 film on the surface. PECVD is performed before spin coating because the device contains high-aspect-ratio sidewall gratings. If HSQ were spin-coated directly, air could be trapped in the grating trenches, leading to non-uniform coverage and degraded passivation and spectral response. PECVD, by contrast, employs plasma-enhanced reactions to conformally coat the device surface and trench interiors, achieving the first dense passivation layer. To further improve passivation quality and uniformity, HSQ is spin-coated at 4000 RPM to a thickness of about 400 nm, then the sample is annealed for 24 hours at 180 ºC in N_2 so that HSQ fully crosslinks and converts to an equivalent SiO_2 layer. This ensures that HSQ in the high-aspect-ratio grating regions is completely converted, yielding a uniform, dense and optically stable passivation cover. After these two steps, a Dektak contact profilometer is used to characterise the surface. The sharp step of approximately 220 nm from the deep-etched ridge waveguide is effectively passivated and levelled to a gradual slope with a height difference of about 50 nm, which evidences excellent planarization from the combined PECVD and HSQ passivation.

After passivation, the process proceeds to metallisation of the MHs, which follows the plasmonic-waveguide metallisation described in the previous chapter. Electron-beam evaporation deposits a multilayer stack comprising 20 nm Ti as an adhesion layer, 160 nm platinum (Pt) as the principal high-resistivity heating material and a 50 nm Au capping layer to prevent oxidation of Pt during high-temperature operation. Surface planarization is crucial for MHs integrated on the surface, since it removes large step heights from the deep-etched waveguides and thus prevents cracking, stress concentration or thickness non-uniformity at

step edges. Smoothing the waveguide region into a gentle slope improves metal adhesion and uniformity, and significantly enhances heater thermoelectric performance and fabrication yield, thereby enabling precise and repeatable thermal tuning. A representative fabricated MH is shown in Figure 4.3(d).

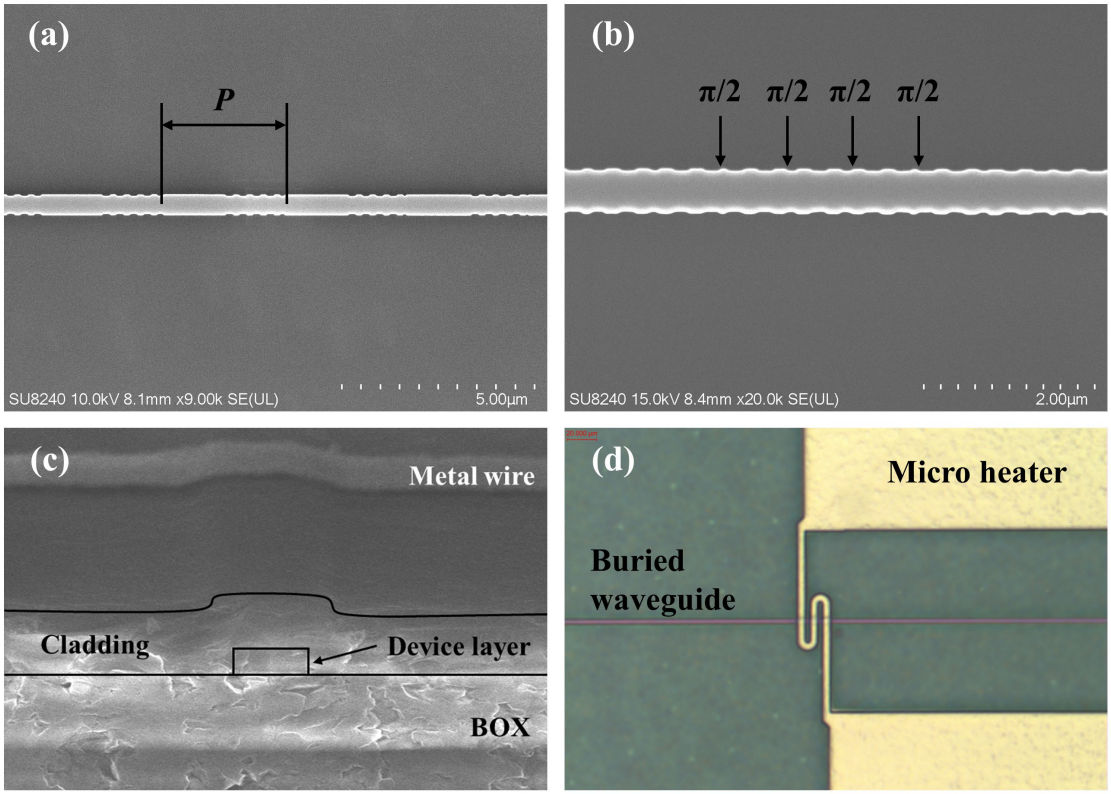

Fig. 4.3 SEM images of etched (a) C-SBG and (b) 4PS-SBG waveguide, (c) device cross-sections and (d) microscope images of MH wiring.

For the SiNOI platform, specifically the devices discussed in Chapters 7 and 8, the detailed fabrication process is as follows.

Devices were fabricated on insulator-on-silicon wafers procured from *University Wafer Inc.*. A thermally grown dry oxide approximately 5 μm thick serves as the buried insulator, providing excellent isolation and suppressing leakage of the optical field into the silicon substrate. The device-layer Si_3N_4 thin film was deposited in an Oxford Instruments System 100 ICP 380 PECVD system at 300 ºC with precursor flows of 30 sccm SiH_4 and 24 sccm N_2. The relatively slow growth (7 nm/min) yields a dense, uniform film with favourable internal stress and interface adhesion, supporting subsequent nanopatterning with high structural stability and optical performance. The Si_3N_4 layer not only serves as the core layer material of the optical waveguide, but also provides a process window for the subsequent patterning and etching processes. Wet-etch characterisation using 10:1 buffered HF

measured an etch rate of approximately 4 nm/s, consistent with a dense and chemically robust film.

Film thickness and optical constants were measured by ellipsometry at a 632 nm laser. The operating principle of ellipsometry is that when polarised light reflects from or transmits through interfaces between different media, its state of polarisation changes depending on material parameters such as thickness, refractive index, and extinction coefficient. Specifically, linearly polarised incident light reflected from the sample surface is converted into elliptically polarised light, with analysis conducted through the amplitude ratio and phase difference of the reflected light. By fitting the amplitude ratio and phase difference of reflected polarised light to a multilayer optical model, the extracted film thickness is about 340 nm, close to the design value, and the refractive index is 2.02 at 632 nm wavelength, which matches typical Si_3N_4 properties.

The subsequent manufacturing process is basically the same as the process described in this section. To shorten the process and reduce mask count, a one-exposure GC etched synchronously with the grating waveguide was developed. This avoids additional lithography and etching and improves optical performance. Compared with conventional couplers on SOI used in Chapter 6, the single exposure step Si_3N_4 GC exhibits a wider coupling bandwidth, which enlarges the -3 dB coupling window and increases tolerance to wavelength and alignment.

Pattern transfer into Si_3N_4 was performed using an *SPTS* Rapier system. Because Si_3N_4 possesses a higher bond energy and a lower etch rate than Si, the gas mixture was adjusted to 89 sccm of C_4F_8 and 31 sccm of SF_6, while maintaining other parameters consistent with the silicon etching conditions. This recipe provides sufficient etch rate together with effective sidewall passivation, yielding a near vertical sidewall with measured angle around 89.3º, showing excellent anisotropy and almost no overcut effect. The interferometric trace for etching a 340 nm film is shown in Figure 4.4 and demonstrates process stability and the sharp transition between device (Si_3N_4) and isolation (SiO_2) layers. Etching of the ridge waveguide is normally stopped at point A to retain a remaining Si_3N_4 layer that protects the BOX from subsequent wet processing.

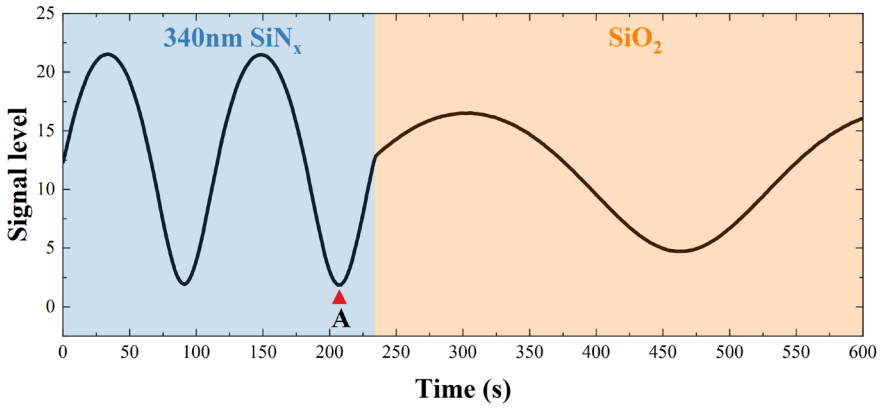

Fig. 4.4 Interferometric monitor trace during Si_3N_4 etching.

Passivation and MH metallisation follow the proven process of the previous sentences. Planarization and a dense SiO_2 passivation layer are formed by PECVD together with HSQ spin coating and annealing. Electron-beam evaporation is then used to deposit a NiCr, Pt and Au multilayer, followed by lift off to pattern the MHs.

Figure 4.5 presents a top-view optical micrograph of the fabricated PF, which measures 1600 µm by 300 µm, corresponding to an area of 0.48 mm^2. The bottom-left inset shows a magnified view of the heating wire of MH and its location relative to the embedded grating waveguide. The central inset provides a SEM image of the 4PS-SBG waveguide, and the bottom-right inset shows the deep-etched output GC formed in a single step with the waveguide. Each MH comprises a top DC injection pad, a common ground pad and a resistive track positioned directly above each PS region.

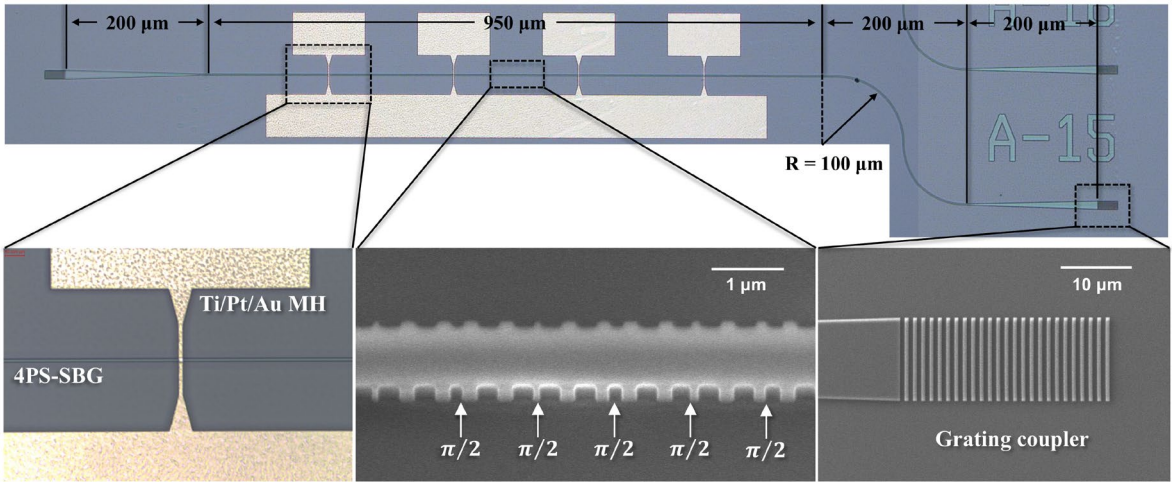

Fig. 4.5 Optical micrograph of the fabricated device with insets showing the heater track, the 4PS-SBG in SEM and the output GC in SEM.

The fabrication process of the PIC in Chapter 8 follows the procedure described in the previous section. Input and output are implemented by GCs at the two ends of the device, which ensures practical experimental testing. The overall structure is shown in Figure 4.6 and comprises the input and output GCs, the MRR, the SSG and the integrated MHs.

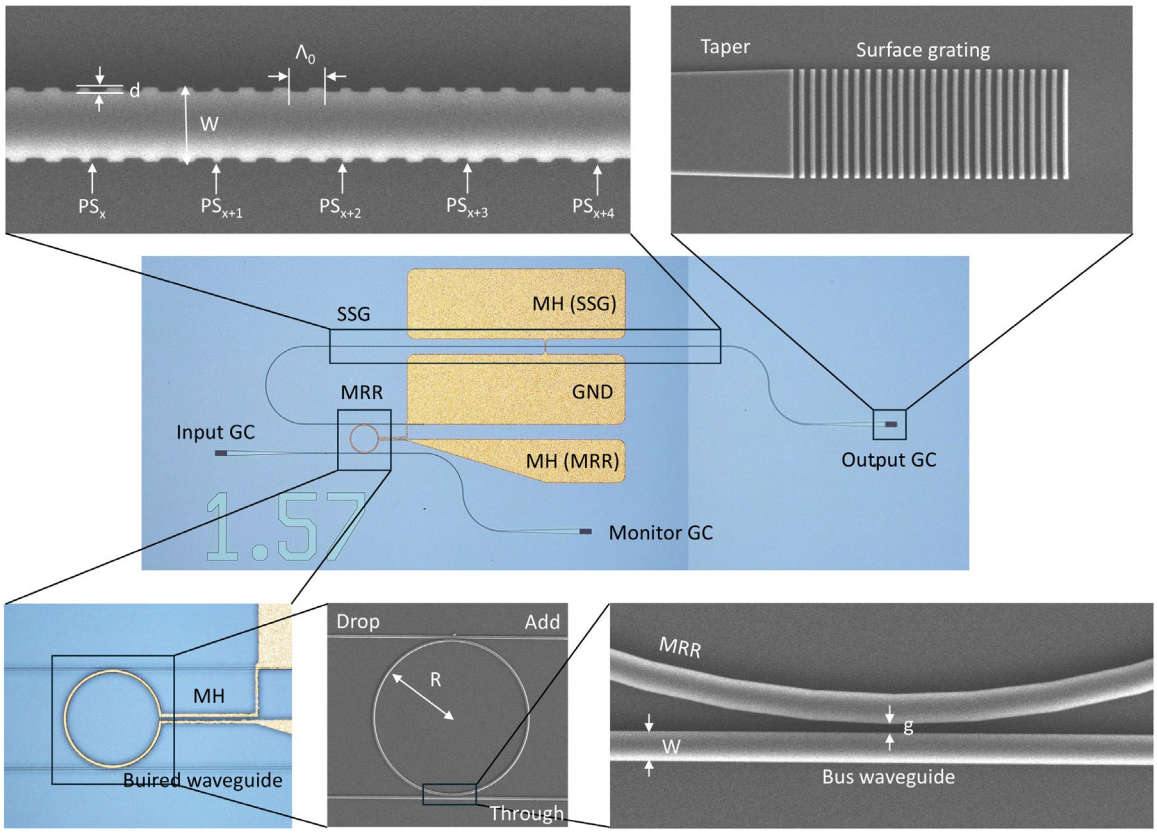

Fig. 4.6 Optical micrograph of the fabricated device together with magnified SEM micrographs of selected regions.

4.3 Characterisation setups

4.3.1 Sensing experimental setup

The characterisation setup at room temperature for the plasmonic sensors presented in Chapter 5 is shown in Figure 4.7. Following fabrication of the biochemical sensor, the chip is secured by vacuum onto a six-axis positioning stage. This measurement setup is designed to utilise a GC to achieve coupling between the on-chip waveguide and the single-mode fibre (SMF) core. The SMF, with a clean and smooth end face and stripped cladding, is mounted on a six-axis alignment stage, which enables precise positioning and is suitable for testing a wide range of passive and active photonic chips due to its versatile adjustment capabilities. The experimental setup includes an SLD with a centre wavelength of 1550 nm and a 3 dB bandwidth of 30 nm as the light source, with a maximum output power of 28 mW. SLD is a

broadband light source that combines the characteristics of a laser and a light-emitting diode (LED), and its working principle is based on the combined action of stimulated and spontaneous radiation. SLDs operate in mirrorless or low-feedback cavity structures, avoiding coherent multimode oscillations in lasers and utilising strong stimulated radiation amplification to achieve high power output while maintaining a wide spectrum and low coherence. Compared with ordinary LEDs, SLDs have higher optical output power and narrower divergence angles; SLDs do not have the narrow linewidth and high coherence of lasers compared to lasers, so they have distinct advantages in applications such as low coherence interference, optical coherence tomography, and fibre optic sensing. Key features include high brightness, wide spectrum, low temporal coherence, and low interference noise. Therefore, it is used as an input light source for sensor transmission spectra and subsequent filter window characterisation.

Connected to the SLD is a 10 μm core diameter SMF. The input and output SMFs are positioned vertically above the GC with an offset of 10.0º. These fibre end faces are vertically aligned with a pair of GCs to facilitate the transmission of input and output signals between the light source and the on-chip sensor. Since the fibre used in the experiment is not a polarization-maintaining fibre, and the polarization state is prone to fluctuations due to changes such as bending and stress, the output SMF is connected to the OSA via a polarization controller (PC) and precisely adjusts the polarization through a mechanical knob or electronic control, so that it is stably coupled into the polarization-sensitive photonic device, to obtain accurate measurement results and ensure that it is characterized only in TE mode. All optical transmission spectra in this thesis are acquired using OSA with a resolution bandwidth (RBW) setting of 0.06 nm. The automated measurement system connects to the instrument via a general-purpose interface bus (GPIB) and is controlled by LabVIEW software, increasing efficiency for fast, accurate data collection. This setup increases measurement throughput and quickly collects measurement data, preventing wavelength drift caused by rapid volatilisation of the analyte. To assess sensor sensitivity, glucose solutions with different mass fractions are placed directly on the surface of the sensor sensing window through a pipette. Once the liquid reaches the chip surface, it is confined by microfluidic channels made of PMMA several μm high and hundreds of μm wide. Microfluidic channels efficiently deliver molecules near the sensor through liquid surface tension, creating a layer of stationary liquid several μm thick to cover all sensors.

As a prospective improvement to the measurement platform, a thermo-electric cooler can be used to stabilise chip temperature. Silicon-photonic devices are highly temperature sensitive

through the TO effect, so tight temperature control suppresses resonance drift, fringe wandering and coupling fluctuations and improves repeatability.

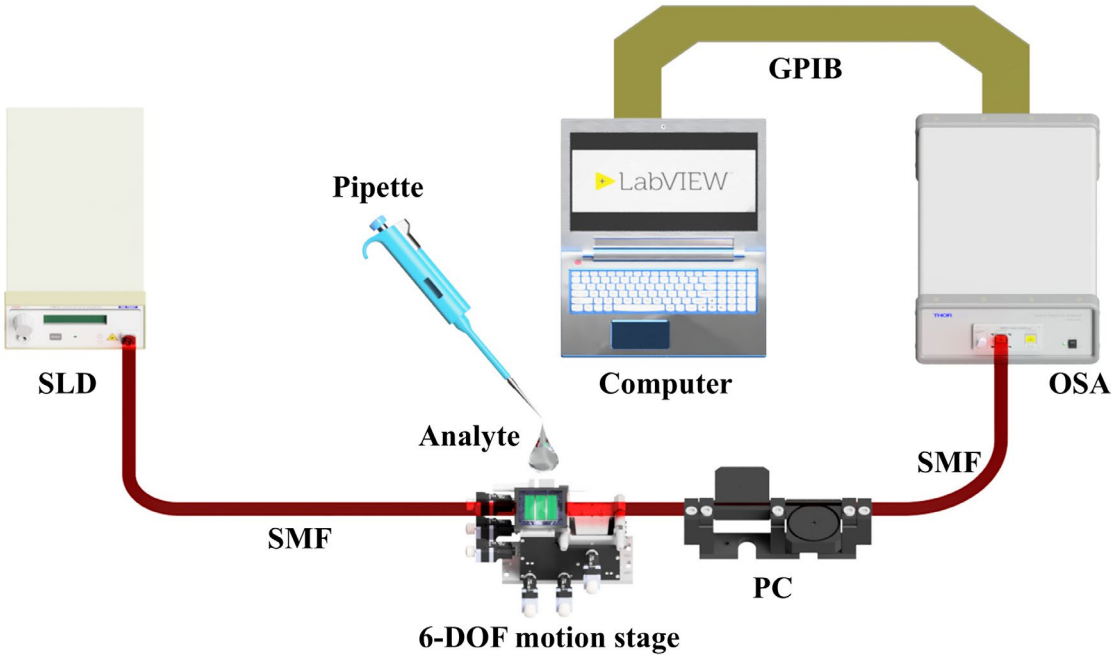

Fig. 4.7 Schematic of the characterisation setup for the on-chip biochemical sensors.

4.3.2 Filtering experimental setup

Figure 4.8(a) shows the room-temperature characterisation setup for the devices described in Chapter 6. The light sources comprise an SLD and an alternative OFC source. The fabricated PF chip is held by vacuum on a 6-axis stage. The setup is designed to couple between on-chip waveguides and single-mode fibres GCs. An SMF connects the SLD to an input GC, and a PC ensures excitation of the TE mode. At the output, an AR-coated lensed SMF couples light from the GC, which markedly reduces backward optical feedback caused by Fresnel reflection at the fibre end facet, thereby suppressing unwanted interference and standing waves between the waveguide and source. This improves coupling efficiency, signal-to-noise ratio (SNR) and measurement stability and repeatability. The input and output fibres are positioned directly above the GCs with a vertical offset angle of 15º, chosen to avoid the 2nd Bragg reflection returning to the fibre end facet, to reduce back-coupling and to better satisfy wave-vector matching. An OSA records the output spectra. The PC is placed before the OSA to guarantee TE-only characterisation. The output wavelengths are tuned by varying the injected current to the MH contact pads, denoted I_{MH}.

For continuous tuning of the filter windows, only the SLD is used as the source, allowing the passband shape and position to be monitored in real-time. For subsequent OFD tests, the C-SBG-based PF is driven by an OFC generated by an ultrafast optical clock referenced to a signal generator with 20 GHz spacing. The ultrafast optical clock outputs evenly spaced pulses whose Fourier transform forms an initial comb in the frequency domain. The signal generator provides a reference that locks the repetition rate or modulation frequency, stabilising comb-line spacing and phase and enabling high repetition rate, narrow linewidth and long-term stability. For the 4PS-SBG-based PF, a 100 GHz SMLL is used as the input source (Figure 4.8(b)). When the SMLL is used, an optical isolator (ISO) is inserted to protect it from reflections from the PF. To demonstrate filter characteristics and parameters, we apply different currents to the MH pads and measure the resulting resonance shifts in the transmission spectra, as summarised in Figure 4.8(c). An automated measurement system interfaces with the instruments over the GPIB and is controlled by LabVIEW, which enables high-throughput acquisition and consistent precision across repeated runs. Figure 4.8(d) shows a photograph of the measurement stage in our laboratory.

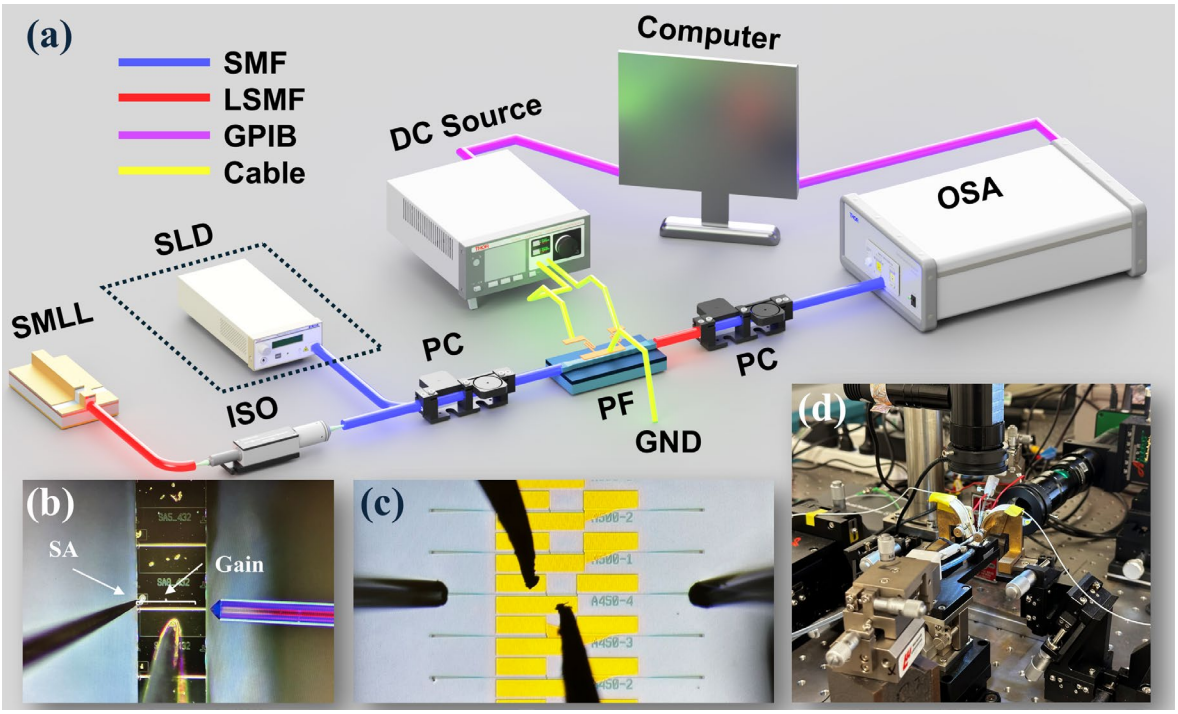

Fig. 4.8 (a) Schematic of the characterisation setup. (b) Coupling from SMLL via a lens fibre. (c) Microscope image of a PF monolithically integrated with GCs showing probe contacts to MHs and SMFs aligned to GCs. (d) Photograph of the measurement bench.

The device characterisation platform and system for Chapter 7 are similar to those in the previous sentences. Figure 4.9 shows the experimental arrangement used at room temperature. In the DWDM/OFD experiments, an OFC is generated by an SMLL built on

the AlGaInAs/InP materials system. The device adopts an asymmetric multiple-quantum well structure. The total cavity length of the SMLL is 890 μm, comprising a 15 μm saturable-absorber (SA) section and an 865 μm gain section, separated by a 10 μm isolation trench. The ridge waveguide width is 2.5 μm. Passive mode locking is achieved by forward biasing the gain section and applying a reverse voltage to the SA section. To assess the PF in OFD multiplexing, the gain-section injection current is set to 185 mA, and a reverse bias of 3 V is applied to the SA, so that the device operates in free-running mode locking with an average output power of 20 mW. As shown in Figure 4.10, during free-running, the centre wavelength is 1553 nm, and the FWHM is 6.3 nm. The OFC spacing of the SMLL is 50 GHz. The grey region in Figure 4.10 shows the reference signal used to generate the input waveguide in Chapter 7. The laser output is passed through an ISO and then coupled into the programmable PF.

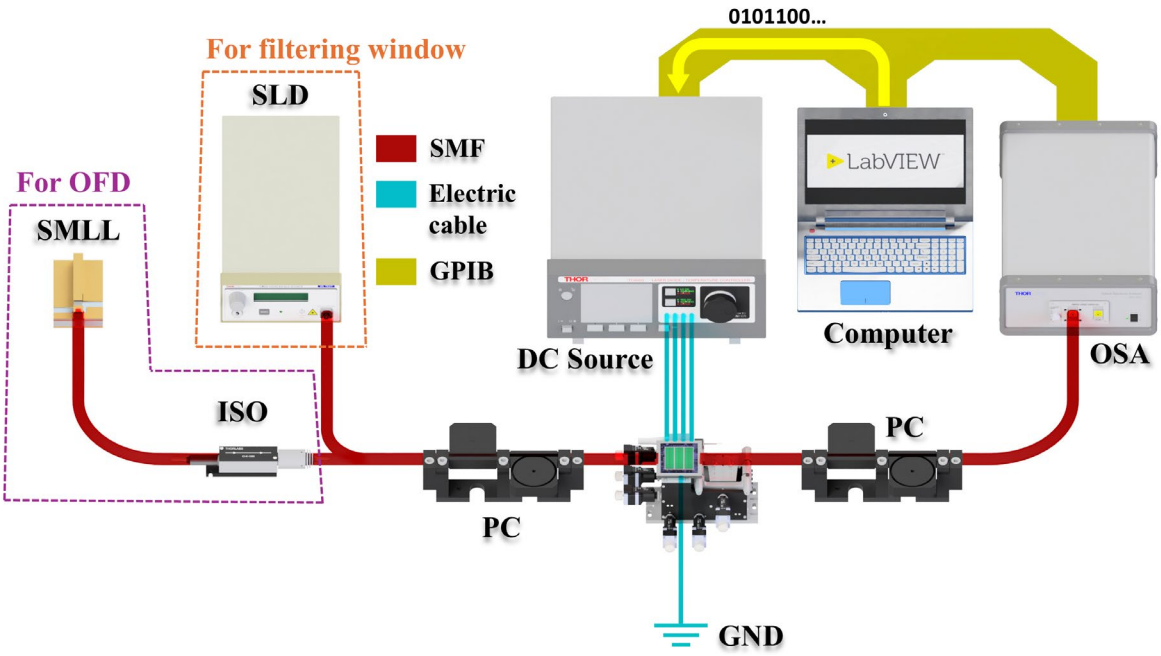

Fig.4.9 Schematic of the characterisation setup.

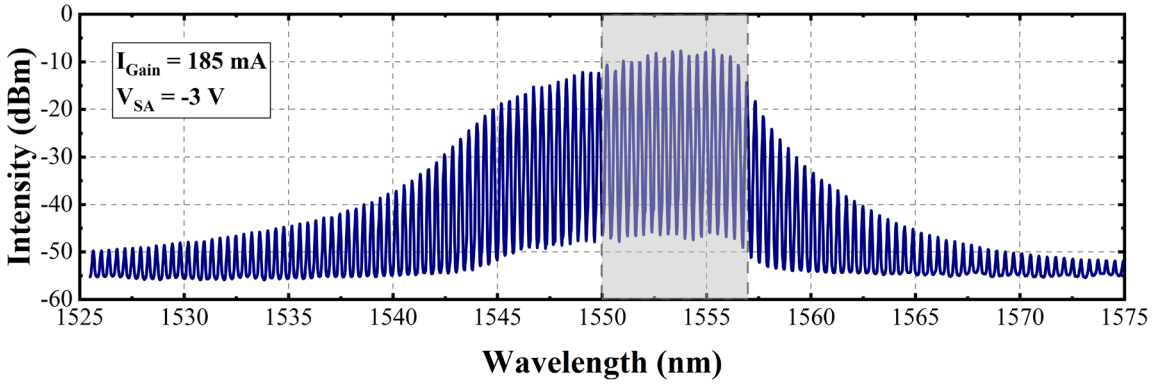

Fig. 4.10 Optical spectrum measured at the facet of the SMLL gain section under mode-locked operation, with an injection current of 185 mA and a -3 V bias applied to the SA.

To evaluate the PF passband windows, we also employ a benchtop fibre-coupled SLD source from *Thorlabs*. The system integrates the SLD, a control unit and a thermos-electric cooler for precise operation. The SLD spectra is shown in Figure 4.11. A dedicated low noise constant current supply and temperature controller ensure stable output. An integrated microcontroller allows fine adjustment of optical power and temperature and monitors system faults. The device is fabricated on an InP substrate, providing a high-power broadband source. An SMF connects the SLD to the input GC. A PC ensures excitation of the TE mode. The output is also routed by an SMF from the GC. Both input and output SMFs are aligned directly above the GCs with a vertical tilt angle of 15º. The output was analysed using an OSA. To evaluate programmable control, different currents are applied to the MH electrodes to perturb resonance peaks in the transmission spectrum, and the shifts are recorded.

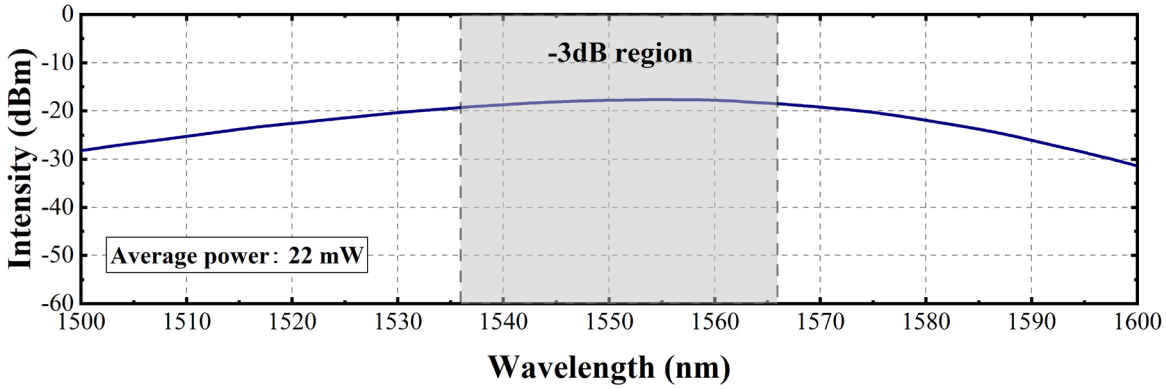

Fig. 4.11 Spectrum of the SLD at 600 mA drive current.

As for the PIC in Chapter 8, its characterisation settings are entirely consistent with those described above; therefore, no further elaboration is provided here.

4.4 Chapter summary

This chapter has presented a unified account of the experimental setup spanning device fabrication and characterisation, providing the methodological backbone for the thesis.

It has outlined the core fabrication modules and their roles in achieving reproducible nanophotonic structures on SOI and SiNOI, including EBL for high-fidelity definition of waveguides, gratings, resonators and heater layouts, high-density plasma etching for controlled pattern transfer with near-vertical sidewalls, PECVD- and HSQ-based passivation and planarization to stabilise optical performance and enable reliable surface metallisation, and electron-beam evaporation and lift-off for implementing plasmonic features and MH stacks.

The chapter has also detailed the measurement infrastructure and protocols used across the thesis, including broadband and comb-based optical sources, grating-coupler fibre coupling with polarisation control, optical spectrum analysis, current-driven thermo-optic tuning, and automated data collection. By defining the process flow, key control variables, and the characterisation chain in one place, this chapter enables direct traceability between design, fabrication, and measured response in the sensing and filtering demonstrations that follow, and provides a reproducible reference framework for future extensions of the platform.

5 Hybrid plasmonic waveguide-based biochemical sensors

Building on the analysis in the preceding chapter, this chapter introduces two biochemical sensors based on the SBW-DSHPW structure. By combining the strong near-field enhancement of surface plasmon modes with the low-loss transport of conventional silicon photonics, the proposed designs address two long-standing constraints in on-chip biochemical sensing, namely, limited footprint and limited sensitivity. We present, in turn, the operating principles, numerical results, and measurement of two implementations, one employing an MRR and the other an MZI. Both realise high-sensitivity refractive-index sensing.[1]

5.1 Working principle

The central idea is modal engineering in a composite cross-section. The SBW-DSHPW uses a silicon slot waveguide to form nm-scale gaps between a high-index silicon core and a low-index analyte cladding. Thin Ag films on both sides excite surface plasmon modes at the metal-dielectric interfaces, which concentrate the optical field within the nanoslots and the liquid immediately above them. By judiciously selecting the silicon rib width *w*, the slot width *g*, the dual outer-slot width *d* set by the silicon-analyte-Ag stack and the metal thickness *h*, the optical power is distributed among the silicon, the interfaces and the analyte to maximise light matter overlap while controlling loss. A representative configuration adopts $w = 300$ nm, $g = 50$ nm and $d = 150$ nm within an overall width of 600 nm, supporting a stable quasi-TE hybrid mode.

In the MRR architecture, the SBW-DSHPW forms part of a closed ring cavity that supports whispering gallery operation. Its resonant conditions are given by the following formula:

$$m\lambda = 2\pi n_{eff} R \tag{5.1}$$

m is the longitudinal modulus order, and *R* is the radius from the centre of the annular cavity to the inner wall of silicon. As shown in Figure 5.1, a change in analyte refractive index perturbs the effective index and shifts the resonance wavelengths, which provides a direct wavelength-tracking readout. To strengthen coupling and mode matching, a side-coupled

[1] Parts of this chapter have been published previously in: S. Zhu *et al*., in *ECOC 2024*: *50th European Conference on Optical Communication* (Frankfurt, Germany, 22-26 Sept. 2024), paper W2A.149.

silicon bus with an offset slot is used together with a partially opened outer gold ring that creates a dedicated coupling window. The offset slot bus improves power transfer and mitigates round-trip loss due to modal mismatch between the closed and open sectors of the metal-clad ring. This arrangement balances nanofabrication feasibility with spectral selectivity.

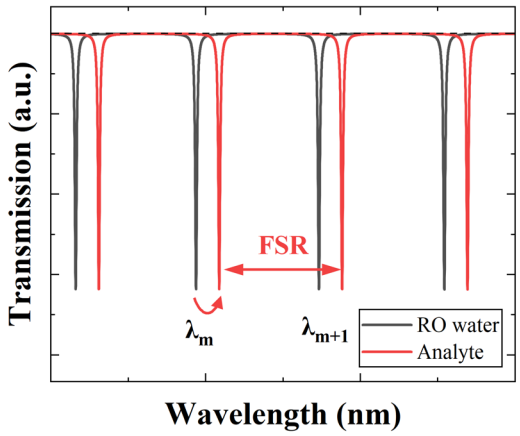

Fig. 5.1 Wavelength shift of the transmission spectrum for MRR-based sensing.

In the MZI architecture, the tri-slot waveguide acts as the active sensing region in one arm, while the reference arm is a conventional 400 nm wide silicon ridge. Silicon tapers couple efficiently between the SOI ridge and the SBW-DSHPW section and ensure high mode overlap and phase stability. In an interferometer, an effective length difference is formed between the two arms, the change of which leads to periodic changes in the interference output wavelength, and the interference resonance wavelength meets the following:

$$\lambda = \Delta L_{eff}/m \tag{5.2}$$

$$\begin{aligned}\Delta L_{eff} = n_{eff,ref} \cdot (2\pi R_{ref} + L_{ref} - 2R_{ref}) - 2\int_{L_{taper}} n_{eff,taper}(l)\,dl \\ - 2\int_{L_{buffer}} n_{eff,buffer}(l)\,dl - n_{eff,SBW-DSHPW} \cdot L\end{aligned} \tag{5.3}$$

The sensitivity of this structure depends on the responsiveness of the n_{eff} to the external refractive index in the SBW-DSHPW, namely:

$$S = \frac{\partial \lambda}{\partial n_{eff}} \cdot \frac{\partial n_{eff}}{\partial n_{Analyte}} \tag{5.4}$$

$\partial n_{eff}/\partial n_{Analyte}$ is mainly determined by the Γ in the area covered by the analyte, which is directly proportional. Through the discussion in Chapter 3, we have coordinated the confinement factor and propagation loss to obtain the structural parameter configuration, which ensures low loss while achieving up to 64% of the optical field concentration in the analyte region, fully mobilising the interaction between the light field and the refractive index perturbation. In addition, the architecture is less sensitive to width changes and has good manufacturing tolerances, which is of great significance for practical chip-level sensing applications. When the n_{eff} changes due to changes in the refractive index of the cladding, the phase difference changes, and the interference trough drifts, as shown in Figure 5.2.

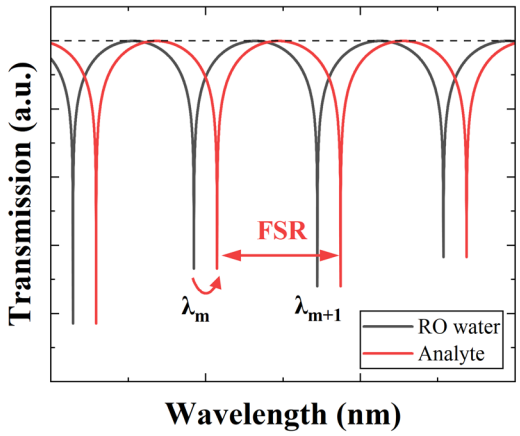

Fig. 5.2 Wavelength shift of the transmission spectrum for MZI-based sensing.

Control of the Q factor is crucial for the MRR. For large radii where radiation loss is negligible, absorption is the dominant contribution to the loaded Q factor. By adjusting the metal coverage angle, a practical balance is struck between sensitivity and quality factor, which suppresses plasmonic absorption at the interface while preserving frequency selectivity. In the MZI, the strong SBW-DSHPW sensitivity allows the required PS to be produced within a compact sensing length, providing a favourable trade-off between footprint and sensitivity.

For measurement, the sensing window is defined by EBL, while the cladding above GCs is retained to maximise fibre coupling. Analytes are dispensed onto the sensing area, and the resulting wavelength drift is recorded by an OSA. The drift is mapped to a refractive-index

change through calibration, which enables quantitative, label-free detection with high sensitivity.

This chapter employs aqueous glucose solutions as a representative biochemical analyte. Glucose is widely used as a calibration standard in refractive-index sensing because its concentration can be accurately prepared by mass fraction and its refractive index is well characterised in the near-infrared. In addition, glucose solutions prepared in halide-free reverse-osmosis water minimise chemical attack on silver compared with chloride-containing buffers or saline environments. Silver is known to form corrosion products such as AgCl in high-chloride environments and Ag_2S in sulphur-containing atmospheres, which can degrade optical performance and long-term stability.

Accordingly, the present demonstrations are intended as a proof-of-concept for high-sensitivity refractive-index sensing on an Ag-based hybrid plasmonic platform, rather than direct operation in complex biofluids. Strategies to extend compatibility to realistic samples, such as conformal dielectric passivation of the Ag surface and microfluidic isolation, will be developed in the future.

In general, this series of devices highly integrates plasma enhancement mechanism, sub-wavelength mode field regulation and silicon photonics platform, and combines the advantages of MRR and MZI sensing architectures to achieve high-sensitivity, low-power, and compact integrated refractive index sensors on the chip. Its core innovation lies in the precise regulation of the optical model by the three-slot structure and the multi-objective collaborative optimisation of sensitivity, loss and Q-factor of structural parameters, which lays a technical foundation for the subsequent construction of integrated biochemical sensing and on-chip photonic systems.

5.2 Design and simulation results

Both high-sensitivity all-pass MRR and MZI devices are designed on a commercial SOI platform comprising a 220 nm crystalline-silicon layer above a 2 μm BOX layer on a silicon substrate. The 220 nm thickness is a widely adopted standard that supports single-mode guidance with low loss and compact integration.

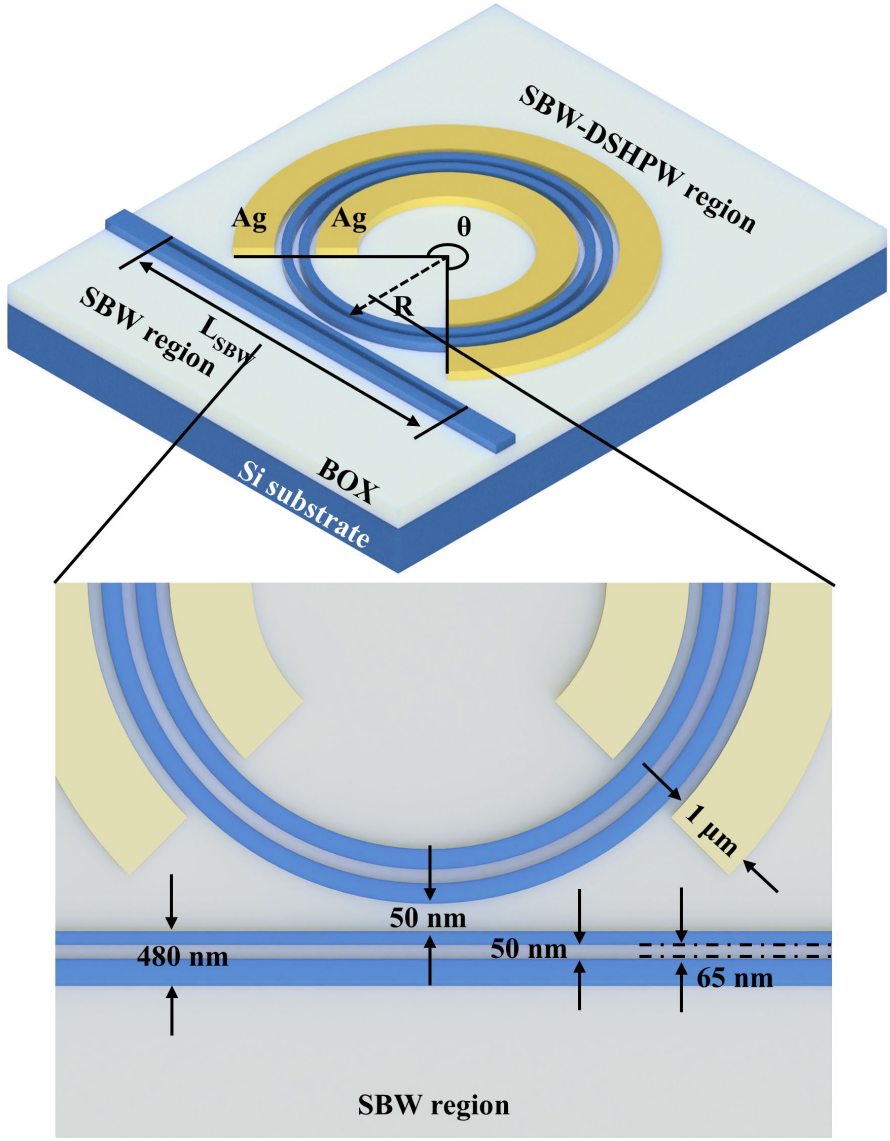

Fig. 5.3 Schematic of a side-offset-slot silicon bus waveguide side-coupled to an SBW-DSHPW MRR sensor with magnified view.

The SBW-DSHPW MRR (Figure 5.3) consists of a silicon slot-waveguide MRR surrounded by a concentric silver annulus. The structural parameters follow Chapter 3: w = 300 nm, g = 50 nm and d = 150 nm. The silicon etch depth matches the metal height at 210 nm. The MRR radius R, measured from the centre to the centreline of the inner silicon slot waveguide, is 4.9 μm. An offset-slot bus is preferred to a conventional ridge bus because the latter suffers from severe low coupling with slot-type rings. According to what we discussed in Chapter 2, the slot waveguide is actually a waveguide that can limit the propagation of light at the diffraction limit, and the power density in the slot is very high, so even the MRR composed of the slot waveguide and traditional slot-centred SBW will still lead to low coupling efficiency, because the slot in the bus waveguide has too strong ability to limit light, making it very difficult for the light in the bus waveguide to escape from the slot to propagate in the slot attached to the ring. In the chosen design, the bus maintains the same slot width as the

ring at 50 nm, the slot is offset by 65 nm from the bus centre, and the bus width is 480 nm to match the GC access waveguide. The offset-slot section length is 20 μm, and the ring to bus gap is 50 nm. Since a continuous outer Ag ring would block coupling, a partial opening is introduced over the coupling sector. Let θ denote the angular coverage of the metal. For a full MRR, θ equals 360º, whereas here θ is set to 270º to create an efficient coupling window.

The analyte fills the nanoslots and wets the device surface. GCs are used at both terminations for fibre coupling. Figure 5.4 shows FDTD simulations with reverse-osmosis (RO) water cladding yield a through-port spectrum in the C band with a periodic train of notches that correspond to MRR resonances. At resonance (Figure 5.4(b) and (c)), energy couples into the ring and circulates, producing a pronounced dip at the through port; away from resonance, light remains in the bus with high transmission. The response exhibits a Lorentzian notch profile. A representative FSR is about 22 nm. For the notch centred at 1537.5 nm the ER is about 10 dB, and the loaded Q factor is about 1114. This value is lower than that of typical low-loss all-dielectric SOI MRR, where Q factors can be orders of magnitude higher, because the inclusion of Ag introduces additional absorption and interface scattering that reduce photon lifetime. A reduced Q broadens the resonance linewidth and can, in turn, degrade the minimum resolvable wavelength shift and the achievable detection limit under a fixed measurement noise floor. Nevertheless, the hybrid plasmonic configuration substantially increases the field overlap with the analyte, which raises the wavelength sensitivity. The present design, therefore, represents a deliberate trade-off between spectral selectivity (Q factor) and light-matter interaction (confinement in the analyte).

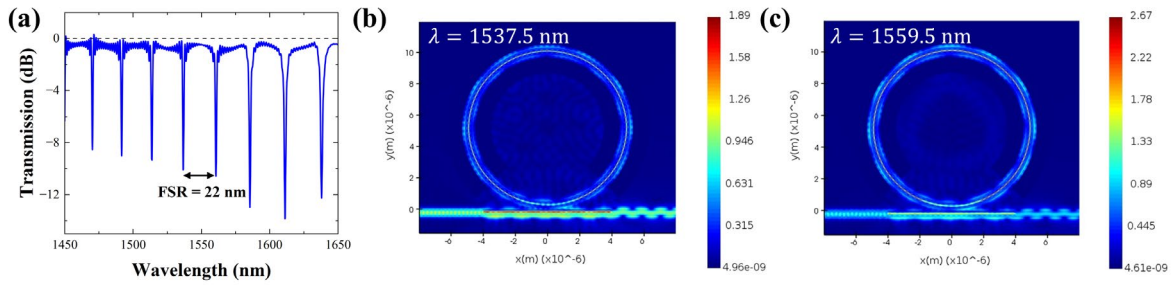

Fig. 5.4 Simulated (a) through-port spectrum and field distributions at (b) 1537.5 nm and (c) 1559.5 nm for RO water cladding of refractive index 1.31.

Field maps reveal that, in a bent SBW-DSHPW MRR, the outer slot carries higher optical power than the inner slot, leading to an imbalance relative to a straight section. This imbalance increases propagation loss and low Q factor because much of the optical energy is concentrated near the outer analyte-silver interface. A practical mitigation is to make the

outer slot slightly wider than the inner slot, which is in line with the conformal mapping theory of the MRR cavity and also reduces the n_{eff} mismatch between the open and closed sectors and thereby lowers round-trip loss [181].

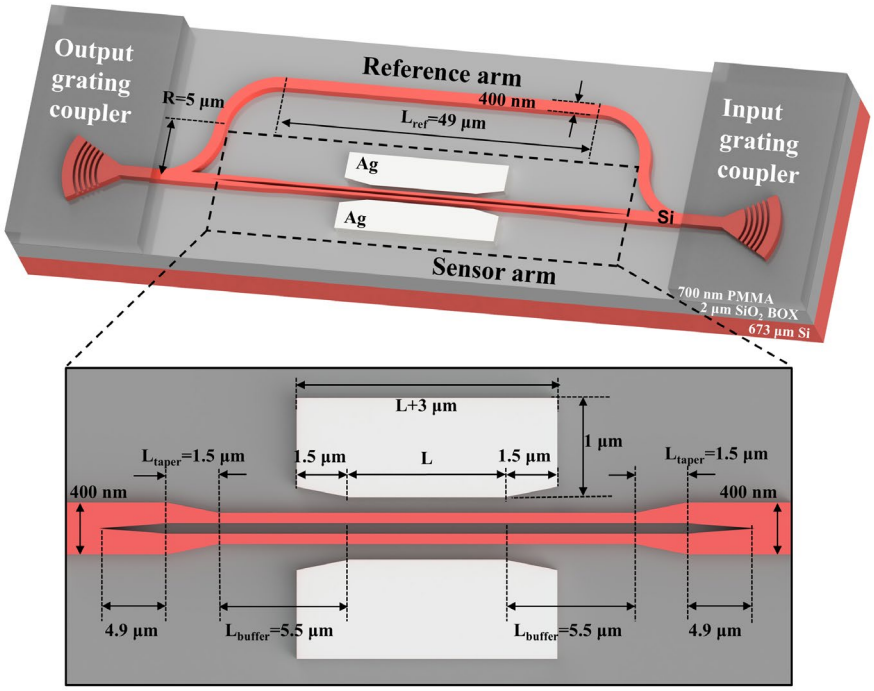

Fig. 5.5 3D schematic of the MZI-based biochemical sensor using SBW-DSHPW.

Figure 5.5 is a 3D schematic of an MZI-based biochemical sensor proposed by SBW-DSHPW. The designed MZI integrates SBW-DSHPW in one arm as a high PS sensing area. To mitigate significant propagation losses in the sensing arm, an asymmetrical Y-splitter is employed to improve the ER. The splitter consists of a straight waveguide and an S-shaped curved waveguide with a bending radius R of 5 µm that serves as a reference arm. The Y splitter is designed to route more optical power (61%) to the sensing arm than a typical 3 dB splitter, effectively compensating for coupling and propagation losses in the SBW-DSHPW sensing region. The splitter is connected to the input and output GCs. The reference arm (L_{ref}) is designed to be 49 µm long and 400 nm wide. In the sensing arm, the coupler is formed by a 1.5 µm long silicon taper that connects a 400 nm wide striped silicon-ridged waveguide to the DSHPW, promoting increased light-silver pad interaction. In addition, the reverse groove waveguide taper (4.9 µm long) is used as a coupler between the 400 nm wide Si ridge waveguide and the SBW. Each silver pad is 3 µm longer and 1 µm wide than the DSHPW length (L) and is located on either side of the SBW to form the DSHPW. The taper configuration of the Ag pad is designed to perform photonic-to-hybrid plasma mode

conversion and minimise coupling losses from the SOI waveguide to the DSHPW. The cross-sectional design parameters of the SBW-DSHPW are the same as those of MRR, with L ranging from 20 μm to 35 μm in 5 μm increments. The Γ of RO water within the SBW-DSHPW triple-slot configuration was determined to be 64%. Similarly, the modes of the SBW-DSHPW, discussed in the preceding Chapter 3, clearly highlight the presence of plasmonic modes. The hybrid plasmonic modes generated within the DSHPW can propagate along both the metallic and silicon sidewalls, interfering with the output SOI bus waveguide following the Y-splitter to establish a double-arm MZI interferometer. The fundamental TE mode propagates within the reference arm, serving as the reference signal. Variations in analyte concentration induce highly sensitive phase shifts within the SBW-DSHPW region, resulting in resonant wavelength shifts at the interferometer output. Notably, a 5.5 μm buffer zone exists between the Si taper and Ag taper to stabilise the SBW-supported mode.

Nanofabrication constraints were incorporated at the design stage by selecting feature sizes that are compatible with EBL and lift-off processing on SOI. In particular, g = 50 nm and d = 150 nm were set in the nominal designs to remain within a manufacturable regime. Furthermore, the metal pads were deliberately extended beyond the nominal hybrid section length, and a buffer region was introduced between the silicon taper and the Ag taper to reduce sensitivity to overlay errors. Alignment between the Ag features and the Si slot waveguide is especially critical in hybrid plasmonic structures. A small longitudinal or lateral misalignment breaks modal symmetry, redistributes the field towards one metal-dielectric interface, and can therefore increase absorption and scattering loss sharply. This consideration is reflected in the adopted geometry and transition design, which prioritise robust mode conversion and tolerance to realistic lithographic offsets.

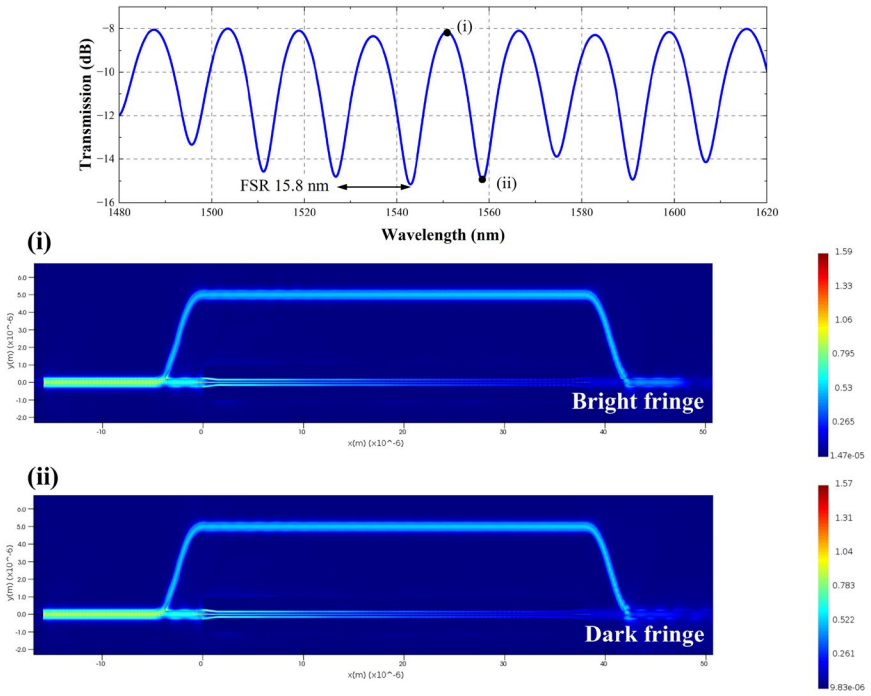

Fig. 5.6 Simulated transmission spectrum for L = 35 µm with RO water cladding and optical field near 1550 nm showing (i) bright and (ii) dark fringes.

Figure 5.6 shows the transmission spectra and optical field distributions of the mixed plasma MZI with the above parameters simulated using FDTD with an SBW-DSHPW length of 35 µm using RO water as the cladding. 3D simulations were performed in *Ansys Lumerical* FDTD Solutions. A fundamental quasi-TE mode source was launched from a mode port placed at the input (left) access waveguide. At the output side (right), the transmitted signal was collected using a mode-expansion monitor located in the straight output waveguide section, ensuring that the reported transmission corresponds to the guided fundamental mode rather than total field power in the simulation region. The spectral response of MZI at the output of the C-band exhibits a classical series of periodic transmission notches corresponding to the dark fringe wavelengths that satisfy the MZI. When the input light is divided into two beams at the beam splitter, it propagates in the reference arm and the sensing arm, respectively and remerges at the output, because there is a difference in n_{eff} and geometric length between the two arms, which will cause a phase difference, resulting in the appearance of interference fringes. When the phase difference between the reference arm and the sensing arm is an odd number π, the phases of the two beams are opposite, and destructive interference occurs, forming obvious transmission attenuation (Figure 5.6(ii)). The opposite is mutual interference (Figure 5.6(i)). It is worth noting that, like our waveguide simulation in the previous Chapter 3, even if we optimise the structural parameters to reduce the losses introduced by the metal, the attenuation of its power is still noticeable. When the

refractive index of the cladding of the sensing arm changes, the n_{eff} changes, which leads to a change in the optical path difference between the two arms, which is manifested as a more obvious movement of peaks and troughs and a weak FSR change in the spectral response. Its transmission spectrum has the characteristics of the square form of the sinusoidal function. A representative FSR is about 15.8 nm, corresponding to an equivalent optical-path difference of approximately 152.1 μm. Around the C band, the ER is about 7 dB.

The FDTD models in this chapter assume a homogeneous refractive-index change in the liquid cladding, which is appropriate for well-mixed glucose solutions where the concentration is spatially uniform at the device scale. For biosensing scenarios dominated by surface binding, the refractive-index perturbation is intrinsically localised to a thin region near the waveguide surface. In that case, the sensor response should be modelled using a localised adlayer approach, where a thin layer with altered refractive index is introduced within the evanescent-field region, or by defining spatially non-uniform perturbations confined to the functionalised surface. This extension would enable quantitative prediction of local binding responses and facilitate a direct connection between bulk sensitivity and surface sensitivity for practical assays.

All FDTD simulations in this thesis were carried out using *Ansys Lumerical* FDTD Solutions 2023 R2. Simulations were executed on a workstation equipped with a 12th Gen *Intel* Core i7-1270P CPU (2.20 GHz) and 16 GB RAM under a 64-bit operating system.

5.3 Characterisation results

Glucose solutions of different concentrations were prepared by mass fraction. High-purity glucose powder (99.99%) was weighed using an analytical balance and mixed with RO water to obtain the desired mass fraction, defined as $w = m_{glucose}/(m_{glucose} + m_{RO\ water})$. The mixture was stirred until fully dissolved and allowed to equilibrate to laboratory temperature before use.

The SBW-DSHPW MRR was first characterised. Using waveguides of different lengths, the propagation loss of deep-etched SOI ridge waveguides with PMMA overcladding was determined to be about 1.5 dB/cm. With a 10% glucose cladding, the measured FSR was 23.2 nm, slightly larger than the simulated 22 nm. The resonance near 1535.48 nm exhibited a loaded Q factor of around 360. The enlarged FSR is attributed to modal compression and enhanced group velocity caused by metal-surface roughness and boundary effects that are

not captured by idealised models. Especially in plasmonic waveguides, the absorption loss and scattering of metals are more significant than in conventional all-dielectric waveguides, resulting in faster energy dissipation and thus a lower Q value. Additionally, factors such as environmental disturbances in the test platform or fibre alignment deviations can also lead to widening of the resonant linear. The transmission spectra of 15% glucose are shown in the blue line in Figure 5.7. At 1550 nm wavelength and 20 ºC, the refractive indices of 10% and 15% glucose solutions were 1.33125 and 1.33898, respectively [182]. When the cladding was changed to 15% glucose, the resonance red-shifted by about 3.7 nm. Increasing glucose concentration increases the refractive index of the cladding solution, which perturbs the n_{eff} of the hybrid mode supported by the SBW-DSHPW section. For the MRR, the resonance condition requires an integer multiple of the round-trip phase, so an increase in n_{eff} increases the optical path length and leads to a red shift of the resonance wavelength. In the measurements, replacing 10% glucose with 15% glucose produced an approximately 3.7 nm red shift of the resonance near 1.55 µm, consistent with the expected increase in cladding refractive index and the strong modal overlap with the analyte region. Between successive measurements, the die was rinsed with RO water and IPA to avoid cross-contamination. From the resonance drift and the refractive-index change between 10% and 15% glucose, the measured wavelength sensitivity was approximately 694 nm/RIU, compared with a simulated value near 1193 nm/RIU. The sensitivity achieved is more than twice that of the optimised single-strip SOI reference TM MRR [183].

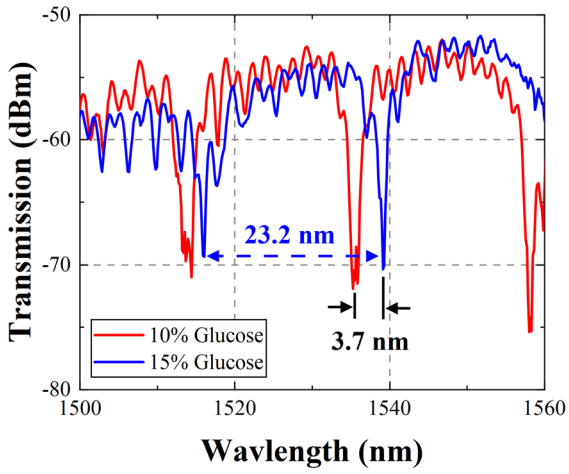

Fig. 5.7 Experimental spectral response of the SBW-DSHPW MRR sensor under 10% and 15% glucose claddings.

As shown in Figure 5.8, the SBW-DSHPW MZI sensors were then evaluated with sensing-arm lengths L of 20, 25, 30 and 35 µm. For L = 35 µm under a 10% glucose cladding, the

measured FSR was 14.7 nm, close to the simulated 15.8 nm, and the measured ER was 8.0 dB, slightly higher than the simulated 7.2 dB. Across all devices, increasing *L* enlarged the interaction area and effective optical path length, resulting in progressively larger red shifts when the cladding refractive index increased from 10% to 15% glucose. The wavelength shifts were approximately 2.6, 3.2, 5.1 and 7.1 nm for *L* of 20, 25, 30 and 35 µm, respectively. Measured sensitivities were about 336 nm/RIU for *L* = 20 µm and 659 nm/RIU for *L* = 30 µm, both exceeding values achieved by DSHPW-only MZI sensors of the same sensing length [128]. For the 35 µm SBW-DSHPW device, linear fitting of wavelength shift to refractive index over 10% to 30% glucose yielded an experimental sensitivity near 908 nm/RIU. The experiment is very close to the sensitivity reported in [128]. The results of our 35 µm SBW-DSHPW and 49 µm reference arm (with 8 dB ER) showed a 12.5% reduction in length compared to the 40 µm long DSHPW-only, a 27% reduction in length compared to the 67 µm long reference arm, and a 3 dB improvement in ER compared to the 5 dB reported in [128].

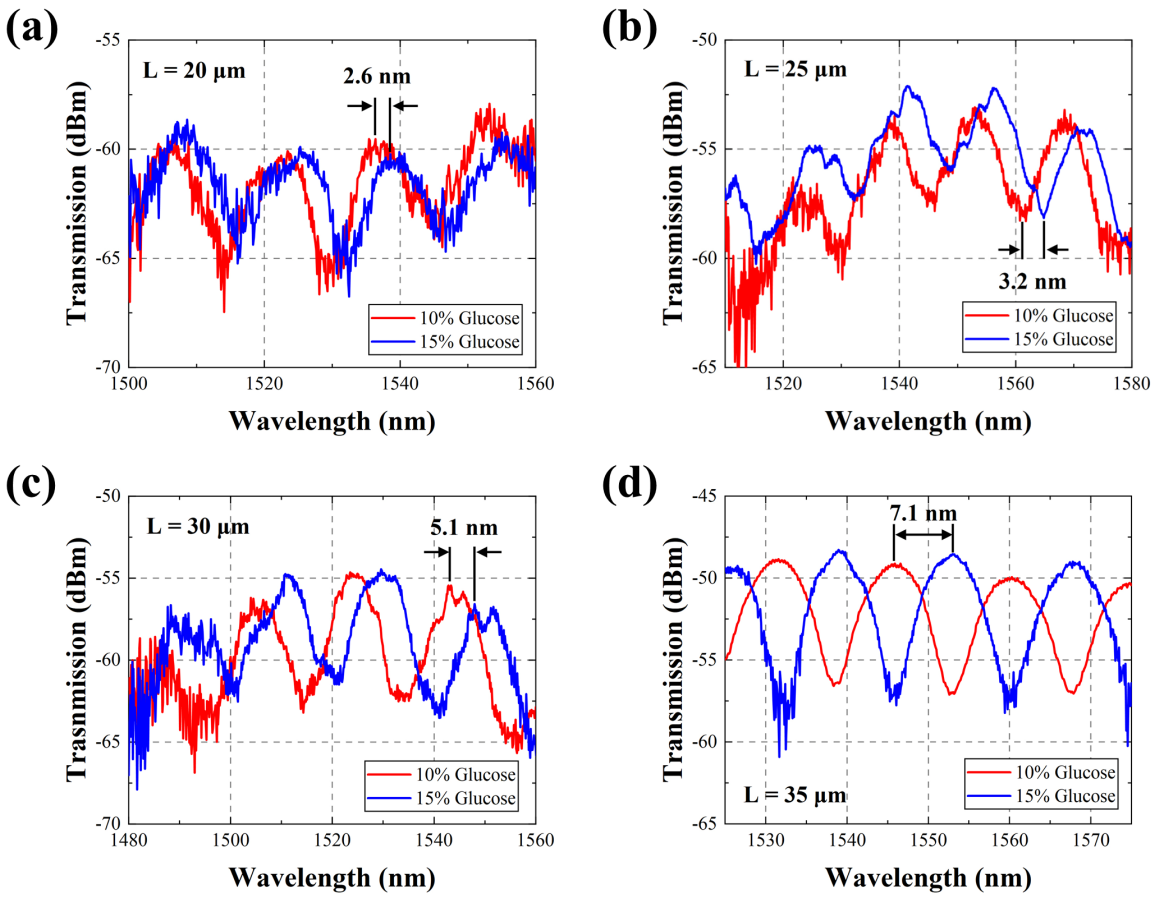

Fig. 5.8 Experimental spectral responses of SBW-DSHPW MZI sensors with (a) *L* = 20 µm, (b) 25 µm, (c) 30 µm and (d) 35 µm under 10% and 15% glucose claddings.

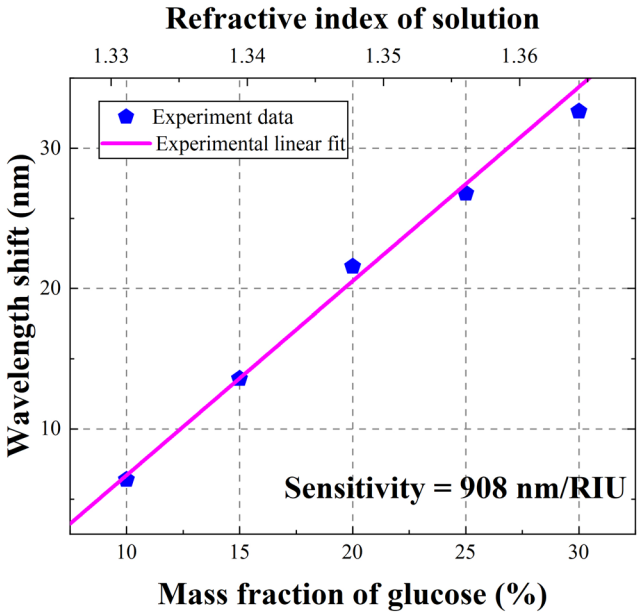

Fig. 5.9 Relationship between wavelength shift and refractive index of the glucose solutions for the 35 µm SBW-DSHPW MZI; linear fitting provides the sensitivity.

The Ag film enables strong surface-plasmon enhancement but introduces material-stability considerations that are less critical for all-dielectric silicon photonics. In ambient atmospheres, silver commonly undergoes tarnishing, where corrosion films are dominated by Ag_2S, and in chloride-rich environments, AgCl formation can occur, both of which modify the optical boundary condition and increase absorption and scattering losses.

To provide practical evidence of this limitation, the Ag-coated devices were subjected to an accelerated exposure test in saline solution overnight (Figure 5.10). Visible surface degradation was observed after exposure, consistent with chloride-driven corrosion mechanisms.

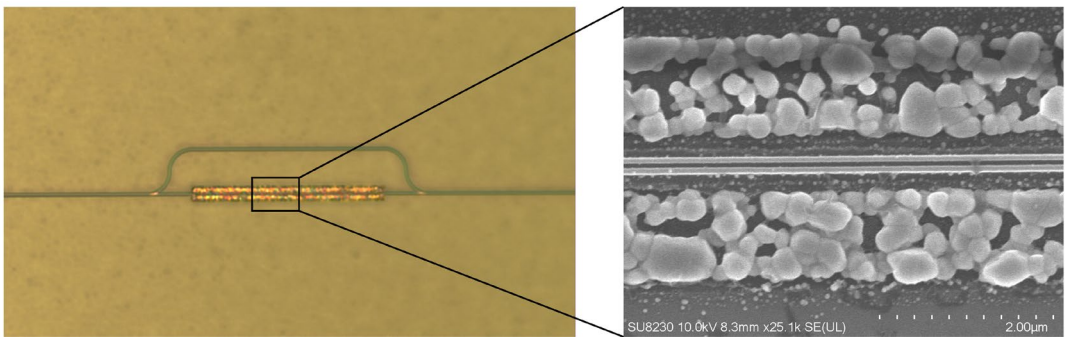

Fig 5.10 Optical micrographs and zoomed in SEM image of the MZI configure device after overnight immersion in saline solution, showing corrosion-induced surface degradation.

5.4 Chapter summary

This chapter has investigated on-chip biochemical sensors based on the SBW-DSHPW hybrid plasmonic waveguide. Two high-sensitivity integrated architectures were proposed and realised, namely an MRR and an MZI. Both combine surface-plasmon near-field enhancement with low-loss silicon-photonic transport to address long-standing constraints in sensitivity and footprint.

For the MRR, a side-coupled offset-slot silicon bus and a partially opened outer metal ring establish efficient coupling and enable precise control of resonance characteristics. The device exhibits clear periodic notches in the C band with controllable FSR and Q factor. For the MZI, embedding the SBW-DSHPW section in one arm, together with a Y splitter and tapered transitions, achieved modal matching and loss compensation, raising sensitivity while preserving compactness. In glucose assays, both architectures delivered pronounced red shifts and refractive-index sensitivities up to and beyond 600 nm/RIU (MRR) and 900 nm/RIU (MZI), outperforming comparable designs. Their dimensions imply a markedly higher sensitivity per unit device length than many state-of-the-art interferometric or resonant refractive-index sensors that rely on longer interaction paths or larger cavities to reach similar sensitivities. In addition, the sensing operation is intrinsically passive and does not require active tuning during measurement, so the electrical power consumption on chip is effectively negligible, aside from any optional stabilisation or control hardware used at the system level. Finally, the use of a standard SOI process flow and GC interfacing supports straightforward replication into dense sensor arrays and multiplexed layouts.

In the present work, the proposed devices operate as refractive-index sensors using resonance or interference wavelength shifts, and do not measure an absorption spectrum of the analyte. Consequently, the platform cannot independently identify chemical species from spectral fingerprints. Glucose is therefore used here as a controlled, well-characterised refractive-index perturbation to quantify sensitivity and validate device operation. In applications where chemical specificity is required, this photonic readout can be complemented by selective surface chemistry and appropriate material passivation, or by an external spectroscopic modality.

The SBW-DSHPW concept unifies subwavelength optical confinement, high coupling efficiency and process compatibility, demonstrating strong refractive-index detection and high integration potential for on-chip biochemical sensing.

6 Dual passband tunable photonic filters based on reconstruction equivalent chirp technique

MPFs find extensive use in radar navigation, electronic countermeasures and phased-array antennas, and are also applicable to emerging broadband wireless-access networks such as wireless local-area networks, Worldwide interoperability for microwave access and local multipoint distribution services [184].

Broadly tunable microwave and MMW filters are indispensable across signal generation, transmission and processing. Leveraging integrated photonics to realise filtering for MWP is a promising direction. Conventional electrical filters are constrained by their transmission media and components, making wide-range frequency tuning difficult. This chapter addresses the thesis theme of reconfigurable, compact on-chip spectral processing on the SOI platform by developing dual-passband tunable photonic filters for OFD and frequency-agile microwave and MMW synthesis. Building on the sampled Bragg grating framework and the REC concept established earlier in the thesis, the work here translates those design principles into practical devices that can programmably select pairs of lines from an OFC generated by a passive SMLL. The guiding philosophy is to replace cascaded resonator networks with a single grating waveguide that offers design-level control of passband centres, bandwidth and spacing, while retaining electrical programmability via integrated MHs. Two implementations are presented in a deliberate progression: a chirped C-SBG that validates independent dual-passband tuning enabled by REC, followed by a more compact 4PS-SBG that strengthens the grating coupling and improves spectral selectivity, thereby extending the tuning range and enhancing channel purity[2]. Together, these results provide a scalable route to integrated MWP subsystems with high spectral purity and dense integrability.

6.1 Working principle

Several approaches exist for generating microwave signals photonically. The first employs two independent continuous-wave lasers whose wavelengths are tuned to create a frequency offset; the two optical tones are heterodyned on a high-speed PD to form a microwave signal. The method is conceptually simple but suffers from poor frequency stability, as inter-laser phase noise and drift degrade spectral purity, making it difficult to meet low phase-noise requirements in high-Q systems. The second uses EO modulation, for example, with a Mach-

[2] Parts of this chapter have been published previously in: S. Zhu *et al*., *IEEE Photonics Technology Letters*, **37**, 169-172 (2025); and S. Zhu *et al*., *ACS Photonics*, **12**, 899-907 (2025).

Zehnder modulator, to create optical sidebands from a single laser. Two desired components are then filtered and heterodyned. Although controllable and mature, this route faces limits in modulation depth, an upper frequency ceiling below 100 GHz and relatively high-power consumption. Nonlinear distortion and carrier-suppression constraints also affect spectral purity. The third relies on Kerr nonlinearity in high-Q microcavities to generate OFC through four-wave mixing. While such combs offer ultrabroad bandwidth and low noise, they demand stringent pump power, thermal management and cavity design, and the line-spacing control is limited, with high start-up threshold and stability challenges.

In contrast, the present work adopts the route illustrated in Figure 6.1. A semiconductor passive SMLL provides a coherent OFC. A tunable PF selects two comb lines with programmable spacing. The selected pair is heterodyned on a PD to yield a microwave signal. An SMLL delivers a high-repetition-rate, broadband and phase-stable OFC at low power and compact size with favourable integrability. With a well-designed PF, any two comb lines with a desired separation can be extracted, enabling frequency-agile microwave generation from several of GHz and potentially into the THz regime. The system features excellent frequency stability and low phase noise without the need for high-power external modulators or dual-laser locking, and is therefore well suited to future high-capacity communications, radar and sensing.

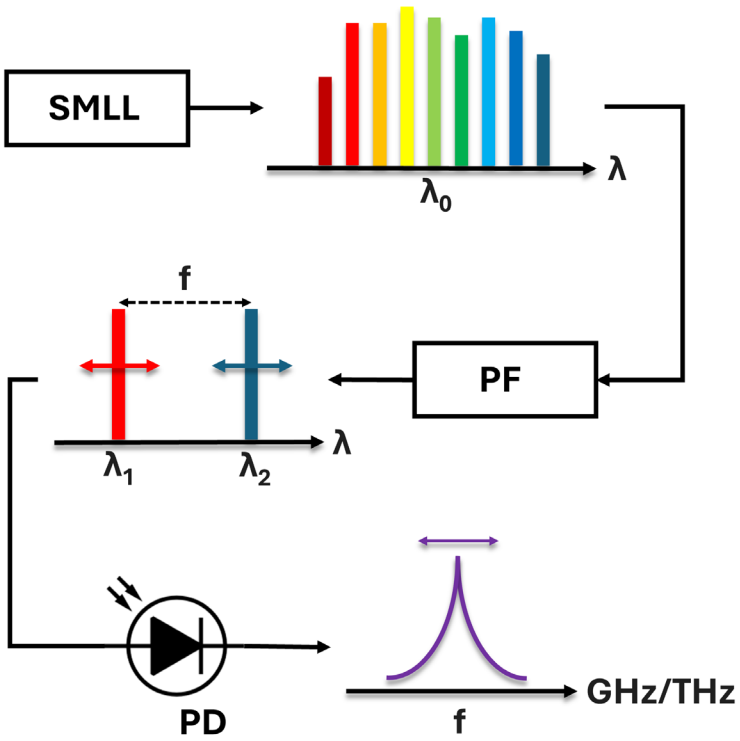

Fig. 6.1 The technical roadmap for PF described in microwave signal generation.

For on-chip bandpass PFs, several mature architectures are available. The most common are MRRs, MZIs and Bragg gratings. MRRs are attractive for their high Q factor, compact footprint and intrinsic frequency selectivity. By tuning the optical pathlength or n_{eff}, their FSR and resonance centre can be controlled to realise single- or multi-channel filters. However, the periodic response limits non-periodic channel selection and wideband operation, temperature stability is modest, and the coupling strength is highly sensitive to fabrication errors. MZIs use interference to implement filtering with good linearity and bandwidth, suiting flat responses and modest spectral resolution, although comb-line selection can suffer leakage and crosstalk, the footprint is larger, and multi-stage cascades increase complexity and thermal-control burden. AWGs provide powerful demultiplexing but usually occupy a large area and require complex design and fabrication.

Bragg-grating-based bandpass PFs exhibit strong advantages in integration level, bandwidth control and spectral shaping. In particular, the SBG with equivalent chirp achieves precise spectral selectivity through accurate control of sampling period and local phase modulation. In a compact waveguide, the structure delivers a tunable dual-channel response with high SMSR and low insertion loss. Unlike MRRs and MZIs, no closed-loop resonance or long interferometric path is required, which favours dense integration and large-scale arrays. Through the REC concept, the passband centres, bandwidth and spacing can be designed flexibly from GHz to THz, reducing insertion loss relative to cascaded-device solutions while preserving compactness. The architecture also offers favourable tunability and thermal stability, enabling precise phase adjustment through integrated MHs, and thereby provides an ideal platform for high-performance, programmable, multi-channel on-chip PFs.

The core operating principle is to use a grating-type PF based on REC to select two spectral components precisely from the comb for subsequent heterodyning. A single grating-waveguide structure embeds two π EPS regions together with REC-controlled sampling. Local sampling together with global equivalent chirp yields a dual-passband response. Under static bias, the two passband centres are pre-positioned at the designed optical frequencies. Two independent MHs integrated above the two π PS regions provide independent tuning by locally modifying the refractive index through the TO effect. The channel spacing f equals the frequency difference between the two passband centres and is adjusted by finely controlling the two currents of MHs. This approach replaces multiple discrete filters with a single waveguide, enabling multi-passband selection and wide-range tuning in a compact structure with high thermal efficiency and strong selectivity. After being beaten by the PD, the dual optical passbands map to a microwave signal with programmable centre frequency

and controllable bandwidth, realising wide-range and stable frequency synthesis from an OFC.

A narrow optical passband is required because the filter is used as a line selector for an OFC. In OFD, the detected microwave tone is determined by the frequency separation of the selected comb lines. If the optical passband is overly wide, adjacent comb lines can leak through the filter and generate additional heterodyne products at the PD, which degrades the SMSR and reduces the effective spectral purity of the synthesised microwave signal. Conversely, a sufficiently narrow passband improves channel isolation, suppresses spurious beating components and increases the robustness of comb-line selection across a wide tuning range. In this chapter, the measured -3 dB passband bandwidth is approximately 27 to 29.4 GHz for the C-SBG device and can be reduced to about 16 GHz in the 4PS-SBG implementation, consistent with the strengthened grating coupling and improved spectral selectivity.

6.2 Design and simulation results

We first design a dual-bandpass PF whose filtering section comprises an equivalent chirped C-SBG with two π EPSs (Figure 6.2). The equivalent modulation of the sampling separates the photon distributions of the two passbands spatially, which enables independent tuning of the passband wavelengths. By using the TO effect to change the phase amplitudes at the two EPSs, the two passband centres can be adjusted.

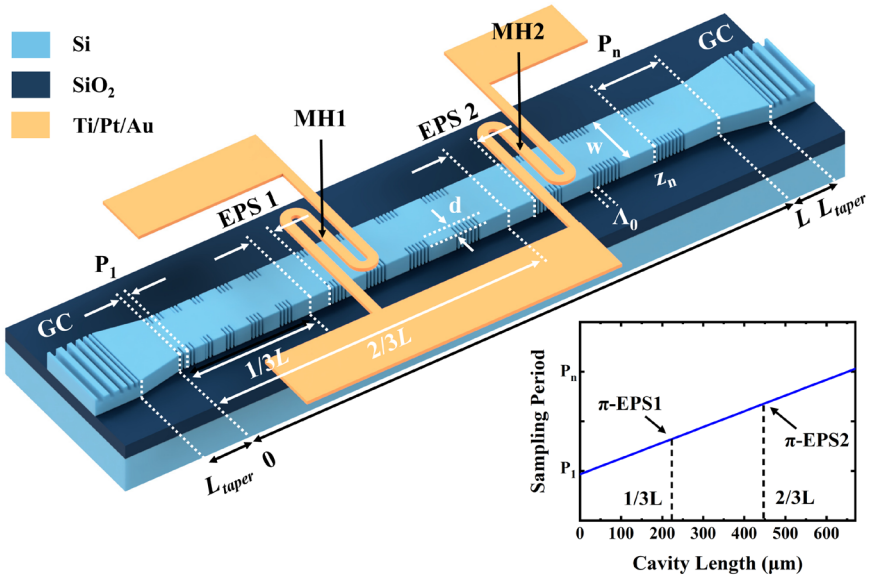

Fig. 6.2 Schematic of the REC-based C-SBG incorporating two π EPSs, integrated input and output GCs and two MHs located above the EPSs.

The device is implemented on a commercial 220 nm SOI platform. To generate two passbands in the +1st sub-grating channel, EPS1 and EPS2 are placed strategically at 1/3 and 2/3 of the cavity length L of the chirped C-SBG, balancing spectral resolution and tuning range. Two MHs are positioned directly above the two EPSs. Here, Λ_0 denotes the period of the seed grating. The linear-chirp sampling distribution satisfies the following relation.

$$P_n = P_1 + C \cdot z_n \tag{6.1}$$

$$C = (P_n - P_1)/L \tag{6.2}$$

Equation (6.1) is the equivalent linear chirp sampling period P distribution along the cavity, where P_1 is the first sampling period, P_n is the period at position z_n through cavity L, and C is the chirp rate, defined as the ratio of the difference between the maximum and minimum period ($P_n - P_1$) to the cavity length L (equation (6.2)). By introducing linear frequency modulation onto the P, the P at the two EPS positions diverge. This causes the two passbands to originate from distinct optical cavities, thereby enabling independent tuning of the passbands. Concurrently, this equivalent chirp is achieved through linear modulation of the μm-scale P. Compared to modulating the nm-scale Λ_0, this approach significantly reduces manufacturing complexity [185].

The C-SBG section, with L = 670 μm, is located at the device centre. Two symmetric tapers of length (L_{taper}) 250 μm connect the C-SBG to the GCs. Highly localised MHs fabricated on the upper cladding at the EPS locations allow independent adjustment through current injection. Each MH comprises contact pads and a serpentine resistive element positioned directly above the two EPS regions. Each region has a width of 0.9 μm and a spacing of 0.8 μm, and the resistance is 10.7 Ω at 20 ºC. Sidewall gratings are arranged symmetrically, and a UBG serves as the seed grating. The seed has a period Λ_0 = 351 nm, recess depth (d) 20 nm and ridge waveguide width (W) 520 nm. The n_{eff} of the C-SBG waveguide is 2.47 at 1550 nm.

The sampling method follows Equation (6.1). The cavity contains 215 full sampling cells, denoted n = 215. The C is set to 100 nm/mm. The P_1 = 3.079 μm, aligning the +1st order channel near 1550 nm. A P difference of 66.9 nm is realised accurately by EBL.

Figure 6.3 (a) shows the transmission spectrum calculated using the TMM [186]. Within the stopband centred at 1550 nm, two narrow passbands are evident with a Q factor of 6.2×10^4.

We denote them passband 1 and passband 2, with centres λ_1 and λ_2, corresponding to the phase discontinuities induced by EPS1 and EPS2, respectively. The initial frequency spacing between the two passbands is 111.8 GHz, and the grating ER is 20 dB.

For a uniform grating, the photon distributions of passband 1 and passband 2 almost overlap. This indicates that the passbands arise from the joint accumulation of the optical field at the two EPS points before transmission through the exit end. When either EPS phase is adjusted, the overlap causes both passbands to change together, preventing independent tuning. The behaviour follows from the distributed-feedback nature of a uniform grating, which lacks a fixed reflection location at a given position. To overcome this, an equivalent-chirp design is introduced so that specific frequencies are reflected at specific regions of the grating. In Figure 6.3(b), transfer-matrix analysis of the chirped grating shows that the photons associated with λ_1 and λ_2 concentrate at the two EPS locations and become spatially separated, reducing mutual interaction. Consequently, changing one EPS moves only its associated wavelength while leaving the other essentially fixed.

When current is injected into an MH, Joule heating raises the local temperature. Heat conducts through the deposited SiO_2 overcladding, whose thermal conductivity is approximately 1.1 W/(m·K). Because silicon has a large TO coefficient of 1.84×10^{-4}/K, the refractive index changes with temperature, which changes the EPS phase.

Figure 6.3(c) plots the spacing between λ_1 and λ_2 as functions of EPS1 and EPS2 when the other EPS is held at 1.0π. Increasing the PS at EPS1 produces a red shift of λ_1, while λ_2 exhibits only small fluctuations of about ±0.03 nm across 1π to 1.75π modulation of EPS2, reducing the spacing from 111.8 GHz to 5 GHz at 1.75π. Conversely, holding EPS1 at 1.0π and increasing EPS2 largely fixes λ_1 within ±0.02 nm while shifting λ_2 away from λ_1, increasing the spacing to 259 GHz at 1.75π. Thermal modelling of the equivalent chirped C-SBG PF is carried out in 3D using COMSOL Multiphysics. The relation between PS and temperature change ΔT is given by the following expression.

$$\Delta\phi = \frac{2\pi}{\lambda} L \left(\frac{\partial n_{eff}}{\partial T} \right) \Delta T \tag{6.3}$$

where n_{eff} is the effective refractive index, L is the cavity length, and λ is the operating wavelength.

As shown in Figure 6.3(d), when only MH2 is driven at 45 mA, the calculated thermal crosstalk, defined as the ratio of phase amplitude change in the unmodulated waveguide to that in the modulated waveguide, is about 0.9%. This demonstrates excellent thermal isolation, with negligible thermal effects at separations beyond about 225 μm.

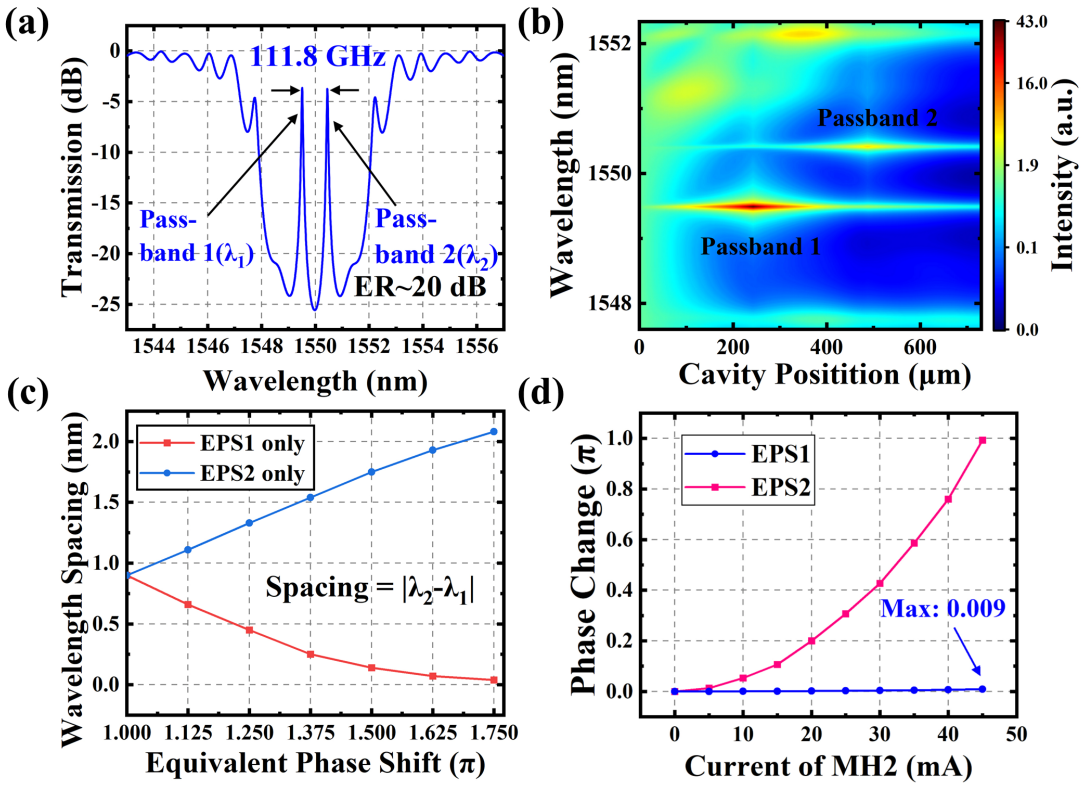

Fig. 6.3 (a) Simulated transmission spectrum showing two passbands. (b) Photon distribution along the cavity. (c) Passband spacing versus EPS1 and EPS2 phase values. (d) PS amplitude versus injected current at only MH2 for EPS1 and EPS2.

Chapter 3 established that the κ of the $+1^{st}$ sub-grating in a C-SBG is approximately $1/\pi$ of that of a UBG. A lower κ yields a narrower stopband and weaker ER, which constrains tuning range and side-mode suppression. A common remedy is a longer cavity, but on SOI single-mode waveguides, this raises scattering and propagation loss and runs counter to compact integration. To address this, we employ a 4PS-SBG structure. In a 4PS-SBG, each P is divided into four segments with $\pi/2$ PSs inserted between them. Fourier analysis shows that the κ of the $+1^{st}$ channel is about 0.9 times that of a UBG. Therefore, when using the $+1^{st}$ channel as the operating passband, a 4PS-SBG permits a shorter cavity while maintaining the same ER and a wider stopband. The 4PS sampling also suppresses the 0^{th} channel, preventing spurious crosstalk into the microwave signal.

In the new device, the C is increased to 200 nm/mm. Because of the equivalent chirp structure, the sampling periods corresponding to the two π PSs differ. Each PS introduces a

transmission peak at its local Bragg condition. Figure 6.4(a) shows the transmission spectrum of the chirped 4PS-SBG computed by the TMM. Two narrow passbands are observed within the stopband, denoted passband 1 and passband 2, with centres λ_1 and λ_2 corresponding to PS1 and PS2. The initial spacing between the two passbands is 220 GHz. A higher chirp rate enlarges the spacing and reduces spectral overlap in the initial spectrum. The photon distributions in Figure 6.4(b) reveal that the two passbands are spatially concentrated near the two π PSs and are clearly separated, demonstrating their independence. Within the stopband, longer wavelengths are reflected near the grating end, where the period is longer, whereas shorter wavelengths are reflected near the start, where the period is shorter. The chirp thus introduces distinct reflection positions for the two passbands. Consequently, the optical power reaching PS2 is lower than that at PS1, which leads to different peak intensity through the optical field in the grating.

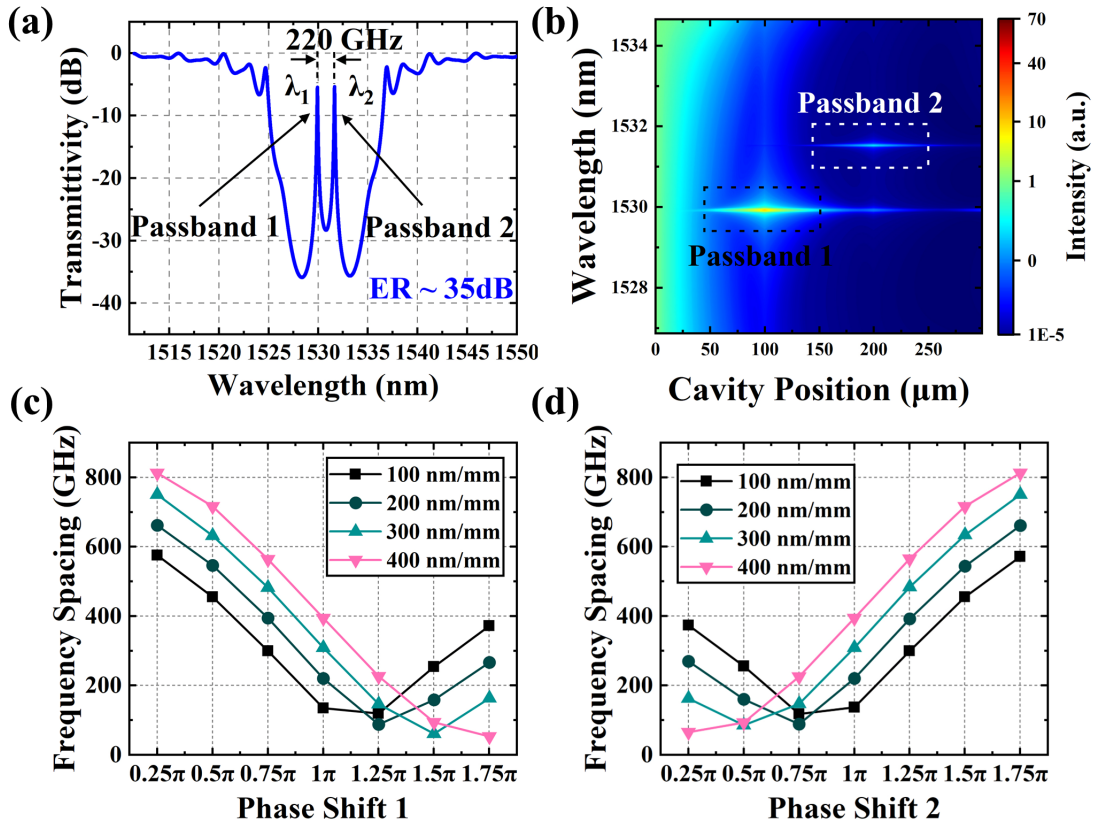

Fig. 6.4 (a) Transmission spectrum of the equivalent chirped 4PS-SBG. (b) Photon distribution along the cavity. (c) Passband spacing versus PS1 amplitude for different *C*. (d) Passband spacing versus PS2 amplitude for different *C*.

When only one PS is tuned, only its associated wavelength moves while the other remains unchanged. Figure 6.4(c) plots the passband spacing versus the amplitude of PS1 while PS2 is fixed at 1.0π for several chirp rates. Increasing PS1 produces a red shift in λ_1 and reduces spacing. Figure 6.4(d) shows the converse when PS2 is increased. A higher *C* yields wider

spacing. Calculations indicate that at 200 nm/mm, the spacing can be tuned beyond 600 GHz, a significant improvement over the C-SBG case.

Figure 6.5 depicts the device layout. The 4PS-SBG section has L = 300 μm and is centred between two symmetric tapers of length 250 μm that connect to GCs of width 12 μm and length 16 μm. Buffer waveguides of length 10 μm on each side connect the tapers (L_{taper} = 250 μm) to the GCs of different widths to ensure smooth mode conversion. The SOI wafer comprises a 220 nm top-silicon device layer and a 2 μm BOX on a 675 μm silicon substrate. Two π PSs are embedded at 1/3 and 2/3 of the 4PS-SBG cavity. The sidewall gratings are arranged symmetrically. The seed period Λ_0 is 351 nm, the recess depth d is 25 nm, and the ridge width W is 520 nm. The n_{eff} is 2.47 at 1535 nm. The sampling distribution follows Equation (6.1) with n = 96 sampling cells in the cavity. The C is 200 nm/mm, and P_1 is 3.083 μm to align the +1st channel near 1530 nm. A 60 nm difference between P_1 and P_n is implemented by EBL with 0.5 nm resolution.

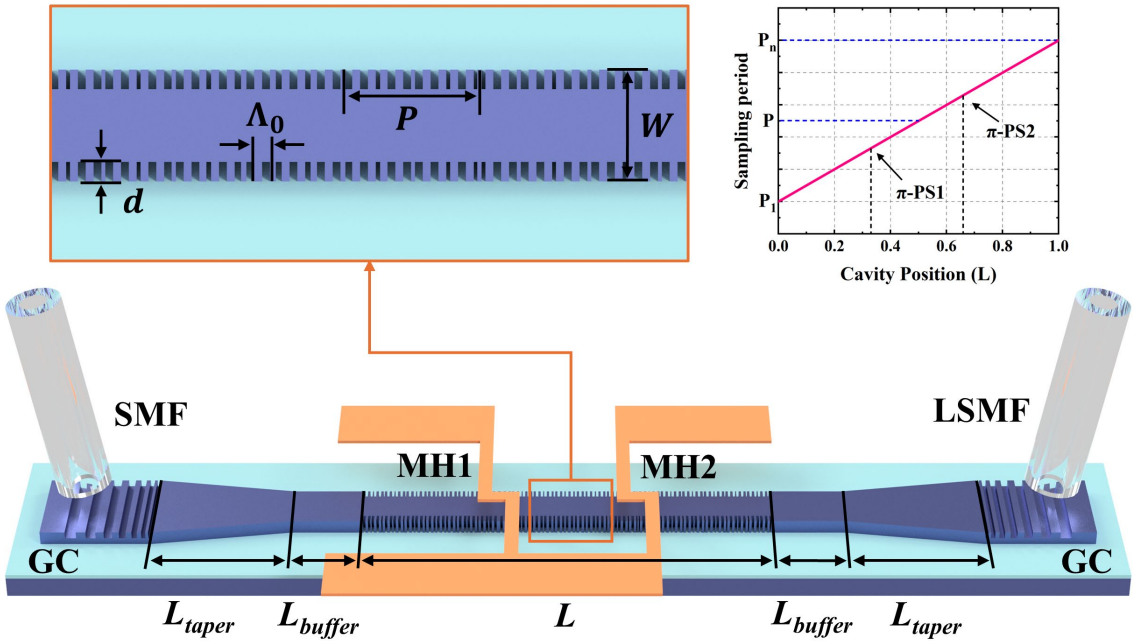

Fig. 6.5 Schematic representation of the equivalent chirped PF comprising GCs, 4PS-SBG and MHs.

Compared with conventional MZI and MRR architectures, the grating-based PF achieves narrower passbands and a tuning range unconstrained by FSR [90], offering unique advantages in wavelength selectivity and multiplexing. By reducing the number of resonators required to process multiple signals, the method provides a compact solution for PIC.

As before, COMSOL and Equation (6.3) are used to evaluate thermal crosstalk during tuning. Two thin-film MHs, MH1 and MH2, are placed on the oxide overcladding with 100 µm spacing and a common ground plane. In the simulation, only MH2 is biased to assess thermal coupling. Figure 6.6 shows that the surface temperature change under MH1 is negligible, while MH2 exhibits highly local heating. Assuming ideal vertical heat conduction at the PS points, cross-sectional temperature profiles confirm that when only one MH is active, the silicon waveguide below the other remains unchanged in temperature. Heat from the active heater transfers vertically through the SiO_2 overcladding with little lateral diffusion.

Figure 6.7 plots the PS amplitudes beneath MH1 and MH2 when only MH2 is driven. With 91 mA, PS2 reaches a phase amplitude change of 1.0π, while PS1 changes by only about 0.012π. For the given geometry, the thermal crosstalk is approximately 1.2%, and the thermal effect between adjacent phase shifters is negligible beyond 100 µm.

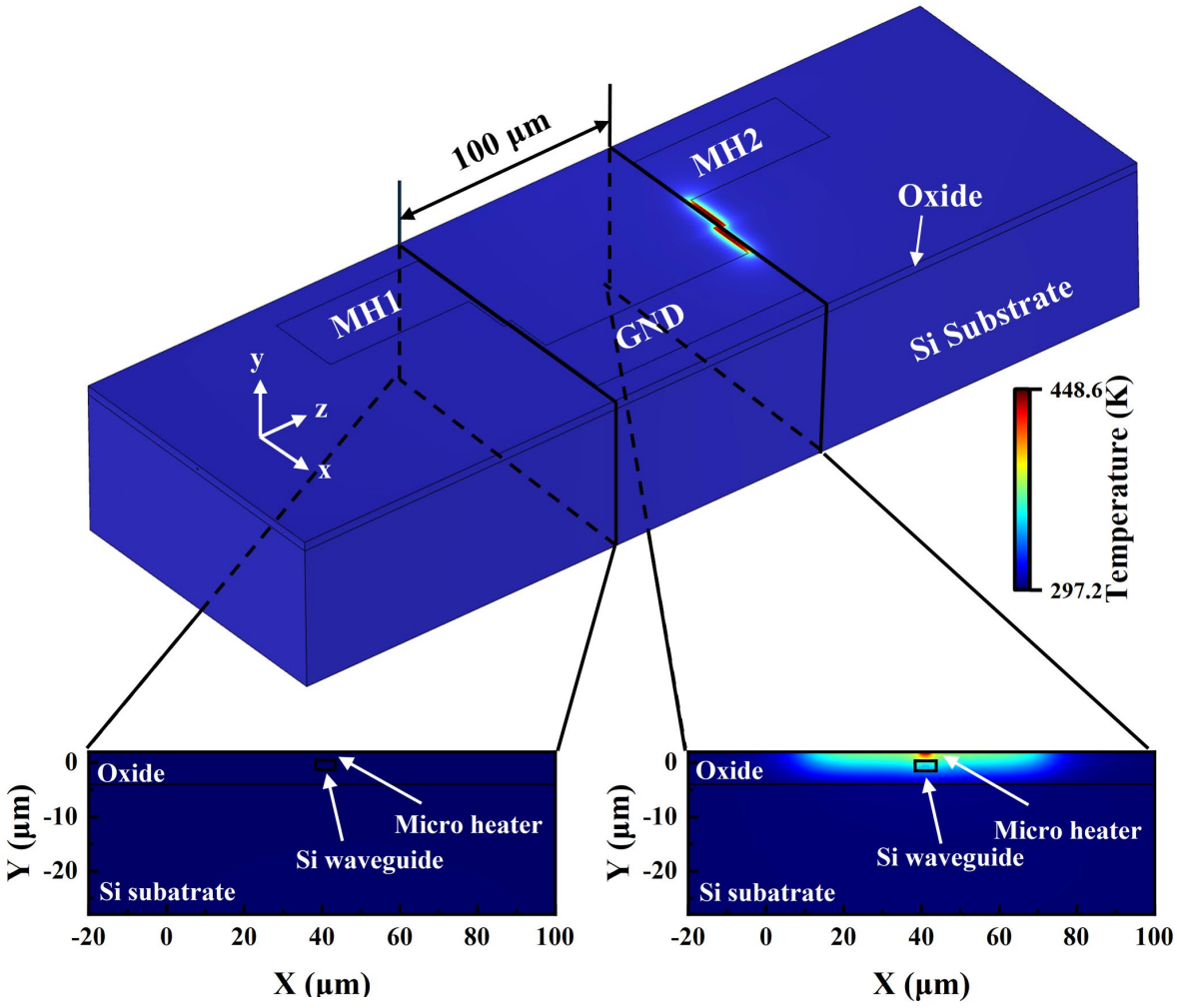

Fig. 6.6 Simulated temperature distribution when only MH2 is active, with cross-sections at the positions of MH1 and MH2.

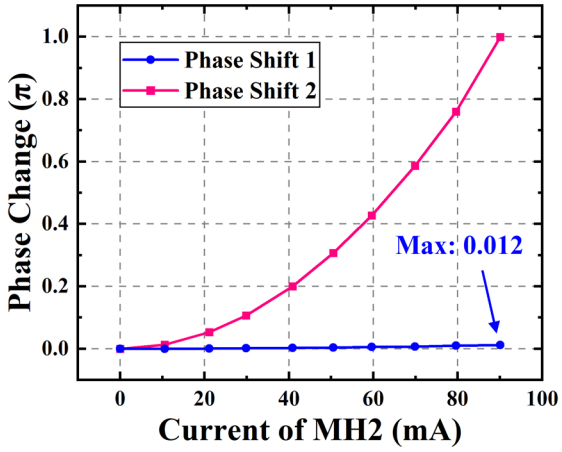

Fig. 6.7 PS amplitude beneath MH1 and MH2 when only MH2 is driven by an injected current.

6.3 Characterisation results

We first report measurements for the REC-modulated C-SBG PF. Figure 6.8(a) shows the transmission spectrum without current injected into the MHs. Within a 4 nm span centred on the 1553.4 nm stopband, two passbands are observed with a Q factor of 1.48×10^4. The minus 3 dB bandwidths are 27 GHz for passband 1 and 28 GHz for passband 2. The frequency spacing is 109.2 GHz, and the ER is 17 dB, in close agreement with simulation, with balanced and consistent intensity distribution. Relative to simulation, the 3.4 nm red shift of the centre wavelength is attributed to etching the ridge waveguide to 210 nm rather than 220 nm, which increases the n_{eff} and the centre wavelength. The lower Q factor compared with lossless simulation likely arises from the finite RBW of OSA and fabrication imperfections such as ridge roughness that introduce scattering loss. The grating κ of the $+1^{st}$ order channel is 102/cm.

The tuning solutions in this section are implemented by independently driving the two MHs, which locally modify the refractive index through the TO effect and therefore change the effective phase at the embedded EPS regions. As a result, the primary response shift occurs at the passband centres rather than as a global translation of the grating stopband. This behaviour is evidenced experimentally by the negligible drift of the untuned passband when only one heater is swept, demonstrating independent dual-passband control. When the tuning drives the two passbands into proximity, or when a passband approaches the long-wavelength edge of the stopband, the effective spectral resolution can be reduced, and the passband may broaden, which allows edge-mode leakage and produces spurious peaks.

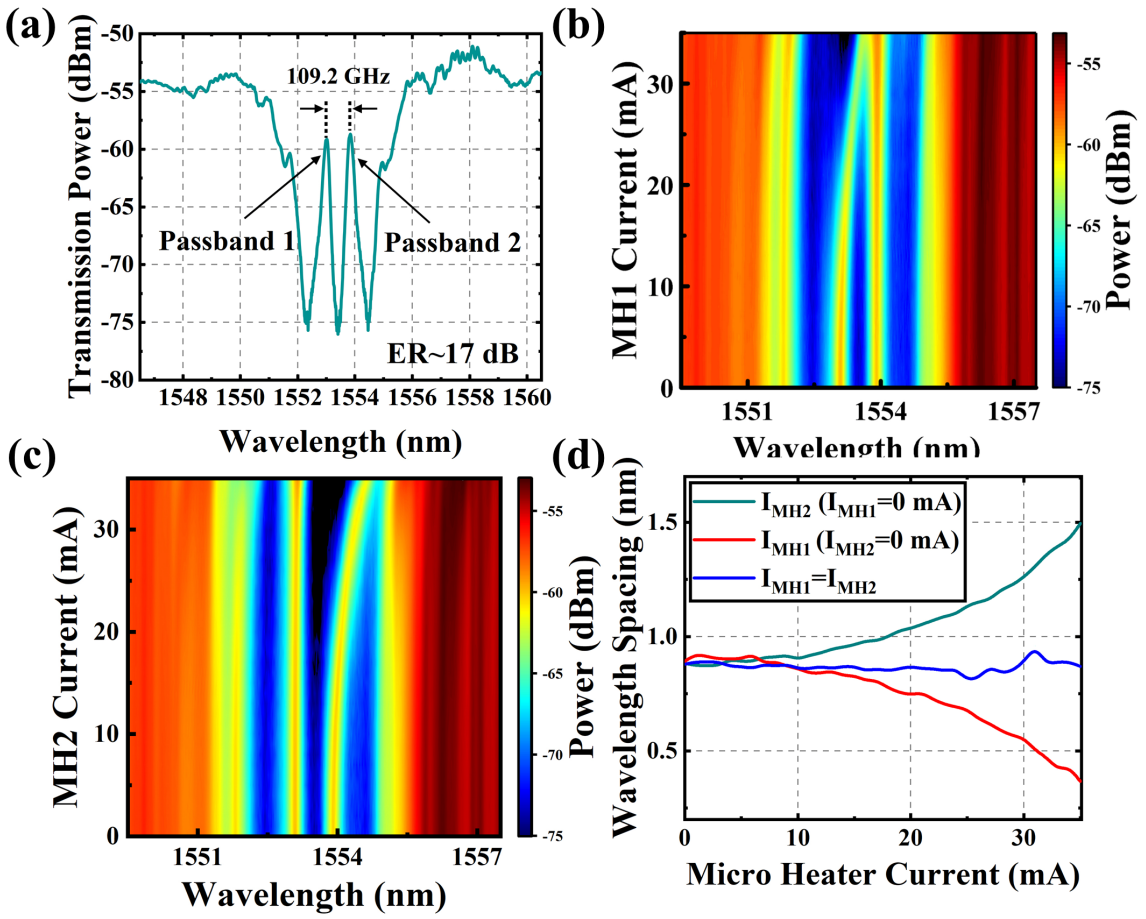

Fig. 6.8 (a) Transmission spectrum without MH current. (b) Two-dimensional spectra with only MH1 modulation. (c) Two-dimensional spectra with only MH2 modulation. (d) Passband spacing versus MH current.

Figure 6.8(b) shows 2D spectra when only I_{MH1} is scanned from 0 mA to 35 mA. The TO effect at the EPS produces a red shift of passband 1. While modulating MH1, the centre wavelength of passband 2 drifts by only 0.012 nm, which is below the OSA RBW, thereby achieving independent tuning of a single passband. The spacing changes from 109.2 GHz to 37.2 GHz. The fixed position of the stopband indicates precise alignment and geometry of the MHs with minimal residual thermal leakage. Similarly, Figure 6.8(c) shows that varying I_{MH2} enables independent tuning of passband 2. When I_{MH2} is scanned from 0 mA to 35 mA with I_{MH1} fixed at 0 mA, the spacing changes from 109.2 GHz to 186.1 GHz, while the wavelength deviation of passband 1 remains only 0.03 nm (<RBW). During this process, passband 2 maintains its narrowband character, with -3 dB bandwidth increasing slightly from 28 GHz to 29.4 GHz. Figure 6.8(d) summarises the passband spacing versus MH current from 0 mA to 35 mA, demonstrating continuous tuning from 37.2 GHz to 186.1 GHz, with excellent device repeatability and stable wavelength modulation across multiple cycles. According to the simulation in Figure 6.3(c), optimising the MH wiring to prevent breakage at higher currents beyond 35 mA could extend the tunable spacing to 259 GHz. We also

performed synchronous tuning of I_{MH1} and I_{MH2} from 0 mA to 35 mA to achieve simultaneous modulation of the two passbands while maintaining a relatively fixed spacing, which further confirms independent dual-passband control.

We conducted additional repeatability experiments with independent current modulation of MH1 and MH2 while ensuring that the MHs were not damaged at or below 35 mA. LabVIEW swept the injected current from 0 mA to 35 mA in 1 mA steps with a second dwell per step, and each experiment was repeated over ten full cycles. The results confirm excellent repeatability, stable wavelength modulation and reliable MH operation, as summarised in Figure 6.9.

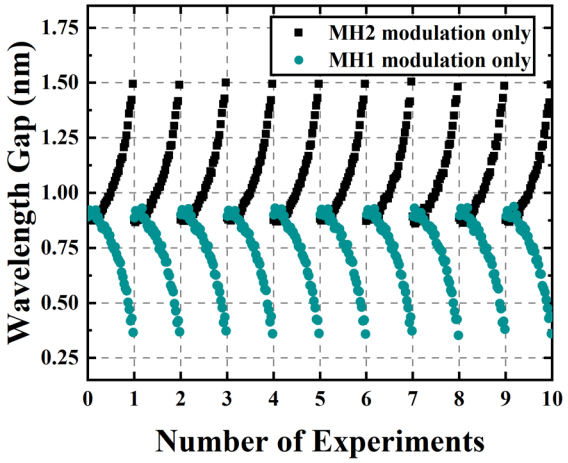

Fig. 6.9 Passband spacing as a function of repeat count in repeatability tests.

An OFC produced by a ultrafast optical clock with centre wavelength 1553.4 nm and 20 GHz FSR (Figure 6.10(a)) was also used to characterise the device. The output spectra in Figures 6.10(b) to (f) and the normalised PF transmission were obtained by adjusting the drive currents to MH1 and MH2 as indicated. The trends agree with those observed with the SLD in Figure 6.8. Specifically, when only MH1 is swept from low to high current, passband 1 approaches passband 2 and the PF spacing decreases. Conversely, sweeping only MH2 moves passband 2 away from passband 1 and the spacing increases. Five filtering configurations are shown with spacings of 60, 80, 100, 140 and 180 GHz and the corresponding I_{MH1} and I_{MH2} values. At 180 GHz, a pronounced difference in peak heights arises from an imbalance in the OFC source and asymmetry in PF transmission.

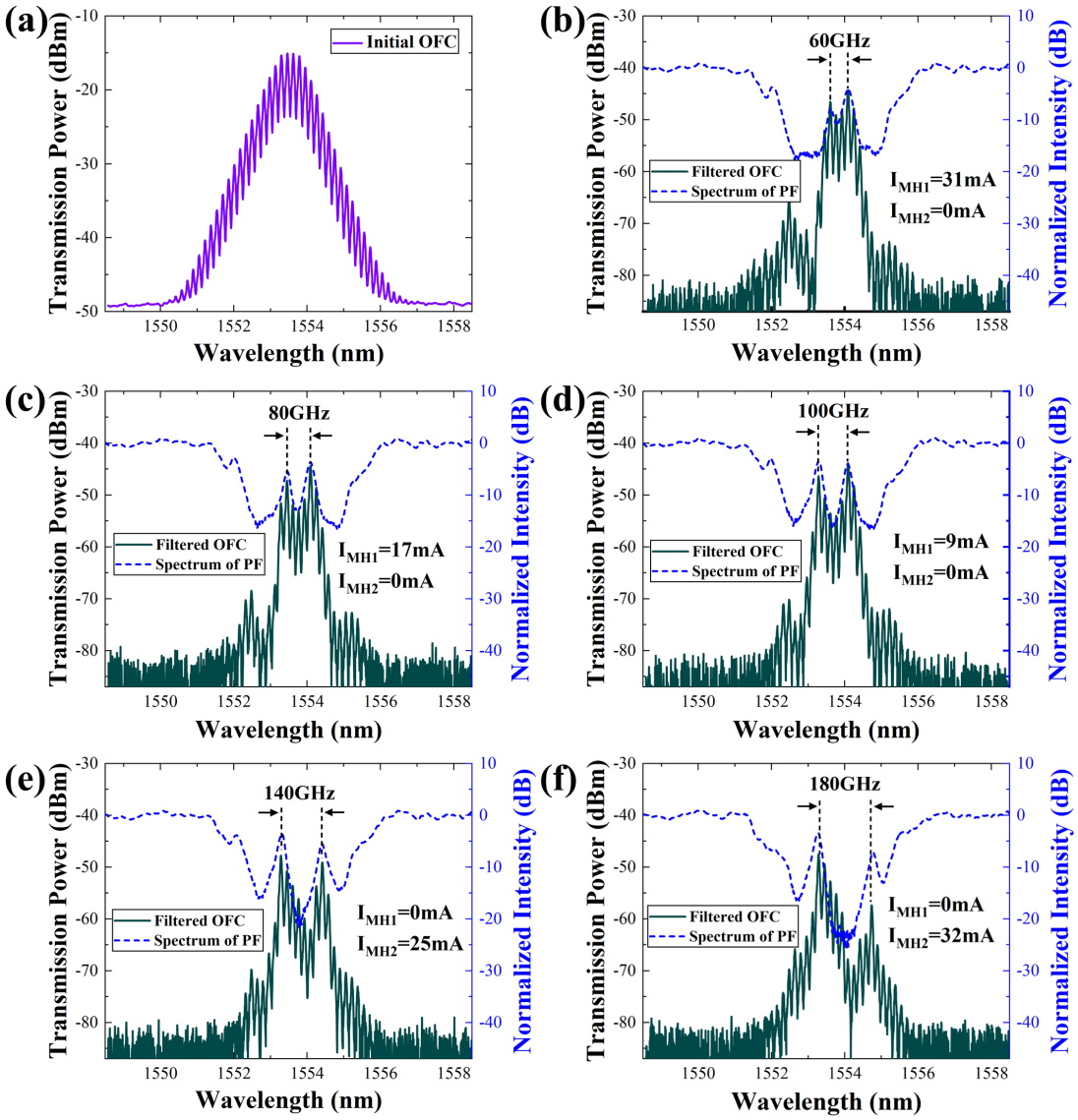

Fig. 6.10 (a) Spectrum of the unfiltered OFC. (b-f) Spectra of the OFC after filtering with spacings of 60, 80, 100, 140 and 180 GHz, together with normalised PF transmission.

In earlier work, the C-SBG PF achieved high ER and a good tuning range, offering a solid basis for broadband tunable filtering. As application needs move to higher frequency, wider tuning and higher channel purity, potential limitations of the C-SBG emerge in tuning range, selectivity and compactness. To overcome these, we introduce a 4PS-SBG. By incorporating multiple PSs within a single grating cavity and optimising cavity length, the 4PS-SBG expands tuning range, improves sidelobe suppression and extinction, and significantly shortens the cavity. This raises integration density and improves spectral characteristics, paving the way for high-performance microwave-photonic and OFD applications.

Figure 6.11(a) shows 2D spectra when only I_{MH1} is scanned from 0 mA to 85 mA for the 4PS-SBG PF. At 0 mA, two passbands are evident within a 7.5 nm span centred on the stopband at 1534.9 nm, with a Q factor of 1.18×10^4 and a spacing of 216.3 GHz, in close

agreement with simulation and with balanced intensity. Relative to simulation, the 4.1 nm red shift of the centre wavelength is attributed to etching the ridge to 210 nm rather than 220 nm. The lower Q factor is again attributed to OSA RBW and fabrication roughness. The measured κ of the $+1^{st}$ order is 241/cm, and the propagation loss of the designed 4PS-SBG waveguide at 1550 nm is 10.9 dB/cm.

In Figure 6.11(a), scanning I_{MH1} from 0 mA to 85 mA red shifts the centre of passband 1 via the TO effect at the PS. The centre wavelength of passband two remains fixed, thereby achieving independent tuning of a single passband. The spacing changes from 216.3 GHz to 52.1 GHz. The fixed stopband position again indicates accurate MH alignment with negligible residual thermal leakage. Similarly, Figure 6.11(b) shows that scanning I_{MH2} from 0 mA to 85 mA with I_{MH1} equal to 0 mA independently tunes passband 2 and changes the spacing from 216.3 GHz to 439.5 GHz. Figure 6.12 summarises that the continuous tuning range spans 52.1 GHz to 439.5 GHz. According to the simulation in Figure 6.4, optimising the MH wiring at currents above 85 mA could extend the tunable gap to 661 GHz. Synchronous tuning of I_{MH1} and I_{MH2} from 0 mA to 85 mA was also carried out to maintain an approximately fixed spacing while translating both passbands, which confirms independent dual-passband control.

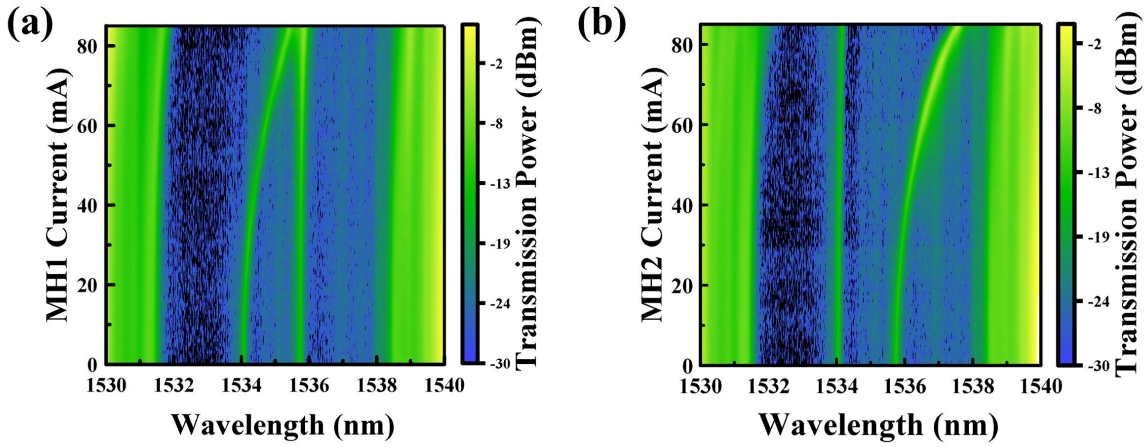

Fig. 6.11 2D optical spectra with (a) only MH1 modulation and (b) only MH2 modulation.

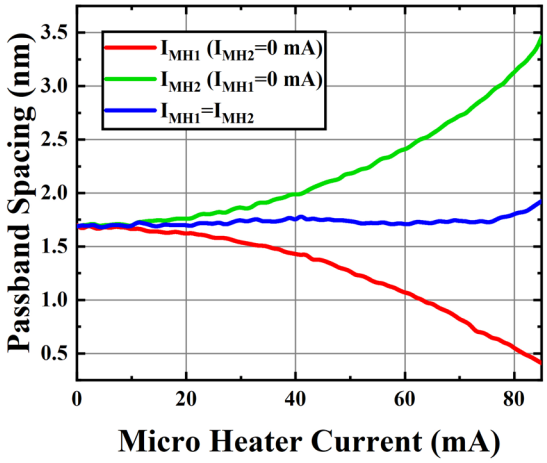

Fig. 6.12 Wavelength gap between the two passbands as a function of MH currents.

For the OFD experiments with the 4PS-SBG PF, a passive SMLL based on the AlGaInAs on InP materials system generated an OFC with 100 GHz line spacing. The isolated laser output was coupled into the PF. A DC signal from a source controller was applied to the MHs through contact pads. After polarisation adjustment by the PC, the PF output was sent to the OSA. The output spectra in Figures 6.13(a) to (d) were obtained by adjusting the MH currents as indicated. The solid blue curves are the filtered OFC spectra, and the dashed pink curves are reference spectra from an SMLL transmitted through an SOI ridge waveguide of the same length as the PF. The trends closely match those observed with the SLD in Figure 6.11. Increasing the current on MH1 moves passband 1 towards passband 2 and reduces spacing. Modulating MH2 moves passband two away from passband 1 and increases spacing. Four filtering configurations are shown with spacings of 100, 200, 300 and 400 GHz and the corresponding I_{MH1} and I_{MH2} values. In Figure 6.13(a), side modes appear near the desired main mode because at 100 GHz spacing, passband 1 approaches passband 2 and partially overlaps, reducing the Q factor and allowing side-mode leakage into the main window. A similar effect is seen in Figure 6.13(d), where passband 2 exhibits a wider bandwidth when it lies near the long-wavelength edge of the grating stopband, reducing suppression of edge modes. The most direct mitigation is to increase the grating κ to raise the passband resolution. At 200 GHz spacing, the maximum SMSR exceeds 10 dB. The minimum measured PF insertion loss is 0.85 dB at wavelength 1536.5 nm.

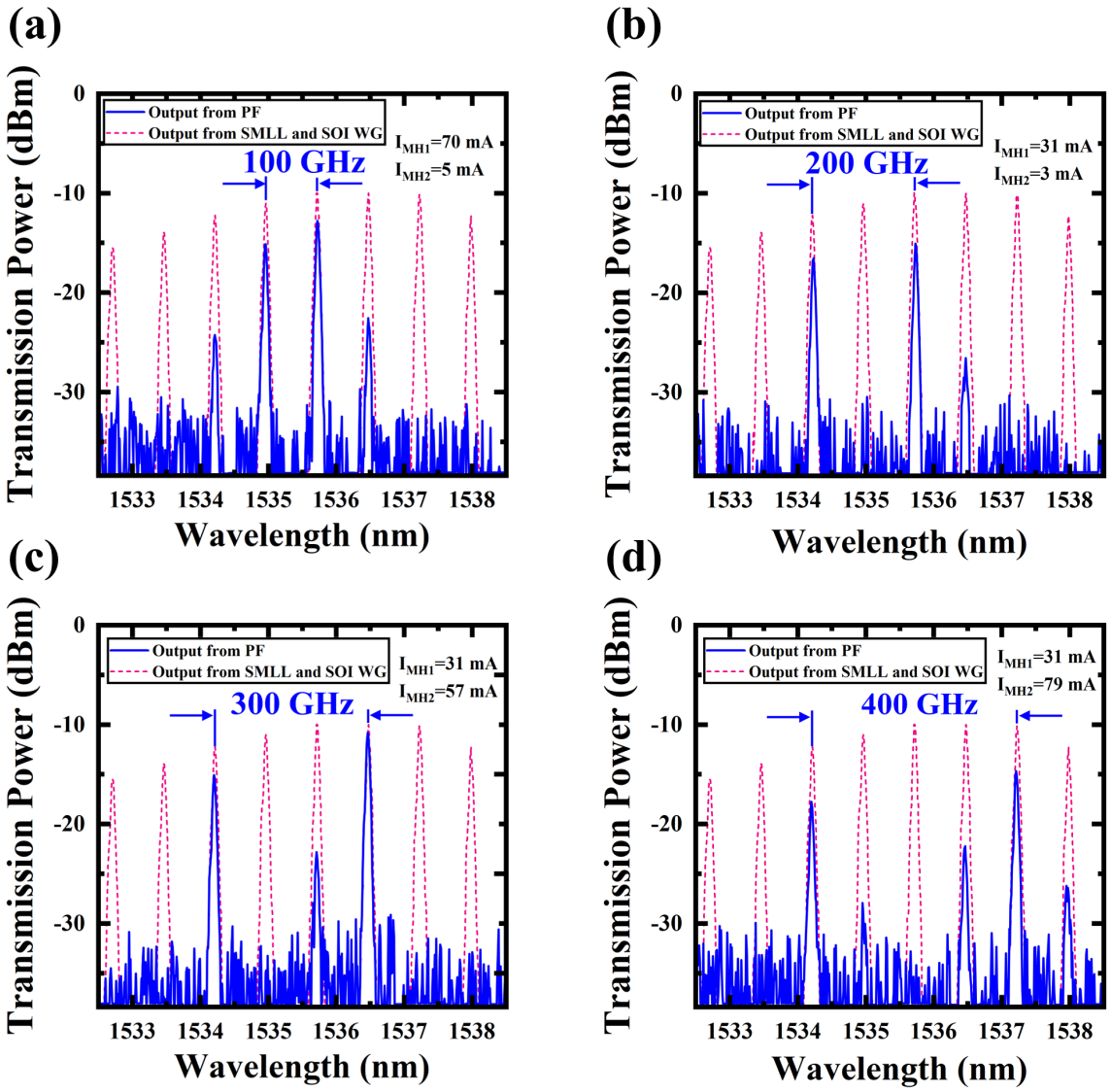

Fig. 6.13 Output spectrum of the OFC from the SMLL and SOI ridge waveguide, and the OFC filtered by the PF with spacings of (a) 100 GHz, (b) 200 GHz, (c) 300 GHz and (d) 400 GHz.

Figures 6.13(a) and (d) appear to show multiple peaks. To clarify, Figure 6.14 plots the normalised single-passband modulation spectrum with the input SMLL spectrum as reference. In Figure 6.14, I_{MH1} is 70 mA, and the spectral response of passband 1 is plotted in black. Compared with the unmodulated case plotted in red, passband 1 approaches passband 2 and the two begin to merge, which increases both Q factor and bandwidth. The reduced resolution lowers suppression of edge modes, and in Figure 6.13(a), two spurious peaks appear near the main mode. In Figure 6.13(d), injecting 79 mA into MH2 red shifts passband 2. As passband 2 approaches the long-wavelength edge of the grating stopband, its bandwidth increases because group delay is larger near the edge at long wavelengths, which raises dispersion and broadens the transmitted peak. Edge modes then leak into the passband 2 window, producing two distinct spurious peaks near passband 2.

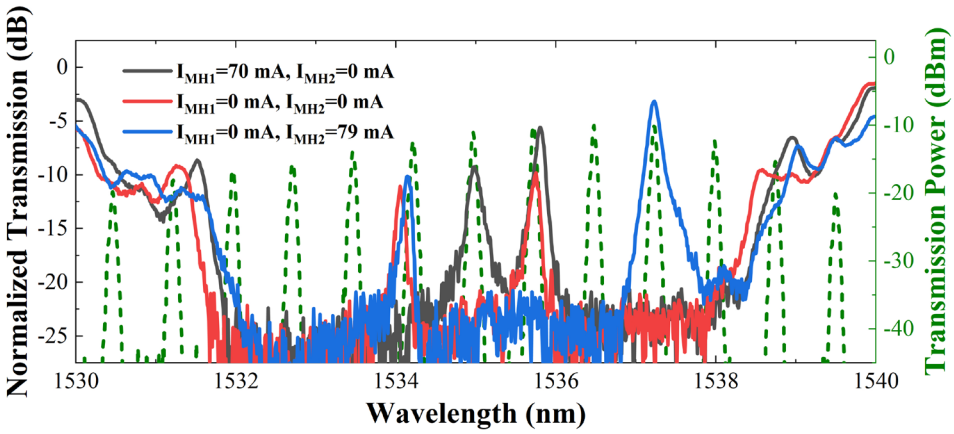

Fig. 6.14 Comparison between the normalised transmission of the filter under different current settings and the OFC from the SMLL and SOI ridge waveguide.

Replacing the C-SBG with the 4PS-SBG yields significant improvements in multiple performance metrics, with gains of up to a factor of two in some cases. In SLD-based continuous-tuning experiments, the continuous tuning range expands from 37.2 to 186.1 GHz to 52.1 to 439.5 GHz, a near 2.36-fold increase, which enables processing across wider microwave and terahertz bands. The ER rises from 25.7 dB to 29.5 dB, an improvement of about 3.8 dB. The stopband width grows from 4 nm to 7.5 nm, roughly a 1.88-fold increase, which benefits filtering with broadband sources. Meanwhile, the -3dB bandwidth narrows from 29.4 GHz to 16 GHz, a reduction of about 45.6%, improving frequency selectivity and channel isolation. In OFD tests, the SMSR increases from about 5 dB to about 10 dB, improving channel purity and system SNR. Notably, the L shortens from about 700 μm to about 300 μm, reducing size to roughly 43% of the former value and thereby raising integration density while lowering delay and power.

6.4 Chapter summary

This chapter has presented two dual-passband PFs based on equivalent-chirp modulation and sampled Bragg grating design. We detailed the operating principle, structural design, transfer-matrix verification, fabrication and experimental characterisation to achieve high-performance, wide-tuning and integrable on-chip filtering. Combined with an SMLL-generated OFC, the filter enables microwave frequency synthesis from tens to hundreds of GHz, meeting demands for multi-channel, high-purity signals in high-frequency communications and sensing.

Structurally, a C-SBG with two π EPSs achieves independent thermal tuning of two passband centres via integrated MHs, with passband spacing adjustable from 37.2 GHz to

186.1 GHz. Introducing a 4PS-SBG significantly raises κ and sidelobe suppression, extends spacing to 52.1 to 439.5 GHz, narrows passband bandwidth, lowers insertion loss and shrinks cavity size, thereby improving spectral selectivity and integration potential.

In addition to the spectral metrics, the proposed REC-based grating-waveguide PFs offer clear system-level advantages in footprint, power consumption, and scalability relative to representative state-of-the-art line-selection solutions. In terms of footprint, the filtering function is realised within a single grating cavity, with a cavity length of 670 μm for the C-SBG and only 300 μm for the 4PS-SBG, while simultaneously improving selectivity and tuning span. Electrically, dual-passband programmability is achieved using only two localised MHs, enabling independent control of two passband centres without the proliferation of resonators or multi-stage interferometric sections; in the C-SBG device, each heater exhibits a resistance of 10.7 Ω and is operated within 0-35 mA in the experiments, implying a per-heater electrical power on the order of 0-13 mW during tuning, with no requirement for high-power external EO modulation. From a scalability perspective, the measured thermal crosstalk remains low (approximately 0.9-1.2% in the presented configurations), supporting dense placement of multiple programmable filter units and extension towards higher channel counts through additional PS sections and heater pixels, while maintaining a compact and fabrication-tolerant SOI-compatible footprint.

We further described the extensive measurements with continuous sources and OFC sources. The results demonstrate excellent repeatability and performance in tuning range, Q factor, ER, SMSR and compactness. The 4PS-SBG retains precise dual-passband control while realising higher Q factor, shorter cavity and cleaner spectra, and thus offers a sturdy foundation for OFD, multi-channel processing and high-density integration in the next generation of MWP.

7 Reconfigurable and programmable multi-passband photonic filter

Driven by optical I/O interfaces for data-centre interconnect and high-performance computing, together with elastic optical networks, the demand for on-chip programmable optical processing continues to increase. Bragg gratings, owing to compact geometry, low loss and strong selectivity, are among the most fundamental filtering units in photonic integration. In conventional implementations, the refractive index modulation is fixed after fabrication, which makes it difficult to realise run-time programming of spectral profile, phase and inter-band spacing while preserving low insertion loss. This tension constrains scalability for flexible multiplexing and signal shaping on a chip. In response, the research community has explored the concept of a reconfigurable grating so that the spectral response of the filter is no longer fixed at design time but can instead be programmed during operation while maintaining integration density and line rate processing.

This chapter advances an on-chip reconfigurable PF tailored to multi-channel programmable OFD. The device is realised on a SiNOI platform and employs a 4PS-SBG with the REC technique. MHs located at the PS positions provide programmable control of spectral shape and independent tuning of each passband through the TO effect. We present the operating mechanism, structural design and together with the characterisation results. Static and programmable spectral characteristics are measured and analysed, and OFC based experiments demonstrate multi-channel selection with flexible control of passband spacing.[3]

This chapter constitutes the programmable endpoint of the filtering theme of this thesis. Whereas conventional Bragg grating photonic filters provide a fixed spectral response after fabrication, many target applications in optical I/O, elastic optical networks and DWDM require dynamic control of passband number, spacing and spectral shape. By combining REC with a 4PS-SBG and an integrated MH array, the device presented in this chapter enables run-time reconfiguration among multi-passband and band stop modes, together with wide range tuning of inter-band spacing for optical frequency division. The chapter, therefore, links the thesis-level device physics and fabrication constraints to system-facing programmability and scalable on-chip spectral processing.

[3] Parts of this chapter have been published previously in: S. Zhu *et al*., *Nanophotonics*, **14**(15), 2619-2631 (2025).

7.1 Working principle

In high-speed optical interconnects, reconfigurable optical networks and EON, an on-chip PF must provide high selectivity and low loss together with dynamic adjustment of channel count, band spacing and spectral shape to meet time-varying configuration and multi-functional signal processing requirements. However, after fabrication, the refractive index modulation and structural period of a conventional Bragg grating filter are fixed, which precludes dynamic programmability. We therefore propose an on-chip reconfigurable PF based on equivalent chirp and a 4PS-SBG structure. Combined with TO modulation, the device enables flexible switching among multiple operating modes and channels and supports tunable passband spacing, thereby raising adaptability and functional density in photonic integrated systems.

The device core is a 4PS-SBG implemented on the SiNOI platform. To obtain higher κ, a broader stopband and stronger tunability, four $\pi/2$ PSs are inserted uniformly within each sampling period P, and four 0.7π PS points are embedded across the grating cavity. Four transmission peaks are thereby formed in the $+1^{st}$ sub-grating channel, each corresponding to a DFB-type resonant cavity centred at the standing wave mode of the PS positions.

To overcome the mutual coupling between channels in a uniform multi-PSs grating, which prevents independent tuning, we introduce the REC technique. By accurately distributing the P along the propagation direction, the reflection locations for different wavelengths are separated longitudinally within the grating. The standing wave regions associated with different transmission passbands are thus spatially decoupled, which reduces inter-channel interaction, enhances the independence of phase tuning, and broadens the tuning range while retaining a compact cavity. An equivalent chirp differs from a physical chirp structure in that it does not change the lithographic period of the recess. Instead, a reconstruction of the refractive index profile is used to engineer the desired group-delay distribution. This avoids aspect ratio-dependent etching effects and confers advantages in fabrication feasibility, tuning flexibility and phase control precision.

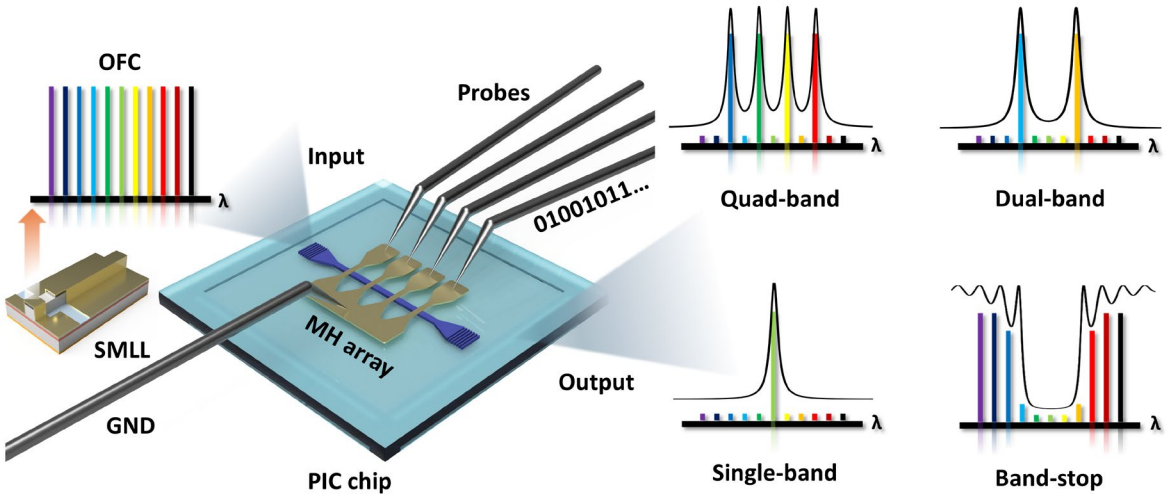

Fig. 7.1 Conceptual schematic of the on-chip reconfigurable and programmable photonic filter, illustrating quad-band, dual-band, single-band, and band-stop operation modes.

A highly integrated MH is placed above each PS location. The four parallel MHs form a heater matrix. A common ground plane beneath connects to a ground electrode through a probe, and local refractive index control is affected via the TO mechanism. In a Bragg grating with PSs, the stopband centre is determined by the grating period and refractive index distribution, whereas the positions of narrow passbands within the stopband are governed by the equivalent optical path at the PSs. When a DC is applied to one MH, the local temperature rises, which increases the refractive index and red shifts the wavelength that meets the new Bragg condition. Because equivalent chirp spatially separates the reflection regions of each passband, thermal tuning at a given PS acts mainly on its targeted passband with strong optical isolation. Experimentally, this appears as continuous tuning of the target passband over several hundred GHz while non-target passbands drift by far less than twice the RBW of the OSA. As the MHs are confined to the PS sections, the n_{eff} and period distribution of the overall Bragg structure are barely perturbed, so the stopband centre remains essentially fixed.

Besides single MH tuning, the device supports cooperative multi-MH tuning. When identical thermal modulation is applied to multiple PS regions, the entire transmission spectrum translates while the passband spacing remains unchanged. Applying different power ratios to distinct PS regions adjusts the spacing and may even alter the number of passbands. For example, excessive heating of a PS section increases the optical path length. When the accumulated phase reaches 2.0π, the PS modulation cancels, and the structure behaves as a uniform grating without PS, which provides an effective passband switching function. The default operating mode is quad-band. Driving three PS regions to high current yields a

single-band. Selecting and tuning two PS regions produces a dual-band. Turning off all PSs realises a band-stop filter. Mode switching is purely electrical and governed by TO dynamics, typically on the μs scale, with high repeatability and stability.

As shown in Figure 7.1, different tuning modes map naturally to different applications and OFC selection strategies. A single-band setup suits narrowband channel selection in RoF, single-frequency laser filtering and intrinsic optical generation, where strong channel selectivity suppresses adjacent channel interference. A dual-band mode serves MWP frequency difference generation, dual wavelength beating and dual frequency radar transmission, with comb spacing chosen to match the required frequency steps. A quad-band configuration is tailored to multi-channel simultaneous transmission, photonic multibeam radar and parallel signal processing, increasing the degree of parallelism in orthogonal frequency-division multiplexing and DWDM. A band-stop mode is useful for spectral suppression, such as removing selected comb lines during comb shaping, interference rejection or spectral isolation.

Through the combined design of SBG, multiple PSs, REC technique and TO modulation, the device delivers high integration, rapid mode switching and tunable interband spacing with high SMSR. It realises fast programmable switching among single-band, dual-band, quad-band and band-stop spectral shapes and supports dynamic adjustment of channel spacing over several hundred GHz. These features provide a flexible filtering core for EON and on-chip OFD systems. Subsequent sections present the structural design methodology, chirp reconstruction strategy and MH layout optimisation, and further explore the applications of the device in DWDM and on-chip programmable optical signal processing.

7.2 Design and simulation results

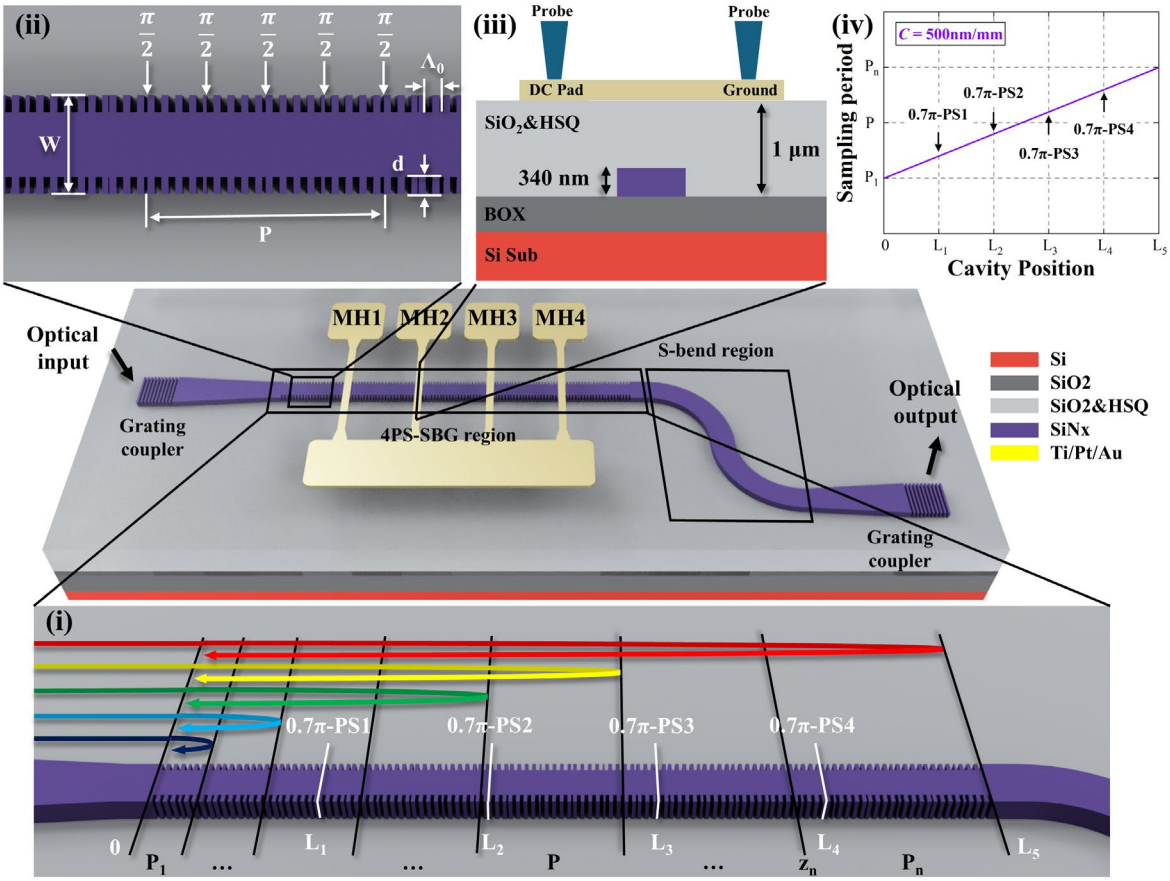

Fig. 7.2 Schematic of the PF with GCs, the 4PS SBG waveguide and MHs. (i) Grating waveguide within the PF. (ii) Magnified view of the 4PS-SBG. (iii) Cross-section of the PF at the MH positions. (iv) P distribution along the grating cavity.

Uniform insertion of four PSs into an SBG produces four transmission peaks within the +1st order stopband. However, in a uniform grating, the DFB behaviour causes these passbands to share a common cavity and to couple to one another, which suppresses independent tuning. To address this, we adopt a linearly equivalent chirped grating that integrates multiple PSs. The design generates specific reflection positions within the grating so that wavelengths near the Bragg condition are reflected at distinct locations. As in the previous Chapter 6, equivalent chirp spatially decouples photon interactions among the PS cavities, enabling independent control of each resonance. The 4PS-SBG architecture shortens the cavity, increases the κ and suppresses the 0th order reflection to minimise inter-band crosstalk. These properties improve phase matching at detuned wavelengths and reduce unwanted resonator interaction, thereby enhancing the independence of bandwidth tuning for each passband.

The chirped modulation grating supports photon isolation among bands, broadens the stopband and provides a wider tuning bandwidth. From a manufacturing perspective, the

REC technique improves phase accuracy by roughly two orders of magnitude compared with direct modulation of the seed grating, thereby ensuring precise wavelength control of the passbands.

The PF integrates two GCs, a linearly equivalent chirped 4PS-SBG waveguide, an output S bend, the two GCs located at both ends and four MHs labelled MH1 to MH4. The MHs lie above the PS points and are independently addressable through strategically placed electrodes that also ensure electrical isolation and prevent current crosstalk. Applying a DC to any MH changes the local refractive index through the TO effect and thereby adjusts the local PS amplitude. Integrated MHs are employed for thermal tuning because, compared with selectively doped resistive heaters, they offer simpler fabrication and higher yield, together with lower power consumption and superior thermal isolation. Each MH is realised as a NiCr, Pt and Au stack with a total thickness of 0.23 μm. NiCr provides adhesion and initial resistive heating owing to its high resistivity, Pt raises heating efficiency, and Au offers oxidation resistance. The heating track is 3 μm wide. After fabrication, the resistance of a single heating track measured at room temperature is 27.1 Ω. COMSOL simulations confirm that thermal crosstalk and drift are negligible for this geometry. By programming the current distribution across the MHs, one can reconfigure the n_{eff} modulation in the grating and produce diverse spectral responses. Although metal films can perturb the local refractive index and add absorption loss to the evanescent field, the films cover only a narrow region above the waveguide, so the effect is negligible.

A linearly chirped 4PS SBG with four 0.7π PSs is used. Although a 1.0π PS is commonly adopted in single-channel filters for uniform side-mode suppression, using four 0.7π PSs shifts the passbands slightly toward shorter wavelength and yields modestly non-uniform peak intensities compared with 1.0π. These offsets intentionally fill a modulation gap on the short-wavelength side of PB1 and thus extend the wavelength-tuning range without sacrificing SMSR. The linear-frequency P distribution still obeys the pre-mentioned equation (6.1).

Figure 7.2(i) and (ii) illustrate the P distribution along the grating cavity. The seed grating operates at a Bragg wavelength of 1650 nm with seed period Λ_0 = 523 nm, ridge width W = 1.2 μm and recess depth d = 70 nm. To realise transmission peaks at 1547.2, 1548.4, 1549.5 and 1550.7 nm, the average P is 7.718 μm, and the chirp rate C is 500 nm/mm. Under these conditions, the centre wavelength of the $+1^{st}$ sub-grating of the equivalent-chirped 4PS-SBG is 1554.5 nm.

Figure 7.2(iii) presents a cross-sectional view of the grating waveguide. The MHs are fabricated on the surface of a 1 μm thick cladding formed by PECVD of SiO_2 together with HSQ. In Figure 7.2(iv), the positions of the 0.7π PSs are marked as L_1, L_2, L_3 and L_4 with end points labelled 0 and L_5 at 190, 380, 570, 760 and 950 μm, respectively.

Optical characteristics—including transmission (lower half of Figure 7.3), reflection (upper half of Figure 7.3), and group delay (Figure 7.4)—were calculated using the TMM. The calculated spectra reveal four pronounced transmission peaks within the stopband, labelled PB1 to PB4. The photon distributions (Figure 7.5) along the cavity demonstrate effective spatial separation of the modal fields, which markedly reduces cross-interference and ensures the independence and stability of each passband.

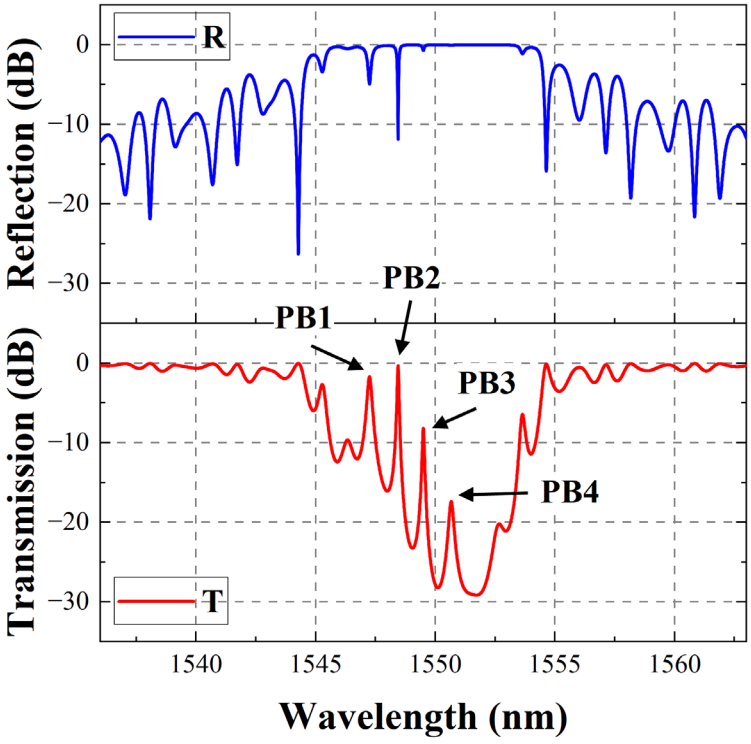

Fig. 7.3 Simulated reflection shown in blue and transmission shown in red for the linearly chirped 4PS-SBG with four 0.7π PSs.

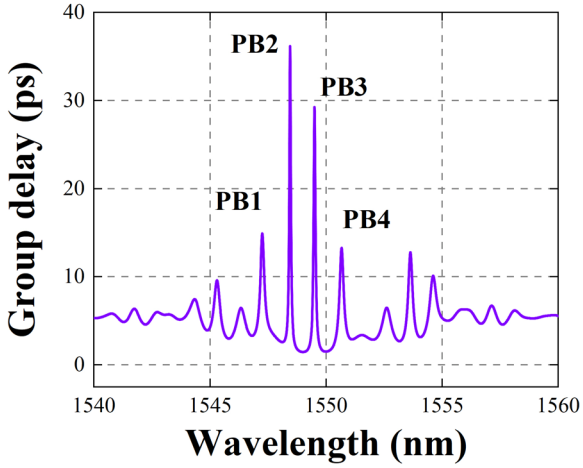

Fig.7.4 Simulated group-delay spectrum.

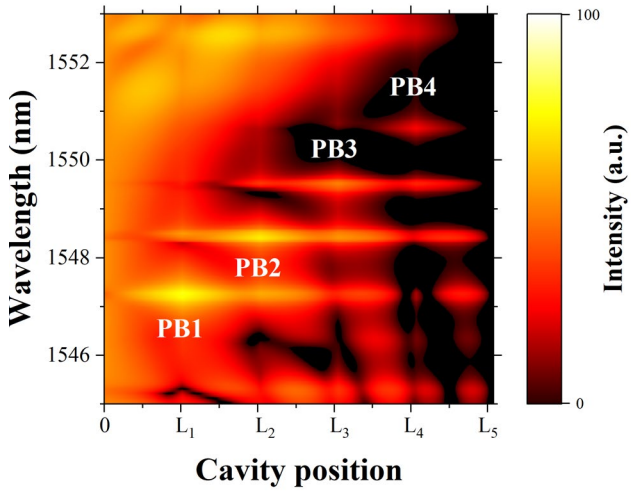

Fig. 7.5 Simulated photon distribution along the cavity of the four 0.7π PSs 4PS-SBG.

In arrays of multiple MHs, thermal drift and thermal crosstalk are critical because the heat used to tune the local refractive index may diffuse into adjacent sections and cause unintended spectral shifts. Thermal drift undermines long-term stability, and thermal crosstalk degrades independent control among channels. We therefore carried out detailed thermal simulations using COMSOL. As shown in Figure 7.6, we activated MH1 only, then MH1 to MH2, then MH1 to MH3 and finally all four MHs to analyse the resulting temperature distributions. Slight interactions are present. For example, when keeping MH1 active and injecting 50 mA to MH2, the peak temperature of MH1 rises from 325 K to 328 K. Similar small cumulative effects are observed in subsequent cases, with increments of only a few K.

Two factors limit the impact of these drifts. First, heat generated by an MH must pass through the upper cladding to reach the buried waveguide. The cladding has low thermal conductivity

and considerable thickness, so vertical thermal conduction is inefficient, and the waveguide core experiences only small temperature changes. Second, the waveguide platform is Si_3N_4, whose TO coefficient is much smaller than that of Si. Temperature fluctuations of just a few kelvins induce only minor changes in the effective index, resulting in a negligible impact on the spectral response.

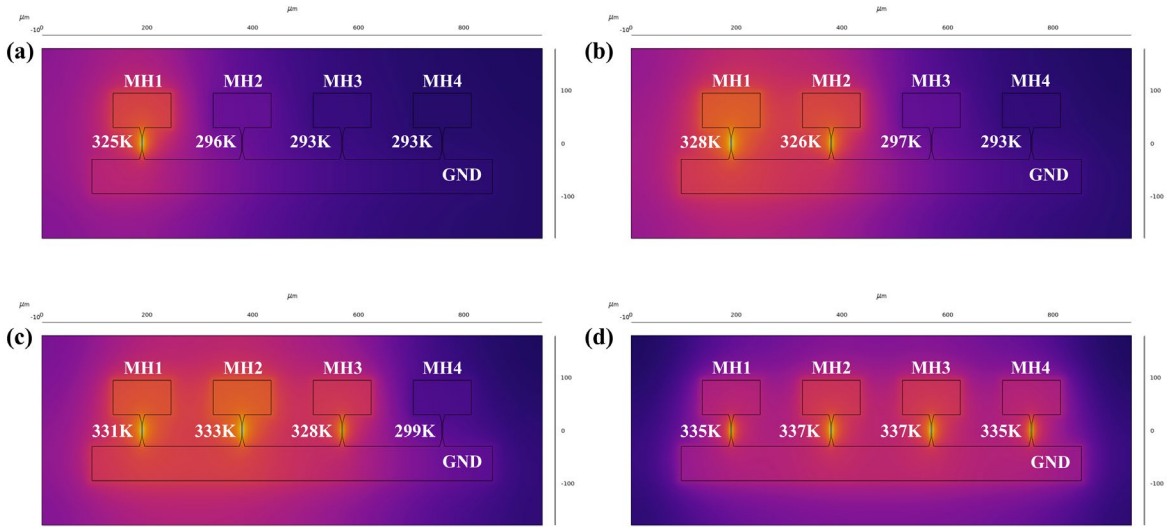

Fig. 7.6 Simulated surface-temperature distributions when (a) only MH1 is active, when (b) MH1 and MH2 are active, when (c) MH1 to MH3 are active and when (d) all four MHs are active.

To quantify crosstalk, we biased only one MH at a time. In Figure 7.7(a), when MH1 alone is active, MH2, MH3 and MH4 remain at nearly constant temperature while MH1 exhibits pronounced local heating. Assuming ideal vertical conduction at the PS points, the Si_3N_4 waveguides beneath inactive heaters remain unchanged in temperature, and heat from the active heater transfers vertically through the Si_3N_4 with minimal lateral diffusion. Figure 7.7(b) reports the PS amplitudes at all four PS points as a function of injected current when only MH1 is biased. At 97 mA, PS1 reaches a phase change of π while the non-target PS amplitude changes by only 0.043π. Defining thermal crosstalk as the ratio of unintended phase change beneath an inactive heater to the phase change beneath the active heater, the lowest crosstalk observed is 4.3%, indicating strong thermal isolation over the 190 µm spacing between phase shifters. Similar behaviour is observed when the other MHs are driven independently. In all cases, the crosstalk is below 10%, with a maximum measured value of 6.9% between MH4 and PS2.

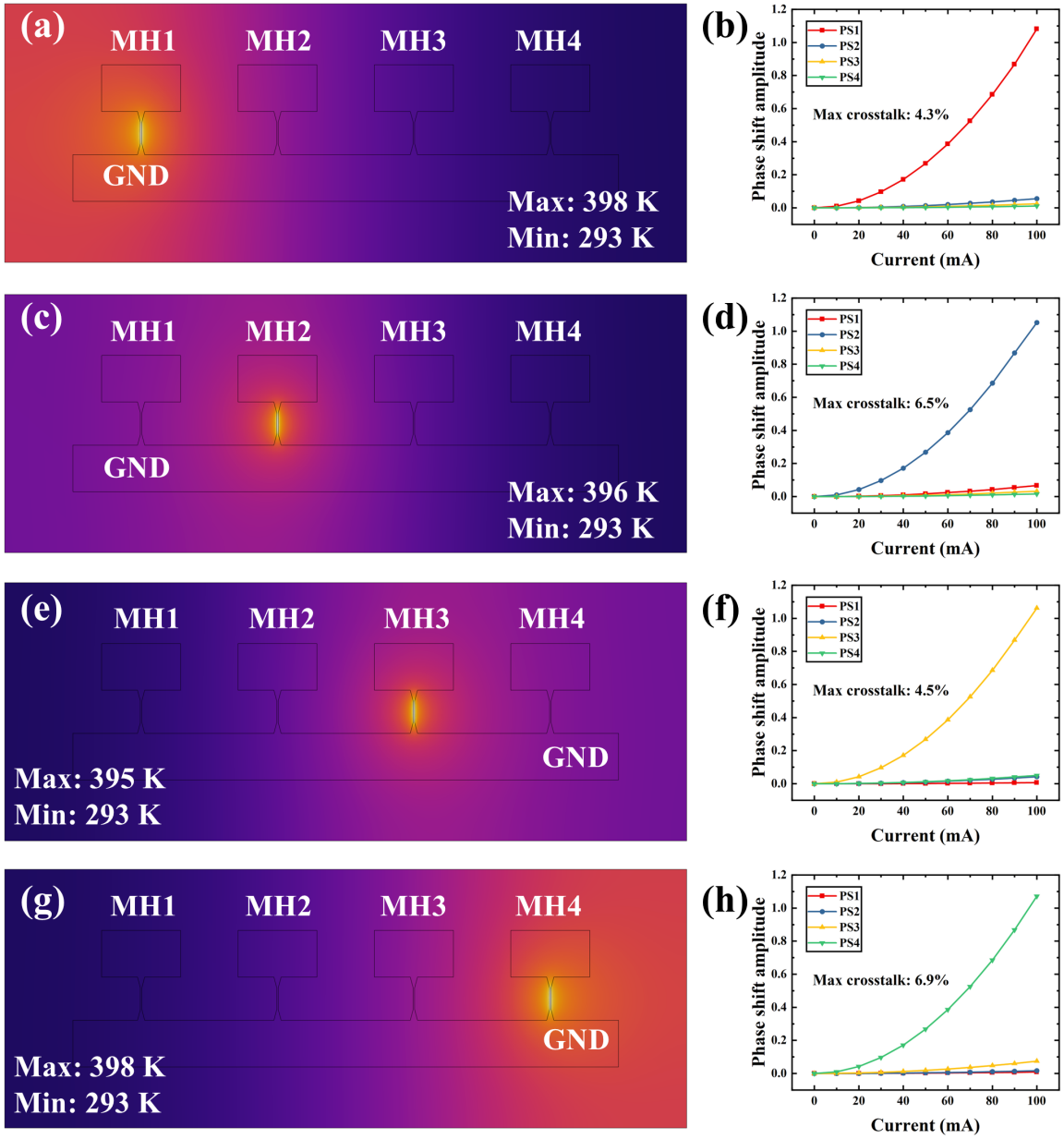

Fig. 7.7 Simulated temperature distributions when only (a) MH1, (c) MH2, (e) MH3 and (g) MH4 are active, and PS amplitudes versus current when only (b) MH1, (d) MH2, (f) MH3 and (h) MH4 are driven, respectively.

These results confirm that PS noise arising from thermal leakage between adjacent PSs is negligible, enabling each MH to independently modulate its corresponding phase shifter. This capability underscores the device's precision and efficacy in applications demanding meticulous thermal management and phase control, such as advanced photonic circuits where precise optical signal modulation is paramount. This configuration demonstrates the efficacy of our approach in integrating robust, efficient MHs into photonic devices, ensuring precise control over PSs while maintaining high performance and structural integrity.

7.3 Characterisation results

We first analyse the PF passband windows and static characteristics using the SLD as the source, with the laboratory held at 20 ºC. Static transmission spectra are captured and evaluated on the OSA. As shown by the blue solid line in Figure 7.8(a), four narrow transmission peaks appear within the $+1^{st}$ stopband, which is characteristic of a multi-PS Bragg grating. The -3dB bandwidths of passbands PB1 to PB4 are 33, 21, 23 and 38 GHz, respectively. The measured frequency spacings between PB1 and PB2, PB2 and PB3 and PB3 and PB4 are 141, 116 and 140 GHz. The measured stopband centre is 1553.1 nm, which is 3.6 nm longer than the simulated value. The deviation likely arises from a slightly shallower Si_3N_4 etch depth in the dry etch step, namely 330 nm rather than the planned 340 nm. Because the initial PS amplitude is 0.7π rather than the optimum 1.0π, the peaks are not uniformly centred within the stopband. Notably, PB1 overlaps with sidelobes, producing unequal peak intensities. By fine-tuning the MH currents, we mitigate these intensity fluctuations effectively.

To illustrate the programmable spectral properties of the PF, we synchronise the injection currents to all four MHs and centre the peaks within the stopband to emulate a uniform 1.0π PS. Each MH current is set to 45 mA, as shown by the red curve in Figure 7.8(b). The new spacings between PB1 and PB2, PB2 and PB3 and PB3 and PB4 are 143, 115 and 142 GHz, and the corresponding -3 dB bandwidths are 28, 19, 19 and 27 GHz. During modulation from 0.7π to 1.0π, the spacings remain almost unchanged while the -3 dB bandwidths decrease slightly, which indicates that the four PSs operate independently and stably with improved spectral resolution. All passbands now exhibit the typical Lorentzian profile. The ERs are 15.0, 17.5, 17.4 and 16.1 dB for PB1 to PB4. As an optimisation strategy, equalisation and broadening of ER can be achieved by increasing the spacing between phase shifts or through inverse design in which ER uniformity is imposed as a constraint in the joint optimisation of the number, positions and profiles of PS elements. These methods, however, usually reduce photon independence among passbands.

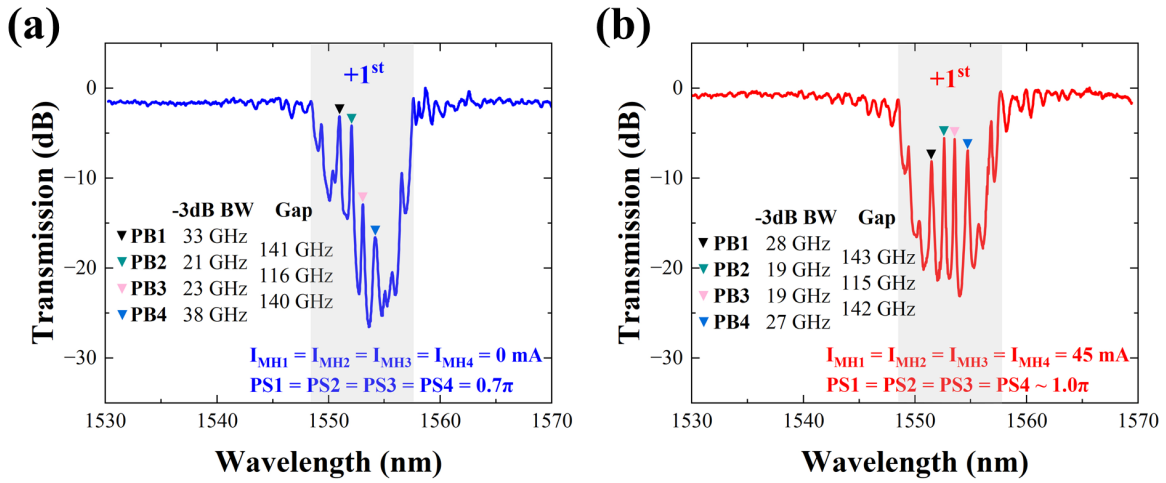

Fig. 7.8 Measured transmission spectra of the PF with all injected currents I_{MH} set to 0 mA in (a) and 45 mA in (b).

We then adjust the current at each PS point individually to examine its impact on the transmission spectrum, as shown in Figure 7.9. The experiments show that adjustment of a single PS primarily affects its own transmission peak while the overall structure of the +1st stopband remains stable. For example, in Figure 7.9(a), changing only PS1 shifts the centre frequency of PB1 by 72 GHz with negligible influence on the other peaks. The largest collateral shift is a 12 GHz change of PB3, well below twice the RBW. This confirms effective optical isolation among passbands and demonstrates independent modulation of each passband. The stopband width also remains essentially unchanged during these adjustments. Similarly, when only PS2 is adjusted as in Figure 7.9(b), PB2 shifts by 62 GHz and the largest collateral shift is 14 GHz for PB3, which is also below twice the RBW. Modulating PS3 in Figure 7.9(c) mainly affects the long wavelength side, shifting PB3 by 90 GHz and PB4 by 23 GHz, while peaks at shorter wavelengths remain stable. Modulating PS4 in Figure 7.9(d) chiefly influences PB4, which shifts by 115 GHz, with minimal influence on shorter wavelength passbands.

The single passband modulation experiments in Figures 7.9(a) to (d) show that the overall stopband structure and ER remain constant, while only the centre frequency of the targeted passband changes. This highlights the effective optical isolation among PS points and confirms independent tuning capability. Applying TO modulation simultaneously to all four PS points produces a global frequency shift of all transmission peaks rather than isolated adjustment of a single passband, as shown in Figure 7.9(e). The spacings PB1 to PB2, PB2 to PB3 and PB3 to PB4 remain at 143, 115 and 142 GHz. This indicates that coordinated multi-point modulation translates the entire spectrum without changing the relative spacings. The stopband shape remains almost unchanged, and only a slight red shift appears near the

stopband edges, together with a slight broadening of the stopband when transmission peaks approach the edges. These results confirm that the PF supports both precise single passband tuning and collective phase modulation for global spectral translation. We refer to the spectral response under these modulations as the quad-band operating mode of the PF.

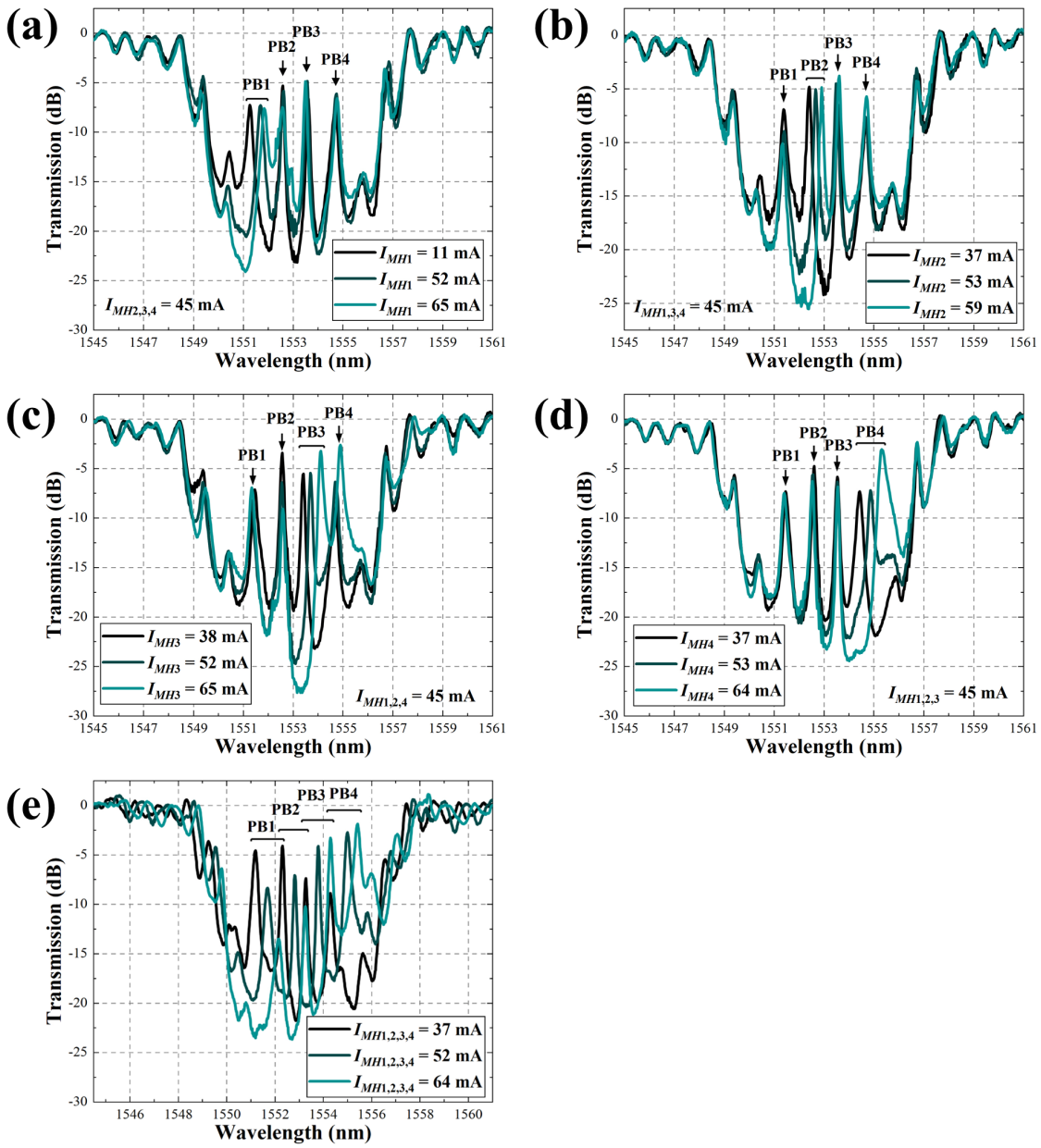

Fig. 7.9 Measured spectra of the fabricated grating PF with the SLD input under different modulation conditions: (a-d) single modulation of MH1, MH2, MH3 and MH4 in the quad-band mode and (e) simultaneous modulation of all MHs in the quad-band mode.

Dynamic selection of passbands is realised by adjusting the PS amplitudes with the MHs. Setting a PS amplitude to an integer multiple of 2.0π effectively turns that channel off. This enables dual-band and single-band filter modes. In one configuration, only PS2 and PS3 are active while the amplitudes of PS1 and PS4 are set to 2.0π. Only PB2 and PB3 then remain in the $+1^{st}$ stopband, while PB1 and PB4 redshift due to the TO effect. As PB4 red shifts, it

merges with the edge modes and passes beyond the stopband, while PB1 weakens and is gradually swallowed by the stopband. This phenomenon constitutes the dual-band mode transition.

In the experiments of Figure 7.10, we investigate the dual-band mode PF, in which only the passbands from PS2 and PS3 are active within the stopband, and the amplitudes of PS1 and PS4 are estimated to be 2.0π. In Figure 7.10(a), when only PS2 is modulated, PB2 shifts by 118 GHz and PB3 exhibits only 9 GHz of fluctuation, confirming stability. Figure 7.10(b) shows the converse, where only PS3 is modulated and PB3 shifts by 110 GHz while PB2 shifts by just 3 GHz, which is below the OSA RBW. In the coordinated modulation of Figure 7.10(c), despite modulating over a range of 112 GHz, the spacing between the two active peaks remains constant at 168 GHz, which is critical to efficient operation in a dual-band configuration. Figure 7.10(d) demonstrates precise control of currents to PS2 and PS3, realising separation of the dual passband centres from 168 GHz to 367 GHz while maintaining a fixed centre wavelength. This dynamic control of spacing highlights the advanced tuning capability achieved by managing the TO effect.

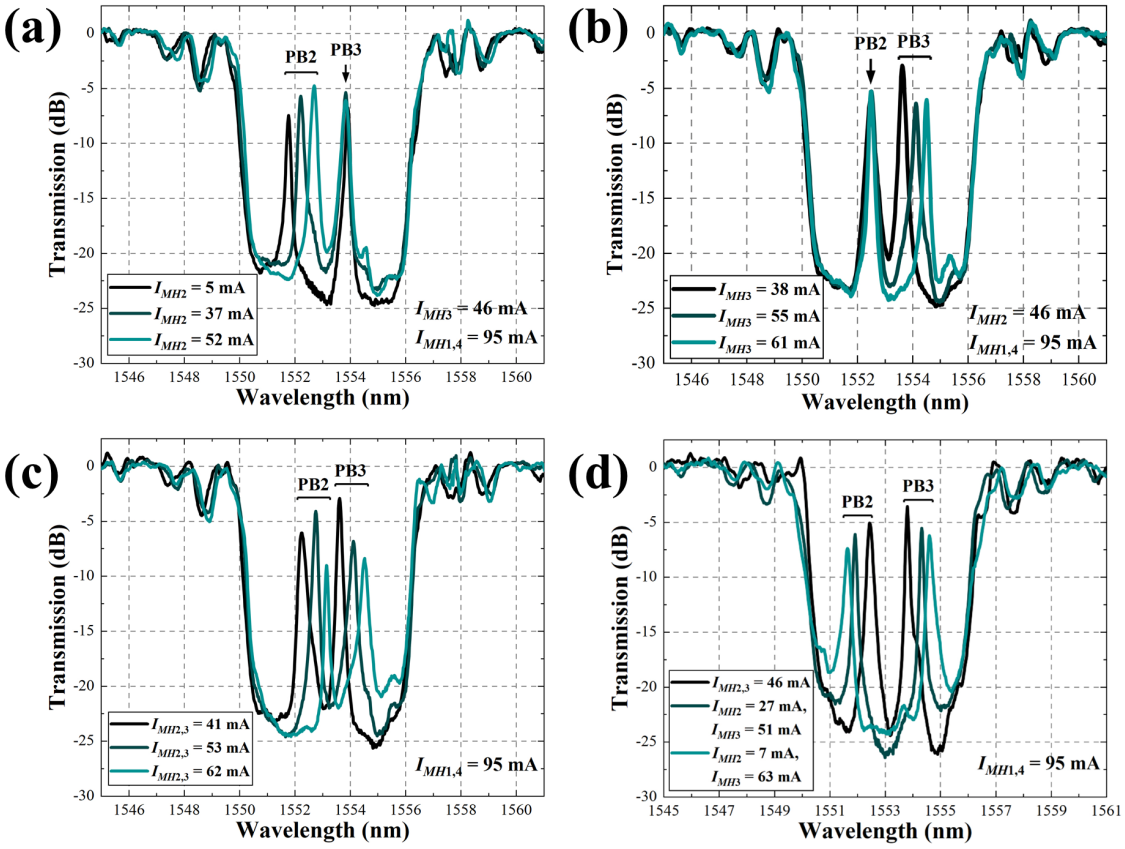

Fig. 7.10 Measured spectra of the fabricated grating PF in dual-band mode with the SLD input: (a-b) single modulation of MH2 and MH3, (c) simultaneous modulation of all MHs with constant spacing and (d) simultaneous modulation with variable spacing.

In the single-band trials of Figure 7.11(a), only PS2 is active, so that PB2 is the sole transmission peak. The results show that the PF preserves the overall stopband structure and achieves excellent single-channel filtering. By switching PS1 to PS4 in turn, the filter window can be configured flexibly across the entire stopband to realise comprehensive spectral adjustment. When all PSs are turned off, as in Figure 7.11(b), the spectral response resembles that of a normal grating stopband without PS. Compared with a uniform sampled grating, side lobes are markedly suppressed due to the chirp effect, which suppresses the side lobes in the $+1^{st}$ stopband and converts the band-pass response into a smooth band-stop response. In this configuration, the absence of a PS cavity that would otherwise accumulate energy lowers the noise floor relative to the case with active passbands, and an ER of 33 dB is achieved.

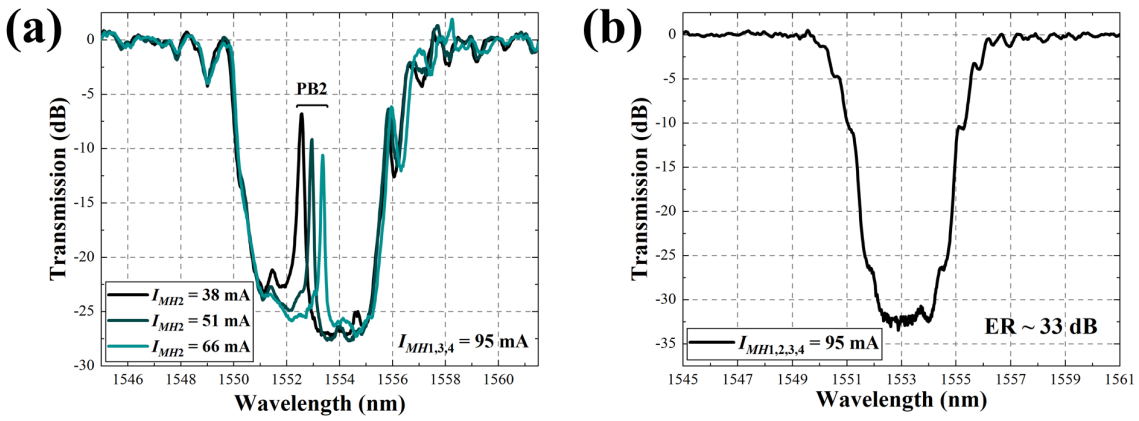

Fig. 7.11 Measured spectra of the fabricated PF: (a) single-band mode with MH2 modulation and (b) band-stop mode.

Out-of-band suppression is also a key parameter for DWDM. The values differ across operating modes. In the quad-band mode, the suppression ranges from 20.5 to 25 dB. In the dual-band mode, it ranges from 23 to 26.4 dB. In the single-band mode, it stabilises around 27.4 dB, and in the band-stop mode, the maximum suppression reaches 33 dB.

To assess repeatability, we repeatedly injected 45 mA ten times in the unmodulated state, as shown in Figure 7.12. In each iteration, the centre wavelengths of PB1, PB2, PB3 and PB4 were recorded. After ten complete modulation cycles, the centre wavelengths and spacings remained stable without notable change, which confirms excellent repeatability and reliability.

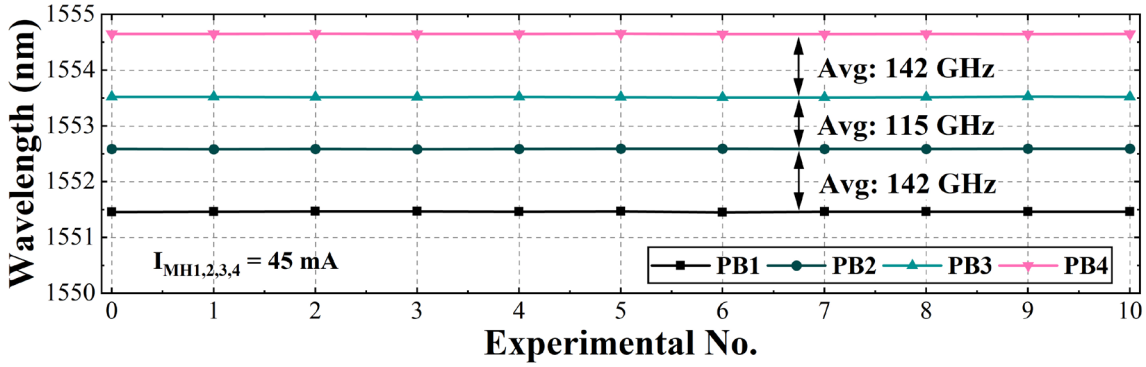

Fig. 7.12 Spectral analysis of centre-wavelength and spacing stability over ten repeated simultaneous-modulation cycles in the quad-band mode.

These experiments confirm that by independently or cooperatively modulating multiple PSs of the PF, we can control passband locations, spacings and band stop characteristics both flexibly and globally. The four PS points increase spectral complexity and programmability. The results further show that adjusting the PS amplitude allows dynamic control of the number of active passbands, realising transitions from quad-band to dual-band to single-band and even to band-stop modes.

We further analyse the modulation characteristics of the transmission spectra and the evolution of the passband windows to evaluate applicability in DWDM. In these experiments, an SMLL serves as the input source with FSR = 50 GHz and produces an evenly spaced comb. When frequency components pass through the tuned PF, selective spectral transmission and suppression shape the output comb. By programming the modulation states of different PS points, the positions and spacings of laser modes are controlled precisely, so that the input comb is dynamically reconstructed.

In Figure 7.13, grey dashed traces denote the reference signal after transmission through a SiNOI ridge waveguide of equal length, and the other traces denote the filtered outputs. In Figures 7.13(a) to (c), the PF is configured in the quad-band mode. In Figure 7.13(a), the filter transmits signals with a 150 GHz spacing, corresponding to three times the SMLL line spacing. Every 3rd SMLL comb line is selected while the others are suppressed, yielding a four-wavelength output with equal spacing. Figure 7.13(b) shows the case of 100 GHz spacing, where the adjacent selected lines are separated by 100 GHz. Figure 7.13(c) demonstrates a 50 GHz filter configuration in which the transmitted spacing matches the source FSR and unselected components remain strongly suppressed. In all these quad-band configurations, the SMSR exceeds 10 dB and meets optical network signal quality requirements. In the quad-band OFD experiments, the minimum insertion loss occurs at 50

GHz spacing, where PB2 at 1553.6 nm exhibits only 1.5 dB insertion loss. Because of the limitation of our SMLL, the minimum spectral resolution demonstrated here is 50 GHz, even though the theoretical 3 dB resolution can be as low as 19 GHz. As an optimisation, using buried gratings or SBG with the multi-phase-shift technique can improve resolution effectively.

In the dual-band experiments of Figures 7.13(d) and (e), the number of PF windows is reduced to two while preserving flexible control of spacing. In Figure 7.13(d), the spacing is 150 GHz, and in Figure 7.13(e), it is 250 GHz. These configurations demonstrate that the PF can transmit widely separated frequency components while suppressing other lines. In these dual-band configurations, the minimum insertion loss is 0.5 dB for PB3 at 1553.6 nm, and the SMSR exceeds 15 dB. Only two dual-band custom spectra are shown here at 150 and 250 GHz; in principle, the spacing can be tuned continuously from 50 to 450 GHz. This performance highlights selective transmission across different spacings while preserving high signal integrity, which is advantageous for precise optical signal processing and radio frequency transceiver tasks [98,187,188].

In the single-frequency division experiment of Figure 7.13(f), a single narrow passband is configured. Laser modes are tuned precisely to 1552.4, 1552.8 and 1553.2 nm with 50 GHz spacing. The transmitted spectrum isolates the target optical frequency and strongly suppresses other modes. Such control within a narrow band suits applications that require selective channel operation and narrowband filtering. The single frequency mode records a minimum insertion loss of 1 dB at 1552.8 nm and maintains SMSR above 15 dB.

Overall, the experiments verify that by carefully adjusting multiple PSs, either independently or cooperatively, the PF dynamically controls OFD signals. The device flexibly supports operating modes from four passbands to a single passband and achieves programmable filtering through precise phase control. The results highlight the advantages of low insertion loss and high SNR while maintaining precise spectral control, which indicates strong potential for high-speed optical communications, adaptable photonic signal processing and OFC based systems. As a potential route to further improvement, industrially mature heterogeneous integrated laser technology could be adopted to reduce insertion loss and improve associated metrics [189].

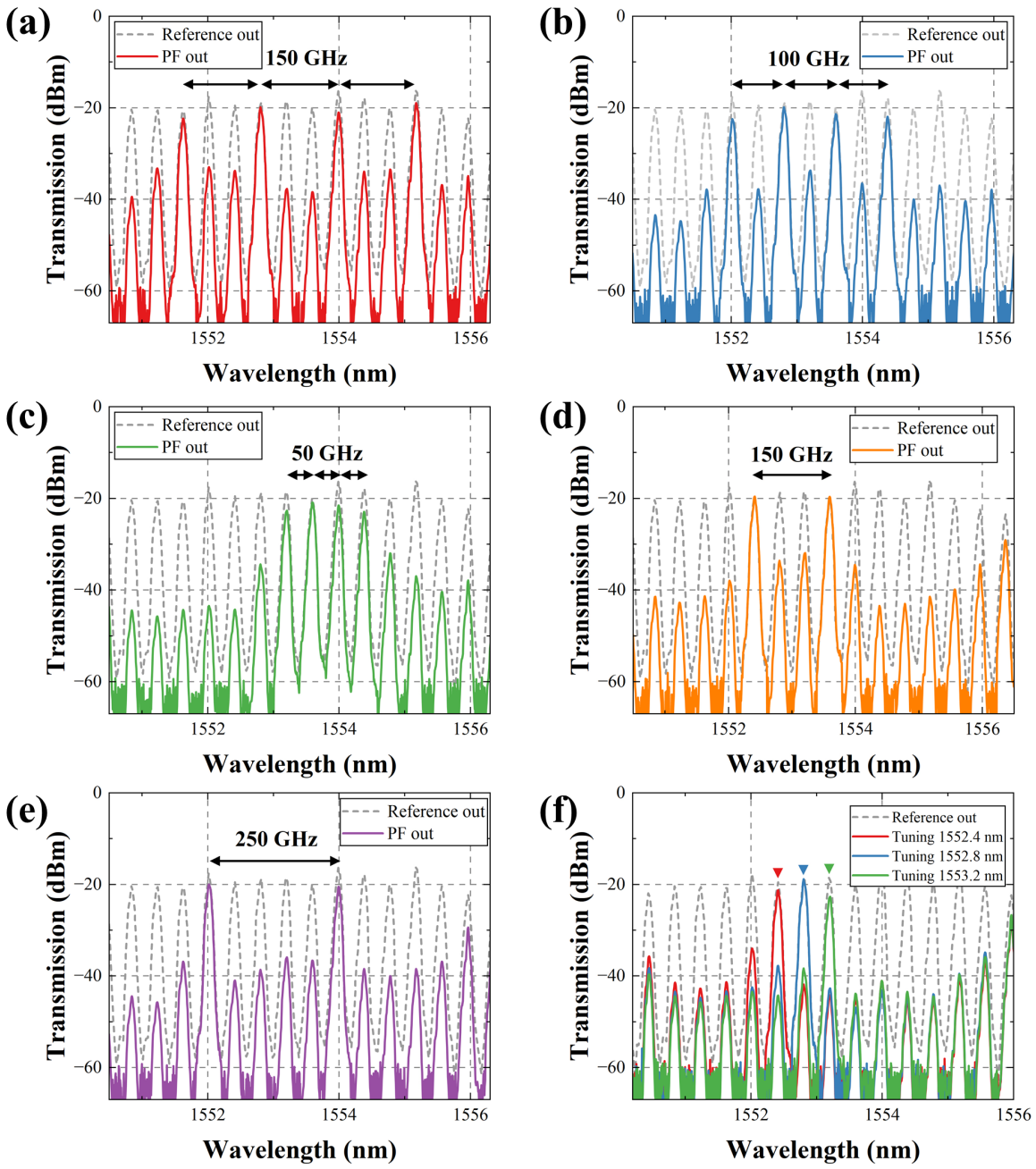

Fig. 7.13 Output spectra of the OFC from the SMLL and the SiNOI waveguide shown as grey dashed traces, together with the OFC filtered by the PF under quad-band settings with spacings of (a) 150 GHz, (b) 100 GHz and (c) 50 GHz, under dual-band settings with spacings of (d) 150 GHz and (e) 250 GHz, and configured to single-band mode in (f).

7.4 Chapter summary

Within the overall thesis, this chapter completes the transition from design-time fixed Bragg grating filters to run-time programmable spectral processing on a SiNOI photonic integrated platform.

This chapter has proposed and systematically examined an on-chip reconfigurable and programmable multi-passband PF on the SiNOI platform, aimed at the urgent need for

flexible tuning and high integration in high-speed communications, optical I/O, EON and multi-functional optical processing. By combining REC with a 4PS-SBG and an MH array, the device achieves independent control of multiple passbands with real-time programmable tuning.

In design, a linearly equivalent chirp reconstructs the index distribution so that the transmission peaks become spatially decoupled within the grating, which markedly improves inter-band independence and tuning precision. Four PS positions of 0.7π are each addressed by an integrated MH, enabling local TO modulation of specific passbands. The architecture supports free switching of passband count from one to four, adjustment of inter-channel spacing from 50 to 450 GHz and selection between band-pass and band-stop spectral forms. It therefore provides multiple operating modes, namely single band, dual band, quad band and band stop filtering.

In quantitative terms, the proposed programmable PF achieves high functional density within a sub-mm grating cavity and with a clearly bounded tuning power budget. The four PS sites are distributed along a cavity of approximately 950 μm, and programmability from single band to quad band and to band stop is realised using only four local MHs positioned at these sites. Each heater has a measured room temperature resistance of 27.1 Ω, so the representative programming condition of 45 mA corresponds to an electrical power of about 55 mW per MH, while a phase excursion approaching π at 97 mA corresponds to about 255 mW per MH. This localised actuation, together with the spatial decoupling enabled by REC, yields low inter-channel interaction, with simulated thermal crosstalk remaining below 10 % and reaching 4.3 % in the best case. These quantitative characteristics directly support scalability: extending the number of programmable bands primarily increases the count of PS pixels and heaters, rather than requiring multi-stage interferometric meshes or large footprint demultiplexers, thereby preserving a compact layout while maintaining independent channel control.

Experimental characterisation demonstrates excellent repeatability, low thermal crosstalk, high SMSR exceeding 15 dB and low insertion loss with a minimum of 0.5 dB. The device performs strongly in DWDM, tunable channel selection and spectral shaping.

This chapter has also detailed the thermal management strategies and spectral measurements under a variety of programming operations. Experiments verify that the programmable filter flexibly reconstructs OFC outputs, achieving high fidelity gating and spectral

reconfiguration. In summary, the device combines high integration, flexible spectral shaping and precise control, and thus offers a strong technological foundation for next-generation on-chip programmable optical processing.

8 Evolutionary algorithm-assisted photonic filters based on superstructure grating

With the rapid progress of on-chip photonic integration, achieving wide-range tunable multi-channel filtering and frequency multiplication within a single device has become a central topic in MWP and optical communications. Although an SMLL can generate an OFC with a high repetition rate, its FSR is difficult to adjust flexibly once fabrication is complete. Frequency-domain multiplication typically depends on nonlinear or second-harmonic mechanisms, which are limited in efficiency and scalability [190,191].

Within the filtering theme, the preceding Chapters 6 and 7 develop Bragg grating-based multi-passband PFs and establish TO programmability for elastic channel selection and OFD. This chapter fits into the thesis by extending that capability from single device multi-passband control to system-facing frequency grid reconstruction in the sub-THz and THz regime. Specifically, it introduces a cascaded architecture that combines a superstructure grating, which offers Fourier series control of channel allocation through the axial phase distribution $\varphi(z)$ and sampling period P, with a high Q MRR that provides narrowband preselection of comb lines. By integrating a SaDE framework with periodic memetic local refinement, the chapter demonstrates algorithm-assisted synthesis of $\varphi(z)$ to balance passband flatness, out-of-band suppression and centre power. The resulting platform enables reconfigurable frequency multiplication and frequency hopping via purely linear spectral filtering, thereby providing a scalable route towards programmable THz photonic signal processing that is compatible with the SiNOI process flow used throughout the thesis.[4]

8.1 Working principle

The reconfigurable filter relies on the complementary properties of Bragg gratings and MRRs, and on the SSG capability to reconfigure the spectral response. The design converts a frequency-domain control task into the engineering of the grating phase distribution $\varphi(z)$ and sampling period P so that the structure matches and redistributes the comb lines generated by an SMLL. Programmable multiplication and hopping in the THz regime are then obtained.

[4] Parts of this chapter have been published previously in: S. Zhu *et al*., in *2025 European Conference on Optical Communications* (*ECOC*) (Copenhagen, Denmark, 28 Sept. 2025 - 2 Oct. 2025).

In a conventional Bragg grating, the reflectance spectrum is determined primarily by the κ, the locations of PSs and the overall length. To overcome the limitation of a single narrow passband, multi-passband responses can be achieved by introducing multiple PSs or periodic modulation. The SSG is an effective realisation route in which a periodic sampling function modulates a parent Bragg grating [192]. As shown in Chapter 3, the sampling function along the propagation direction can be expanded into a discrete Fourier series; the Fourier coefficients F_m set the reflectance strengths of different frequency channels. For the m^{th} order channel, the reflectance can be approximated by an expression involving the base κ, the effective interaction length L and the modulus of F_m, as indicated below.

$$R_m = \tanh^2(|\kappa_0 F_m| L) \tag{8.1}$$

Hence, the spectral response is governed jointly by the P and the axial phase distribution $\varphi(z)$: the former determines the channel spacing, and the latter sets the power allocation and suppression level of each channel.

Complementarily, the MRR provides a high Q factor and narrowband selectivity. Its operation is based on the resonance condition in a ring waveguide, $m\lambda = n_{eff} L_{ring}$. As illustrated in Figure 8.1, by cascading an MRR with an SSG, one preserves the narrowband filtering of the MRR while employing the SSG to multiply or reconstruct the channel spacing. In practice, the MRR first performs comb-line selection from the dense OFC, after which the SSG, via appropriate combinations of $\varphi(z)$ and P, realises channel multiplication, frequency hopping or intensity redistribution. Due to the excessively high frequency, the filtered OFC is anticipated to undergo beat frequency generation when input to the uni-travelling-carrier photodiode following EDFA amplification, thereby achieving genuine frequency hopping within the THz band in the RF domain. The system thus dispenses with nonlinear harmonic generation and achieves multiplication and tuning purely by linear spectral filtering.

The mechanism offers three principal advantages. First, controllable spacing: because channel spacing is linearly related to the P, design-stage selection of the period allows tuning from hundreds of GHz into the THz range. Second, programmable channel intensity: by optimising the phase distribution, one can suppress or enhance specified channels while keeping spacing fixed, enabling programmable control of the number of passbands for multiplication or hopping. Third, integration compatibility: both SSG and MRR are

realisable on SOI or SiNOI platforms with good on-chip interoperability and can be dynamically tuned via the TO effect.

Spectrally, introducing PSs within the Bragg stopband produces multiple transmission windows inside the stopband. These windows correspond to the intensities set by the F_m, thereby forming a multi-channel filtering response. When MHs modulate the PS regions, the transmission windows red shift, enabling programmable switching among channels and enhancing reconfigurability.

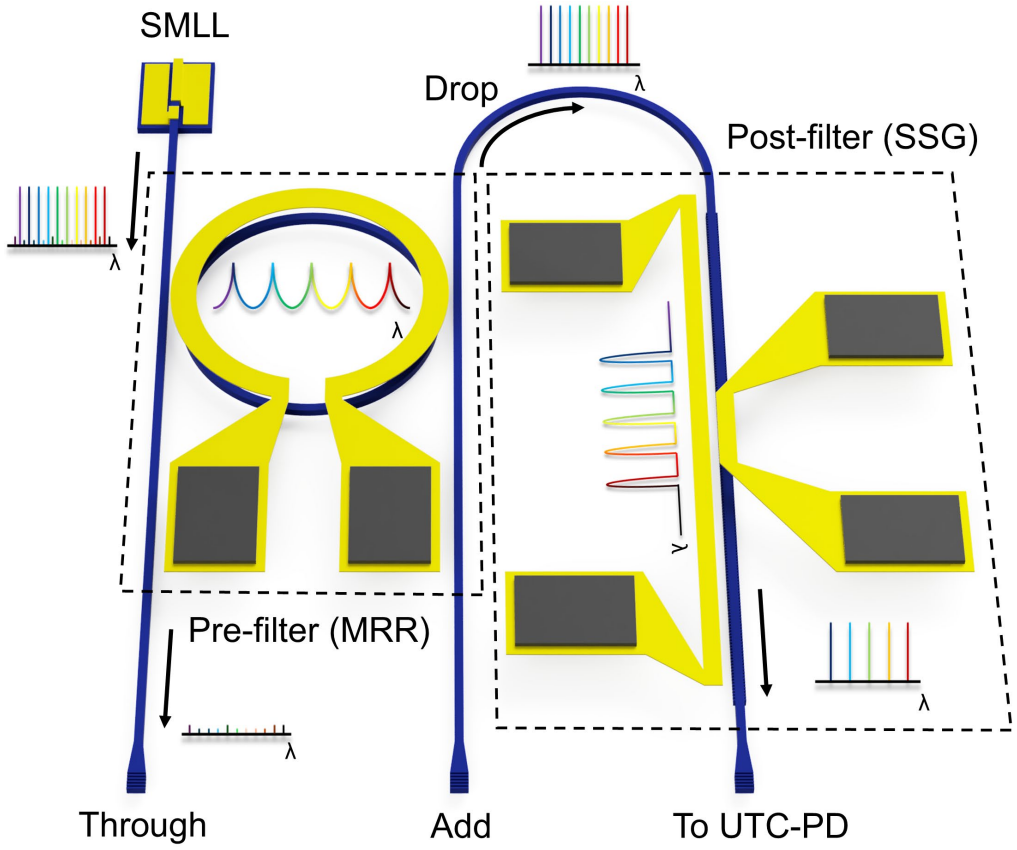

Fig. 8.1 Schematic of an on-chip THz frequency-multiplication solution with two-stage filtering.

In summary, the cascaded SSG-MRR PF provides flexible multiplication of line spacing and selective channel control through joint engineering of P and $\varphi(z)$, thereby overcoming tuning limits of conventional SMLL and offering an efficient, integrable solution for THz-band multiplication and hopping.

8.2 Self-adaptive differential evolution framework

As shown in Figure 8.2, each P in the SSG contains thirty uniformly distributed PS points embedded in a conventional sidewall grating. Through Fourier synthesis of phase and

amplitude, the internal structure redistributes reflected power among frequency channels. Achieving the target spectral response requires balancing several competing objectives in the $\varphi(z)$ design. Intuitively, one seeks a passband that is as flat as possible to reduce ripple, high in-band transmitted power to limit loss and strong out-of-band suppression to mitigate sidelobes and crosstalk. Manual design alone struggles to locate an optimal compromise in a high-dimensional parameter space. Therefore, this chapter adopts SaDE as the optimisation framework and combines it with SQP to couple global exploration with local convergence efficiently.

The spectral performance is mapped to three quantitative indicators: *edgesum*, the sum of intensities at the edges and unwanted channels; *centervar*, the variance of intensities at the central wanted channels; and *centersum*, the sum of intensities at the central wanted channels. A lower *edgesum* indicates lower edge leakage; a lower *centervar* indicates a flatter channel distribution; a larger *centersum* indicates higher overall transmittance. These are combined in a weighted multi-objective function:

$$\begin{aligned} f(x) = {} & w_1 \cdot edgesum(x) \\ & + w_2 \cdot centervar(x) \\ & - w_3 \cdot centersum(x) \end{aligned} \tag{8.2}$$

where x denotes the set of $\varphi(z)$ parameters and w_1, w_2, and w_3 are weights that can be chosen to suit the application. Minimising f reduces leakage and ripple while penalising loss of centre power.

In implementation, SaDE adapts both the differential-mutation strategy and the crossover probability so that the population explores globally in early generations and progressively transitions toward local convergence [193]. The steps are as follows: initialise parameters to generate a population of candidate $\varphi(z)$; apply differential mutation using difference vectors between individuals to create new candidates; apply crossover to mix candidates and increase diversity; and select the better performers according to the objective. As iterations proceed, the population approaches an optimum.

To accelerate convergence, a periodic memetic strategy is employed. After a fixed number of generations (e.g., 40), an SQP-based local search is applied in parallel to the entire population. This both avoids premature convergence and rapidly identifies refined phase

distributions in the neighbourhoods of promising solutions, thereby improving speed while maintaining global robustness [194].

For encoding, the complete $\varphi(z)$ is discretised into a finite-dimensional parameter vector, each dimension corresponding to a sampling point or phase segment in the grating. This discretisation ensures computational tractability while preserving design freedom. Manufacturability constraints on the phase range, continuity and physical implementability are imposed during optimisation to ensure the solutions remain realisable.

SaDE supports both single-objective and multi-objective optimisation. In this application, *edgesum* and *centervar* are minimised, and *centersum* is maximised. A weighted sum converts these into a single objective, and appropriate weight selection enables flexible trade-offs among the indicators.

In summary, the SaDE optimisation framework provides an effective solution for the $\varphi(z)$ design of the SSG. It balances global search and local convergence and simultaneously improves channel flatness and out-of-band suppression while maintaining high transmittance. The resulting reconfigurable filter achieves a strong overall balance of functionality and metrics, providing a firm basis for subsequent design and experimental validation. Figure 8.3 outlines the algorithmic framework.

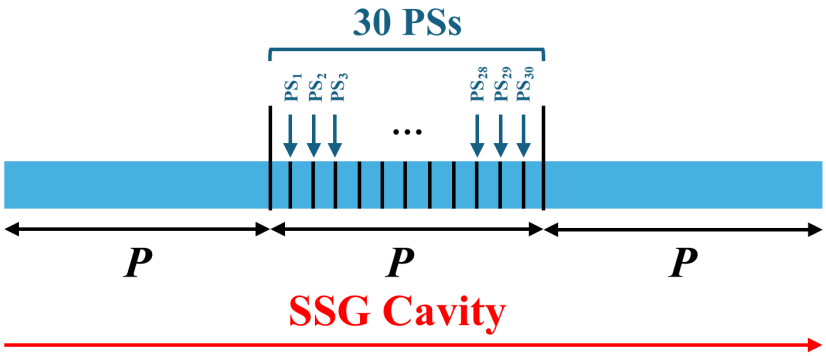

Fig. 8.2 Schematic of the SSG.

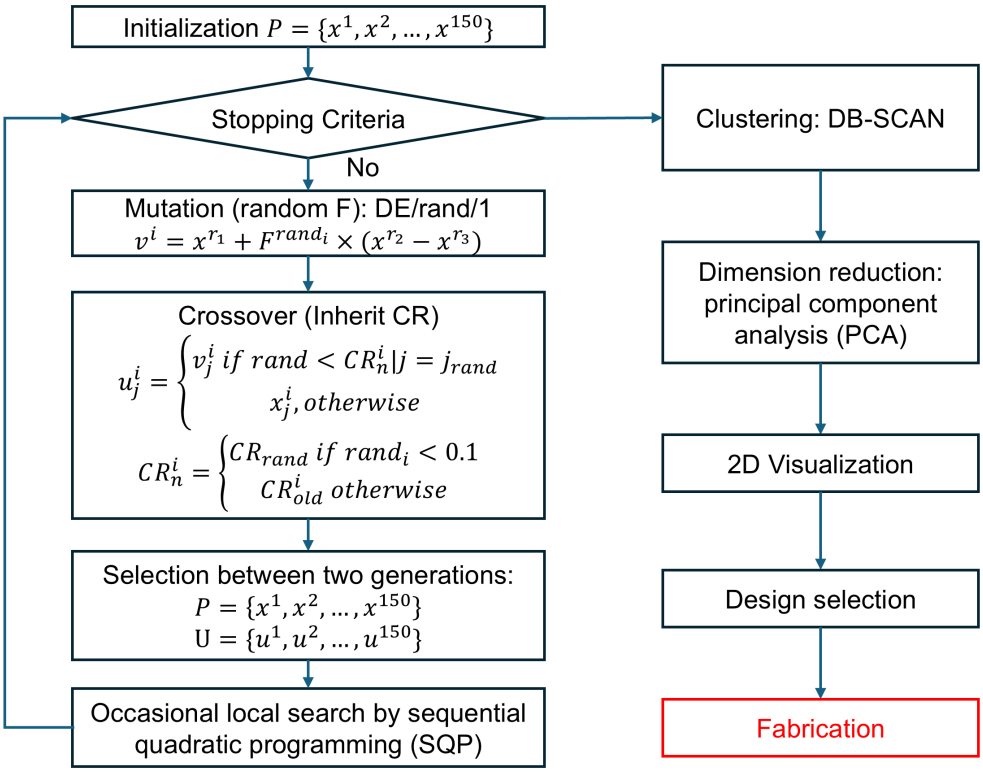

Fig. 8.3 Flow chart of the optimisation algorithm.

8.3 Design and simulation results

The proposed reconfigurable PF adopts a cascaded architecture of an MRR and an SSG to realise flexible frequency multiplication and frequency hopping of the comb lines generated by an SMLL. The whole device is integrated on a SiNOI platform, which provides favourable process compatibility and low loss.

Using the drop port of the MRR is the most straightforward method for multi-passband filtering. Owing to its sharp resonance and steep roll-off, the MRR is a valuable wavelength-selective element. However, a single MRR is limited in narrowband filtering on its own, and post-fabrication tuning of an individual resonance peak is difficult. To control transmission peaks across a wide spectral range, a cascaded tunable band-stop strategy is required.

Bragg gratings provide strong selectivity. By matching the Bragg wavelength to the MRR resonance, unwanted transmission peaks can be suppressed effectively. Cascading multiple gratings with different centre wavelengths enables multi-peak selective modulation, but this may introduce non-uniform passband intensities and increased scattering loss.

As the primary narrowband selector, the MRR here has a resonance radius of about 74.2 μm, a waveguide width of about 1.2 μm and a coupling gap of about 300 nm. This configuration yields an FSR around 350 GHz in the C-band and provides the basis for subsequent matching with the SSG. The MRR transmission shows a high Q factor greater than 10^5 and narrowband characteristics, enabling precise selection of a single or a few comb lines from the SMLL. At resonance, light couples into the ring and forms a standing wave, producing a sharp band-pass peak. MHs on the MRR allow thermal tuning of its resonance to match the SSG channels. In combination with the SSG, dynamic switching can be achieved between the wavelength grids set by the MRR and by the SSG.

Cascaded with the MRR, the SSG performs frequency multiplication and channel reconstruction. A uniform Bragg parent grating is modulated by a periodic PS sequence so that a multi-channel Fourier spectrum is formed. Each P contains thirty PS points that together realise an equivalent phase-modulation function.

In implementation, the SSG uses a Si_3N_4 waveguide with a thickness of 340 nm and a width (W) of 1.2 μm, with a sidewall etch recess depth (d) of about 60 nm. The grating period (Λ_0) is 443 nm to cover the MRR resonance band. Three different P are adopted, namely 116.3 μm, 90.9 μm and 74.5 μm, which realise frequency spacings of 670 GHz, 869 GHz and 1.05 THz, respectively. A central π PS is introduced, and TO tuning is provided by an integrated MH located above the grating. The MH adopts a Ti, Pt and Au multilayer structure, and a typical drive current of 11 mA enables continuous tuning of the local phase amplitude.

To obtain a high-quality multi-channel spectral response, a periodic-memetic SaDE framework is employed to design the SSG $\varphi(z)$. By combining SaDE with SQP, in a memetic manner, the PS amplitudes are optimised with rapid convergence while avoiding local minima. For a 5-channel design, the optimised transmission exhibits uniform notches at the target sub-grating channels while suppressing other channels effectively. As illustrated in Figures 8.4(a) and (b), the optimised $\varphi(z)$ and the reflection spectra obtained using TMM are given, and the passband variance is minimised compared with existing optimisation methods [195].

The new multi-objective function for the design is defined as follows.

$$f(x) = \max\left(\sqrt{centervar} - 0.001, 0\right) \times 100 + \max\left(centersum - 0.3 \times p, 0\right) \times 1 + edgesum \times 1 \tag{8.3}$$

Here, p = 5 denotes the number of designed channels. The weight ratio is set to 100:1:1 so that flatness dominates the optimisation.

Regarding optimisation dimensionality, the design variables are thirty continuous parameters in the range -1 to 1, corresponding to the $\varphi(z)$ within a single P. The population size (NP) is 250, and a local SQP search is triggered every 40 generations. The convergence condition is $f(x) < 0.5$. Under this criterion, designs typically satisfy specifications on flatness, channel intensity and suppression simultaneously. The optimisation environment is MATLAB 2023 using parallel computation on a 12-core central processing unit. In practical runs, the periodic-memetic SaDE obtains more than 100 qualified designs after an average of 4200 generations, whereas pure SaDE sometimes fails to converge. This demonstrates advantages in convergence speed and stability.

To avoid redundant solutions and to aid design selection, density-based spatial clustering of applications with noise and principal-component analysis are employed to post-process the optimisation results [196,197]. The solutions cluster primarily into two distinct groups whose spectra differ in passband flatness and out-of-band suppression, which allows selection according to application needs (right side of Figure 8.3). Figure 8.4 presents the optimised $\varphi(z)$ and corresponding transmission spectra for the 5-channel cases.

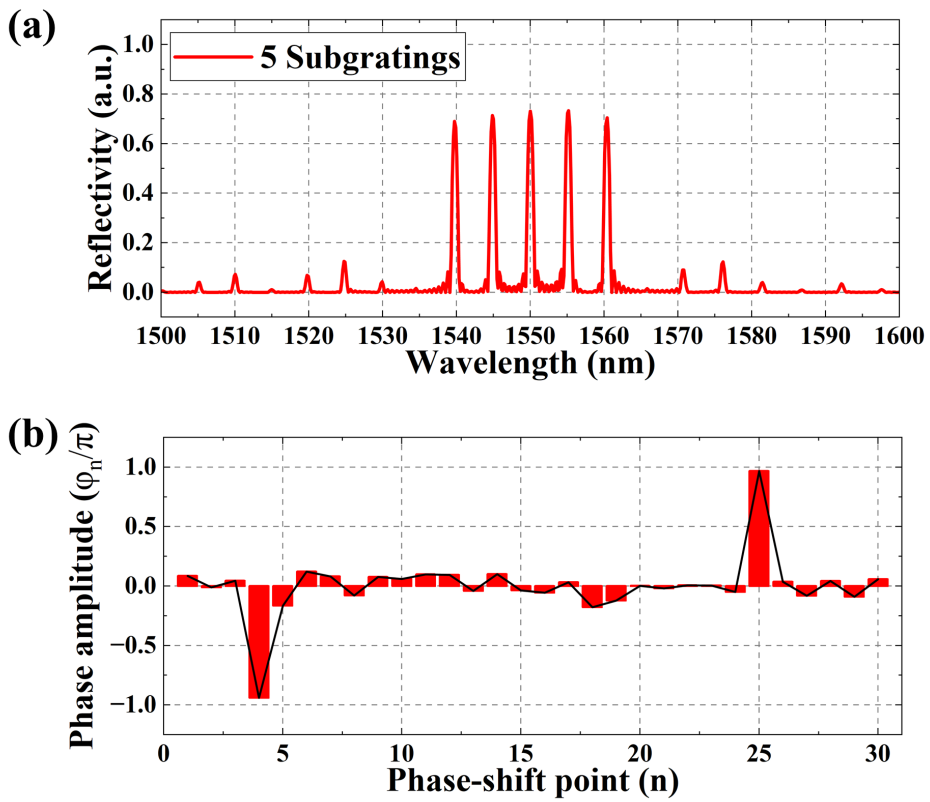

Fig. 8.4 (a) Simulated 5-channel SSG reflection and (b) optimised PS amplitude distribution $\varphi(z)$.

It is noteworthy that the frequency spacing is independent of the number of channels. Hence, a given optimised power-allocation scheme can be reused across different SSG designs. This decoupling of structure and function enhances design flexibility and facilitates integration across platforms. Figure 8.5 shows the results of other optimisations: examples of reflected spectra corresponding to channels 5 to 15.

In multi-bandpass or multi-channel PF, maintaining consistent group delay across channels is of paramount importance. As each channel corresponds to distinct centre wavelengths and phase responses, considerable time delay variations between passbands will induce relative phase drift and temporal misalignment in signals after filter processing. Such non-uniform group delay not only compromises the coherence of multi-channel signals but also introduces intersymbol interference and signal distortion in parallel data transmission or multi-carrier systems, thereby degrading the system's modulation fidelity and bit error performance. For OFC-based signal processing, strict phase relationships between comb teeth are essential for achieving precise frequency division and difference frequency synthesis. Any inter-channel delay mismatch may disrupt the comb's phase-equal distribution, resulting in increased phase noise or frequency drift in the generated MMW or THz signals. Furthermore, for pulsed signals, differing delays cause varying degrees of pulse

broadening. Consequently, a high-performance multi-channel PF must not only exhibit high sideband suppression and controllable bandwidth in terms of amplitude characteristics, but also ensure the group delay across all passbands is as consistent as possible. This guarantees the temporal synchronisation and coherent stability of the system's output signal. To further validate the consistency of the designed PF's time-domain characteristics, we conducted numerical simulations of its group delay distribution. As shown in Figure 8.6, the delay curves for each passband maintain high overlap within the central region, with minimal delay differences between channels. This aligns with the balanced variation in transmission intensity observed in their amplitude responses, indicating that this structure effectively maintains inter-channel time consistency while realising multi-channel operation.

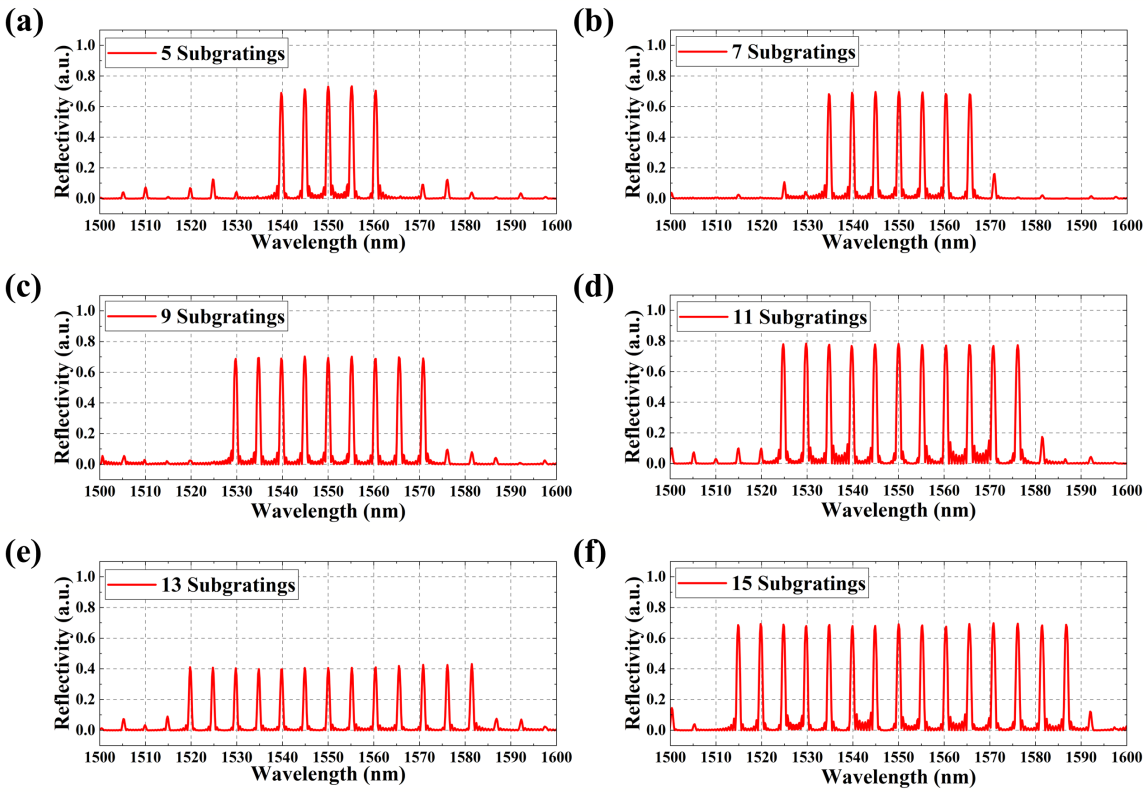

Fig. 8.5 Optimised SSG simulated reflectance spectra for (a) 5, (b) 7, (c) 9, (d) 11, (e) 13 and (f) 15 channels.

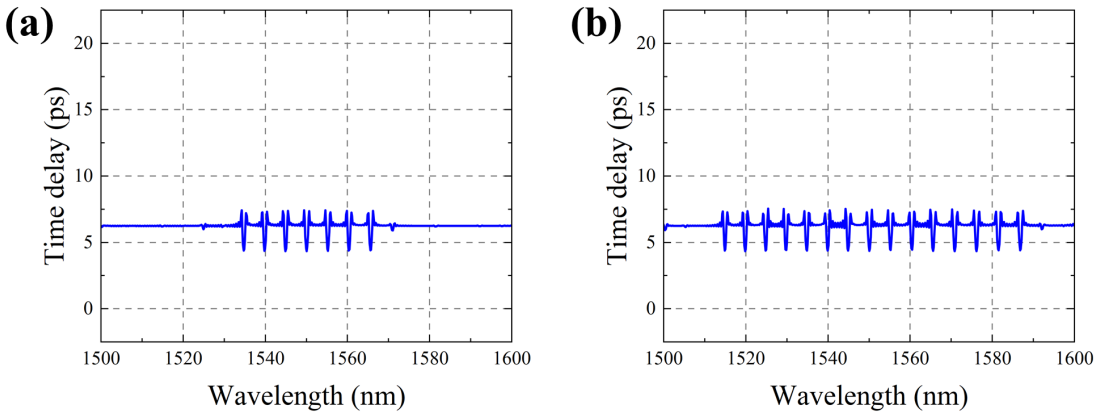

Fig. 8.6 Time delay diagrams for (a) 7-channel and (b) 15-channel setups of SSG simulated using TMM.

8.4 Characterisation results

To validate the performance of the proposed reconfigurable PF, we carried out a comprehensive experimental characterisation of its spectral response.

Before characterising the cascaded device, the MRR was characterised independently to confirm baseline filtering performance, as shown in Figure 8.7. It is noteworthy that both the independently characterised devices and the cascaded filter are fabricated on the same chip. The FSR is approximately 335 GHz, consistent with the theoretical design. The through-port transmission exhibits clear periodic notches. The drop-port response within 1550 to 1560 nm shows pronounced resonance transmission peaks that correspond to the notches at the through port. The measured Q factor is about 4.3×10^3. This confirms that using the MRR as a prefilter is reasonable, since it can accurately select comb lines from a broadband input and provide stable spectral selectivity for subsequent cascading with the SSG. The high Q factor yields a 3 dB bandwidth near 52 GHz.

To analyse the role of the SSG in multi-channel filtering, we next measured its spectral response under different operating states. The SSG was first characterised on the same wafer without the MRR. Within each *P,* a pre-optimised PS amplitude distribution $\varphi(z)$ was applied. Figure 8.8 shows the measured spectra for 5-channel SSG filters with frequency spacings of 670 GHz, 869 GHz and 1.05 THz. The 5-channel SSG transmission in Figure 8.8(a) confirms the presence of tunable passbands inside each sub-grating stopband, thereby forming an equal-spacing frequency grid. Without any heating current, the spectrum shows uniformly distributed channels with spacings that match the *P* by design. Applying 66 mA to the I_{MH} on the centre π PS of the SSG, denoted $I_{MH\text{-}SSG}$, induces a local TO shift of the n_{eff}. When the

central PS departs from 1.0π, the interference condition is disrupted and the passband intensities decrease until they vanish, at which point the SSG returns to a reflection configuration. Restoring the PS to 1.0π enables synchronous on-off control of all passbands.

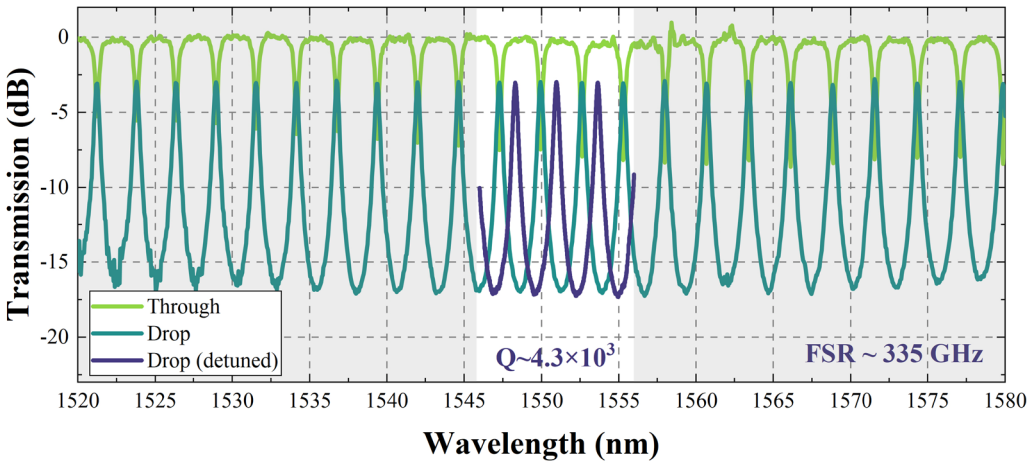

Fig. 8.7 Measured spectra of the MRR under SLD input: through-port and drop-port responses, together with the drop-port spectrum under thermal tuning.

In addition to the 670 GHz configuration in Figure 8.8(a), we adjusted the *P* to test the 869 GHz and 1.05 THz configurations shown in Figures 8.8(b) and (c). For the 5-channel case, the performance indicators are highly consistent and show excellent signal quality. The 5-channel variance is 3.6×10^{-6}. Crosstalk suppression exceeds 20 dB, which ensures independence and integrity of adjacent channels. Insertion loss has a best value of 0.8 dB and a worst value of only 1.2 dB, demonstrating high transmission efficiency and low loss. These indicators align with the needs of optical communication systems. Low variance supports stable operation in DWDM and thereby stabilises intensity modulation, while high crosstalk suppression meets the signal-to-noise requirements of high-speed large-capacity transmission.

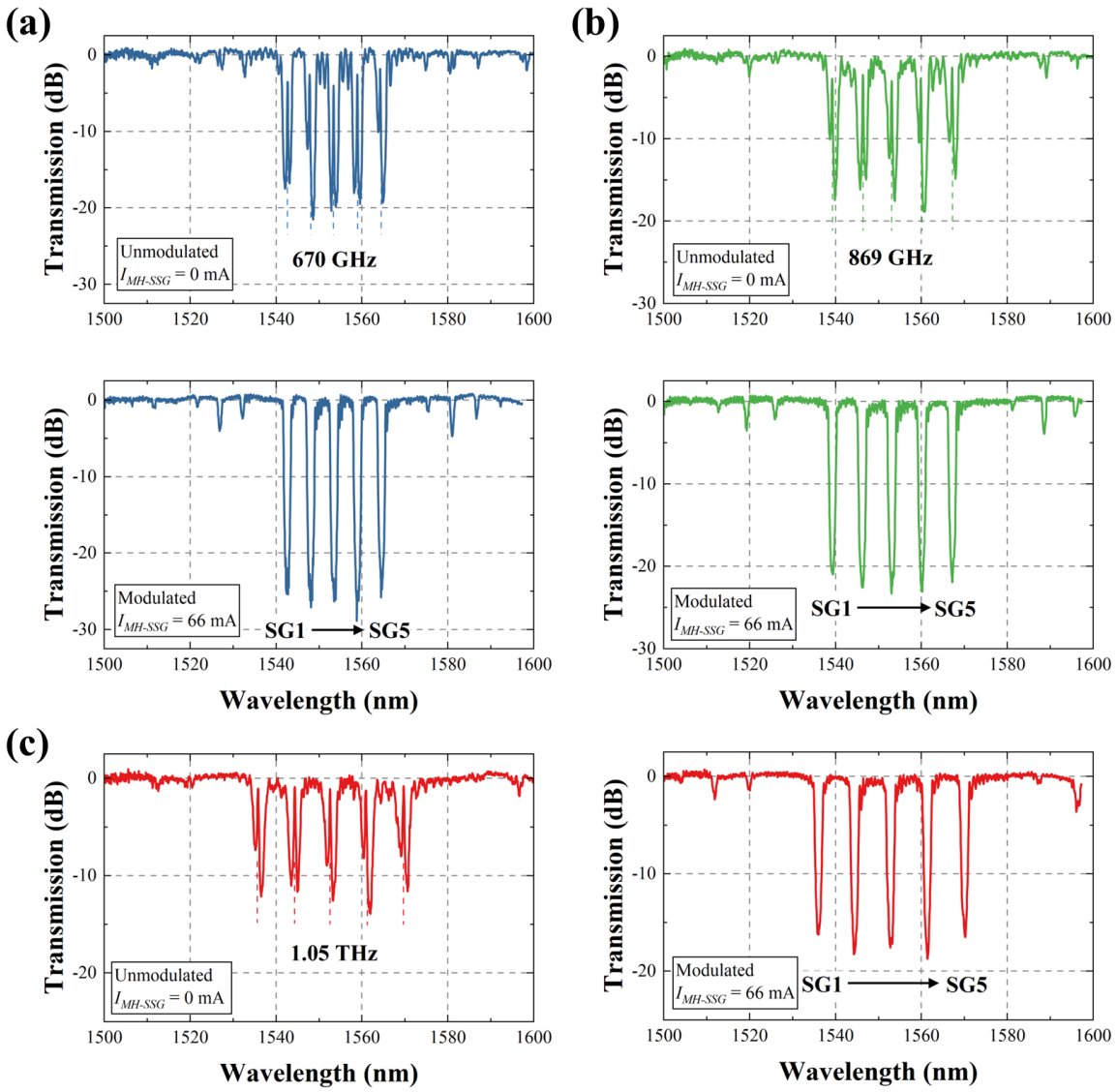

Fig. 8.8 Measured spectra for a 5-channel SSG with frequency spacings of (a) 670 GHz, (b) 869 GHz and (c) 1.05 THz.

Both unmodulated and modulated spectra show consistent control of the existence and spacing of the passbands. A key observation is that decoupling the channel spacing from the number of channels *n* is essential, since it avoids rigid coupling constraints in design. This enables independent adjustment of the channel count while keeping *P* fixed or, conversely, changing *P* without sacrificing the established channel grid. Such decoupling significantly increases freedom in frequency selection and channel allocation and provides flexibility for a wide range of operating modes and application scenarios.

Figures 8.9(a) to (d) present measured spectra for a 670 GHz SSG configured for 7, 9, 11 and 13 channels after optimisation. In both unmodulated and modulated states, the stopband ER remains uniform and non-target sub-gratings are effectively suppressed. For 7, 9, 11 and 13 channels, thermal tuning produces clear channel erasure effects, which confirms the

flexibility of channel reconstruction. When the number of sub-gratings increases while the total waveguide length remains fixed, coupled-mode theory indicates that the reflectance of each sub-grating decreases because the available coupling strength per unit length is limited. This can be compensated for by increasing the κ of each grating unit or by extending the SSG length. For the 7-channel case, the variance is 1.41×10^{-5} and insertion loss remains within 0.6 to 1.2 dB, which meets DWDM requirements for low power loss and precise channel control. Although crosstalk suppression is 15 dB, slightly lower than the 5-channel case, it still ensures basic signal independence. As the channel count extends to 9 and 11, the variances are 2.55×10^{-5} and 2.74×10^{-5}, respectively. Insertion loss remains within 1 to 3 dB, and crosstalk suppression increases to 16 dB. This demonstrates that the device maintains favourable transmission characteristics as channels are added and supports future higher-capacity optical interconnects. When expanded to 13 channels, the variance rises to 5.33×10^{-4}, and crosstalk suppression decreases to 6.8 dB, while the best insertion loss falls to 0.1 dB, which shows the potential for extremely low loss. Overall, the results reveal both advantages and challenges in balancing channel expansion and performance. For optical networks, 7 to 11 channels are well suited to robust DWDM filtering, whereas 13 channels indicate the possibility of larger bandwidth utilisation under ultra-low-loss constraints. Moreover, the results of the SaDE-assisted SSG characterised individually above demonstrate superiority in flatness, integration, and sideband suppression compared to previously reported methods for generating similar passive platform-wide range multichannels, indicating the superiority of the algorithm described herein and the manufacturability of this design [198–202].

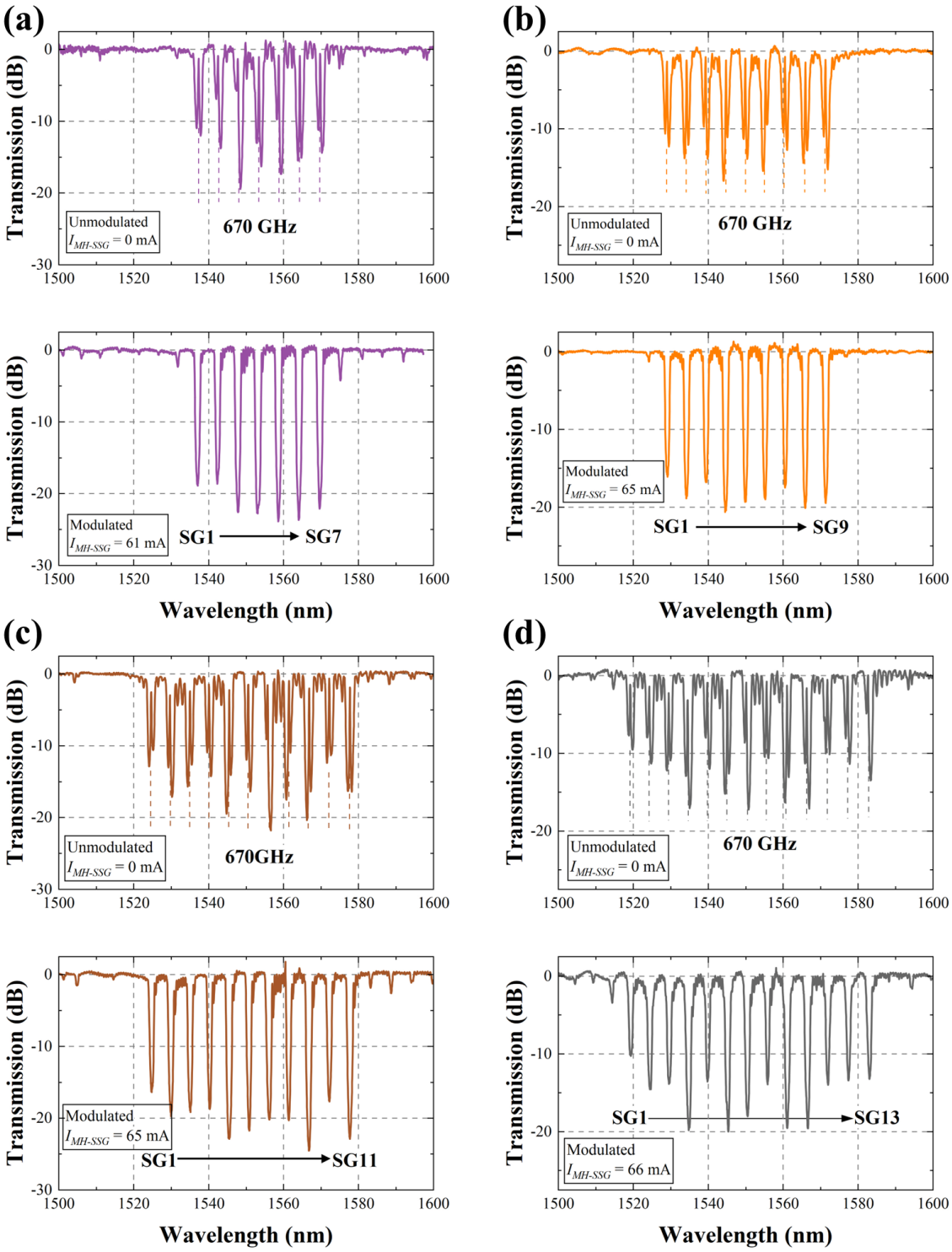

Fig. 8.9 Measured spectra for an SSG with 670 GHz spacing configured for (a) 7-channel, (b) 9-channel, (c) 11-channel and (d) 13-channel.

After confirming the independent performance of the MRR and the SSG, we measured the cascaded output. For system-level evaluation, an SLD was used as the source to drive a cascade of the MRR and a 5-channel 670 GHz SSG. Fabrication tolerances can misalign the MRR resonance with the SSG passbands, which was corrected by red-shift tuning of the MRR using an 11-mA current applied to the MRR-integrated MH, denoted $I_{MH\text{-}MRR}$. After

alignment, the output spectrum in the 0 to 5-second interval of Figure 8.11(a) presents 9 equally spaced channels with 335 GHz spacing. The composite filtering of the SSG and MRR yields an enhanced ER of about 10 dB across sub-grating bands SG1 to SG5. In addition, the 3 dB bandwidth of the MRR resonance narrows from about 52 GHz to 15 GHz under the dual filtering effect, as illustrated in Figure 8.10. This narrowing is important for future applications since, in THz-band multiplication and hopping, a narrower bandwidth increases channel isolation and thereby reduces crosstalk and improves both security and robustness. After alignment, the SSG transmission peaks couple efficiently to the MRR with exceptionally low loss. In the range 1540 to 1568 nm, 9 channels are observed in the unmodulated state.

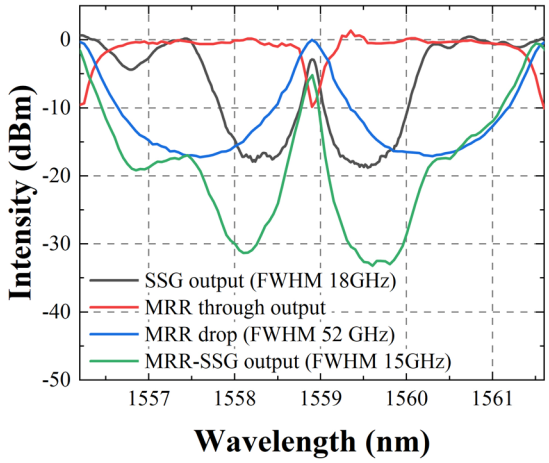

Fig. 8.10 Locally magnified measured transmission spectra of the SSG, the MRR and the cascaded MRR–SSG.

When thermal modulation is applied to the SSG, as in the 5 to 10 seconds interval of Figure 8.11(a), the passbands SG1 to SG5 vanish as the PS reaches 2.0π and are replaced by deep stopbands with ER above 30 dB, even when spectral alignment is maintained. After modulation, only four channels remain within 1540 to 1568 nm, and the spacing increases to 670 GHz, which is twice the original 335 GHz. Beyond the SSG modulation range, the 335 GHz spacing remains unchanged. This frequency doubling confirms that coordinated alignment of the MRR and SSG together with TO phase control enables dynamic switching of the channel spacing. Frequency hopping is achieved in both 7-channel and 9-channel cascaded systems, as shown in Figures 8.11(b) and (c). The 9-channel system covers 48 nm from 1526 to 1574 nm. The corresponding $I_{MH\text{-}MRR}$ and $I_{MH\text{-}SSG}$ values are indicated in Figures 8.11(a) and (c).

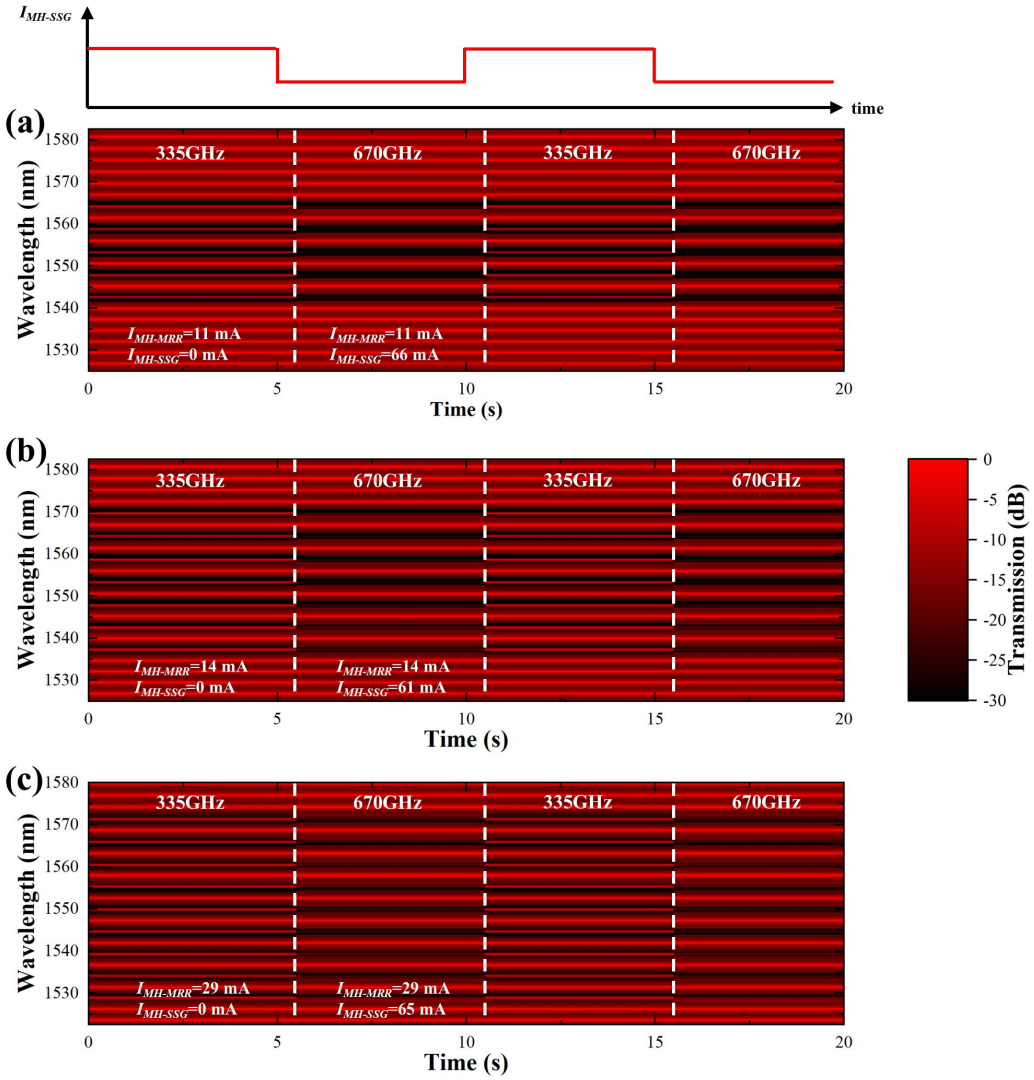

Fig. 8.11 2D optical spectra under thermal modulation in the intervals 5 to 10 seconds and 15 to 20 seconds for (a) 5-channel, (b) 7-channel, and (c) 9-channel SSGs with 670 GHz spacing cascaded with an MRR with 335 GHz spacing.

The experiments above used simple square-wave thermal modulation to demonstrate erasure and regeneration of passbands, maintenance of doubled spacing and large-range hopping across multiple channels, all in the frequency domain. These results confirm excellent spectral reconstruction and repeatability under steady-state conditions. To investigate dynamic behaviour further, we carried out time-domain experiments using chirped thermal modulation. By injecting a linearly chirped drive current $I_{MH\text{-}SSG}$, the system alternates between 335 GHz and 670 GHz operating regions, thereby validating dynamic frequency multiplication. Relative to uniform modulation, time-domain chirp modulation introduces a non-uniform phase-accumulation process under dynamic drive and enables refined shaping of the spectral structure in time. This approach avoids the increased inter-channel coupling and bandwidth limitations associated with uniform modulation and, through dynamic control

of transient frequency drift and accumulated phase difference, significantly improves the degrees of freedom for frequency multiplication, bandwidth expansion and spectral reconstruction. The method exhibits superior stability and scalability, particularly under high channel counts and high tuning speeds.

To provide a comprehensive view under different time-domain conditions, we implemented four configurations with 5, 7, 9 and 11 channels and observed the spectral evolution continuously under chirped-current drive. Figure 8.12 shows that the transmission spectra display clear alternating transitions with time across channel configurations. With spectral resolution maintained at 15 GHz, the system completes frequency multiplication exceeding 300 GHz in a stable manner. As the channel count increases, the response under chirped modulation remains linear and stable, which confirms the application potential of this integrated structure in high-speed reconfigurable photonic systems. These results demonstrate robust control of multi-channel spectra under dynamic conditions and provide key support for future realisations of on-chip high-speed, broadband and programmable photonic signal processing.

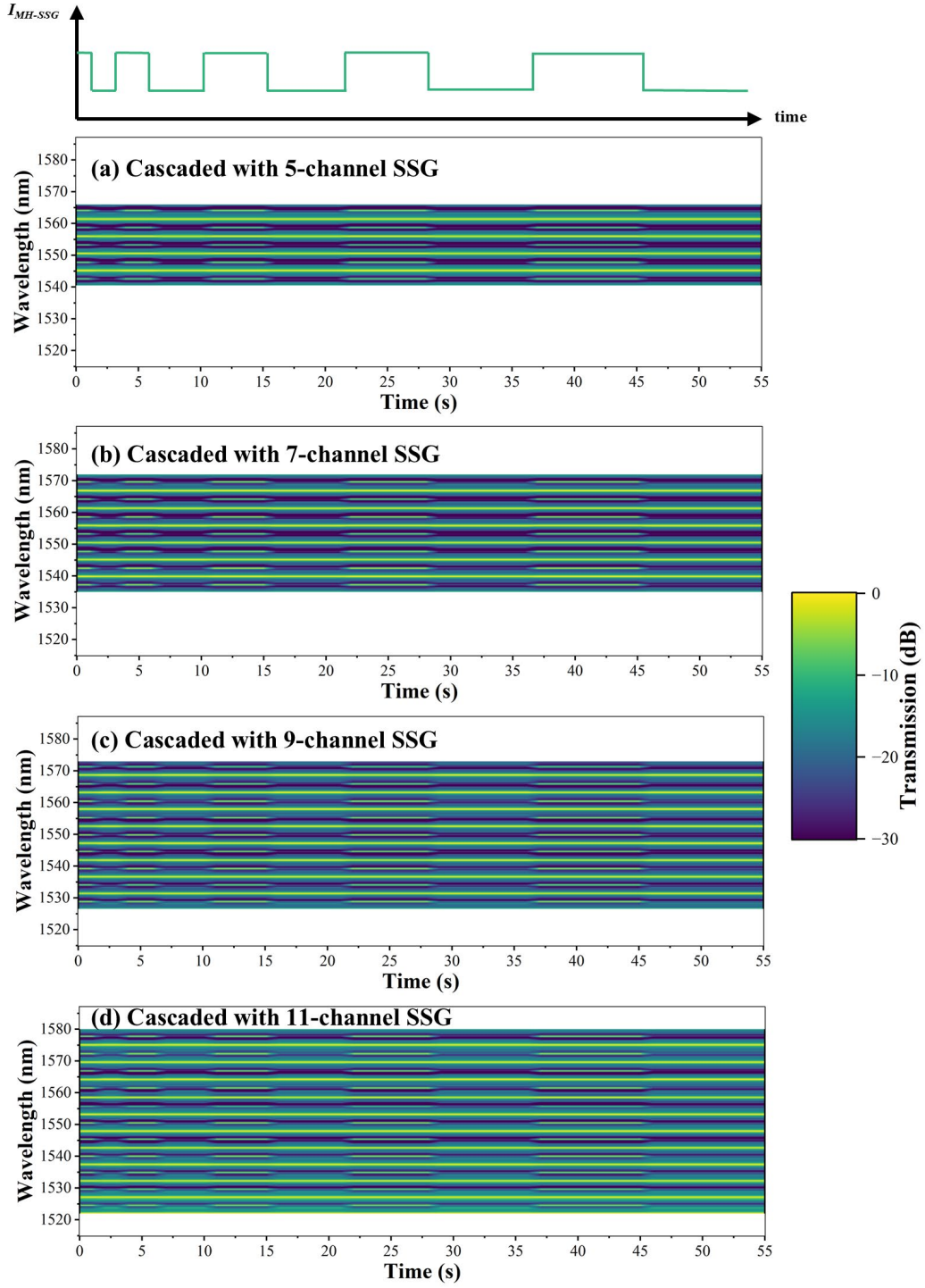

Fig. 8.12 2D optical spectra under time-domain chirped thermal modulation from 0 to 55 seconds for (a) 5-channel, (b) 7-channel, (c) 9-channel, and (d) 11-channel SSGs with 670 GHz spacing cascaded with an MRR with 335 GHz spacing.

8.5 Chapter summary

Within the overall thesis, this chapter advances the reconfigurable filtering theme from programmable multi-passband responses to algorithm-synthesised frequency grid reconstruction for sub-THz and THz signal generation on a SiNOI photonic integrated platform.

This chapter has proposed and systematically investigated a reconfigurable PF based on the cascade of an SSG and an MRR. Together with a SaDE algorithm, for a $\varphi(z)$ optimised design, the device realises reconfigurable control of frequency spacing for both multiplication and hopping. The approach overcomes the tuning bottleneck of conventional OFC techniques and provides an efficient and flexible solution for on-chip dynamic filtering and channel reconstruction in the THz band.

Beginning from working principles, the chapter analysed the Fourier series control mechanism of the SSG and its complementarity with the high Q-factor resonance of the MRR. On this basis, a periodic memetic optimisation framework that combines SaDE with SQP was adopted to optimise the $\varphi(z)$ under multiple objectives. The method balances channel flatness, centre power and edge mode suppression, thereby improving spectral quality and expanding the degrees of freedom for control. Density-based spatial clustering and principal-component analysis were used to screen the optimisation results and to extract reusable design families with strong spectral controllability and manufacturability.

Structurally, the filter is integrated on a low-loss SiNOI platform. Decoupled sampling periods from 116.3 to 74.5 μm enable control of frequency spacing from 670 GHz to 1.05 THz. An integrated MH precisely modulates the central π PS to realise thermal tuning and synchronous on/off switching of channels. Across configurations with 7, 9, 11 and 13 channels, the device exhibits low insertion loss with a minimum of 0.1 dB, high channel uniformity with variance below 10^{-4} and excellent crosstalk suppression with maxima exceeding 20 dB. These results satisfy the core requirements of DWDM for multi-channel operation with low crosstalk.

From a quantitative benchmarking viewpoint, the proposed SSG-MRR platform provides a favourable trade-off among footprint, tuning power budget and scalability compared with representative state-of-the-art frequency-grid and multi-channel filtering approaches reviewed in Chapter 2. In footprint terms, the narrowband pre-selection is implemented by a compact MRR with a radius of about 74.2 μm, while the channel spacing is set by the SSG sampling period P without requiring large demultiplexing structures. Power consumption is constrained by the fact that reconfiguration relies on only two TO control points in the cascade, namely the MRR heater for spectral alignment (11 mA in the reported measurements) and the SSG heater for synchronous channel on-off switching (66 mA in the demonstrated operation), rather than a large array of independently driven tuning elements. Scalability is supported on three levels: the channel spacing is decoupled from channel count,

the same design methodology produces 5 to 13-channel filters with low variance and crosstalk performance retained in the multi-channel regime, and the algorithm-assisted synthesis of $\varphi(z)$ enables reusable design families that can be selected and ported across different P values and channel configurations. Collectively, these attributes highlight the relative advantage of the chapter contribution as a compact, control-efficient and extensible route to sub-THz and THz frequency-grid reconstruction via purely linear spectral filtering.

In addition, time domain chirped thermal modulation experiments verified spectral reconstruction under dynamic control. With linearly modulated drive current, the channel spacing transitions dynamically from 335 GHz to 670 GHz and supports spectral hopping and bandwidth expansion for up to 11 channels. The findings indicate substantial potential for high-speed signal processing, optical frequency hopping communication and on-chip programmable photonic systems.

In summary, through integrated theoretical design, algorithmic optimisation and experimental validation, the chapter has demonstrated the core advantages of the SSG-MRR cascaded structure for on-chip programmable THz photonic filtering. This work provides a solid foundation for the development of next-generation high-speed, high-capacity and reconfigurable photonic systems.

9 Conclusions and future work

9.1 Summary

In this thesis, two types of biochemical sensors and three types of integrated PFs based on HPWs, MRRs, MZIs and equivalent-chirp phase-shifted Bragg gratings, and SaDE algorithm-assisted SSG were proposed, fabricated, and experimentally demonstrated, aiming at applications in high-sensitivity biochemical sensing, programmable filtering, and reconfigurable THz/MMW-band photonic systems.

Firstly, two hybrid plasmonic biochemical sensors were developed on an SOI platform, employing slot-buried waveguides integrated with MRRs and MZIs. These sensors achieved refractive index sensitivities exceeding 900 nm/RIU with a compact footprint and low insertion loss, demonstrating compatibility with lab-on-chip biosensing applications.

Secondly, a dual-band PF based on Bragg gratings based on REC technology and integrated MHs was proposed and demonstrated. Using a passive SMLL as the OFC source, the device achieved reconfigurable passband spacings from 52.1 to 439.5 GHz with high Q-factors, narrow 3 dB bandwidths, and minimal footprint, showing immense potential for OFD and photonic MMW generation.

Thirdly, a fully programmable multi-passband filter based on 4PS-SBGs was designed and experimentally validated on the SiNOI platform. The structure supports tunable passband number (1 to 4), flexible channel spacing (50 to 450 GHz), and spectral shaping (pass or reject) via TO modulation. The device achieved SMSR > 15 dB, insertion loss as low as 0.5 dB, and high tuning repeatability, enabling dynamic spectral slicing for DWDM systems.

Finally, a reconfigurable PF based on a cascaded SSG-MRR architecture was designed with the assistance of a SaDE optimisation framework. By optimising the phase modulation profile in the SSG, the filter achieved uniform passband power, low ripple, and strong out-of-band suppression. Experimental results demonstrated real-time channel spacing doubling and hopping from 335 GHz to 670 GHz, as well as time-domain chirp modulation across 5 to 11 channel configurations. This approach provides a robust, low-cost and scalable solution for on-chip THz signal synthesis and high-speed photonic processing.

These results collectively demonstrate the feasibility and versatility of integrated PFs for both biochemical and MMW/THz photonic applications, especially in achieving compact,

low-loss, and highly reconfigurable devices using advanced grating design, integration techniques, and optimisation algorithms.

9.2 Future work

To further enhance the performance, integration level, and industrial applicability of the on-chip reconfigurable PFs proposed in this thesis, future work will focus on comprehensive optimisation across material platforms, structural designs, tuning mechanisms, and characterisation methodologies.

9.2.1 Heterogeneous integration to replace hybrid integration

The current PFs rely on hybrid integration for introducing OFC sources. While this approach offers design flexibility, it leads to increased insertion loss and system complexity. Future work will explore the use of heterogeneous epitaxial growth or heterogeneous bonding technologies to realise fully integrated comb sources and filtering units on a single chip. This strategy is expected to reduce coupling losses, simplify packaging, and enable compact integration. Furthermore, highly integrated comb generators based on nonlinear optical effects will be investigated using SiNOI, TFLN, or III-V-on-silicon platforms. These sources are anticipated to provide high-repetition-rate, low-noise, and CMOS-compatible performance, supporting practical applications in MWP, chip-level optical interconnects, and coherent communication systems.

9.2.2 Replacing sidewall gratings with low-loss buried gratings

The widely used sidewall gratings, although fabrication-friendly, are limited by etching roughness and scattering loss, forming a bottleneck for further performance improvement. Future designs will adopt buried Bragg gratings fabricated through epitaxial growth and multi-step lithography. These structures are expected to substantially reduce backscattering and insertion loss while enabling precise control over higher-order coupling modes, thus improving filter Q-factors and side-lobe suppression ratios, and better scalability in DWDM systems.

9.2.3 Transition from thermo-optic to electro-optic modulation

Currently, MHs are used for phase modulation, which limits response speed and energy efficiency. To meet the demands of future high-speed, low-power photonic systems, we will

explore EO modulation based on selectively doped silicon waveguides. By optimising dopant profiles and carrier distributions, stable and high-speed phase tuning can be achieved via free-carrier injection/depletion mechanisms. This transition is expected to push modulation speeds into the GHz range, significantly boosting the utility of the device in fast-reconfigurable photonic computing and neuromorphic systems.

9.2.4 Development of high-speed characterisation platforms

To align testing conditions with real-world deployment environments, future work will incorporate advanced instrumentation with higher bandwidth and sampling precision. This includes PDs with >70 GHz -3dB bandwidth, high-speed arbitrary waveform generators, ultra-fast oscilloscopes, and bit-error-rate testers. This platform will enable the evaluation of key performance metrics such as spectral flatness, jitter tolerance, insertion loss, dynamic response, and system-level bit-error-rate. These capabilities will facilitate direct comparisons with industrial specifications and support the deployment of the proposed filters in emerging applications such as 6G transceivers, THz front-ends, and CPO.

In summary, the above developments will collectively push the boundaries of device performance and integration from four complementary directions: materials, structure, control mechanisms, and testing environments. These efforts will not only enable the construction of next-generation, high-density, low-power, programmable photonic processing platforms, but also inject new momentum into the industrialisation of technologies in optical communications, MWP, and THz sensing.

References

1. D. M. Pozar, *Microwave Engineering: Theory and Techniques*, Fourth edition, international adaptation (Wiley, 2021).
2. R. Sorrentino and G. Bianchi, *Microwave and RF Engineering*, Microwave and Optical Engineering No. v. 2 (Wiley, 2010).
3. J. Capmany and D. Novak, "Microwave photonics combines two worlds," Nature Photon **1**, 319–330 (2007).
4. J. Yao, "Microwave Photonics," J. Lightwave Technol. **27**, 314–335 (2009).
5. K. L. Fuller, "To see and not be seen," IEE Proc. F Radar Signal Process. UK **137**, 1 (1990).
6. A. J. Seeds and K. J. Williams, "Microwave Photonics," J. Lightwave Technol. **24**, 4628–4641 (2006).
7. D. Marpaung, C. Roeloffzen, R. Heideman, A. Leinse, S. Sales, and J. Capmany, "Integrated microwave photonics: Integrated microwave photonics," Laser & Photonics Reviews **7**, 506–538 (2013).
8. C. Lim, A. Nirmalathas, M. Bakaul, P. Gamage, Ka-Lun Lee, Yizhuo Yang, D. Novak, and R. Waterhouse, "Fiber-Wireless Networks and Subsystem Technologies," J. Lightwave Technol. **28**, 390–405 (2010).
9. R. Waterhouse and D. Novack, "Realizing 5G: Microwave Photonics for 5G Mobile Wireless Systems," IEEE Microwave **16**, 84–92 (2015).
10. H. Chi and J. Yao, "Frequency Quadrupling and Upconversion in a Radio Over Fiber Link," J. Lightwave Technol. **26**, 2706–2711 (2008).
11. D. Dolfi, F. Michel-Gabriel, S. Bann, and J. P. Huignard, "Two-dimensional optical architecture for time-delay beam forming in a phased-array antenna," Opt. Lett. **16**, 255 (1991).
12. B.-M. Jung, J.-D. Shin, and B.-G. Kim, "Optical True Time-Delay for Two-Dimensional X-Band Phased Array Antennas," IEEE Photon. Technol. Lett. **19**, 877–879 (2007).
13. H. Xu, L. Wang, Y. Zu, W. Gou, and Y. Hu, "Application and Development of Fiber Optic Gyroscope Inertial Navigation System in Underground Space," Sensors **23**, 5627 (2023).
14. Z. Li, C. Wang, X. Gui, X. Fu, Y. Wang, Z. Wang, and Y. Wang, "A High-Performance Fiber-Optic Hydrophone for Large Scale Arrays," J. Lightwave Technol. **41**, 4201–4210 (2023).
15. X. Zou, X. Liu, W. Li, P. Li, W. Pan, L. Yan, and L. Shao, "Optoelectronic Oscillators (OEOs) to Sensing, Measurement, and Detection," IEEE J. Quantum Electron. **52**, 1–16 (2016).
16. J. Hervas, A. L. Ricchiuti, W. Li, N. H. Zhu, C. R. Fernandez-Pousa, S. Sales, M. Li, and J. Capmany, "Microwave Photonics for Optical Sensors," IEEE J. Select. Topics Quantum Electron. **23**, 327–339 (2017).
17. J. Yao, "Optoelectronic Oscillators for High Speed and High Resolution Optical Sensing," J. Lightwave Technol. **35**, 3489–3497 (2017).
18. W. N. Ye and Y. Xiong, "Review of silicon photonics: history and recent advances," Journal of Modern Optics **60**, 1299–1320 (2013).
19. H. Subbaraman, X. Xu, A. Hosseini, X. Zhang, Y. Zhang, D. Kwong, and R. T. Chen, "Recent advances in silicon-based passive and active optical interconnects," Opt. Express **23**, 2487 (2015).
20. L. A. Coldren, "Photonic Integrated Circuits for microwave photonics," in *2010 IEEE International Topical Meeting on Microwave Photonics* (IEEE, 2010), pp. 1–4.

21. D. Erickson, S. Mandal, A. H. J. Yang, and B. Cordovez, "Nanobiosensors: optofluidic, electrical and mechanical approaches to biomolecular detection at the nanoscale," Microfluid Nanofluid **4**, 33–52 (2008).
22. P. D'Orazio, "Biosensors in clinical chemistry," Clinica Chimica Acta **334**, 41–69 (2003).
23. X. Fan, I. M. White, S. I. Shopova, H. Zhu, J. D. Suter, and Y. Sun, "Sensitive optical biosensors for unlabeled targets: A review," Analytica Chimica Acta **620**, 8–26 (2008).
24. P. Kozma, F. Kehl, E. Ehrentreich-Förster, C. Stamm, and F. F. Bier, "Integrated planar optical waveguide interferometer biosensors: A comparative review," Biosensors and Bioelectronics **58**, 287–307 (2014).
25. S. Kumar and R. Singh, "Recent optical sensing technologies for the detection of various biomolecules: Review," Optics & Laser Technology **134**, 106620 (2021).
26. M. C. Estevez, M. Alvarez, and L. M. Lechuga, "Integrated optical devices for lab-on-a-chip biosensing applications," Laser & Photonics Reviews **6**, 463–487 (2012).
27. C. Zhao, L. Xu, and L. Liu, "Ultrahigh Sensitivity Mach−Zehnder Interferometer Sensor Based on a Weak One-Dimensional Field Confinement Silica Waveguide," Sensors **21**, 6600 (2021).
28. A. Manolis, E. Chatzianagnostou, G. Dabos, N. Pleros, B. Chmielak, A. L. Giesecke, C. Porschatis, P. J. Cegielski, L. Markey, J.-C. Weeber, A. Dereux, and D. Tsiokos, "Plasmonics co-integrated with silicon nitride photonics for high-sensitivity interferometric biosensing," Opt. Express **27**, 17102 (2019).
29. M. Dubrovsky, M. Blevins, S. V. Boriskina, and D. Vermeulen, "High contrast cleavage detection," Opt. Lett. **46**, 2593 (2021).
30. W. Cheng, S. Ye, B. Yuan, J. H. Marsh, and L. Hou, "Subwavelength Grating Cascaded Microring Resonator Biochemical Sensors with Record-High Sensitivity," ACS Photonics **11**, 3343–3350 (2024).
31. C. Wang, P. Yi, J. Li, H. Dong, C. Chen, D. Zhang, H. Shen, and B. Fu, "Polymer Optical Waveguide Grating-Based Biosensor to Detect Effective Drug Concentrations of Ginkgolide A for Inhibition of PMVEC Apoptosis," Biosensors **11**, 264 (2021).
32. J. Høvik, M. Yadav, J. Wook Noh, and A. Aksnes, "Waveguide asymmetric long-period grating couplers as refractive index sensors," Opt. Express **28**, 23936 (2020).
33. Y. Liang, M. Zhao, Z. Wu, and G. Morthier, "Bimodal Waveguide Interferometer RI Sensor Fabricated on Low-Cost Polymer Platform," IEEE Photonics J. **11**, 1–8 (2019).
34. Y. H. Isayama and H. E. Hernández-Figueroa, "High-Order Multimode Waveguide Interferometer for Optical Biosensing Applications," Sensors **21**, 3254 (2021).
35. R. Dwivedi and A. Kumar, "Refractive Index Sensing Using Silicon-on-Insulator Waveguide Based Directional Coupler," IEEE Sens. Lett. **2**, 1–4 (2018).
36. Q. Quan, D. L. Floyd, I. B. Burgess, P. B. Deotare, I. W. Frank, S. K. Y. Tang, R. Ilic, and M. Loncar, "Single particle detection in CMOS compatible photonic crystal nanobeam cavities," Opt. Express **21**, 32225 (2013).
37. Yi Zou, S. Chakravarty, D. N. Kwong, Wei-Cheng Lai, Xiaochuan Xu, Xiaohui Lin, A. Hosseini, and R. T. Chen, "Cavity-Waveguide Coupling Engineered High Sensitivity Silicon Photonic Crystal Microcavity Biosensors With High Yield," IEEE J. Select. Topics Quantum Electron. **20**, 171–180 (2014).
38. W. Hong, F. Liang, D. Schaak, M. Loncar, and Q. Quan, "Nanoscale Label-free Bioprobes to Detect Intracellular Proteins in Single Living Cells," Sci Rep **4**, 6179 (2014).
39. J. D. Suter, I. M. White, H. Zhu, H. Shi, C. W. Caldwell, and X. Fan, "Label-free quantitative DNA detection using the liquid core optical ring resonator," Biosensors and Bioelectronics **23**, 1003–1009 (2008).

40. L. He, Ş. K. Özdemir, J. Zhu, W. Kim, and L. Yang, "Detecting single viruses and nanoparticles using whispering gallery microlasers," Nature Nanotech **6**, 428–432 (2011).
41. H. Yan, N. Tang, G. A. Jairo, S. Chakravarty, D. A. Blake, and R. T. Chen, "High-sensitivity high-throughput chip based biosensor array for multiplexed detection of heavy metals," in B. L. Miller and B. T. Cunningham, eds. (2016), p. 972507.
42. F. Kish, V. Lal, P. Evans, S. W. Corzine, M. Ziari, T. Butrie, M. Reffle, H.-S. Tsai, A. Dentai, J. Pleumeekers, M. Missey, M. Fisher, S. Murthy, R. Salvatore, P. Samra, S. Demars, N. Kim, A. James, A. Hosseini, P. Studenkov, M. Lauermann, R. Going, M. Lu, J. Zhang, J. Tang, J. Bostak, T. Vallaitis, M. Kuntz, D. Pavinski, A. Karanicolas, B. Behnia, D. Engel, O. Khayam, N. Modi, M. R. Chitgarha, P. Mertz, W. Ko, R. Maher, J. Osenbach, J. T. Rahn, H. Sun, K.-T. Wu, M. Mitchell, and D. Welch, "System-on-Chip Photonic Integrated Circuits," IEEE J. Select. Topics Quantum Electron. **24**, 1–20 (2018).
43. S. Shekhar, W. Bogaerts, L. Chrostowski, J. E. Bowers, M. Hochberg, R. Soref, and B. J. Shastri, "Roadmapping the next generation of silicon photonics," Nat Commun **15**, 751 (2024).
44. S. Arafin and L. A. Coldren, "Advanced InP Photonic Integrated Circuits for Communication and Sensing," IEEE J. Select. Topics Quantum Electron. **24**, 1–12 (2018).
45. S. Liu, Y. Zhang, A. Hariri, A.-R. Al-Hallak, and Z. Zhang, "Fabrication of Ultra-Low-Loss, Dispersion-Engineered Silicon Nitride Photonic Integrated Circuits via Silicon Hardmask Etching," ACS Photonics **12**, 1039–1046 (2025).
46. "RG405 MULTICOMP PRO, Coaxial Cable, Per Metre, Semi Rigid," https://uk.farnell.com/multicomp-pro/rg405/coaxial-cable-rg405-50-ohm-1m/dp/2064901.
47. Z. Xiao, W. Liu, S. Xu, J. Zhou, Z. Ren, and C. Lee, "Recent Progress in Silicon-Based Photonic Integrated Circuits and Emerging Applications," Advanced Optical Materials **11**, 2301028 (2023).
48. Y. Su, Y. Zhang, C. Qiu, X. Guo, and L. Sun, "Silicon Photonic Platform for Passive Waveguide Devices: Materials, Fabrication, and Applications," Adv Materials Technologies **5**, 1901153 (2020).
49. D. Zhu, Z. Xu, and D. Lu, "Athermal AWG with hybrid material structure waveguide," in S. Jian, S. Shen, and K. Okamoto, eds. (2002), p. 485.
50. V. R. Balaji, M. Murugan, S. Robinson, and G. Hegde, "A Novel Hybrid Channel DWDM Demultiplexer Using Two Dimensional Photonic Crystals Meeting ITU Standards," Silicon **14**, 617–628 (2022).
51. X. Zhou, R. Urata, and H. Liu, "Beyond 1Tb/s Datacenter Interconnect Technology: Challenges and Solutions (Invited)," in *Optical Fiber Communication Conference (OFC) 2019* (OSA, 2019), p. Tu2F.5.
52. X. Shen, B. Chen, Y. Zhu, and W. Shi, "Silicon photonic integrated circuits and its application in data center," in *Seventh Symposium on Novel Photoelectronic Detection Technology and Applications*, J. Chu, Q. Yu, H. Jiang, and J. Su, eds. (SPIE, 2021), p. 369.
53. T. Qian, B. Schuler, Y. D. Gupta, M. Deumer, E. Andrianopoulos, N. K. Lyras, M. Kresse, M. Weigel, J. Reck, K. Mihov, P. Winklhofer, C. Keuer, L. V. Emden, M. Amberg, C. Zawadzki, M. Kleinert, S. Nellen, D. D. Felipe, H. Avramopoulos, R. B. Kohlhaas, N. Keil, and M. Schell, "Hybrid Photonic Integrated Circuits for Wireless Transceivers," Photonics **12**, 371 (2025).
54. H. Wang, H. Chai, Z. Lv, Z. Zhang, L. Meng, X. Yang, and T. Yang, "Silicon photonic transceivers for application in data centers," J. Semicond. **41**, 101301 (2020).

55. P. Dong, J. Chen, A. Melikyan, T. Fan, T. Fryett, C. Li, J. Chen, and C. Koeppen, "Silicon Photonics for 800G and Beyond [invited]," in *Optical Fiber Communication Conference (OFC) 2022* (Optica Publishing Group, 2022), p. M4H.1.
56. H. Zhang, M. Li, Y. Zhang, D. Zhang, Q. Liao, J. He, S. Hu, B. Zhang, L. Wang, X. Xiao, N. Qi, and S. Yu, "800 Gbit/s transmission over 1 km single-mode fiber using a four-channel silicon photonic transmitter," Photon. Res. **8**, 1776 (2020).
57. H. He, H. Xue, Y. Sun, F. Liu, and L. Cao, "Design and Realization of Multi-Channel and High-Bandwidth 2.5D Transmitter Integrated With Silicon Photonic MZM," J. Lightwave Technol. **40**, 5201–5215 (2022).
58. B. Corcoran, A. Mitchell, R. Morandotti, L. K. Oxenløwe, and D. J. Moss, "Optical microcombs for ultrahigh-bandwidth communications," Nat. Photon. **19**, 451–462 (2025).
59. L. Chang, S. Liu, and J. E. Bowers, "Integrated optical frequency comb technologies," Nat. Photon. **16**, 95–108 (2022).
60. "Scaling AI Factories with Co-Packaged Optics for Better Power Efficiency," https://developer.nvidia.com/blog/scaling-ai-factories-with-co-packaged-optics-for-better-power-efficiency/.
61. J. S. Fandiño, P. Muñoz, D. Doménech, and J. Capmany, "A monolithic integrated photonic microwave filter," Nature Photon **11**, 124–129 (2017).
62. F. Gao, W. Xie, J. Y. S. Tan, C. Leong, C. Li, X. Luo, and G.-Q. Lo, "Comprehensive Investigation of Thermo-Optic Phase Shifters on a Multi-Layered SiN-on-SOI Platform," J. Lightwave Technol. **41**, 3108–3114 (2023).
63. S. Shi, H. Niu, W. Shi, D. Lin, S. Li, S. Pan, and B. Yun, "Integrated Optical Tunable Delay Line and Microwave Photonic Beamforming Chip: A Review," Laser & Photonics Reviews **19**, 2400663 (2025).
64. L. Yu, P. Wang, P. Ma, L. Cui, Z. Wang, Y. Yang, Y. Zhang, and J. Pan, "Two-dimensional beam scanning of passive optical phased array based on silicon nitride delay line," J. Lightwave Technol. 1–10 (2023).
65. J. Chen, W. Li, Z. Kang, Z. Lin, S. Zhao, D. Lian, J. He, D. Huang, D. Dai, and Y. Shi, "Single soliton microcomb combined with optical phased array for parallel FMCW LiDAR," Nat Commun **16**, 1056 (2025).
66. W. Bogaerts, D. Pérez, J. Capmany, D. A. B. Miller, J. Poon, D. Englund, F. Morichetti, and A. Melloni, "Programmable photonic circuits," Nature **586**, 207–216 (2020).
67. H. Zhang, M. Gu, X. D. Jiang, J. Thompson, H. Cai, S. Paesani, R. Santagati, A. Laing, Y. Zhang, M. H. Yung, Y. Z. Shi, F. K. Muhammad, G. Q. Lo, X. S. Luo, B. Dong, D. L. Kwong, L. C. Kwek, and A. Q. Liu, "An optical neural chip for implementing complex-valued neural network," Nat Commun **12**, 457 (2021).
68. T. Fu, J. Zhang, R. Sun, Y. Huang, W. Xu, S. Yang, Z. Zhu, and H. Chen, "Optical neural networks: progress and challenges," Light Sci Appl **13**, 263 (2024).
69. F. Brückerhoff-Plückelmann, I. Bente, M. Becker, N. Vollmar, N. Farmakidis, E. Lomonte, F. Lenzini, C. D. Wright, H. Bhaskaran, M. Salinga, B. Risse, and W. H. P. Pernice, "Event-driven adaptive optical neural network," Sci. Adv. **9**, eadi9127 (2023).
70. S. Hua, E. Divita, S. Yu, B. Peng, C. Roques-Carmes, Z. Su, Z. Chen, Y. Bai, J. Zou, Y. Zhu, Y. Xu, C. Lu, Y. Di, H. Chen, L. Jiang, L. Wang, L. Ou, C. Zhang, J. Chen, W. Zhang, H. Zhu, W. Kuang, L. Wang, H. Meng, M. Steinman, and Y. Shen, "An integrated large-scale photonic accelerator with ultralow latency," Nature **640**, 361–367 (2025).
71. K. Wu, N. P. O'Malley, S. Fatema, C. Wang, M. Girardi, M. S. Alshaykh, Z. Ye, D. E. Leaird, M. Qi, V. Torres-Company, and A. M. Weiner, "Vernier microcombs for integrated optical atomic clocks," Nat. Photon. **19**, 400–406 (2025).

72. S. Sun, M. W. Harrington, F. Tabatabaei, S. Hanifi, K. Liu, J. Wang, B. Wang, Z. Yang, R. Liu, J. S. Morgan, S. M. Bowers, P. A. Morton, K. D. Nelson, A. Beling, D. J. Blumenthal, and X. Yi, "Microcavity Kerr optical frequency division with integrated SiN photonics," Nat. Photon. **19**, 637–642 (2025).
73. B. Wang, Z. Yang, X. Zhang, and X. Yi, "Vernier frequency division with dual-microresonator solitons," Nat Commun **11**, 3975 (2020).
74. D. Lee, G. Song, C. Lee, C. Lee, and M. Jang, "Reconstructive spectrometer using double-layer disordered metasurfaces," Sci. Adv. **11**, eadv2376 (2025).
75. L. Zhang, M. Zhang, T. Chen, D. Liu, S. Hong, D. Dai, State Key Laboratory for Modern Optical Instrumentation, Center for Optical & Electromagnetic Research, College of Optical Science and Engineering, International Research Center for Advanced Photonics, Zhejiang University, Zijingang Campus, Hangzhou 310058, China, and Ningbo Research Institute, Zhejiang University, Ningbo 315100, China, "Ultrahigh-resolution on-chip spectrometer with silicon photonic resonators," OEA **5**, 210100–210100 (2022).
76. A. Li and Y. Fainman, "On-chip spectrometers using stratified waveguide filters," Nat Commun **12**, 2704 (2021).
77. C. Yao, M. Chen, T. Yan, L. Ming, Q. Cheng, and R. Penty, "Broadband picometer-scale resolution on-chip spectrometer with reconfigurable photonics," Light Sci Appl **12**, 156 (2023).
78. W. Cheng, X. Sun, S. Ye, B. Yuan, Y. Sun, J. H. Marsh, and L. Hou, "Sidewall grating slot waveguide microring resonator biochemical sensor," Opt. Lett. **48**, 5113 (2023).
79. V. Toccafondo and C. J. Oton, "Robust and low-cost interrogation technique for integrated photonic biochemical sensors based on Mach–Zehnder interferometers," Photon. Res. **4**, 57 (2016).
80. Y. Liu, J. Hotten, A. Choudhary, B. J. Eggleton, and D. Marpaung, "All-optimized integrated RF photonic notch filter," Opt. Lett. **42**, 4631 (2017).
81. Y. Xie, G. Liu, J. Liu, Z. Lu, P. J. Poole, P. Zhao, P. Barrios, and L. R. Chen, "Microwave Photonic-assisted Analog-to-digital Converters Using Quantum Dash Mode-locked Laser," J. Lightwave Technol. 1–8 (2025).
82. X. Xue, Y. Xuan, H.-J. Kim, J. Wang, D. E. Leaird, M. Qi, and A. M. Weiner, "Programmable Single-Bandpass Photonic RF Filter Based on Kerr Comb from a Microring," J. Lightwave Technol. **32**, 3557–3565 (2014).
83. M. Ding, Z. Feng, D. Marpaung, X. Zhang, M. Komanec, D. Suslov, D. Dousek, S. Zvanovec, E. R. N. Fokoua, T. D. Bradley, F. Poletti, D. J. Richardson, and R. Slavik, "Optical Fiber Delay Lines in Microwave Photonics: Sensitivity to Temperature and Means to Reduce it," J. Lightwave Technol. **39**, 2311–2318 (2021).
84. S. Hong, L. Zhang, Y. Wang, M. Zhang, Y. Xie, and D. Dai, "Ultralow-loss compact silicon photonic waveguide spirals and delay lines," Photon. Res. **10**, 1 (2022).
85. Y.-F. Gao, Y.-H. He, Y. Li, S. Rouzi, M.-C. Jin, Y. He, and S.-Y. Zhou, "Topological waveguide-cavity coupling system based on valley photonic crystals," Optics & Laser Technology **175**, 110799 (2024).
86. Y. Liu, Z. Qiu, X. Ji, A. Lukashchuk, J. He, J. Riemensberger, M. Hafermann, R. N. Wang, J. Liu, C. Ronning, and T. J. Kippenberg, "A photonic integrated circuit–based erbium-doped amplifier," Science **376**, 1309–1313 (2022).
87. P. Chen, W. Huang, Q. Feng, Y. Liu, and Y.-S. Lin, "MEMS-based metamaterial grating waveguide for tunable optical attenuator and modulator applications," Optics & Laser Technology **156**, 108488 (2022).
88. Q. Yi, G. Cheng, Z. Yan, Q. Li, F. Xu, Y. Zou, T. Li, Y. Sun, Y. Zou, Y. Yu, and L. Shen, "Silicon MMI-based power splitter for multi-band operation at the 1.55 and 2 μm wave bands," Opt. Lett. **48**, 1335 (2023).

89. H. Liu, B. Pan, Y. Huang, J. He, M. Zhang, Z. Yu, L. Liu, Y. Shi, and D. Dai, "Ultra-compact lithium niobate photonic chip for high-capacity and energy-efficient wavelength-division-multiplexing transmitters," gxjzz **4**, 1 (2023).
90. Y. Liu, A. Choudhary, D. Marpaung, and B. J. Eggleton, "Integrated microwave photonic filters," Adv. Opt. Photon. **12**, 485 (2020).
91. A. Prencipe, M. A. Baghban, and K. Gallo, "Tunable Ultranarrowband Grating Filters in Thin-Film Lithium Niobate," ACS Photonics **8**, 2923–2930 (2021).
92. J. Xu, Y. Zhang, X. Guo, Q. Huang, X. Zhang, and Y. Su, "Ultra-narrow passband-tunable filter based on a high-Q silicon racetrack resonator," Opt. Lett. **46**, 5575 (2021).
93. Y. Liu, Y. Chen, L. Wang, Y. Yu, Y. Yu, and X. Zhang, "Tunable and Reconfigurable Microwave Photonic Bandpass Filter Based on Cascaded Silicon Microring Resonators," J. Lightwave Technol. **40**, 4655–4662 (2022).
94. L. Liu, M. Ye, and W. Xue, "Silicon-on-Insulator-Based Narrowband Microwave Photonic Filter With Widely Tunable Bandwidth," J. Lightwave Technol. **41**, 6341–6347 (2023).
95. Y. Ding, S. Tao, X. Wang, C. Shang, A. Pan, C. Zeng, and J. Xia, "Thermo-optic tunable optical filters with GHz-bandwidth and flat-top passband on thin film lithium niobate platform," Opt. Express **30**, 22135 (2022).
96. C. Porzi, M. Reza, P. Ghelfi, M. Sorel, and A. Bogoni, "Silicon-on-Insulator Microwave Photonic Filter With Widely Tunable and Reconfigurable Flat-Top Bandpass Functionality," J. Lightwave Technol. **40**, 6666–6675 (2022).
97. S. Gertler, N. T. Otterstrom, M. Gehl, A. L. Starbuck, C. M. Dallo, A. T. Pomerene, D. C. Trotter, A. L. Lentine, and P. T. Rakich, "Narrowband microwave-photonic notch filters using Brillouin-based signal transduction in silicon," Nat Commun **13**, 1947 (2022).
98. M. Garrett, Y. Liu, M. Merklein, C. T. Bui, C. K. Lai, D.-Y. Choi, S. J. Madden, A. Casas-Bedoya, and B. J. Eggleton, "Integrated microwave photonic notch filter using a heterogeneously integrated Brillouin and active-silicon photonic circuit," Nat Commun **14**, 7544 (2023).
99. H. Xu and Y. Shi, "Flat-Top CWDM (De)Multiplexer Based on MZI With Bent Directional Couplers," IEEE Photon. Technol. Lett. **30**, 169–172 (2018).
100. D. Liu, M. Zhang, Y. Shi, and D. Dai, "Four-Channel CWDM (de)Multiplexers Using Cascaded Multimode Waveguide Gratings," IEEE Photon. Technol. Lett. **32**, 192–195 (2020).
101. X. Shen, C. Li, W. Zhao, H. Li, Y. Shi, and D. Dai, "Ultra-Low-Crosstalk Silicon Arrayed-Waveguide Grating (De)multiplexer with 1.6-nm Channel Spacing," Laser & Photonics Reviews **18**, 2300617 (2024).
102. K. Abdelsalam, E. Ordouie, M. G. Vazimali, F. A. Juneghani, P. Kumar, G. S. Kanter, and S. Fathpour, "Tunable dual-channel ultra-narrowband Bragg grating filter on thin-film lithium niobate," Opt. Lett. **46**, 2730 (2021).
103. O. Daulay, G. Liu, K. Ye, R. Botter, Y. Klaver, Q. Tan, H. Yu, M. Hoekman, E. Klein, C. Roeloffzen, Y. Liu, and D. Marpaung, "Ultrahigh dynamic range and low noise figure programmable integrated microwave photonic filter," Nat Commun **13**, 7798 (2022).
104. W. Zhang and J. Yao, "A fully reconfigurable waveguide Bragg grating for programmable photonic signal processing," Nat Commun **9**, 1396 (2018).
105. S. Hou, P. Chen, M. Shah, I. Briggs, W. Xing, Z. Liu, and L. Fan, "Programmable Optical Filter in Thin-Film Lithium Niobate with Simultaneous Tunability of Extinction Ratio and Wavelength," ACS Photonics **10**, 3896–3900 (2023).
106. L. Liu, L. Zhang, C. Chen, X. Li, Y. Qiu, P. Zhao, C. Hu, and J. Duan, "Programmable Optical Filter Combining a FIR Structure and Intelligent Algorithms," IEEE Photon. Technol. Lett. **36**, 1169–1172 (2024).

107. W. Liu, S. Xu, and C. Lee, "Ultracompact on-chip spectral shaping using pixelated nano-opto-electro-mechanical gratings," Science **389**, 806–810 (2025).
108. R. Das, K. Chen, Y. Xie, and A. P. Knights, "Reconfigurable integrated photonic filters for optical signal processing using a silicon photonic platform," Opt. Lett. **49**, 1345 (2024).
109. Y. Liu, Y. Yu, L. Wang, Y. Yu, and X. Zhang, "Reconfigurable Microwave Photonic Bandpass Filter Based on CROW," J. Lightwave Technol. **42**, 1597–1604 (2024).
110. T. Li, Y. Liu, L. Xing, S. Lang, Z. Ge, D. Han, Z. Hui, H. Du, and H. Shu, "Improved Optical Signal Processing with On-Chip Programmable Filter," Photonics **12**, 416 (2025).
111. P. Zheng, X. Xu, G. Hu, R. Zhang, B. Yun, and Y. Cui, "Integrated Multi-Functional Optical Filter Based on a Self-Coupled Microring Resonator Assisted MZI Structure," J. Lightwave Technol. **39**, 1429–1437 (2021).
112. Sitao Chen, Xin Fu, Jian Wang, Yaocheng Shi, Sailing He, and Daoxin Dai, "Compact Dense Wavelength-Division (De)multiplexer Utilizing a Bidirectional Arrayed-Waveguide Grating Integrated With a Mach–Zehnder Interferometer," J. Lightwave Technol. **33**, 2279–2285 (2015).
113. T. Aihara, T. Hiraki, T. Fujii, K. Takeda, T. Tsuchizawa, T. Kakitsuka, H. Fukuda, and S. Matsuo, "Heterogeneously integrated widely tunable laser using lattice filter and ring resonator on Si photonics platform," Opt. Express **30**, 15820 (2022).
114. D. Liu, C. Zhang, D. Liang, and D. Dai, "Submicron-resonator-based add-drop optical filter with an ultra-large free spectral range," Opt. Express **27**, 416 (2019).
115. Q. Xu, V. R. Almeida, R. R. Panepucci, and M. Lipson, "Experimental demonstration of guiding and confining light in nanometer-size low-refractive-index material," Opt. Lett. **29**, 1626 (2004).
116. X. Wang and C. K. Madsen, "Highly sensitive compact refractive index sensor based on phase-shifted sidewall Bragg gratings in slot waveguide," Appl. Opt. **53**, 96 (2014).
117. X. Wang, J. Flueckiger, S. Schmidt, S. Grist, S. T. Fard, J. Kirk, M. Doerfler, K. C. Cheung, D. M. Ratner, and L. Chrostowski, "A silicon photonic biosensor using phase-shifted Bragg gratings in slot waveguide," Journal of Biophotonics **6**, 821–828 (2013).
118. X. Wu, T. Fan, A. A. Eftekhar, A. H. Hosseinnia, and A. Adibi, "High-Q ultrasensitive integrated photonic sensors based on slot-ring resonator on a 3C-SiC-on-insulator platform," Opt. Lett. **46**, 4316 (2021).
119. Q. Liu, Z. Gu, M. K. Park, and J. Chung, "Experimental demonstration of highly sensitive optical sensor based on grating-assisted light coupling between strip and slot waveguides," Opt. Express **24**, 12549 (2016).
120. P. Steglich, C. Villringer, S. Pulwer, F. Heinrich, J. Bauer, B. Dietzel, C. Mai, A. Mai, M. Casalboni, and S. Schrader, "Hybrid-Waveguide Ring Resonator for Biochemical Sensing," IEEE Sensors J. **17**, 4781–4790 (2017).
121. O. A. Marsh, Y. Xiong, and W. N. Ye, "Slot Waveguide Ring-Assisted Mach–Zehnder Interferometer for Sensing Applications," IEEE J. Select. Topics Quantum Electron. **23**, 440–443 (2017).
122. I. Khodadad, N. Clarke, M. Khorasaninejad, D. Henneke, and S. S. Saini, "Optimization of multiple-slot waveguides for biochemical sensing," Appl. Opt. **53**, 5169 (2014).
123. W. Cheng, X. Sun, S. Ye, B. Yuan, J. Xiong, X. Liu, Y. Sun, J. H. Marsh, and L. Hou, "Double slot micro ring resonators with inner wall angular gratings as ultra-sensitive biochemical sensors," Opt. Express **31**, 20034 (2023).
124. D. S. Akil, P. Hesham, H. A. Attia, M. E. Ahmed, and M. A. Swillam, "Silicon nitride based biosensor using array of coupled multi slot waveguide structure," J. Opt. **27**, 095801 (2025).

125. M. Pi, C. Zheng, R. Bi, H. Zhao, L. Liang, Y. Zhang, Y. Wang, and F. K. Tittel, "Design of a mid-infrared suspended chalcogenide/silica-on-silicon slot-waveguide spectroscopic gas sensor with enhanced light-gas interaction effect," Sensors and Actuators B: Chemical **297**, 126732 (2019).
126. P. T. Lin, S. W. Kwok, H.-Y. G. Lin, V. Singh, L. C. Kimerling, G. M. Whitesides, and A. Agarwal, "Mid-Infrared Spectrometer Using Opto-Nanofluidic Slot-Waveguide for Label-Free On-Chip Chemical Sensing," Nano Lett. **14**, 231–238 (2014).
127. W. Zhou, Z. Cheng, X. Wu, B. Zhu, X. Sun, and H. K. Tsang, "Fully suspended slot waveguides for high refractive index sensitivity," Opt. Lett. **42**, 1245 (2017).
128. X. Sun, D. Dai, L. Thylén, and L. Wosinski, "High-sensitivity liquid refractive-index sensor based on a Mach-Zehnder interferometer with a double-slot hybrid plasmonic waveguide," Opt. Express **23**, 25688 (2015).
129. X. Sun, L. Thylén, and L. Wosinski, "Hollow hybrid plasmonic Mach–Zehnder sensor," Opt. Lett. **42**, 807 (2017).
130. X. Sun, D. Dai, L. Thylén, and L. Wosinski, "Double-Slot Hybrid Plasmonic Ring Resonator Used for Optical Sensors and Modulators," Photonics **2**, 1116–1130 (2015).
131. M. F. O. Hameed, A. S. Saadeldin, E. M. A. Elkaramany, and S. S. A. Obayya, "Label-Free Highly Sensitive Hybrid Plasmonic Biosensor for the Detection of DNA Hybridization," J. Lightwave Technol. **35**, 4851–4858 (2017).
132. R. Halir, P. J. Bock, P. Cheben, A. Ortega-Moñux, C. Alonso-Ramos, J. H. Schmid, J. Lapointe, D. Xu, J. G. Wangüemert-Pérez, Í. Molina-Fernández, and S. Janz, "Waveguide sub-wavelength structures: a review of principles and applications," Laser & Photonics Reviews **9**, 25–49 (2015).
133. J. Gonzalo Wangüemert-Pérez, P. Cheben, A. Ortega-Moñux, C. Alonso-Ramos, D. Pérez-Galacho, R. Halir, I. Molina-Fernández, D.-X. Xu, and J. H. Schmid, "Evanescent field waveguide sensing with subwavelength grating structures in silicon-on-insulator," Opt. Lett. **39**, 4442 (2014).
134. J. Flueckiger, S. Schmidt, V. Donzella, A. Sherwali, D. M. Ratner, L. Chrostowski, and K. C. Cheung, "Sub-wavelength grating for enhanced ring resonator biosensor," Opt. Express **24**, 15672 (2016).
135. H. Yan, L. Huang, X. Xu, S. Chakravarty, N. Tang, H. Tian, and R. T. Chen, "Unique surface sensing property and enhanced sensitivity in microring resonator biosensors based on subwavelength grating waveguides," Opt. Express **24**, 29724 (2016).
136. L. Torrijos-Morán and J. García-Rupérez, "Single-channel bimodal interferometric sensor using subwavelength structures," Opt. Express **27**, 8168 (2019).
137. M. Odeh, K. Twayana, K. Sloyan, J. E. Villegas, S. Chandran, and M. S. Dahlem, "Mode Sensitivity Analysis of Subwavelength Grating Slot Waveguides," IEEE Photonics J. **11**, 1–10 (2019).
138. M. Wang, J. Hiltunen, C. Liedert, S. Pearce, M. Charlton, L. Hakalahti, P. Karioja, and R. Myllylä, "Highly sensitive biosensor based on UV-imprinted layered polymeric–inorganic composite waveguides," Opt. Express **20**, 20309 (2012).
139. L. Ahmadi, M. Hiltunen, J. Hiltunen, S. Aikio, J. Saarinen, S. Honkanen, and M. Roussey, "Influence of an Al_2O_3 surface coating on the response of polymeric waveguide sensors," Opt. Express **25**, 25102 (2017).
140. A. J. Maker, B. A. Rose, and A. M. Armani, "Tailoring the behavior of optical microcavities with high refractive index sol-gel coatings," Opt. Lett. **37**, 2844 (2012).
141. R. Ahmed, A. A. Rifat, A. K. Yetisen, M. S. Salem, S.-H. Yun, and H. Butt, "Optical microring resonator based corrosion sensing," RSC Adv. **6**, 56127–56133 (2016).
142. Y. Ishizaka, S. Makino, T. Fujisawa, and K. Saitoh, "A Metal-Assisted Silicon Slot Waveguide for Highly Sensitive Gas Detection," IEEE Photonics J. **9**, 1–9 (2017).

143. N. Zhong, M. Chen, H. Chang, T. Zhang, Z. Wang, and X. Xin, "Optic fiber with Er3+:YAlO3/SiO2/TiO2 coating and polymer membrane for selective detection of phenol in water," Sensors and Actuators B: Chemical **273**, 1744–1753 (2018).
144. W. Zhang, S. Serna, X. Le Roux, L. Vivien, and E. Cassan, "Highly sensitive refractive index sensing by fast detuning the critical coupling condition of slot waveguide ring resonators," Opt. Lett. **41**, 532 (2016).
145. S. Sun, X. Xiong, J. Liang, Y. Xu, and L. Shen, "Envelope Spectrum of the Subwavelength Grating Slot Waveguide Microring Resonator for High-Sensitivity and Wide-Range Refractive Index Sensing Applications," J. Lightwave Technol. **42**, 5390–5398 (2024).
146. M. Yang, S. Han, H. Gao, K. Fang, S. Zhang, Y. Liu, Y. Yan, X. Hao, M. Zhao, and Z. Wu, "High-sensitivity and wide-range refractive index sensing based on the envelope spectrum of the subwavelength grating waveguide racetrack microring resonator," Opt. Lett. **49**, 5603 (2024).
147. N. Saha and A. Kumar, "Toward 100 Micrometer per Refractive Index Unit Sensitive Sensor Using a Compact Long-Period Grating Inscribed Metal Clad Ridge Waveguide," J. Lightwave Technol. **36**, 2024–2030 (2018).
148. N. Saha and A. Kumar, "Highly Sensitive Refractive Index Sensor Based on Mode Transition in a Dual Resonance Long Period Grating Inscribed Ridge Waveguide," J. Lightwave Technol. **37**, 5576–5582 (2019).
149. A. Tsarev, "Effect of Dispersion-Enhanced Sensitivity in a Two-Mode Optical Waveguide with an Asymmetric Diffraction Grating," Sensors **21**, 5492 (2021).
150. X. Han, X. Han, Y. Shao, Z. Wu, Y. Liang, J. Teng, S. Bo, G. Morthier, and M. Zhao, "Polymer integrated waveguide optical biosensor by using spectral splitting effect," Photonic Sens **7**, 131–139 (2017).
151. P. Azuelos, P. Girault, N. Lorrain, L. Poffo, M. Guendouz, M. Thual, J. Lemaître, P. Pirasteh, I. Hardy, and J. Charrier, "High sensitivity optical biosensor based on polymer materials and using the Vernier effect," Opt. Express **25**, 30799 (2017).
152. Y. Liu, Y. Li, M. Li, and J.-J. He, "High-sensitivity and wide-range optical sensor based on three cascaded ring resonators," Opt. Express **25**, 972 (2017).
153. Y. Chang, B. Dong, Y. Ma, J. Wei, Z. Ren, and C. Lee, "Vernier effect-based tunable mid-infrared sensor using silicon-on-insulator cascaded rings," Opt. Express **28**, 6251 (2020).
154. Y. Zhang, J. Zou, Z. Cao, and J.-J. He, "Temperature-insensitive waveguide sensor using a ring cascaded with a Mach–Zehnder interferometer," Opt. Lett. **44**, 299 (2019).
155. L. Liu, Z. Hu, M. Ye, Z. Yu, C. Ma, and J. Li, "On-Chip Refractive Index Sensor With Ultra-High Sensitivity Based on Sub-Wavelength Grating Racetrack Microring Resonators and Vernier Effect," IEEE Photonics J. **14**, 1–7 (2022).
156. M. F. Limonov, M. V. Rybin, A. N. Poddubny, and Y. S. Kivshar, "Fano resonances in photonics," Nature Photon **11**, 543–554 (2017).
157. L. Fang, L. Gu, J. Zheng, Q. Zhao, X. Gan, and J. Zhao, "Controlling Resonance Lineshapes of a Side-Coupled Waveguide-Microring Resonator," J. Lightwave Technol. **38**, 4429–4434 (2020).
158. Xiaoyan Zhou, Lin Zhang, A. M. Armani, Jing Liu, Xuexin Duan, Daihua Zhang, Hao Zhang, and Wei Pang, "An Integrated Photonic Gas Sensor Enhanced by Optimized Fano Effects in Coupled Microring Resonators With an Athermal Waveguide," J. Lightwave Technol. **33**, 4521–4530 (2015).
159. A. Bera, M. Kuittinen, S. Honkanen, and M. Roussey, "Silicon slot waveguide Fano resonator," Opt. Lett. **43**, 3489 (2018).
160. B. Zhao, A. Jian, M. Li, Y. Xue, K. Wang, Y. Li, L. Sang, T. Yan, and S. Sang, "Fano Resonance Sensor Based on Microhole Array Waveguides for Ultrasensitive Label-Free Biosensing," ACS Sens. **10**, 6263–6271 (2025).

161. L. A. Coldren, S. W. Corzine, and M. Mashanovitch, *Diode Lasers and Photonic Integrated Circuits*, 2nd ed, Wiley Series in Microwave and Optical Engineering No. 218 (Wiley, 2012).
162. H. Kogelnik and C. V. Shank, "Coupled-Wave Theory of Distributed Feedback Lasers," Journal of Applied Physics **43**, 2327–2335 (1972).
163. J. Buus, M.-C. Amann, and D. J. Blumenthal, *Tunable Laser Diodes and Related Optical Sources* (IEEE, 2005).
164. Y. Dai, X. Chen, L. Xia, Y. Zhang, and S. Xie, "Sampled Bragg grating with desired response in one channel by use of a reconstruction algorithm and equivalent chirp," Opt. Lett. **29**, 1333 (2004).
165. Y. Dai, X. Chen, J. Sun, and S. Xie, "Wideband multichannel dispersion compensation based on a strongly chirped sampled Bragg grating and phase shifts," Opt. Lett. **31**, 311 (2006).
166. X.-H. Jia, D.-Z. Zhong, F. Wang, and H.-T. Chen, "Dynamic single-mode and modulation characteristics analyses for λ/4 phase-shifted distributed feedback lasers with chirped grating," Optics Communications **279**, 356–363 (2007).
167. M. J. Strain, S. Thoms, D. S. MacIntyre, and M. Sorel, "Multi-wavelength filters in silicon using superposition sidewall Bragg grating devices," Opt. Lett. **39**, 413 (2014).
168. M. Poulin, Y. Vasseur, F. Trépanier, M. Guy, M. Morin, Y. Painchaud, and J. Rothenberg, "Apodization of a multichannel dispersion compensator by phase modulation coding of a phase mask," in *Optical Fiber Communication Conference and Exposition and The National Fiber Optic Engineers Conference* (Optica Publishing Group, 2005), p. OME17.
169. H. Ishii, Y. Tohmori, Y. Yoshikuni, T. Tamamura, and Y. Kondo, "Multiple-phase shift super structure grating DBR lasers for broad wavelength tuning," IEEE Photon. Technol. Lett. **5**, 613–615 (1993).
170. Y. Nasu and S. Yamashita, "Densification of Sampled Fiber Bragg Gratings Using Multiple-Phase-Shift (MPS) Technique," J. Lightwave Technol. **23**, 1808 (2005).
171. W. H. Loh, F. Q. Zhou, and J. J. Pan, "Sampled fiber grating based-dispersion slope compensator," IEEE Photon. Technol. Lett. **11**, 1280–1282 (1999).
172. T. Tsuchizawa, K. Yamada, H. Fukuda, T. Watanabe, Jun-ichi Takahashi, M. Takahashi, T. Shoji, E. Tamechika, S. Itabashi, and H. Morita, "Microphotonics devices based on silicon microfabrication technology," IEEE J. Select. Topics Quantum Electron. **11**, 232–240 (2005).
173. M. N. Polyanskiy, "Refractiveindex.info database of optical constants," Sci Data **11**, 94 (2024).
174. A. D. Rakić, A. B. Djurišić, J. M. Elazar, and M. L. Majewski, "Optical properties of metallic films for vertical-cavity optoelectronic devices," Appl. Opt. **37**, 5271 (1998).
175. J.-O. Plouchart, "Applications of SOI Technologies to Communication," in *2011 IEEE Compound Semiconductor Integrated Circuit Symposium (CSICS)* (IEEE, 2011), pp. 1–4.
176. V. Lashkaryov Institute of Semiconductor Physics, NAS of Ukraine, 45, prospect Nauky, 03680 Kyiv, Ukraine, T. E. Rudenko, A. N. Nazarov, V. Lashkaryov Institute of Semiconductor Physics, NAS of Ukraine, 45, prospect Nauky, 03680 Kyiv, Ukraine, V. S. Lysenko, and V. Lashkaryov Institute of Semiconductor Physics, NAS of Ukraine, 45, prospect Nauky, 03680 Kyiv, Ukraine, "The advancement of silicon-on-insulator (SOI) devices and their basic properties," SPQEO **23**, 227–252 (2020).
177. Y. Ding, L. Liu, C. Peucheret, and H. Ou, "Fabrication tolerant polarization splitter and rotator based on a tapered directional coupler," Opt. Express **20**, 20021 (2012).
178. "Review on Optical Waveguides," in *Emerging Waveguide Technology* (InTech, 2018).

179. T. Fujisawa, S. Makino, T. Sato, and K. Saitoh, "Low-loss, compact, and fabrication-tolerant Si-wire 90° waveguide bend using clothoid and normal curves for large scale photonic integrated circuits," Opt. Express **25**, 9150 (2017).
180. L. Zhang, L. Jie, M. Zhang, Y. Wang, Y. Xie, Y. Shi, and D. Dai, "Ultrahigh-Q silicon racetrack resonators," Photon. Res. **8**, 684 (2020).
181. V. Van, *Optical Microring Resonators: Theory, Techniques, and Applications*, 0 ed. (CRC Press, 2016).
182. J. E. Saunders, C. Sanders, H. Chen, and H.-P. Loock, "Refractive indices of common solvents and solutions at 1550 nm," Appl. Opt. **55**, 947 (2016).
183. S. TalebiFard, S. Schmidt, W. Shi, W. Wu, N. A. F. Jaeger, E. Kwok, D. M. Ratner, and L. Chrostowski, "Optimized sensitivity of Silicon-on-Insulator (SOI) strip waveguide resonator sensor," Biomed. Opt. Express **8**, 500 (2017).
184. J. Capmany, B. Ortega, and D. Pastor, "A tutorial on microwave photonic filters," J. Lightwave Technol. **24**, 201–229 (2006).
185. N. Ayotte, A. D. Simard, and S. LaRochelle, "Long Integrated Bragg Gratings for SoI Wafer Metrology," IEEE Photon. Technol. Lett. **27**, 755–758 (2015).
186. D. N. Maywar and G. P. Agrawal, "Transfer-matrix analysis of optical bistability in DFB semiconductor laser amplifiers with nonuniform gratings," IEEE J. Quantum Electron. **33**, 2029–2037 (1997).
187. X. Xu, J. Wu, M. Tan, T. G. Nguyen, S. T. Chu, B. E. Little, R. Morandotti, A. Mitchell, and D. J. Moss, "Orthogonally Polarized RF Optical Single Sideband Generation and Dual-Channel Equalization Based on an Integrated Microring Resonator," J. Lightwave Technol. **36**, 4808–4818 (2018).
188. G. Carpintero, R. C. Guzman, C. Gordon, G. Kervella, M. Chitoui, and F. Van Dijk, "Photonic Integrated Circuits for Radio-Frequency Signal Generation," J. Lightwave Technol. **34**, 508–515 (2016).
189. T. Hiraki, T. Aihara, K. Hasebe, K. Takeda, T. Fujii, T. Kakitsuka, T. Tsuchizawa, H. Fukuda, and S. Matsuo, "Heterogeneously integrated III–V/Si MOS capacitor Mach–Zehnder modulator," Nature Photon **11**, 482–485 (2017).
190. M. Clementi, L. Zatti, J. Zhou, M. Liscidini, and C.-S. Brès, "Ultrabroadband Milliwatt-Level Resonant Frequency Doubling on a Chip," Nat Commun **16**, 6164 (2025).
191. J. Chen, C. Tang, M. Jin, Z. Li, Z. Ma, H. Fan, S. Kumar, Y. M. Sua, and Y. Huang, "Efficient Frequency Doubling with Active Stabilization on Chip," Laser & Photonics Reviews **15**, 2100091 (2021).
192. Y. Nasu and S. Yamashita, "Densification of sampled fiber Bragg gratings using multiple-phase-shift (MPS) technique," J. Lightwave Technol. **23**, 1808–1817 (2005).
193. B. Liu, H. Yang, and M. J. Lancaster, "Synthesis of Coupling Matrix for Diplexers Based on a Self-Adaptive Differential Evolution Algorithm," IEEE Trans. Microwave Theory Techn. **66**, 813–821 (2018).
194. Y. Yu, B. Liu, Y. Wang, M. J. Lancaster, and Q. S. Cheng, "A General Coupling Matrix Synthesis Method for All-Resonator Diplexers and Multiplexers," IEEE Trans. Microwave Theory Techn. **68**, 987–999 (2020).
195. Y. Fan, M. Al-Rubaiee, S. Zhu, B. Yuan, X. Sun, Y. Sun, A. E. Kelly, J. H. Marsh, and L. Hou, "Mode-Locked DBR and DFB Lasers With Multiple Phase-Shifted Gratings for THz Generation," J. Lightwave Technol. **43**, 7752–7760 (2025).
196. A. A. Bushra and G. Yi, "Comparative Analysis Review of Pioneering DBSCAN and Successive Density-Based Clustering Algorithms," IEEE Access **9**, 87918–87935 (2021).
197. M. Greenacre, P. J. F. Groenen, T. Hastie, A. I. D'Enza, A. Markos, and E. Tuzhilina, "Principal component analysis," Nat Rev Methods Primers **2**, 100 (2022).
198. M. Li, H. Li, and Y. Painchaud, "Multi-channel notch filter based on a phase-shift phase-only sampled fiber Bragg grating," Opt. Express **16**, 19388 (2008).

199. L. Deng and F. Luo, "Novel optical comb filter based on full-duty-cycle sampled fiber Bragg grating with spectral Talbot effect," Optics Communications **285**, 5132–5137 (2012).
200. J.-J. Guo, M. Li, Y. Deng, N. Huang, J. Liu, and N. Zhu, "Multichannel optical filters with an ultranarrow bandwidth based on sampled Brillouin dynamic gratings," Opt. Express **22**, 4290 (2014).
201. S. Sengupta and S. K. Ghorai, "Ultra-narrow band optical comb filter using Gaussian-sampled fiber Bragg grating with periodic chirp effect," Opt Quant Electron **48**, 482 (2016).
202. M. Han, X. Li, S. Zhang, H. Han, J. Liu, and Z. Yang, "Tunable and channel spacing precisely controlled comb filters based on the fused taper technology," Opt. Express **26**, 265 (2018).